

Washington University in St. Louis

## Washington University Open Scholarship

---

Arts & Sciences Electronic Theses and  
Dissertations

Arts & Sciences

---

Winter 12-15-2014

### Comparison of Conventional and Bayesian Analysis for the Ultrasonic Characterization of Cancellous Bone

Amber Groopman

*Washington University in St. Louis*

Follow this and additional works at: [https://openscholarship.wustl.edu/art\\_sci\\_etds](https://openscholarship.wustl.edu/art_sci_etds)



Part of the [Physics Commons](#)

---

#### Recommended Citation

Groopman, Amber, "Comparison of Conventional and Bayesian Analysis for the Ultrasonic Characterization of Cancellous Bone" (2014). *Arts & Sciences Electronic Theses and Dissertations*. 372. [https://openscholarship.wustl.edu/art\\_sci\\_etds/372](https://openscholarship.wustl.edu/art_sci_etds/372)

This Dissertation is brought to you for free and open access by the Arts & Sciences at Washington University Open Scholarship. It has been accepted for inclusion in Arts & Sciences Electronic Theses and Dissertations by an authorized administrator of Washington University Open Scholarship. For more information, please contact [digital@wumail.wustl.edu](mailto:digital@wumail.wustl.edu).

WASHINGTON UNIVERSITY IN ST. LOUIS

Department of Physics

Dissertation Examination Committee:

James G. Miller, Chair

R. Martin Arthur

Mark S. Conradi

Mark R. Holland

Jonathan I. Katz

Comparison of Conventional and Bayesian Analysis for the Ultrasonic Characterization of  
Cancellous Bone

by

Amber Mae Groopman

A dissertation presented to the  
Graduate School of Arts and Sciences  
of Washington University in  
partial fulfillment of the  
requirements for the degree  
of Doctor of Philosophy

December 2014

St. Louis, Missouri

© Copyright by

Amber M. Groopman

2014

All rights reserved

# Contents

<b>List of Figures</b>	<b>vi</b>
<b>List of Tables</b>	<b>xxi</b>
<b>Acknowledgments</b>	<b>xxiv</b>
<b>Abstract</b>	<b>xxvi</b>
<b>1 Introduction</b>	<b>1</b>
1.1 Background and Motivation . . . . .	1
1.2 Overview of the Dissertation . . . . .	2
Bibliography . . . . .	4
<b>2 Background</b>	<b>5</b>
2.1 Preface . . . . .	5
2.2 Bone Structure and Physiology . . . . .	5
2.3 Osteoporosis . . . . .	8
2.3.1 Prevalence . . . . .	9
2.3.2 Diagnosis . . . . .	9
2.4 Quantitative Ultrasound . . . . .	12
2.4.1 Comparison to DEXA . . . . .	16
2.5 Fast and slow waves in bone . . . . .	18
2.5.1 Theoretical Models . . . . .	19
2.5.2 Complications arising from two wave modes . . . . .	21
2.6 Summary . . . . .	25
Bibliography . . . . .	26
<b>3 Methods of Conventional and Bayesian Analysis</b>	<b>32</b>
3.1 Preface . . . . .	32
3.2 Background . . . . .	33
3.3 Conventional Data Analysis . . . . .	34
3.3.1 Broadband Phase Spectroscopy . . . . .	34
Determining the Experimental Phase Difference . . . . .	37
Kramers-Kronig Relations . . . . .	42
3.3.2 Determination of the Attenuation Coefficient . . . . .	44

3.4	Bayesian Probability Data Analysis . . . . .	51
3.4.1	Background . . . . .	51
3.4.2	Two-mode wave propagation model . . . . .	52
3.4.3	Bayesian parameter estimation . . . . .	55
3.5	Comparison of conventional and Bayesian methods of analysis . . . . .	60
3.6	Other potential complicating factors . . . . .	62
	Bibliography . . . . .	64
<b>4</b>	<b>Effects of Interfering Fast and Slow Waves on the Ultrasonic Properties of Human Calcaneal Bone</b>	<b>69</b>
4.1	Preface . . . . .	69
4.2	Introduction . . . . .	70
4.3	Methods . . . . .	72
4.3.1	Calcaneal sample preparation . . . . .	72
4.3.2	MicroCT measurements . . . . .	72
4.3.3	Ultrasonic measurements . . . . .	75
4.3.4	Bayesian parameter estimation . . . . .	77
4.3.5	Data Analysis . . . . .	79
4.4	Results . . . . .	81
4.4.1	Phase velocity . . . . .	81
4.4.2	Broadband ultrasound attenuation (nBUA) . . . . .	85
4.4.3	Correlation with structural parameters . . . . .	89
4.5	Discussion . . . . .	90
4.6	Conclusions . . . . .	96
4.7	Acknowledgments . . . . .	97
	Bibliography . . . . .	98
<b>5</b>	<b>Simulation of the Effects of Overlapping Fast and Slow Waves on the Apparent Attenuation of Cancellous Bone</b>	<b>100</b>
5.1	Preface . . . . .	100
5.2	Abstract . . . . .	101
5.3	Introduction . . . . .	101
5.4	Methods . . . . .	103
5.4.1	Generating simulated ultrasonic waves . . . . .	103
5.4.2	Methods of analysis of attenuation properties . . . . .	106
	<i>Time-domain analysis of unseparated wave</i> . . . . .	106
	<i>Frequency-domain analysis of separated fast waves and slow waves</i> . . . . .	107
5.5	Results . . . . .	108
5.5.1	Simulated ultrasonic waves . . . . .	108
5.5.2	Time-domain analysis results of unseparated wave . . . . .	108
5.5.3	Frequency-domain analysis results of separated fast waves and slow waves . . . . .	110
5.6	Discussion . . . . .	113

5.7	Acknowledgments . . . . .	120
	Bibliography . . . . .	121
<b>6</b>	<b>Study of Systematically Shortened Equine Cancellous Bone</b>	<b>125</b>
6.1	Introduction . . . . .	125
6.2	Methods . . . . .	126
6.2.1	Data acquisition . . . . .	126
6.2.2	Data analysis . . . . .	129
	Bayesian parameter estimation analysis . . . . .	129
	Conventional analysis . . . . .	132
	Estimation of apparent frequency . . . . .	133
	Estimation of segmental attenuation . . . . .	137
6.3	Results . . . . .	139
6.3.1	Results of Bayesian parameter estimation . . . . .	139
6.3.2	Results of conventional analysis . . . . .	144
6.3.3	Results of apparent frequency . . . . .	148
6.3.4	Results of segmental attenuation . . . . .	150
6.3.5	Trends with sample thickness . . . . .	152
6.4	Discussion and Conclusions . . . . .	164
6.5	Acknowledgments . . . . .	166
	Bibliography . . . . .	167
<b>7</b>	<b>Exploring unexpected sample thickness-dependence using plastic phantoms</b>	<b>168</b>
7.1	Preface . . . . .	168
7.2	Plastics . . . . .	168
7.3	Initial plastic phantom studies . . . . .	169
7.3.1	Checking dependences of the parameters in the Bayesian model . . . . .	174
	Amplitude test . . . . .	175
	Sample length test . . . . .	175
	Additional Bayesian tests . . . . .	176
7.3.2	Noise levels . . . . .	177
7.3.3	Removing Kramers-Kronig requirement . . . . .	180
7.3.4	Explicitly defining A . . . . .	181
7.3.5	Checking for nonlinearities . . . . .	186
7.3.6	Introducing quadratic attenuation term . . . . .	188
7.4	Systematic shortening of Lexan <sup>TM</sup> sample . . . . .	190
7.4.1	Frequency filtering . . . . .	198
7.4.2	Iteration of the Bayesian method . . . . .	204
7.5	Position of sample within the ultrasonic field . . . . .	206
7.6	Systematically varying the surface losses . . . . .	210
7.7	Constant thickness while varying surface losses . . . . .	219
7.8	Effects of Diffraction . . . . .	225

7.9	Effects of receiver location relative to the transmitting transducer . . . . .	246
	Analysis of reference and sample data from same axial locations . . . . .	247
	Analysis of reference and sample data from different axial locations . . . . .	252
7.10	Discussion . . . . .	257
7.11	Summary and conclusions . . . . .	259
	Bibliography . . . . .	262
<b>8</b>	<b>Summary and concluding remarks</b>	<b>263</b>

# List of Figures

2.1	Top picture: bones of the foot. The calcaneus (heel) is circled. Left bottom: A sagittal cross section of an <i>ex vivo</i> human calcaneus harvested from a cadaver donor. A thin layer of cortical bone and some residual soft tissue surround interior cancellous (trabecular) bone. (Photo by Christian C. Anderson, used with permission). Right bottom: a three dimensional image of trabecular bone from a human calcaneus specimen reconstructed from microCT measurements. (Photo by Amber Groopman). . . . .	7
2.2	Diagnostic criteria for bone quality based on bone mineral density (BMD) proposed by the World Health Organization (WHO). The normal distribution of bone mineral density is based on the values for young (30 years old) adult white females. A value of BMD between 1 and 2.5 standard deviations below the mean BMD is classified as low bone mass, which is also referred to as osteopenia. A BMD more than 2.5 standard deviations below the mean is defined as osteoporosis. . . . .	11
2.3	Left: An image of the General Electric Achilles Insight <sup>®</sup> used for heel quantitative ultrasound. The subject's foot (either right or left) is placed between the two transducer housings. Ultrasonic signals are propagated through the calcaneus (heel) bone in the mediolateral direction as illustrated on the right. The patient's information (age, sex, height, weight, etc.) can be input using the LCD touchscreen. The screen also displays an image of the heel bone to ensure correct positioning and displays the results at the end of testing. Photograph of the GE Achilles Insight <sup>®</sup> by Christian Anderson (used with permission). . . . .	14
2.4	Left: Ultrasonic insonification parallel to (or along) the predominant trabecular alignment. Right: Insonification perpendicular to the predominant trabecular alignment. From (Hosokawa and Otani, 1998). . . . .	20
2.5	Panel A: The nearly linear attenuation coefficient of an excised human calcaneus specimen. Panel B: The measured phase velocity (black circles) displays anomalous negative dispersion, which is in disagreement with the positive dispersion predicted by the Kramers-Kronig relations (gray curve). Reprinted with permission from (Anderson, 2010). . . . .	24



3.1	Experimental set-up for a through-transmission experiment that measures the frequency dependence of the phase velocity. The top panel depicts the reference signal in which the ultrasonic pulse travels a distance $L$ through water only before being detected. The bottom panel shows the sample signal which travels the same path as the reference except that a sample of thickness $d$ is inserted between the transducers. . . . .	35
3.2	The effects of shifting the radiofrequency (rf) trace. The top panel shows that if a signal is not shifted (or symmetrized) the phase rapidly changes over the bandwidth. In the bottom panel, the same signal has been shifted using the peak positive criterion, allowing the phase to change more gradually over the bandwidth. . . . .	40
3.3	The effects on the phase velocity results by using different phase sheet offsets ( $m-n$ ). The correct phase sheet is $(m-n) = 0$ , which produces the least amount of dispersion. By changing the phase sheet offset by one integer the phase velocity as a function of frequency changes quite dramatically. . . . .	41
3.4	The phase velocity as determined by phase spectroscopy of the plastic Lexan along with the dispersion prediction by the nearly-local Kramers-Kronig relations with one subtraction. . . . .	44
3.5	The steps needed to determine the attenuation coefficient of the sample. The first step is to calculate the power spectra of the reference and sample traces. The signal loss is obtained by the difference between the sample and reference power spectra. Next the insertion losses, or the losses at the boundaries, must be subtracted from the signal loss. The attenuation coefficient is obtained by then dividing the result of the previous step by the sample thickness. . . . .	48
3.6	The insertion losses of Lexan determined using two methods: (1) the intercept of a least-squares fit to the signal loss vs. frequency curve (gray dashed line) and (2) calculation of the transmission coefficients in the last term of Equation 3.23. The solid black line is the experimentally acquired 2.25 MHz Lexan data. The right panel is a zoomed in portion of the left panel and shows that the intercept of the signal loss curve produces a negative insertion loss. . . . .	50
3.7	Effects of performing conventional one-mode analysis on a simulated mixed-mode signal. The top two rows show individual waves and their respective phase velocities and attenuation coefficients. The bottom row shows the mixed-mode signal resulting from adding signal 1 and signal 2 along with the phase velocity and attenuation coefficient obtained from conventional (one-mode) analysis. Both the phase velocity and attenuation coefficient results of the mixed-mode signal display artifacts caused by the interference of the two waves. . . . .	53
3.8	The two-mode wave propagation model used in the Bayesian probability theory analysis. The incident (input) wave is divided into a fast wave and a slow wave in the bone specimen. The output (mixed-mode) wave is the sum of the fast and slow waves. . . . .	54
3.9	Schematic illustrating the use of the Bayesian algorithm. . . . .	56

4.1	MicroCT images of the eight human calcaneal samples studied. The first column shows the first slice in the volume of interest (VOI). The second column shows the last slice in the VOI. The third column shows the last slice in the VOI after the threshold has been applied (white = bone, black = not bone). The green boxes represent the region of interest segmented for the measurements of bone histomorphometry in each slice. . . . .	74
4.2	Sample holder consisting of a custom-cut piece of high density styrofoam fit into a Delrin frame. The Delrin frame was attached to a computer-controlled motion controller. Photograph by Amber Groopman. . . . .	76
4.3	Bone specimen with raster scan locations. The spacing between sites was approximately 4 mm. Photograph by Amber Groopman. . . . .	77
4.4	Top panel: The acquired sample radiofrequency data (solid black line) along with the model generated with the parameters estimated by the Bayesian algorithm (dashed orange line). Bottom panel: The individual fast wave (red line) and slow wave (blue line) that comprise the model waveform shown in the top panel. . . . .	80
4.5	Left: The phase velocity and dispersion of the 72 sites investigated (9 sites per sample). The black circles represent sites with positive dispersion and the green circles represent sites displaying negative dispersion. Right: The number (out of 9 possible) sites in each sample that displayed negative dispersion using single mode analysis. . . . .	82
4.6	The fast and slow wave phase velocities (N=9 sites) as a function of frequency for bone sample B-4. The red lines represent the fast wave and the blue lines represent the slow wave. Both fast and slow wave phase velocities display positive dispersion as required by the model. . . . .	83
4.7	The fast and slow wave phase velocities for all sites (N=72). The red circles represent the fast wave and the blue circles represent the slow wave. . . . .	84
4.8	The average ( $\pm$ SD) phase velocity at 500 kHz over nine central sites of the fast wave (red squares), slow wave (blue squares), and the unseparated sample wave (black squares). . . . .	84
4.9	The one mode attenuation coefficient as a function of frequency for bone sample B-4. The black lines are the attenuation coefficients at each spatial site and the orange line is the average $\pm$ one SD. For all 9 sites, the attenuation coefficients were approximately linear with frequency. . . . .	85
4.10	The average (N=9) attenuation coefficients obtained from one mode analysis for each of the eight bone samples. . . . .	86
4.11	The fast and slow wave attenuation coefficients (N=9 sites) as functions of frequency for bone sample B-4. The red lines represent the fast wave and the blue lines represent the slow wave. Both fast and slow wave attenuation coefficients were linear with frequency and displayed similar values. . . . .	87
4.12	The nBUA values for the fast and slow waves at all 72 sites. The red circles represent the fast wave and the blue circles represent the slow wave. . . . .	88

4.13	The average normalized slope of attenuation over nine central sites of the fast wave (red squares), slow wave (blue squares), and the unseparated sample wave (black squares). . . . .	88
4.14	The Bayesian-derived parameters plotted against sample porosity. The top plots show the three fast wave parameters and the bottom plots show the three slow wave parameters. Porosity was determined by microCT. Each value shown is the mean of nine independent sites plus or minus one standard deviation. . . . .	90
4.15	The average phase velocity using one mode (phase-spectroscopy) analysis (black squares) and the predicted one mode phase velocity (gray asterisks) using the weighted sum of fast and slow wave velocities found in Eq. 4.6. . . . .	92
4.16	The phase velocities and normalized slopes of attenuation (nBUA) obtained from one mode analysis plotted versus porosity. Porosity was determined by microCT. Each point is the mean plus or minus one standard deviation of nine spatial sites. . . . .	93
4.17	Left: The average ( $N = 9$ ) $\pm$ one standard deviation nBUA values obtained from the one-mode conventional analysis (black squares) and from the one-mode Bayesian analysis (gray diamonds) as a function of sample porosity. Right: The mean difference in $\beta$ , $\Delta\beta$ , between conventional one-mode analysis and Bayesian one-mode analysis (shown in the left panel) plotted versus sample porosity. . . . .	95
5.1	(a) Reference (water-path only) waveform. Simulated sample waveforms traveling through (b) 6 mm, (c) 10 mm and (d) 15 mm of sample. . . . .	109
5.2	The dependence of the attenuation, $\alpha_{time}$ , of the fast wave on propagation distance using the time-domain analysis method. . . . .	110
5.3	The top panels show the sample waveform comprised of overlapping fast and slow waves for sample thicknesses of 6 mm, 10 mm, and 15 mm, respectively. The middle and bottom panels display the individual fast waves and individual slow waves, respectively, for the three sample thicknesses. . . . .	111
5.4	The attenuation coefficient of the separated fast wave, $\alpha_{fast}(f)$ , and slow wave, $\alpha_{slow}(f)$ , at 1 MHz as a function of propagation distance. . . . .	113
5.5	The attenuation behavior as a function of sample thickness results when applying, panel (a): the time-domain method to the unseparated fast wave, panel (b): log-spectral subtraction to the entire sample wave, consisting of overlapping wave modes, panel (c): the time-domain method to the individual fast wave and slow wave, and panel (d): log-spectral subtraction to the separated fast wave and slow wave. . . . .	115
5.6	The attenuation coefficients determined using the frequency-domain technique for the entire sample wave (solid line) and the separated fast and slow waves (dashed lines) for three propagation distances: 6 mm (panel a), 10 mm (panel b), and 15 mm (panel c). . . . .	117

6.1	The equine trabecular specimen was obtained from the distal end of the left radius. The ultrasonic signal was propagated along the main bone axis, which is the predominant trabecular orientation. Adapted from Fujita <i>et al.</i> (2013).	126
6.2	Through-transmission arrangement for the ultrasonic measurements. For each sample thickness, the bone sample was placed in an acoustic tube approximately 75 mm from the transmitting transducer. The two rectangular PVDF transducers were separated by a distance of 100 mm. Figure adapted from Fujita <i>et al.</i> (2013).	127
6.3	Water-path-only reference signal with a center frequency of 1 MHz.	127
6.4	Power spectrum of the reference signal shown in Figure 6.3. Left: The power spectrum around 1 MHz, the center frequency of the transducer. Right: The same power spectrum over a wider frequency range. As is evident from the figure, the reference trace contained high levels of the harmonic frequencies.	128
6.5	Acquired experimental data on the equine sample at 24 different lengths. As the sample thickness decreased, the originally separated fast and slow waves became more overlapped until the received signal appeared to contain only a single wave.	130
6.6	The received signals shown in Figure 6.5 with the maximum voltage normalized to unity for each thickness. This normalization permitted the fast waves present in the longer sample lengths to be visible. As the sample thickness decreased, the location of the fast wave moved closer to the location of the slow wave. The slow wave also shifted to earlier times as the sample thickness changed.	131
6.7	Representative 90% Tukey windows used to separate the fast waves (red) and the slow waves (blue). The specific windows plotted were for sample length $d = 11.8$ mm. Window lengths varied depending on the degree of separation of the fast and slow waves and the systematic variation in frequency of the fast and slow waves.	133
6.8	Average $\pm$ one standard deviation signal loss of the fast waves (red) and slow waves (blue) over 13 sample lengths ranging from $d = 6.0$ mm to 11.8 mm. The gray lines are the linear fits over the usable bandwidth. In principle, the zero - frequency intercepts of the gray lines represent the insertion losses of the fast and slow waves.	134
6.9	The average ( $N = 13$ ) $\pm$ one standard deviation insertion loss for the fast and slow waves as determined by the zero-frequency intercepts of the signal loss curves, as shown in Figure 6.8, for sample thicknesses from 6.0 mm to 11.8 mm.	134
6.10	Fits to the reference power spectrum (black) of Gaussians with $\sigma^2 = 0.105$ MHz <sup>2</sup> (green) and $\sigma^2 = 0.08$ MHz <sup>2</sup> (blue).	136
6.11	The downshifts in the center frequency of the fast and slow waves as determined by Equation 6.1.	137

6.12	Left: The bulk attenuation method referred to as conventional analysis in this thesis. In the bulk method the sample trace is compared to a water-path-only reference trace. In this method, the resulting attenuation is the loss in the whole sample of thickness $d_1$ . Right: The segmental attenuation method, in which the signal at sample thickness $d_1$ is compared to a signal at a sample thickness of $d_2$ . In the segmental method, the resulting attenuation is the loss in the sample thickness $d_1-d_2$ . . . . .	139
6.13	Model results constructed using the parameters estimated from Bayesian probability theory for four representative thicknesses of the equine sample. For each sample thickness: the top panel shows the experimental data along with the model constructed from the Bayesian estimates, the middle panel shows the residual or difference between the data and model, and the bottom panel shows the individual fast and slow waves that make up the model signal. In each panel, the vertical scale was adjusted to facilitate visualizing the signals.	141
6.14	The average value $\pm$ one standard deviation over sample lengths $d = 3.5$ mm to 11.8 mm ( $N = 18$ ) of $c_{fast}$ and $c_{slow}$ as estimated by Bayesian methods. The error bars are too small to be seen. . . . .	143
6.15	The average values $\pm$ one standard deviation over sample lengths $d = 3.5$ mm to 11.8 mm ( $N = 18$ ) of $\beta_{fast}$ and $\beta_{slow}$ as estimated by Bayesian methods. The error bars for the slow wave nBUA are too small to be seen. . . . .	144
6.16	The average value $\pm$ one standard deviation over sample lengths $d = 3.5$ mm to 11.8 mm ( $N = 18$ ) of $A_{fast}$ and $A_{slow}$ as estimated by Bayesian methods. .	145
6.17	Phase velocities as a function of frequency for the fast waves (red) and the slow waves (blue) as determined by conventional analysis methods for sample thicknesses $d = 6.0$ mm to 11.8 mm ( $N = 13$ ). . . . .	146
6.18	Average ( $\pm$ one standard deviation) phase velocities at 1 MHz of the fast waves (left) and the slow waves (right) as determined by conventional analysis methods over sample thicknesses $d = 6.0$ mm to 11.8 mm ( $N = 13$ ). The error bars are too small to be seen on this scale. . . . .	146
6.19	Attenuation coefficients of the fast waves (red) and slow waves (blue) as determined by conventional analysis. The vertical dashed lines show the low and high frequencies of the bandwidth. The slopes of the linear fit between those dashed lines are the nBUA values for the fast and slow waves. . . . .	148
6.20	Average ( $\pm$ one standard deviation) slopes of the attenuation coefficients (nBUA) of the fast waves (left) and slow waves (right) as determined using conventional analysis methods over sample thicknesses $d = 6.0$ mm to 11.8 mm ( $N = 13$ ). . . . .	149
6.21	Average values of $A_{fast}$ and $A_{slow}$ determined using conventional methods over sample thickness $d = 6.0$ mm to 11.8 mm ( $N = 13$ ). $A_{fast}$ and $A_{slow}$ were determined using the insertion loss values shown in Figure 6.9. . . . .	150
6.22	The shifting center frequencies of the fast and slow waves as a function of sample length. The center frequencies were determined by calculating the centroid of the Bayesian-separated fast and slow waves. . . . .	152

6.23	Comparison of the apparent frequencies of the fast waves and the slow waves using three different methods. The squares show the shifting center frequencies of the two waves using the (frequency-domain) centroid of the Bayesian-separated fast and slow waves. The black triangles are results presented in Fujita <i>et al.</i> using time intervals. The gray stars represent the predicted center frequency determined using Equation 6.1. . . . .	153
6.24	Left: Segmental attenuation coefficients of the fast waves at each adjacent 0.5 mm step. The attenuation coefficients shown are for $\Delta d = 0.5$ mm. The squares represent the segmental attenuation coefficient using the frequency-domain method from Equation 6.5. The triangles show the results from Fujita <i>et al.</i> (2013), which determined segmental attenuation coefficients using time-domain methods in Equation 6.4. Right: Average values of the segmental attenuation coefficients of the fast waves for the time-domain method (open triangle) and the frequency-domain method over all sample lengths ( $N = 23$ ) (solid square) and over similar lengths used in the time domain method ( $N = 13$ ) (open square). . . . .	154
6.25	Left: Segmental attenuation coefficients of the slow waves at each adjacent 0.5 mm step. The attenuation coefficients shown are for $\Delta d = 0.5$ mm. The squares represent the segmental attenuation coefficient using the frequency-domain method from Equation 6.5. The triangles show the results from Fujita <i>et al.</i> (2013), which determined segmental attenuation coefficients using time-domain methods in Equation 6.4. Right: Average values of the segmental attenuation coefficients of the slow waves for the time-domain method (open triangle) and the frequency-domain method over all sample lengths ( $N = 23$ ) (solid square) and over similar lengths used in the time domain method ( $N = 13$ ) (open square). . . . .	155
6.26	Segmental attenuation coefficients at 1 MHz of the fast waves (left) and slow waves (right) for $\Delta d = 0.5$ mm, 2 mm, 4 mm, 6 mm, 8 mm, 10 mm, and 11 mm. The black stars show the mean attenuation coefficient at 1 MHz for each value of $\Delta d$ . As the thickness, $\Delta d$ , of the segment increases, the estimate of the attenuation coefficient appears to improve. . . . .	155
6.27	Segmental slopes of the attenuation coefficient (nBUA) of the fast waves (left) and slow waves (right) for $\Delta d = 0.5$ mm, 2 mm, 4 mm, 6 mm, 8 mm, 10 mm, and 11 mm. The black stars show the mean nBUA for each value of $\Delta d$ . As the thickness, $\Delta d$ , of the segment increases, the estimate of the nBUA appears to improve. Note the change in scale for the slow wave nBUA. . . . .	156
6.28	Bayesian estimation of the fast wave (right) and slow wave (left) phase velocities at 1 MHz as a function of sample thickness over all sample lengths, $d = 0.5$ mm to 11.8 mm ( $N = 24$ ). . . . .	158
6.29	Comparison of the phase velocities at 1 MHz obtained by conventional (phase-spectroscopy) methods (squares) and by Bayesian probability methods (circles) for the fast wave (left) and the slow wave (right) at sample thicknesses $d = 6.0$ mm to 11.8 mm ( $N = 13$ ). . . . .	159

6.30	Bayesian estimation of $A_{fast}$ and $A_{slow}$ as a function of sample thickness, ranging from $d = 0.5$ mm to 3.5 mm ( $N = 24$ ).	160
6.31	Insertion losses for the fast and slow waves as determined by the zero-frequency intercepts of the signal loss using conventional analysis methods, for sample thicknesses from 6.0 mm to 11.8 mm ( $N = 13$ ).	161
6.32	Comparison of the $A_{fast}$ and $A_{slow}$ obtained by conventional methods (squares) and by Bayesian probability methods (circles) at sample lengths ranging from $d = 6.0$ mm to 11.8 mm ( $N = 13$ ).	162
6.33	The ratio of $A_{fast}$ to $A_{slow}$ as a function of sample thickness ( $d = 6.0$ mm to 11.8 mm) for both Bayesian (circles) and conventional (squares) analysis.	162
6.34	Bayesian estimation of the fast wave (right) and slow wave (left) normalized broadband ultrasound attenuation (nBUA) as a function of sample thickness.	163
6.35	Comparison of $\beta_{fast}$ (right) and $\beta_{slow}$ (left) obtained by using three techniques: (1) conventional method (squares), (2) Bayesian probability method (circles), and (3) segmental (frequency-domain) method (solid dots) at sample thickness ranging from $d = 6.0$ mm to 11.8 mm. The segmental fast and slow nBUA values shown here are the mean ( $\pm$ one standard deviation) segmental nBUA over all values of $\Delta d$ as shown in Figure 6.27.	164
6.36	The prefactor of the received amplitude (at 1 MHz) of the fast waves (left) and slow waves (right) as determined by conventional (squares) and Bayesian (circles) analysis methods. The prefactor of received amplitude at 1 MHz is determined by Equation 6.7.	165
7.1	The average ( $N = 5$ ) phase velocity using conventional phase spectroscopy methods for the three Lexan <sup>TM</sup> samples ( $d = 9.5$ mm, 19 mm, and 38 mm). The error bars represent plus or minus one standard deviation.	170
7.2	The average ( $N = 5$ ) attenuation coefficient using conventional analysis methods for the three Lexan <sup>TM</sup> samples ( $d = 9.5$ mm, 19 mm, and 38 mm). The error bars represent plus or minus one standard deviation and are too small to be seen.	171
7.3	Comparison of the average ( $N = 5$ ) phase velocity (at 1 MHz) obtained using conventional analysis (black squares) and Bayesian analysis (gray diamonds) for three thicknesses of Lexan <sup>TM</sup> . The error bars represent plus or minus one standard deviation.	172
7.4	Comparison of the average ( $N = 5$ ) slope of attenuation (nBUA) obtained using conventional analysis (black squares) and Bayesian analysis (gray diamonds) for three thicknesses of Lexan <sup>TM</sup> . The error bars represent plus or minus one standard deviation and are too small to be seen.	173
7.5	Comparison of the average ( $N = 5$ ) predicted transmission coefficient-related terms (black squares) and the average Bayesian-estimated $A$ terms (gray diamonds) for three thicknesses of Lexan <sup>TM</sup> . The error bars represent plus or minus one standard deviation and are too small to be seen.	174

7.6	Sample signals from the 9.5 mm Lexan <sup>TM</sup> sample with four different levels of added random noise. . . . .	179
7.7	The total transmission coefficients, accounting for both the front and back surfaces, for pressure and for particle velocity. . . . .	184
7.8	Plot of the transmission coefficient-related term $A$ as a function of mass density $\rho$ determined using Equation 7.3 with $c_{slow} = 2200$ m/s, $c_{ref} = 1486$ m/s, and $\rho_{ref} = 1000$ kg/m <sup>3</sup> . The inset is zoomed in around the actual density of Lexan <sup>TM</sup> ( $\rho \approx 1200$ kg/m <sup>3</sup> ). . . . .	186
7.9	Left: Results of the slope of attenuation using conventional analysis for varying driving voltages (input attenuations) on the three Lexan <sup>TM</sup> phantoms. Right: The results of the slope of attenuation using Bayesian analysis for varying driving voltages. The approximately constant $\beta$ with driving voltage suggest that there are no nonlinear propagation effects. . . . .	187
7.10	Left: Lexan <sup>TM</sup> sample with approximately the same (face) dimensions as the equine sample studied in Chapter 6. This Lexan <sup>TM</sup> phantom was gradually shortened from 30 mm down to 10.5 mm in increments of approximately 2 mm. Right: The experimental configuration used on the Lexan <sup>TM</sup> sample. Measurements were taken using both 1 MHz and 2.25 MHz transducers although only the 2.25 MHz data is presented in this thesis. . . . .	191
7.11	The average ( $N = 4$ ) phase velocity at 2.25 MHz as a function of the 11 thicknesses of Lexan <sup>TM</sup> using conventional analysis (black squares) and Bayesian analysis (gray triangles). The error bars represent plus or minus one standard deviation. . . . .	192
7.12	Power spectra of the reference measurements (black line) and the sample measurements (gray line) acquired for each of the 11 thicknesses of the Lexan <sup>TM</sup> sample using the 2.25 MHz transducers. For each sample thickness, four spatial locations on the sample were measured. . . . .	193
7.13	The average attenuation coefficients for each of the 11 thicknesses of Lexan <sup>TM</sup> . For each thickness of the plastic phantom, four spatial locations were measured. The error bars on each of the 11 attenuation coefficients are too small to be seen. . . . .	194
7.14	The average attenuation coefficients ( $N = 4$ ) at 2.25 MHz for each of the 11 thicknesses of Lexan <sup>TM</sup> . The error bars represent plus or minus one standard deviation and are too small to be seen on most of the measurements. . . . .	195
7.15	The average slope of attenuation ( $N = 4$ ) as a function of the 11 thicknesses of Lexan <sup>TM</sup> using conventional analysis (black squares) and Bayesian analysis (gray triangles). The error bars are too small to be seen on this scale. . . . .	196
7.16	The average ( $N = 4$ ) transmission coefficient-related terms as a function of the 11 thicknesses of Lexan <sup>TM</sup> using Bayesian analysis (gray triangles) and the signal loss intercept (gray diamonds). The predicted values for $A$ are represented by black squares. The error bars represent plus or minus one standard deviation. . . . .	197



7.17	Comparison of the average attenuation coefficient of a systematically shortened Lexan <sup>TM</sup> phantom measured by the laboratory of Mami Matsukawa (blue) and by our laboratory (gray). Conventional analysis was performed by our laboratory on both sets of data. The Matsukawa laboratory acquired data on the Lexan <sup>TM</sup> sample at 0.7, 1, and 2 MHz. Our laboratory acquired data at 2.25 MHz. The error bars represent plus or minus one standard deviation. . . . .	199
7.18	Illustration of a low-pass Butterworth filter with a cutoff frequency of 4 MHz and with an order ranging from $n = 1$ to $n = 10$ . . . . .	200
7.19	Reference (water-path only) radiofrequency signals acquired by Mami Matsukawa's laboratory for the three sets of transducers with center frequencies of approximately 0.7 MHz, 1 MHz, and 2 MHz. These signals showed evidence of higher frequency components. . . . .	201
7.20	The power spectra of the three reference signals shown in Figure 7.19 for the shortened Lexa data acquired by Professor Mami Matsukawa's laboratory using transducers with center frequencies of 0.7 MHz, 1 MHz, and 2 MHz. For all three transducer sets, the reference signal contained significant amounts of higher frequency components that were only 10 to 15 decibels lower than the main frequency lobe. . . . .	201
7.21	The effects of applying two different bandpass Butterworth filters to the 2 MHz reference signal and power spectrum acquired by Professory Matsukawa's laboratory. The original (unfiltered) signals and power spectra are shown in blue while the filtered rf signals and power spectra are shown in red. The specifications of the two Butterworth filters are listed in Table 7.10. . . . .	203
7.22	Comparison of the slopes of attenuation (nBUA) for a subset of the 0.7 MHz, 1 MHz, and 2 MHz data acquired by the Matsukawa laboratory using conventional analysis (black circles), Bayesian analysis with the original (unfiltered) signals (blue squares), Bayesian analysis after filtering with Butterworth filter 1 (red squares), and Bayesian analysis after filtering with Butterworth filter 2 (maroon squares). . . . .	204
7.23	Comparison of the original Bayesian (red squares) and the iterated Bayesian (maroon circles) results for nBUA (left panel) and $A$ (right panel) as a function of sample thickness from measurements on the shortened Lexan <sup>TM</sup> sample. . . . .	206
7.24	The experimental configuration for testing if the position of the sample within the ultrasonic field effects the received signal. The same experiment was performed with 1 MHz and 2.25 MHz center frequency transducers using Lexan <sup>TM</sup> samples with thicknesses of 20 mm and 40 mm. . . . .	207
7.25	Radiofrequency signals that have propagated through a 20 mm thick Lexan <sup>TM</sup> sample positioned at 0.5 inches (top panel), 2 inches (middle panel), and 4 inches (bottom panel) from the transmitting transducer. This data was from the 1 MHz set of transducers. . . . .	209

7.26	Peak-to-peak voltages of the rf signals that have propagated through 20 mm and 40 mm thick Lexan <sup>TM</sup> samples positioned at six distances from the 1 MHz transmitting transducer. . . . .	209
7.27	The experimental configuration for varying the surface losses or the Bayesian $A$ term. The number of Lexan <sup>TM</sup> samples ranged from one sample (2 surfaces) between the transducers up to four samples (8 surfaces). This experiment was expected to alter the insertion losses or $A$ term, but not to alter the attenuation coefficient or nBUA. . . . .	211
7.28	The phase velocities as a function of frequency, determined by conventional phase spectroscopy, for the 15 Lexan <sup>TM</sup> sample combinations listed in Table 7.12.	213
7.29	The average phase velocity of the 15 Lexan <sup>TM</sup> sample combinations and the Kramers-Kronig prediction for the dispersion. Error bars are plus or minus one standard deviation. . . . .	214
7.30	Signal losses of the 15 Lexan <sup>TM</sup> sample combinations as listed in Table 7.12. The different shades of black, red, green, and blue represent different combinations (or total thickness) of samples with 2, 4, 6, and 8 interfaces, respectively.	215
7.31	The attenuation coefficients of the 15 Lexan <sup>TM</sup> sample combinations (black lines) along with the average attenuation coefficient (gray line). Error bars represent plus or minus one standard deviation. . . . .	217
7.32	The phase velocities at 1 MHz as a function of total sample thickness using both conventional phase spectroscopy (squares) and Bayesian analysis (crosses) for the 15 combinations of Lexan <sup>TM</sup> samples listed in Table 7.12. The colors of the squares and crosses represent the number of water-sample interfaces that are present for that data set. . . . .	218
7.33	The slopes of attenuation (nBUA) as a function of total sample thickness using both conventional analysis (squares) and Bayesian analysis (crosses) for the 15 combinations of Lexan <sup>TM</sup> samples listed in Table 7.12. The colors of the squares and crosses represent the number of water-sample interfaces that are present for that data set. . . . .	219
7.34	The transmission coefficient-related $A$ terms as a function of total sample thickness using Bayesian analysis (crosses) and calculated (squares) for the 15 combinations of Lexan <sup>TM</sup> samples listed in Table 7.12. The colors of the squares and crosses represent the number of water-sample interfaces that are present for that data set. . . . .	220
7.35	The transmission coefficient-related $A$ terms as a function of total number of interfaces using impedance differences (black squares), Bayesian analysis (gray crosses), and the zero-frequency intercepts of the signal loss curve (red diamonds) for the 15 combinations of Lexan <sup>TM</sup> samples listed in Table 7.12.	221

7.36	The experimental and sample configurations used for varying the number of interfaces while keeping the overall sample thickness approximately constant. In this experiment, two samples (4 interfaces), three samples (6 surfaces), or four samples (8 surfaces) were placed between two matched, focused 0.5 inch diameter transducers with a nominal center frequency of 1 MHz. All five sample combinations yielded a total sample length of approximately 100 mm.	223
7.37	The radiofrequency (rf) traces acquired from going through two samples (red), three samples (green), or four samples (blue) of Lexan <sup>TM</sup> . As the number of samples (and thus interfaces) increased, the rf traces shifted to the left in time and decreased in peak-to-peak amplitude.	224
7.38	The peak-to-peak amplitude of the radiofrequency signals that propagated through the five Lexan <sup>TM</sup> sample combinations that all had an approximate total sample length of 100 mm, as shown in Figure 7.36. As the number of water-sample interfaces increased, the signal amplitude decreased systematically.	225
7.39	Phase velocity at 1 MHz as a function of the number of interfaces of the five Lexan <sup>TM</sup> sample combinations that all had an approximate total sample length of 100 mm, determined using conventional phase spectroscopy (squares) and Bayesian analysis (crosses). The colors of the squares and crosses represent the number of interfaces present.	226
7.40	Signal losses of the five Lexan <sup>TM</sup> sample combinations that all had an approximate total sample length of 100 mm, determined using conventional log-spectral subtraction. At a given frequency, the signal loss increased with an increasing number of interfaces.	227
7.41	Left: Attenuation coefficients versus frequency of the five Lexan <sup>TM</sup> sample combinations that all had an approximate total sample length of 100 mm. Right: The attenuation coefficients at 1 MHz as a function of the number of interfaces.	228
7.42	Slopes of attenuation (nBUA or $\beta$ ) as a function of the number of interfaces of the five Lexan <sup>TM</sup> sample combinations that all had an approximate total sample length of 100 mm, determined using conventional analysis (squares) and Bayesian analysis (crosses). The colors of the squares and crosses represent the number of interfaces present.	229
7.43	Transmission coefficient-related $A$ terms as a function of the number of interfaces of the five Lexan <sup>TM</sup> sample combinations that all had an approximate total sample length of 100 mm, determined using Bayesian analysis (crosses) or calculated (squares). The colors of the squares and crosses represent the number of interfaces present.	230
7.44	Predicted sample signals for conventional (purple) and Bayesian (orange) methods using their respective values of $A$ , $\beta$ , and $c$ in the propagation model discussed in Section 3.4 for the sample combination with 4 interfaces (left) and 8 interfaces (right). The black signal corresponds to the experimentally acquired trace. The bottom panel of each graph shows the residual (or difference) of the experimental signal and the predicted signals.	231

7.45	The experimental configuration for measuring the attenuation properties of the Lexan <sup>TM</sup> samples implementing the diffraction correction. . . . .	232
7.46	Peak-to-peak amplitude of the sample traces for the six Lexan <sup>TM</sup> phantoms for a typical (not diffraction corrected) measurement and one that has been corrected for diffraction. (a) The peak-to-peak amplitudes shown on a log scale. (b) The same peak-to-peak amplitudes displayed on a linear scale. (c) The difference in P-P amplitude between the not diffraction corrected sample signal and the diffraction corrected sample signal. . . . .	235
7.47	The phase velocities as a function of frequency, determined using conventional phase spectroscopy, for the six thicknesses of Lexan <sup>TM</sup> listed in Table 7.14. The average phase velocity ( $\pm$ one standard deviation) is also displayed. . .	236
7.48	The attenuation coefficients plotted as a function of frequency, determined using conventional analysis methods, for the six thicknesses of Lexan <sup>TM</sup> listed in Table 7.14. The black lines represent the measurements that were not diffraction corrected and the gray lines represent the measurements that were diffraction corrected. . . . .	237
7.49	Comparison of the phase velocity at 1 MHz as a function of sample thickness determined using conventional analysis methods (black squares) and Bayesian analysis methods (gray diamonds). . . . .	240
7.50	Comparison of the slope of the attenuation coefficient (nBUA) as a function of sample thickness determined using conventional and Bayesian analysis methods on both measurements not corrected for diffraction and for measurements corrected for diffraction. . . . .	241
7.51	Comparison of the transmission coefficient-related term ( $A$ ) as a function of sample thickness for the six thicknesses of Lexan <sup>TM</sup> . The predicted $A$ was determined using the impedance difference between water and Lexan <sup>TM</sup> with the experimentally-determined velocity and mass density. Bayesian analysis methods were applied to measurements not corrected for diffraction and to measurements corrected for diffraction. The conventional results were determined by the zero-frequency intercept of the signal loss versus frequency curve.	243
7.52	Comparison of model waveforms to the experimental data from the 60 mm thick Lexan <sup>TM</sup> phantom with no diffraction correction. (a) Model waveform generated using the propagation model with the values determined by conventional analysis for $A$ , $\beta$ , and $c$ . In this panel, $A$ is the predicted value of $A = 0.92$ . (b) Model waveform generated with the values determined by conventional analysis. In this panel, $A$ is the value determined by the zero-frequency intercept of the signal loss versus frequency plot. (c) Model waveform generated using the values of $A$ , $\beta$ , and $c$ estimated by the Bayesian algorithm. . .	245

7.53	Comparison of model waveforms to the experimental data from the 60 mm thick Lexan <sup>TM</sup> phantom that was diffraction corrected. (a) Model waveform generated using the propagation model with the values determined by conventional analysis for $A$ , $\beta$ , and $c$ . In this panel, $A$ is the predicted value of $A = 0.92$ . (b) Model waveform generated with the values determined by conventional analysis. In this panel, $A$ is the value determined by the zero-frequency intercept of the signal loss versus frequency plot. (c) Model waveform generated using the values of $A$ , $\beta$ , and $c$ estimated by the Bayesian algorithm. . . . .	245
7.54	The peak-to-peak amplitude of the reference (water-path-only) signal and the sample signal as a function of distance from the transmitting transducer for measurements made on the 40 mm thick Lexan <sup>TM</sup> phantom. $\Delta L = 0$ mm corresponds to the receiving transducer located at twice the focal length (8 inches) from the transmitting transducer. The third panel shows the difference in peak-to-peak voltage of the reference and sample signals as a function of axial location. . . . .	248
7.55	The predicted and actual zero-frequency intercepts of the signal loss as a function of the axial location of the receiving transducer. Reference and sample measurements were analyzed for the same axial location. . . . .	249
7.56	Left panel: Attenuation coefficient as a function of frequency for the 40 mm Lexan <sup>TM</sup> phantom for data acquired at 9 axial locations. Right panel: The attenuation coefficient at 1 MHz as a function of the axial location of the receiving transducer. Reference and sample measurements were analyzed for the same axial location. . . . .	250
7.57	The slope of the attenuation coefficient (nBUA) determined using conventional and Bayesian analysis methods as a function of the axial location of the receiving transducer. Reference and sample measurements were analyzed at the same axial location. . . . .	251
7.58	The transmission coefficient-related $A$ term determined using conventional and Bayesian analysis methods as a function of the axial location of the receiving transducer. The predicted value of $A$ is also displayed. Reference and sample measurements were analyzed at the same axial location. . . . .	253
7.59	The predicted and actual zero-frequency intercepts of the signal loss as a function of the axial location of the receiving transducer. Sample measurements at the nine axial locations of the receiving transducer were compared to the reference measurement at the typical transducer separation ( $\Delta L = 0$ mm). . . . .	254
7.60	Left panel: Attenuation coefficient as a function of frequency for the 40 mm Lexan <sup>TM</sup> phantom for data acquired at 9 axial locations. Right panel: The attenuation coefficient at 1 MHz as a function of the axial location of the receiving transducer. Sample measurements at the nine axial locations of the receiving transducer were compared to the reference measurement at the typical transducer separation ( $\Delta L = 0$ mm). . . . .	255

7.61	The slope of the attenuation coefficient (nBUA) determined using conventional and Bayesian analysis methods as a function of the axial location of the receiving transducer. Sample measurements at the nine axial locations of the receiving transducer were compared to the reference measurement at the typical transducer separation ( $\Delta L = 0$ mm). . . . .	256
7.62	The transmission coefficient-related term $A$ determined using conventional and Bayesian analysis methods as a function of the axial location of the receiving transducer. The predicted values of $A$ are also displayed. Sample measurements at the nine axial locations of the receiving transducer were compared to the reference measurement at the typical transducer separation ( $\Delta L = 0$ mm). . . . .	258

# List of Tables

2.1	The composition of bone by weight. . . . .	6
4.1	Physical characteristics of the human calcaneal samples. The thickness measurements listed are for the medial-lateral direction and are the mean plus or minus one standard deviation of five measurements. The apparent mass density was calculated from the mass and the mean volume. The bone volume fraction (BV/TV) was determined by microCT measurements. . . . .	73
4.2	Definitions and descriptions of the trabecular bone microstructural parameters obtained from microCT. . . . .	75
4.3	Prior probability distributions for each model parameter. The means and standard deviations define Gaussian distributions that are bounded by the minimum and maximum values. . . . .	78
4.4	Pearson's correlation coefficients between the Bayesian parameters and the bone sample's structural parameters. Porosity is defined as $(1-BV/TV)$ . Negative values imply an inverse relationship. . . . .	89
4.5	The mean (over 9 sites) relative standard deviation (RSD) $\pm$ SD of the six Bayesian parameters for the eight calcaneal samples studied. The RSD was calculated after running all 72 sites through the Bayesian algorithm five times. . . . .	96
5.1	The values used for the six parameters in the propagation model. This set of parameter values was used because it maximized the posterior probability of the model. . . . .	106
6.1	Prior probability distributions for each model parameter. The means and standard deviations define Gaussian distributions that are bounded by the minimum and maximum values. . . . .	132
6.2	Goodness-of-fit of the Bayesian-derived model to the experimentally acquired signals. The coefficient of variation (CV) of the root-mean-square-deviation (RMSD), shown in Equation 5.5, was determined to quantify the fit of the model generated by the Bayesian estimated parameters to the experimental data. . . . .	142

6.3	The mean and standard deviation of the parameters estimated using the Bayesian algorithm for sample thicknesses from 3.5 mm to 11.8 mm (N = 18). The values for sample thicknesses under 3.5 mm were not included due to large variabilities and uncertainties. . . . .	147
6.4	The mean and standard deviation of the parameters determined using conventional analysis methods for sample thicknesses from 6.0 mm to 11.8 mm.	151
6.5	Bone volume fraction (BV/TV) for various positions in the trabecular bone specimen. Position 1- 3 mm was located at the distal end of the specimen, which is where the ultrasonic signal entered. Position 9 - 11 mm was at the proximal end of the specimen, from which the sample was shortened. . . . .	157
7.1	Results of the Bayesian algorithm when a sample signal from the 9.5 mm thick Lexan <sup>TM</sup> sample was artificially modified so that its amplitude was half and one quarter of the original amplitude. . . . .	175
7.2	Results of the Bayesian algorithm on a signal from the 9.5 mm thick Lexan <sup>TM</sup> sample when the sample thickness input into the Bayesian algorithm was changed from the original thickness $d$ to $2*d$ and to $4*d$ . Neither the sample nor reference signals were modified before being input into the Bayesian algorithm. . . . .	176
7.3	Input values of the three parameters in the Bayesian algorithm for the tests listed in Table 7.4. These values were determined by conventional analysis methods performed on the data from the three Lexan <sup>TM</sup> phantoms. . . . .	177
7.4	The tests performed on the Bayesian algorithm using data from the three Lexan <sup>TM</sup> phantoms. For these tests, some of the parameters were set to be the value determined by conventional analysis (listed in Table 7.3) and investigating how that affected the Bayesian estimate of the remaining parameter(s).	178
7.5	Results of the Bayesian algorithm on a signal from the 9.5 mm thick Lexan <sup>TM</sup> sample with four different levels of added random noise. . . . .	178
7.6	Results of the Bayesian algorithm with and without the Kramers-Kronig (KK) requirement on one trace from each of the three Lexan <sup>TM</sup> phantoms. . . . .	181
7.7	The measured mass density and the Bayesian-estimated mass density of the three Lexan <sup>TM</sup> samples. . . . .	185
7.8	Bayesian analysis results using the propagation model with the additional quadratic attenuation term (Eq. 7.8) for the three Lexan <sup>TM</sup> phantoms. The original Bayesian estimates for $A$ , $\beta$ , and $c$ are also shown for comparison. . . . .	189
7.9	Bandpass Butterworth filters applied to the data from the shortened Lexan <sup>TM</sup> sample measured in our laboratory. . . . .	202
7.10	Bandpass Butterworth filters applied to the shortened Lexan <sup>TM</sup> sample measured by the laboratory headed by Professor Mami Matsukawa. . . . .	202
7.11	Comparison of the Bayesian-estimated nBUA when $A$ is allowed to vary and when $A$ is set to 1. . . . .	205
7.12	The combination of Lexan <sup>TM</sup> samples used along with their respective effective length and number of surfaces. . . . .	212



---

7.13	The predicted insertion losses and the predicted transmission coefficient-related $A$ terms for the number of total sample interfaces. $A_2$ , $A_4$ , $A_6$ , and $A_8$ represent the $A$ term for 2, 4, 6, and 8 total interfaces, respectively. . . . .	216
7.14	The mean thicknesses of the six Lexan <sup>TM</sup> samples used in the study on diffraction effects. The diffraction corrections were calculated using Equation 7.15. The negative correction indicates that the receiving transducer must be moved closer to the transmitting transducer for the sample measurements. . . . .	234
7.15	The attenuation coefficient at 1 MHz for the six Lexan <sup>TM</sup> phantoms for a typical (not diffraction corrected) measurement and one that has been corrected for diffraction. The difference between the attenuation coefficient at 1 MHz for the not diffraction corrected measurement and the attenuation coefficient at 1 MHz for the diffraction corrected measurement is displayed in the last column. . . . .	238
7.16	The slope of the attenuation coefficient (nBUA) for the six Lexan <sup>TM</sup> phantoms for a typical (not diffraction corrected) measurement and one that has been corrected for diffraction. The difference between the nBUA for the not diffraction corrected measurement and the nBUA for the diffraction corrected measurement is displayed in the last column. . . . .	239
7.17	The slopes of the attenuation coefficient (nBUA) for the 40 mm thick Lexan <sup>TM</sup> phantom for nine axial locations of the receiving transducer determined using conventional and Bayesian analysis methods. Reference and sample measurements were analyzed at the same axial location. . . . .	252
7.18	The slopes of the attenuation coefficient (nBUA) for the 40 mm thick Lexan <sup>TM</sup> phantom for nine axial locations of the receiving transducer determined using conventional and Bayesian analysis methods. Sample measurements at the nine axial locations of the receiving transducer were compared to the reference measurement at the typical transducer separation ( $\Delta L = 0$ mm). . . . .	257

# Acknowledgments

The work in this dissertation would not have been possible without the encouragement and support of so many people. First and foremost I owe the greatest debt of gratitude to my advisor, Dr. James Miller, who heads the Laboratory for Ultrasonics at Washington University in St. Louis. Jim has been a constant source of encouragement through these long and sometimes difficult years. His enthusiasm and passion for research and teaching have inspired me to be a better scientist and communicator.

I must also thank Dr. Mark Holland, who is one of the kindest people I know. Mark was always unselfish with his time, willing to help me whether it be tracking down a piece of lab equipment, clarifying an analysis technique, or editing a manuscript. His invaluable advice and guidance has made this journey be as enjoyable as it could be. I am also grateful to Dr. Jonathan Katz for his many insights and suggestions with these projects. The help and support provided by Dr. Scott Handley were invaluable to me over these years.

During my time as a graduate student, I had the pleasure of working with many wonderful colleagues, including Chris Anderson, Allyson (Gibson) Anderson, Adam Bauer, Ben Johnson, Joseph Hoffman, Todd Krueger, Michelle Milne, and Chris Lloyd. These people created a wonderful and enjoyable work environment. They were all examples of what an

excellent graduate student should be.

Special thanks go to the staff of the physics department. Sarah Atkin, Debbie Barco, Kara Dix, Julia Hamilton, Christina Saldivar, Christine Tilley, and Tammy White-Devine in the physics office have all helped me through this process in so many ways. Anthony Biondo, Todd Hardt, and Dennis Huelsman in the machine shop were also invaluable to so many of the projects that I have worked on in the lab. Their expertise and patience cannot be overstated.

The investigation presented in Chapter 6 is a direct consequence of the creative contributions of Professor Mami Matsukawa at Doshisha University in Kyoto, Japan and her former and current colleagues. The equine bone data analyzed in Chapter 6 were acquired in Kyoto. Some of the studies presented in Chapters 5 and 7 were motivated by the insights gained from our analysis of Professor Matsukawas data.

I must offer great thanks to my parents, Larry and Crystal Nelson, for their constant love and support. They raised me to value learning and hard work, and continue to serve as my role models. We may not always understand each other, but I know that they love me unconditionally and I hope to make them proud.

At last, I must give the largest thanks to my husband Evan. His constant patience, understanding, and love have kept me balanced and focused these past few years. Without him this journey would have been much more difficult. I eagerly look forward to the rest of our lives together.

## ABSTRACT OF THE DISSERTATION

Comparison of Conventional and Bayesian Analysis for the Ultrasonic Characterization of Cancellous Bone

by

Amber Mae Groopman

Doctor of Philosophy in Physics

Washington University in St. Louis, 2014

Professor James G. Miller, Chair

This dissertation investigates the physics underlying the propagation of ultrasonic waves in cancellous bone. Although quantitative ultrasound has the potential to evaluate bone quality even better than the current gold standard X-ray based modality, its clinical utility has been hampered by the incomplete understanding of the mechanisms governing the interaction between ultrasound and bone. Therefore, studies that extend the understanding of the fundamental physics of the relationship between ultrasound and trabecular bone tissue may result in improved clinical capabilities.

Ultrasonic measurements were carried out on excised human calcaneal specimens in order to study the effects of overlapping fast and slow compressional mode waves on the ultrasonic parameters of attenuation and velocity. Conventional analysis methods were applied to received sample signals that appeared to contain only a single wave mode. The same signals were also analyzed using a Bayesian parameter estimation technique that showed that the signals, which appeared to be only a single wave, could be separated into fast and slow wave components. Results demonstrated that analyzing the data under the assumption that only a single wave mode is present, instead of two interfering waves, yielded a phase velocity that lay between the fast and slow wave velocities and a broadband ultrasound attenuation that was much larger than the ultrasound attenuations of the individual fast and slow waves.

The fast and slow wave ultrasonic parameters were found to correlate with microstructural parameters, including porosity, determined by microCT measurements.

Simulations of fast and slow wave propagation in cancellous bone were carried out to demonstrate the plausibility of a proposed explanation for an anticipated sample-thickness dependence of the apparent attenuation in bovine bone. The results showed that an apparent sample-thickness dependence could arise if the fast and slow waves are not separated sufficiently and if frequency-domain analysis is not performed on broadband data.

The sample-thickness dependence of the ultrasonic parameters was explored further using experimental data acquired on an equine cancellous bone specimen that was systematically shortened. The thickness of the sample varied the degree to which the fast and slow waves overlapped, permitting the use of conventional analysis methods for sufficiently long sample lengths. Bayesian parameter estimation was performed successfully on data from all sample lengths. The ultrasonic parameters obtained by both conventional and Bayesian analysis methods were found unexpectedly to display small, systematic variations with sample thickness.

A very thorough and systematic series of studies were carried out on one-mode Lexan phantoms to investigate the potential cause of the observed sample-thickness dependence. These studies ruled out a series of potential contributors to the sample-thickness dependence, but yielded no clear cause. Although the clinical implications of the small but systematic sample-thickness dependence may be negligible, these studies may provide additional insights into the propagation of ultrasonic waves in cancellous bone and how to maximize the quality of information obtained.

# CHAPTER 1

---

## INTRODUCTION

### 1.1 Background and Motivation

The broad theme of this dissertation is to further investigate the physics underlying the interactions of ultrasound with cancellous (trabecular) bone tissue. Ultrasound is a particularly useful modality for characterizing tissue because the wave propagation characteristics can be related to both the material and the structural properties of the medium being interrogated. Therefore, knowledge of the ultrasonic physics within cancellous bone may provide an improved understanding of the microstructure and composition of trabecular bone thereby leading to an improved ability to detect, diagnose, and monitor the effects of pharmacological intervention on diseases such as osteoporosis.

Osteoporosis is characterized by a decrease in bone quality due to structural deterioration and a decrease in bone mass, leading to an increased risk of fragility-related fractures (Laugier and Haiat, 2011; WHO, 2004; NIH, 2001). The current gold standard technique for measuring bone mineral density and diagnosing osteoporosis is dual energy X-ray absorptiometry

(DXA). Quantitative ultrasound (often referred to as QUS) is an alternative technique for evaluating bone quality. Although quantitative ultrasound has many advantages over X-ray based devices, including portability and modest costs, quantitative ultrasound has only been able to equal the fracture prediction capability of DXA rather than surpassing it, as would be anticipated because ultrasound is sensitive to structure as well as bone mineral density which DXA is not (Krieg *et al.*, 2008). The use of quantitative ultrasound in clinical settings has been hampered, in part, by the structural complexity of bone and its role in the interpretation of QUS data. The mechanisms of how ultrasound interacts with bone are still not well understood. In order to interpret the results of ultrasound measurements, it is helpful to understand the propagation of fast and slow wave compressional modes (which are discussed in Chapter 2) and their propagation paths and characteristics (Laugier and Haiat, 2011).

## 1.2 Overview of the Dissertation

This dissertation is arranged such that each chapter represents a relatively self-contained study or series of studies. However, later chapters use methods or build upon results discussed in earlier chapters.

Chapter 2 provides background on bone, specifically cancellous bone, and the pathophysiology of osteoporosis. A brief overview of the current state of quantitative (bone) ultrasound is discussed, as well as some of the complications that arise due to the multi-mode wave propagation that may occur in trabecular bone.

Chapter 3 presents a description of the methods used to analyze the trabecular bone

data presented in this thesis. The analysis method used depends on the experimental arrangement as well as on the specific properties of the sample itself. This chapter discusses both conventional and Bayesian analysis methods, highlighting similarities and differences between the two methods.

The application of both conventional and Bayesian analysis methods to data acquired from excised human heel data are presented in Chapter 4. The results determined by the two analysis methods are compared in order to investigate the effects of overlapping fast and slow waves on the determination of ultrasonic parameters, such as the phase velocity and the frequency dependence of the attenuation coefficient.

The next three chapters address the unanticipated sample-thickness dependences observed in specific ultrasonic parameters. Chapter 5 uses simulated data to investigate the effects of both overlapping fast and slow wave modes and the choice of method of analysis on measurements of the apparent attenuation as a function of sample thickness.

An study analogous to that presented in Chapter 5 is discussed in Chapter 6 using experimental data acquired on an equine bone specimen that was systematically shortened. The unexpected sample-thickness dependence observed in the ultrasonic parameters determined by both conventional and Bayesian analysis methods in Chapter 6 are explored further in a series of systematic studies using one-mode Lexan phantoms in Chapter 7.

A brief summary and concluding remarks are given in Chapter 8.



## Bibliography

- Krieg, M. A., Barkmann, R., Gonnelli, S., Stewart, A., Bauer, D. C., Del Rio Barquero, L., Kaufman, J. J., Lorenc, R., Miller, P. D., Olszynski, W. P., Poiana, C., Schott, A. M., Lewiecki, E. M., and Hans, D. (2008). “Quantitative ultrasound in the management of osteoporosis: the 2007 iscd official positions”, *J Clinical Densitometry* **11**, 163–187.
- Laugier, P. and Haiat, G., eds. (2011). *Bone quantitative ultrasound* (Springer).
- NIH (2001). “Osteoporosis prevention, diagnosis, and therapy”, *JAMA* **285**, 785–795.
- WHO (2004). “Prevention and management of osteoporosis”, *World Health Organ Tech Rep Ser* **921**, 206.

# CHAPTER 2

---

## BACKGROUND

### 2.1 Preface

This Chapter presents an overview of bone structure and physiology as well as the motivation behind the studies presented in this thesis.

### 2.2 Bone Structure and Physiology

Bone is a highly specialized form of connective tissue that provides not only the shape of the body, but also provides mechanical support, protection of organs and bone marrow, and metabolic pathways related with mineral homeostasis (Laugier and Haiat, 2011). Bone is a composite material consisting of an organic and an inorganic or mineral phase. Table 2.1 details the components of bone by percent weight.

There are two primary types of bone tissue: cortical (compact) bone and cancellous

TABLE 2.1: The composition of bone by weight.

Bone Tissue Composition (% weight)		
70%	22-25%	5-8%
Inorganic/mineral: 95% crystalline hydroxyapatite	Organic: 98% Type I collagen	Water

(trabecular) bone, as shown in Figure 2.1. The adult human skeleton is comprised of  $\sim 80\%$  (by mass) cortical bone and  $\sim 20\%$  trabecular bone (Clarke, 2008). Cortical bone is a dense material with typical porosities of up to 15% (Laugier and Haiat, 2011). This type of bone composes the outer shell of all bones. Due to the low porosity of cortical bone, it can be approximated to be a homogenous, isotropic solid for clinically relevant ultrasound frequencies (0.2 - 1.0 MHz). In contrast, cancellous bone is a highly porous material and is found in the interiors of certain bones such as the hip, spine, wrist, heel, and the end of long bones. The three-dimensional structure of cancellous bone is made of connected rods and/or plates, called trabeculae, interspersed with bone marrow. Trabeculae can range from approximately 50 - 400  $\mu\text{m}$  thick and are typically spaced 700 - 2000  $\mu\text{m}$  apart (Thomsen *et al.*, 2002; Ulrich *et al.*, 1999; Njeh *et al.*, 1999). The porosity of human cancellous bone can range from 60% to over 95% (Hodgkinson *et al.*, 1996; Lee *et al.*, 2003; Wear, 2005). The structure of the trabeculae in cancellous bone depends on the magnitude and direction of the loads applied to it (Whitehouse and Dyson, 1974). For example, if the stress pattern is complicated, then the trabecular network will also likely be complicated and asymmetrical. Whereas in bones where the loading is predominantly uniaxial, the trabeculae will arrange

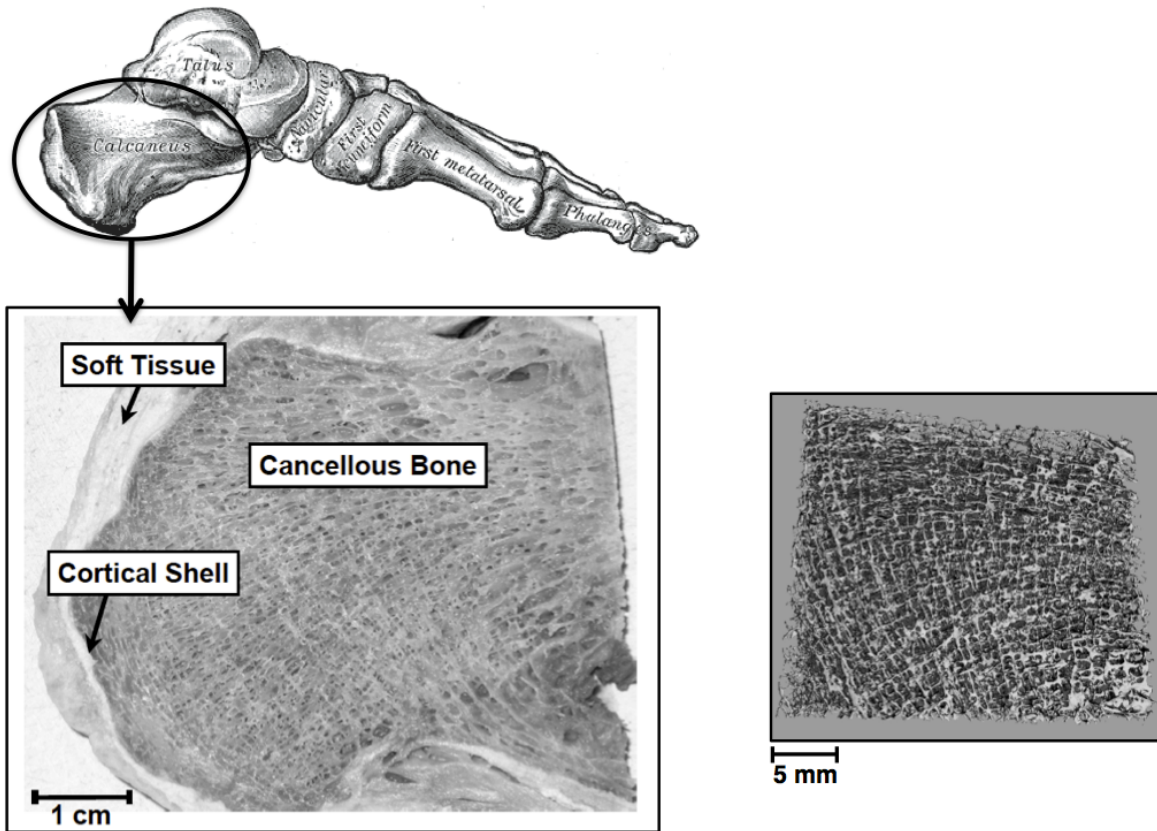


FIGURE 2.1: Top picture: bones of the foot. The calcaneus (heel) is circled. Left bottom: A sagittal cross section of an *ex vivo* human calcaneus harvested from a cadaver donor. A thin layer of cortical bone and some residual soft tissue surround interior cancellous (trabecular) bone. (Photo by Christian C. Anderson, used with permission). Right bottom: a three dimensional image of trabecular bone from a human calcaneus specimen reconstructed from microCT measurements. (Photo by Amber Groopman).

in a more column-like structure (Njeh *et al.*, 1999).

Bone evolves continuously over time due to a process called bone remodeling, in which mature bone tissue is replaced by new bone tissue. Remodeling occurs primarily in the adult skeleton to maintain bone mass and mineral homeostasis, repair microcracks and fractures, and adapt to changes in mechanical loading (Wolff's law) (Wolff, 1986). Activation of bone remodeling depends not only on mechanical stimuli but also on several hormonal stimuli,

such as estrogen and parathyroid hormones, and growth factors (Manolagas and Jilka, 1995; Parfitt, 1984). Specialized bone cells, called osteoclasts, breakdown and resorb the bone matrix at the targeted site. Subsequently, another bone cell known as osteoblasts secrete collagen and proteins into the cleft by resorption. Eventually, this collagen matrix will nucleate and fully mineralize into new bone. The link between bone resorption (osteoclasts) and bone formation (osteoblasts) is referred to as coupling (Njeh *et al.*, 1999). In normal adult bone, the coupling is "perfect" in that bone formation only occurs where bone resorption has already occurred. Both cortical and trabecular bone undergo the remodeling process, although trabecular bone has an eight times higher rate of turnover than that of cortical bone (Njeh *et al.*, 1999; Manolagas and Jilka, 1995). This is because bone turnover is a surface event, and trabecular bone has a much greater surface area than cortical bone.

## 2.3 Osteoporosis

If osteoclast and osteoblast activity become uncoupled in remodeling leading to more bone resorption than formation, the result will be a net loss of bone mass and strength. Cortical bone loss occurs mostly at the endosteal surface, leading to the expansion of the marrow space and thinner cortical thickness. For the more rapidly remodeled trabecular bone, bone loss results in thinner trabeculae and the disconnection of the trabecular network. As this negative imbalance continues over the aging process, bone quality decreases due to structural deterioration and a decrease in bone mass, leading to an increased risk of fragility-related fractures (Laugier and Haiat, 2011). These conditions characterize the disease known as

osteoporosis (WHO, 2004; NIH, 2001).

### 2.3.1 Prevalence

According to the National Osteoporosis Foundation, approximately 54 million Americans over 50 years of age have osteoporosis or osteopenia (low bone mass), with over 12 million having osteoporosis. Of these, approximately eighty percent are women. The clinical endpoint of osteoporosis is a fracture, usually occurring in the wrist, spine, and hip. It was estimated that at least 90% of all hip and spine fractures among elderly white women were attributed to osteoporosis. Hip fractures are the most serious result of osteoporosis and are associated with high degrees of morbidity and mortality. Approximately 20-24% of patients that suffer hip fractures die within the following year due to related complications, and a large percentage of survivors require some kind of living assistance (Leibson *et al.*, 2002; Cooper *et al.*, 1993). Due to the increasing elderly population, the number of people with osteoporosis, and thus the number of osteoporotic-related fractures is expected to increase dramatically, causing a strain on the healthcare system and the economy. In 2008, the medical cost of osteoporosis and related fractures in the United States was estimated at \$22 billion (Blume and Curtis, 2011).

### 2.3.2 Diagnosis

Since there is no current clinical technique that accurately assesses bone quality, the diagnosis of osteoporosis depends on measurements of bone mass, specifically areal bone mineral density (BMD) at the hip or lumbar spine (Gluer *et al.*, 1996; Kanis, 2002). The

current gold standard technique for measuring BMD is dual energy X-ray absorptiometry (DXA), which uses two X-ray beams with different energy peaks in order to differentiate soft tissue from calcified bone. DXA directly measures the bone mineral content (BMC) of the specific site (based on the attenuation of the X-rays), and the bone mineral density (BMD) is derived from dividing the BMC by the area measured. Therefore, the size of the bone can affect the apparent density (Kanis, 2002). Although dual X-ray absorptiometry can be performed on the entire skeleton and on peripheral sites such as the forearms and heels, the gold standard for diagnosis of osteoporosis is BMD measurements of the hip, since it has the highest predictive value for hip fracture (Marshall *et al.*, 1996).

Skeletal mass and density remain relatively constant until approximately 50 years of age (Bonjour and Rizzoli, 1996). The density of bone mineral content in young adults is approximately a normal Gaussian, as illustrated in Figure 2.2. Because of this distribution, the bone density values in subjects can be expressed in terms of standard deviations (SD) from a mean reference population. This number, in units of standard deviations from the mean of a healthy reference population, is defined as a T-score. In 1994, the World Health Organization (WHO) proposed four general diagnostic categories based on hip BMD measurements (T-scores) as assessed by DXA. Normal is classified as a hip BMD greater than one standard deviation below the mean of the young adult female population ( $T\text{-score} \geq -1$ ), low bone mass (osteopenia) is defined as a hip BMD greater than one standard deviation but less than 2.5 standard deviations below the mean ( $-2.5 < T\text{-score} < -1$ ), and osteoporosis is defined as a hip BMD 2.5 or more standard deviations below the young adult mean ( $T\text{-score} \leq -2.5$ ) (Kanis, 2002). Severe or established osteoporosis is classified as osteoporosis along with one

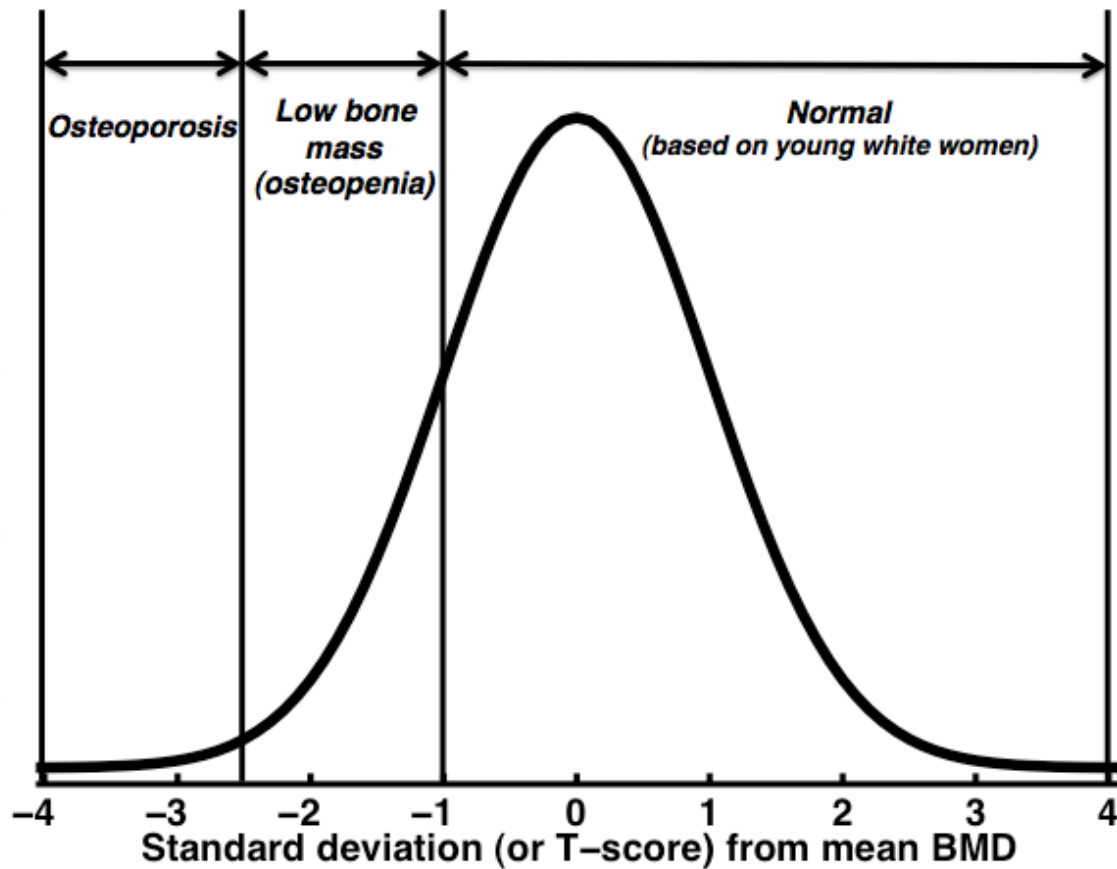


FIGURE 2.2: Diagnostic criteria for bone quality based on bone mineral density (BMD) proposed by the World Health Organization (WHO). The normal distribution of bone mineral density is based on the values for young (30 years old) adult white females. A value of BMD between 1 and 2.5 standard deviations below the mean BMD is classified as low bone mass, which is also referred to as osteopenia. A BMD more than 2.5 standard deviations below the mean is defined as osteoporosis.



or more fragility fractures. Since the WHO classification is based on a reference population of young, healthy, white women, misdiagnoses may occur when applying these definitions to men or other ethnic groups.

In addition to BMD measurements, clinical risk factors are useful in predicting fracture risk and determining the appropriate treatment. There is a tool known as FRAK<sup>®</sup> (Fracture Risk Assessment Tool) that can be used to calculate the individual 10-year risk of fracture (Kanis *et al.*, 2008). It considers factors such as age, sex, height, and weight along with clinical risk factors including previous fragility fractures, premature menopause, family history, smoking, excessive alcohol intake, arthritis, and other causes of secondary osteoporosis (Laugier and Haiat, 2011; Kanis, 2002).

## 2.4 Quantitative Ultrasound

An alternative technique for evaluating bone quality is quantitative ultrasound, which is often referred to as QUS. The first clinical application of ultrasound to bone was in the late 1950s for monitoring fracture healing at the tibia (Siegel *et al.*, 1958). The use of QUS methods in the field of osteoporosis was introduced after a study published in 1984 demonstrated that the slope of the frequency-dependent attenuation at the calcaneus (heel) could discriminate osteoporotic from non-osteoporotic subjects (Langton *et al.*, 1984). Currently, there are a variety of different devices and techniques that have been developed to assess bone quality *in vivo* by measuring the ultrasonic parameters of cancellous or cortical bone at sites such as the calcaneus (Langton *et al.*, 1984), finger phalanges (Fredfeldt, 1986), radius

(Hans *et al.*, 1999), tibia (Foldes *et al.*, 1995), and proximal femur (Barkmann *et al.*, 2008b). The main clinical application of QUS is fracture risk prediction for osteoporosis; however, other bone-related application, such as monitoring fracture healing, may also benefit from QUS measurements (Laugier and Haiat, 2011). Another potential application of QUS would be for monitoring the effectiveness of pharmacological interventions designed to inhibit or reverse bone loss.

Current QUS devices can be classified into two groups based on the type of interrogation employed: transverse transmission and axial transmission. Transverse transmission techniques are more common than axial transmission methods and is the configuration considered throughout this thesis. In the transverse transmission method, two transducers (a transmitter and a receiver) are placed on opposite sides of the site of interest. Typically, these sites are located at the peripheries of the skeleton such as the finger phalanges, the radius (forearm), and, preferentially, the calcaneus (heel). These sites are often used in transverse QUS methods due to their relatively flat surfaces, which aids in coupling and the transmission of the ultrasonic wave through the bone, and the relatively small amount of overlying soft tissue.

The most common clinical QUS devices utilizing transverse transmission are heel bone sonometers, which typically use planar or focused broadband transducers with a center frequency of 0.5 MHz. An image of such a device, the General Electric (GE) Achilles Insight<sup>®</sup>, is shown in Figure 2.3. The Achilles Insight<sup>®</sup> has two fixed transducers: the transmitter is a large, single element transducer that emits a broadband plane wave and the receiver is a 590 element 2D array that permits active focusing. The transducers are

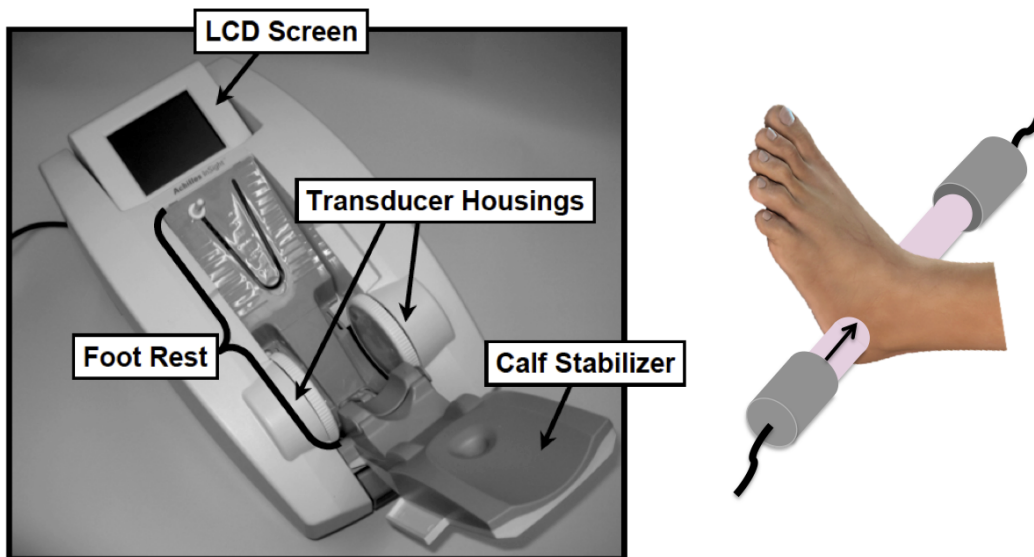


FIGURE 2.3: Left: An image of the General Electric Achilles Insight<sup>®</sup> used for heel quantitative ultrasound. The subject's foot (either right or left) is placed between the two transducer housings. Ultrasonic signals are propagated through the calcaneus (heel) bone in the mediolateral direction as illustrated on the right. The patient's information (age, sex, height, weight, etc.) can be input using the LCD touchscreen. The screen also displays an image of the heel bone to ensure correct positioning and displays the results at the end of testing. Photograph of the GE Achilles Insight<sup>®</sup> by Christian Anderson (used with permission).

encased in temperature-regulated, water-filled membranes that permit better coupling to the patient's skin/heel.

The ultrasound parameters of interest for transverse transmission sonometers are attenuation and velocity, and are obtained using the substitution technique. In the substitution technique, the signal transmitted through the bone of interest is compared to a signal transmitted through a reference medium of known attenuation and speed. For example, the GE Achilles Insight<sup>®</sup> uses a stored reference signal that has traveled through water, maintained at body temperature, a distance corresponding to the transducer separation. In principle, the velocity can be measured using two approaches. The first assumes that the speed is frequency-independent and uses time-of-flight measurements. An issue with this approach is

that various techniques can be used to determine time-of-flight (TOF), such as first arrival point, the first zero-crossing point, or a fixed threshold on the rising front of the received signal (Laugier and Haiat, 2011), leading to inconsistent velocity results among investigators (Nicholson *et al.*, 1996; Wear, 2000). In reality, both attenuation and velocity are frequency-dependent, resulting in the inconsistencies described above when measurements are made in the time-domain as opposed to the frequency-domain (Haiat *et al.*, 2006). The second approach is measuring the frequency-dependent phase velocity. This method eliminates some of the issues present with the time-of-flight velocity, but does require more computation time. Phase velocity measurements will be explained in more detail in Chapter 3. For both methods of determining the velocity, the thickness of the skeletal site must also be known. In some cases, it is simply assumed to be a constant thickness. For the GE Achilles Insight<sup>®</sup>, the heel thickness is assumed to be 40 mm, which may be an underestimate or overestimate of the actual heel thickness, depending on the subject.

Attenuation is usually reported as the slope of a linear fit to the frequency-dependent signal loss, and is referred to as "Broadband Ultrasound Attenuation" (BUA) (Langton *et al.*, 1984; Langton and Njeh, 2008; Wear, 2008). In some instances, BUA is normalized by the bone thickness and is reported as the "normalized Broadband Ultrasound Attenuation (nBUA). Determination of ultrasonic attenuation will be discussed in Chapter 3. Clinical bone sonometers, including the GE Achilles Insight<sup>®</sup>, combine the velocity and BUA measurements into a single index to reflect bone quality. However, there is no standardization for this index among manufacturers (Bonnick, 2004).

In contrast to transverse ultrasound transmission, which is predominantly done on can-

cellous bone sites, axial transmission techniques are performed almost exclusively on cortical bone sites, such as the forearm and tibia. For axial transmission, a transmitter and receiver are aligned along the bone axis to generate and measure guided waves that propagate in the cortical layer of long bones (Laugier and Haiat, 2011). One complication with axial transmission techniques is that the received signals often contain multiple dispersive wave modes making signal analysis challenging. The parameter of interest in current clinical axial transmission devices is the velocity of the first arriving signal (FAS). The FAS velocity was shown, numerically and experimentally, to increase with increasing cortical thickness as long as the cortical thickness was smaller than the wavelength of the compression bulk wave inside the bone (Laugier and Haiat, 2011). Thus, the FAS velocity provides an indirect measure of bone strength.

### 2.4.1 Comparison to DEXA

A limitation of current QUS is that their access is mostly restricted to peripheral sites such as the heel or wrist. In contrast, the X-ray based technology permits measurements at the sites most prone to osteoporotic fracture (hip and spine), allowing for a better assessment of potential fracture risk at those sites. Due to the complexity of the anatomy and the presence of (more) soft tissue, ultrasonic measurements at locations such as the proximal femur (hip) and spine are quite challenging. In recent years, progress has been made to adapt transverse techniques, similar to those of the heel devices, to perform measurements directly at the hip (Barkmann *et al.*, 2008a, 2010).

Another roadblock preventing widespread clinical use of quantitative ultrasound is the

lack of standardization among manufacturers. QUS devices from various manufacturers may have differences in hardware, transducer design, analysis regions, signal processing, modality of transmission (axial or transverse) and coupling agents (Laugier and Haiat, 2011). Due to these differences, there may be significant differences in the measured QUS parameters (BUA and SOS) among the commercial devices. As a consequence, results are not directly comparable between different QUS systems (Cepollaro *et al.*, 2005).

In spite of this, QUS devices may offer advantages over the current gold standard X-ray based devices including the absence of ionizing radiation, portability, and a more modest cost. Additionally, in principle, ultrasound modalities should provide more information about bone quality than DXA because ultrasound wave characteristics are related to both material and structural properties of the propagation medium. In the linear propagation regime, the velocity of an acoustic wave in a medium is directly related the elasticity and density of that medium by

$$v = \sqrt{\frac{M_e}{\rho_e}} \quad (2.1)$$

where  $v$  is the velocity,  $M_e$  is an effective elastic modulus, and  $\rho_e$  is an effective mass density (Shutilov, 1988). The definitions of  $M_e$  and  $\rho_e$  depend on the wave type (bulk compression, bulk shear, guided waves, etc.) and the medium type (liquid, isotropic homogenous solid, anisotropic homogenous solid, etc.). Despite its potential, QUS has only been able to equal the fracture prediction capability of DXA instead of surpassing it (Krieg *et al.*, 2008). The present research is designed to achieve a better understanding of the physics underlying ultrasonic wave propagation in bone with the goal of obtaining additional information on material and structural properties beyond that provided by bone mineral density, thus

improving the evaluation of bone quality and fracture risk.

## 2.5 Fast and slow waves in bone

The presence of two compressional waves propagating in bone, known as fast and slow waves, were first observed in cortical bone by Lakes *et al.* (1983). It was more than 10 years later that Hosokawa and Otani experimentally observed fast and slow waves in bovine cancellous bone (Hosokawa and Otani, 1997). Since then, many other investigators have observed these two wave modes in bovine (Mizuno *et al.*, 2010, 2008; Cardoso *et al.*, 2003; Lee *et al.*, 2003; Lakes *et al.*, 1983; Hosokawa and Otani, 1998), in equine (Fujita *et al.*, 2013), and in human (Mizuno *et al.*, 2009; Sebaa *et al.*, 2006; Nicholson *et al.*, 1998) cancellous bone specimens from various anatomical sites. The complicated, anisotropic, and porous structure of cancellous bone is what seems to give rise to the fast and slow wave modes. From one point of view, the fast wave appears to be associated more with propagation through the hard trabeculae whereas the slow wave appears to be associated more with propagation through the pore spaces. This point of view is supported by studies that observed that the fast wave amplitude increases and the slow wave amplitude decreases with increasing bone volume fraction (Hosokawa and Otani, 1997) and that replacing the fluid filling the pores with marrow, water, or alcohol primarily changes the measured slow wave velocity (Pakula *et al.*, 2009).

The degree of anisotropy and the direction of insonification are factors that influence whether both fast and slow wave modes will be observed in the time domain. Hosokawa

and Otani (1998) found that if the cancellous bone was insonified along (or parallel to) the main trabecular orientation, then separated fast and slow waves would be observed in the received signal, as shown in Figure 2.4. However, as the insonification angle became more perpendicular to the predominant trabecular orientation, the two wave modes became more overlapped, ultimately appearing to merge into a single wave. These results were expanded further by Nicholson *et al.* (1998) who measured the ultrasonic waveforms propagating through human vertebral cancellous bone in three orthogonal directions. In this study, fast and slow waves were only observed in one of the three insonification directions, the one that corresponded to the direction with the highest degree of trabecular orientation. In the other two directions, where the trabecular orientation was not as strong, only one wave was apparent. Other factors that influence the degree to which the fast and slow waves overlap include the porosity of the specimen and the ultrasonic path length (Lee and Choi, 2007; Haiat *et al.*, 2008).

### 2.5.1 Theoretical Models

Several theoretical models have attempted to explain the presence and propagation of fast and slow waves in cancellous bone. The most extensively applied model is Biot theory. The original theory from Biot was introduced in 1956 and modeled wave propagation for fluid-saturated porous rocks (Biot, 1956a,b). The theory is derived by considering the separate motion of the solid elastic frame and the interspersed fluid caused by the ultrasonic wave (Haire and Langton, 1999). Biot theory predicts the existence of two longitudinal waves, which Biot referred to as "waves of the first kind" (now called fast waves) and "waves of



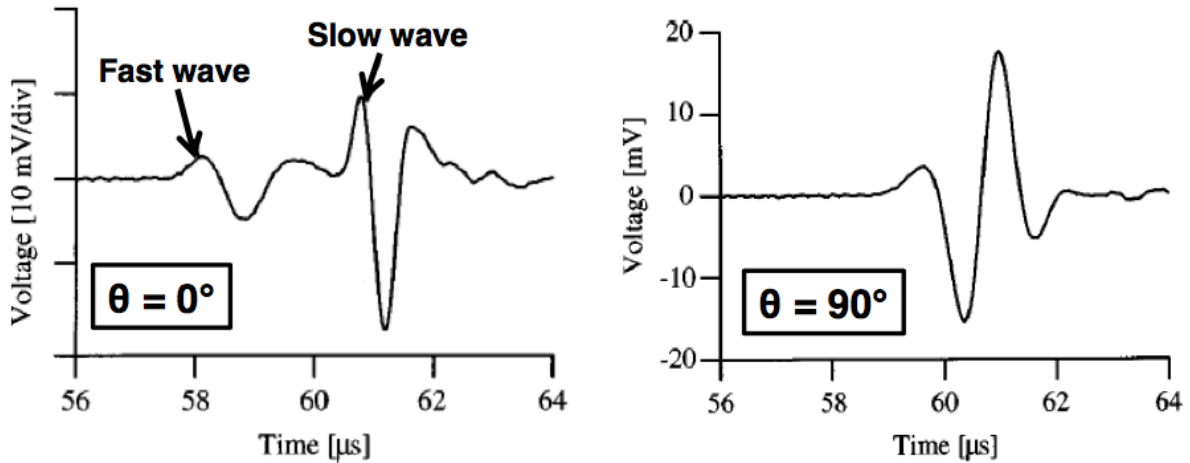


FIGURE 2.4: Left: Ultrasonic insonification parallel to (or along) the predominant trabecular alignment. Right: Insonification perpendicular to the predominant trabecular alignment. From (Hosokawa and Otani, 1998).

the second kind” (now called slow waves). The fast wave in Biot theory represents the fluid and solid moving in-phase, and the slow wave represents the fluid and solid moving out-of-phase. Biot theory was first applied to cancellous bone by McKelvie and Palmer (1991), and has been used extensively since then to predict the velocities of the fast and slow waves as functions of bone porosity (Wear *et al.*, 2005; Williams, 1992; Sebaa *et al.*, 2006; Pakula *et al.*, 2008; Fellah *et al.*, 2008). Although the theoretical predictions for the speeds of the fast and slow waves were found to agree quite well with experimental results, Biot theory predictions for the attenuation were found to deviate significantly from the experimentally measured attenuations. This discrepancy may be due to the fact that Biot’s model only considers absorption loss due to viscous friction at the interfaces between the solid and fluid, and does not account for other sources of energy loss such as scattering, diffraction, or phase cancellation at the receiving transducer (Laugier and Haiat, 2011). One difficulty in the application of Biot theory to cancellous bone is the large number of physical parameters

that must be measured or estimated. For cancellous bone, many of the parameters required are unknown and can only be estimated. Examples include the Young's modulus of the solid, the bulk modulus of the fluid, Poisson's ratio for the solid, the fluid viscosity, and tortuosity.

Schenberg introduced a stratified model, which is composed of periodically alternating solid (trabecular) and fluid layers, that also predicts the existence of fast and slow waves (Schoenberg, 1984). Although this model is easier to implement than Biot theory and can provide insight into the angle-dependency between the trabecular orientation andinsonification angle of the fast and slow wave speeds, it is a highly idealized model that cannot provide a complete understanding of the interaction between ultrasound and the complicated trabecular structures of cancellous bone.

### 2.5.2 Complications arising from two wave modes

The potential presence of two waves in the acquired bone signal can cause complications, especially when analyzing the data and subsequently, interpreting the results. Under certain circumstances, the transit times of the fast and slow waves are sufficiently different that they are separated in the time-domain data. In these cases, windowing can be applied to the data, and the phase velocities and attenuations of the individual wave modes can be measured. Although this approach is relatively straightforward in laboratory settings, clinical bone sonometers may not provide this option (Anderson *et al.*, 2011). In many situations, the transit times of the fast and slow waves are too similar, causing them to overlapping in the acquired signal. The degree to which the fast and slow waves overlap depends on the factors described above, and can vary significantly from sample to sample or even at different sites

within the same sample due to the heterogeneity of trabecular bone (Anderson *et al.*, 2011). If the two wave modes overlap in time, the windowing process becomes difficult because the waves cannot be separated cleanly from each other. Therefore, the ultrasonic properties of the individual fast and slow waves cannot be determined. For some experimental conditions and arrangements, such as perpendicular insonification of the calcaneus, the two waves may overlap to such a degree that it appears as if one wave were propagated. In those cases, the acquired data may be processed assuming only one wave is present, potentially leading to artifacts in the results.

One such artifact of analyzing cancellous bone data comprised of multiple overlapping wave modes under the assumption that only one wave mode is present is negative dispersion (Anderson *et al.*, 2008; Marutyan *et al.*, 2006). Numerous studies of cancellous bone reported finding phase velocities that decreased with increasing frequency (Droin *et al.*, 1998; Haiat *et al.*, 2006; Wear, 2005, 2007; Pakula *et al.*, 2009). This negative dispersion is considered to be anomalous because it conflicts with the causality-imposed Kramers-Kronig relations. For linear ultrasonic wave propagation, the Kramers-Kronig relations connect the real and imaginary parts of the system response. In this context, the real part, which is related to the phase velocity, can be obtained from knowledge of the imaginary part, which is related to the attenuation coefficient (O'Donnell *et al.*, 1981; Mobley *et al.*, 2005; Waters *et al.*, 2003, 2005; Waters and Hoffmeister, 2005). For the frequencies used in clinical bone sonometers, the attenuation coefficient of cancellous bone rises approximately linearly with frequency; this is why the slope of attenuation (BUA) can be used as a clinically relevant parameter. The approximate form of the Kramers-Kronig relations valid for media with linearly increasing

attenuation coefficients predicts that the phase velocity should increase logarithmically with frequency - that is, have positive dispersion. An example of the discrepancy between the Kramers-Kronig prediction and the experimental results for phase velocity is illustrated in Figure 2.5.

Simulations have shown that when two waves with phase velocities and attenuations similar to those exhibited in cancellous bone interfere with one another, negative dispersion can occur even though the apparent attenuation coefficient remains approximately linear with frequency (Anderson *et al.*, 2011). The mixed-mode signal can exhibit anomalous dispersion even though the individual wave modes that comprise it each exhibit positive dispersion, in accordance with the Kramers-Kronig relations.

Since overlapping fast and slow waves may cause artifacts in phase velocity measurements of cancellous bone, it is reasonable to assume that they might also cause artifacts in the attenuation measurements. The effects of overlapping wave modes on measurements of the attenuation coefficient of human calcaneal bone are explored in Chapter 4.

If the interference of fast and slow waves are responsible for artifacts such as negative dispersion, then methods for separating the individual waves from acquired data containing overlapped fast and slow waves may prove useful. Such methods may improve the assessment of bone quality and fracture risk by permitting the individual fast and slow waves to be analyzed in place of or in addition to the analysis of the composite wave. It is possible that the ultrasonic properties of the fast wave alone or the slow wave alone may correlate more strongly to microstructural properties of trabecular bone than the ultrasonic properties of the entire received signal. One such method for recovering the properties of the separated

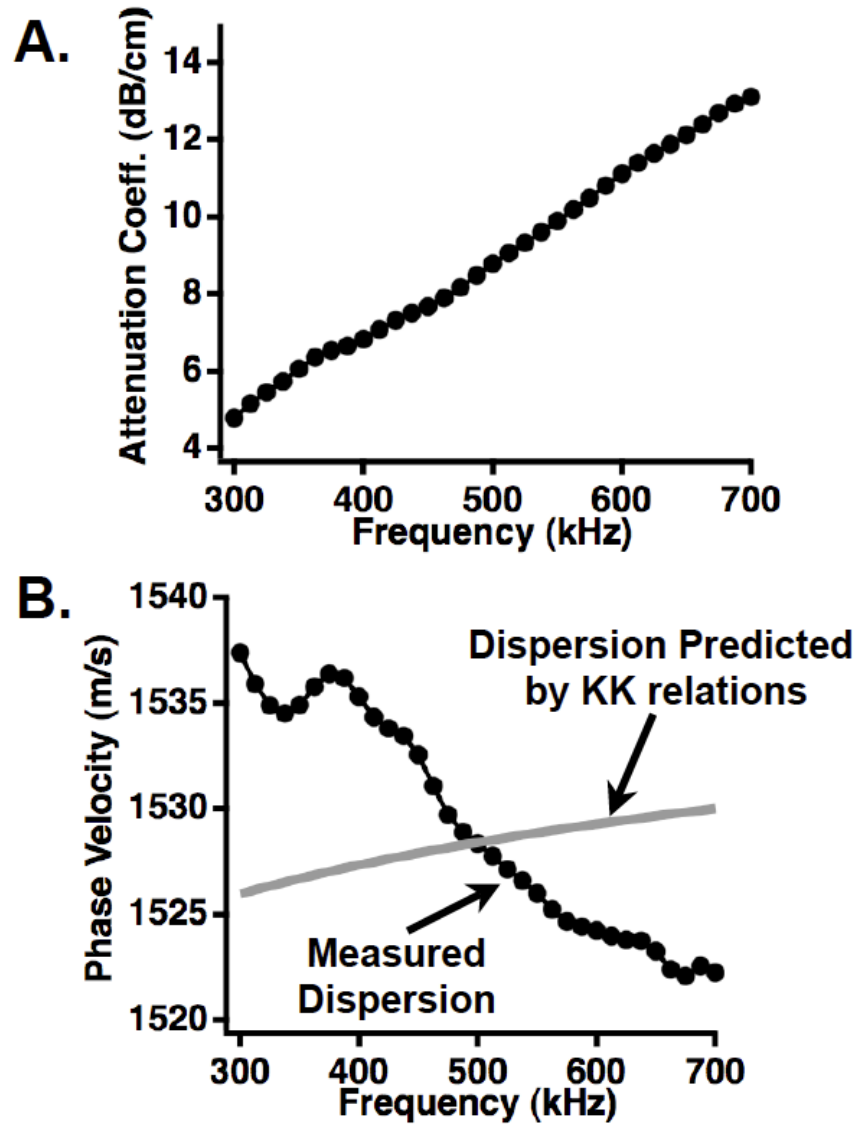


FIGURE 2.5: Panel A: The nearly linear attenuation coefficient of an excised human calcaneus specimen. Panel B: The measured phase velocity (black circles) displays anomalous negative dispersion, which is in disagreement with the positive dispersion predicted by the Kramers-Kronig relations (gray curve). Reprinted with permission from (Anderson, 2010).

fast and slow waves makes use of Bayesian probability theory, which will be discussed in Chapter 3.

## 2.6 Summary

Quantitative ultrasound techniques and devices have been gradually introduced into clinical practice, although this has mainly occurred in countries outside the United States where DXA systems are less widely available. The use of quantitative ultrasound in clinical settings has been hampered, in large part, by the structural complexity of bone and its role in the interpretation of QUS data. The mechanisms of how ultrasound interacts with bone are still not well understood. In order to interpret the results of ultrasound measurements, it is first necessary to understand the propagation of ultrasound through bone with identification of the different (fast and slow) wave modes and their exact propagation paths and characteristics (Laugier and Haiat, 2011).

The use of multi-element receiving transducers may provide an improved approach for evaluating the interaction mechanisms between ultrasound and bone. Although some clinical bone sonometers have receiver arrays, many devices, especially those in developing countries, are limited to the use of a single element receiving transducer. The higher cost of fabrication and the need for substantially increased processing capabilities limit the use of systems with receiving transducer arrays. As a consequence, this dissertation explores approaches for maximizing the quality of information that can be obtained from data acquired with single element receiving transducers.

## Bibliography

- Anderson, C. C. (2010), “Physics of ultrasonic wave propagation in bone and heart characterized using Bayesian parameter estimation”, Ph.D. thesis, Washington University in St. Louis.
- Anderson, C. C., Bauer, A. Q., Marutyan, K. R., Holland, M. R., Pakula, M., Bretthorst, G. L., Laugier, P., and Miller, J. G. (2011), “Phase velocity of cancellous bone: Negative dispersion arising from fast and slow waves, interference, diffraction, and phase cancellation at piezoelectric receiving elements”, in “Bone quantitative ultrasound”, , edited by Laugier, P. and Haiat, G., chapter 12 (Springer Science), 319–330.
- Anderson, C. C., Marutyan, K. R., Holland, M. R., Wear, K. A., and Miller, J. G. (2008), “Interference between wave modes may contribute to the apparent negative dispersion observed in cancellous bone”, *J Acoust Soc Am* **124**, 1781–89.
- Barkmann, R., Dencks, S., Laugier, P., Padilla, F., Brixen, K., Ryg, J., Seekamp, A., Mahlke, L., Bremer, A., Heller, M., and Gluer, C. C. (2010), “Femur ultrasound (FemUS) - first clinical results on hip fracture discrimination and estimation of femoral BMD”, *Osteoporos Int* **21(6)**, 969–976.
- Barkmann, R., Laugier, P., Moser, U., Dencks, S., Klausner, M., Padilla, F., Haiat, G., and Gluer, C. C. (2008a), “A device for in vivo measurements of quantitative ultrasound variables at the human proximal femur”, *IEEE Trans Ultrason Ferroelectr Freq Control* **55(6)**, 1197–1204.
- Barkmann, R., Laugier, P., Moser, U., Dencks, S., Klausner, M., Padilla, F., Haiat, G., Heller, M., and Gluer, C. C. (2008b), “In vivo measurements of ultrasound transmission through the human proximal femur”, *Ultrasound Med Biol* **34(7)**, 1186–1190.
- Biot, M. (1956a), “Theory of propagation of elastic waves in a fluid saturated porous solid: I. low frequency range”, *J Acoust Soc Am* **28**, 168–178.
- Biot, M. (1956b), “Theory of propagation of elastic waves in a fluid saturated porous solid: II. higher frequency range”, *J Acoust Soc Am* **28**, 179–191.
- Blume, S. W. and Curtis, J. R. (2011), “Medical costs of osteoporosis in the elderly Medicare population”, *Osteoporos Int* **22(6)**, 1835–1844.
- Bonjour, J. P. and Rizzoli, R. (1996), “Bone acquisition in adolescence”, in “Osteoporosis”, , edited by Marcus, R., Feldman, D., and J., K. (Academic Press), 465–76.
- Bonnick, S. L. (2004), *Bone densitometry in clinical practice* (Humana Press).
- Cardoso, L., Teboul, F., Sedel, L., Oddou, C., and Meunier, A. (2003), “In vitro acoustic waves propagation in human and bovine cancellous bone”, *J Bone Miner Res* **18(10)**, 1803–1812.

- Cepollaro, C., Gonnelli, S., Montagnani, A., Caffarelli, C., Cadirni, A., Martini, S., and Nuti, R. (2005), “In vivo performance evaluation of the Achilles Insight QUS device”, *J Clinical Densitometry* **8**(3), 341–346.
- Clarke, B. (2008), “Normal bone anatomy and physiology”, *Clin J Am Soc Nephrol* **3**, S131–S139.
- Cooper, C., Atkinson, E. J., Jacobsen, S. J., O’Fallon, W. M., and Melton, L. J. (1993), “Population-based study of survival after osteoporotic fractures”, *Am J Epidemiol* **137**(9), 1001–1005.
- Droin, P., Berger, G., and Laugier, P. (1998), “Velocity dispersion of acoustic waves in cancellous bone”, *IEEE Trans Ultrason Ferroelectr Freq Control* **45**, 581–92.
- Fellah, Z., Sebaa, N., Fellah, M., Mitri, F. G., Ogam, E., Lauriks, W., and Depollier, C. (2008), “Application of the Biot model to ultrasound in bone: direct problem”, *IEEE Trans Ultrason Ferroelectr Freq Control* **55**, 1508–1515.
- Foldes, A. J., Rimon, A., Keinan, D. D., and Popovtzer, M. M. (1995), “Quantitative ultrasound of the tibia: a novel approach assessment of bone status”, *Bone* **17**, 363–367.
- Fredfeldt, K. E. (1986), “Sound velocity in the middle phalanges of the human hand”, *Acta Radiol Diagn* **27**, 95–96.
- Fujita, F., Mizuno, K., and Matsukawa, M. (2013), “An experimental study on the ultrasonic wave propagation in cancellous bone: waveform changes during propagation”, *J Acoust Soc Am* **134**(6), 4775–4781.
- Gluer, C. C., Cummings, S. R., Bauer, D. C., Stone, K., Pressman, A., Mathur, A., and Genant, H. K. (1996), “Osteoporosis: association of recent fractures with quantitative US findings”, *Radiology* **199**(3), 725–732.
- Haiat, G., Padilla, F., Cleveland, R. O., and Laugier, P. (2006), “Effects of frequency-dependent attenuation and velocity dispersion on in vitro ultrasound velocity measurements in intact human femur specimens”, *IEEE Trans Ultrason Ferroelectr Freq Control* **53**, 39–51.
- Haiat, G., Padilla, F., Peyrin, F., and Laugier, P. (2008), “Fast wave ultrasonic propagation in trabecular bone: Numerical study of the influence of porosity and structural anisotropy”, *J Acoust Soc Am* **123**(3), 1694–1705.
- Haire, T. J. and Langton, C. M. (1999), “Biot theory: a review of its application to ultrasound propagation through cancellous bone”, *Bone* **24**(4), 291–295.
- Hans, D., Srivastav, S., Singal, C., Barkmann, R., Njeh, C. F., and Kantorovich, E. (1999), “Does combining the results from multiple bone sites measured by a new quantitative ultrasound device improve discrimination of hip fracture?”, *J Bone Miner Res* **14**, 644–651.



- Hodgskinson, R., Njeh, C. F., Whitehead, M. A., and Langton, C. M. (1996), “The non-linear relationship between BUA and porosity in cancellous bone”, *Phys Med Biol* **41**, 2411–2420.
- Hosokawa, A. and Otani, T. (1997), “Ultrasonic wave propagation in bovine cancellous bone”, *J Acoust Soc Am* **101**, 558–62.
- Hosokawa, A. and Otani, T. (1998), “Acoustic anisotropy in bovine cancellous bone”, *J Acoust Soc Am* **103**, 2718–22.
- Kanis, J. A. (2002), “Diagnosis of osteoporosis and assessment of fracture risk”, *Lancet* **359**, 1929–36.
- Kanis, J. A., Burlet, N., Cooper, C., Delmas, P. D., Reginster, J. Y., Borgstrom, F., and Rizzoli, R. (2008), “European guidance for the diagnosis and management of osteoporosis in postmenopausal women”, *Osteoporos Int* **19**(4), 399–428.
- Krieg, M. A., Barkmann, R., Gonnelli, S., Stewart, A., Bauer, D. C., Del Rio Barquero, L., Kaufman, J. J., Lorenc, R., Miller, P. D., Olszynski, W. P., Poiana, C., Schott, A. M., Lewiecki, E. M., and Hans, D. (2008), “Quantitative ultrasound in the management of osteoporosis: the 2007 ISCD Official Positions”, *J Clinical Densitometry* **11**, 163–187.
- Lakes, R., Yoon, H. S., and Katz, J. L. (1983), “Slow compressional wave propagation in wet human and bovine cortical bone”, *Science* **220**, 513–515.
- Langton, C. M. and Njeh, C. F. (2008), “The measurement of broadband ultrasonic attenuation in cancellous bone - a review of the science and technology”, *IEEE Trans Ultrason Ferroelectr Freq Control* **55**, 1546–1554.
- Langton, C. M., Palmer, S. B., and Porter, S. W. (1984), “The measurement of broadband ultrasonic attenuation in cancellous bone”, *Eng Med* **13**(2), 89–91.
- Laugier, P. and Haiat, G. (Eds.) (2011), *Bone quantitative ultrasound* (Springer).
- Lee, K., Roh, H., and Yoon, S. (2003), “Acoustic wave propagation in bovine cancellous bone: application of the modified Biot-Attenborough model”, *J Acoust Soc Am* **114**, 2284–2293.
- Lee, K. I. and Choi, M. J. (2007), “Phase velocity and normalized broadband ultrasonic attenuation in polyacetal cuboid bone-mimicking phantoms”, *J Acoust Soc Am* **121**, EL263–EL269.
- Leibson, C. L., Tosteson, A. N., Gabriel, S. E., Ransom, J. E., and Melton, L. J. (2002), “Mortality, disability, and nursing home use for persons with and without hip fracture: a population-based study”, *J Amer Geriatrics Soc* **50**(10), 1644–1650.
- Manolagas, S. C. and Jilka, R. L. (1995), “Bone marrow, cytokines, and bone remodeling: emerging insights into the pathophysiology of osteoporosis”, *N Engl J Med* **332**, 305–311.

- Marshall, D., Johnell, O., and Wedel, H. (1996), “Meta-analysis of how well measures of bone mineral density predict occurrence of osteoporotic fractures”, *BMJ* **312**, 1254–59.
- Marutyan, K. R., Holland, M. R., and Miller, J. G. (2006), “Anomalous negative dispersion in bone can result from the interference of fast and slow waves”, *J Acoust Soc Am* **120**, EL55–61.
- McKelvie, M. L. and Palmer, S. B. (1991), “The interaction of ultrasound with cancellous bone”, *Phys Med Biol* **36**, 1331–40.
- Mizuno, K., Matsukawa, M., Otani, T., Laugier, P., and Padilla, F. (2009), “Propagation of two longitudinal waves in human cancellous bone: an in vitro study”, *J Acoust Soc Am* **125**, 3460–3466.
- Mizuno, K., Matsukawa, M., Otani, T., Takada, M., Mano, I., and Tsujimoto, T. (2008), “Effects of structural anisotropy of cancellous bone on speed of ultrasonic fast waves in bovine femur”, *IEEE Trans Ultrason Ferroelectr Freq Control* **55**(7), 1480–1487.
- Mizuno, K., Somiya, H., Kubo, T., Matsukawa, M., Otani, T., and Tsujimoto, T. (2010), “Influence of cancellous bone microstructure on two ultrasonic wave propagations in bovine femur: an in vitro study”, *J Acoust Soc Am* **128**(5), 3181–3189.
- Mobley, J., Waters, K. R., and Miller, J. G. (2005), “Causal determination of acoustic group velocity and frequency derivative of attenuation with finite-bandwidth Kramers-Kronig relations”, *Phys Rev E* **72**, 016604.
- Nicholson, P., Lowet, G., Langton, C. M., Dequeker, J., and Van der Perre, G. (1996), “A comparison of time-domain and frequency domain approaches to ultrasonic velocity measurements in trabecular bone”, *Phys Med Biol* **41**, 2421–2435.
- Nicholson, P., Muller, R., Lowet, G., Cheng, X. G., Hildebrand, T., Ruegsegger, P., Van der Perre, G., Dequeker, J., and Boonen, S. (1998), “Do quantitative ultrasound measurements reflect structure independently of density in human vertebral cancellous bone?”, *Bone* **23**, 425–431.
- NIH (2001), “Osteoporosis prevention, diagnosis, and therapy”, *JAMA* **285**, 785–795.
- Njeh, C. F., Hans, D., Fuerst, T., Gluer, C. C., and Genant, H. K. (Eds.) (1999), *Quantitative ultrasound: assessment of osteoporosis and bone status* (Martin Dunitz).
- O’Donnell, M., Jaynes, E., and Miller, J. G. (1981), “Kramers-Kronig relationship between ultrasonic attenuation and phase velocity”, *J Acoust Soc Am* **69**, 696–701.
- Pakula, M., Padilla, F., and Laugier, P. (2009), “Influence of the filling fluid on frequency-dependent velocity and attenuation in cancellous bones between 0.35 and 2.5 MHz”, *J Acoust Soc Am* **126**(6), 3301–3310.

- Pakula, M., Padilla, F., Laugier, P., and Kaczmarek, M. (2008), “Application of Biot’s theory to ultrasonic characterization of human cancellous bones: determination of structural, material, and mechanical properties”, *J Acoust Soc Am* **123**, 2415–23.
- Parfitt, A. M. (1984), “Age-related structural changes in trabecular and cortical bone: cellular mechanisms and biochemical consequences”, *Calcif Tissue Int* **36**, S123–8.
- Schoenberg, M. (1984), “Wave propagation in alternating solid and fluid layers”, *Wave Motion* **6**, 303–320.
- Sebaa, N., Fellah, E. A., Fellah, M., Ogam, E., Wirgin, A., Mitri, F. G., Depollier, C., and Lauriks, W. (2006), “Ultrasonic characterization of human cancellous bone using the Biot theory: inverse problem”, *J Acoust Soc Am* **120**, 1816–1824.
- Shutilov, V. (1988), *Fundamental physics of ultrasound* (Gordon and Breach).
- Siegel, I., Anast, G. T., and Melds, T. (1958), “The determination of fracture healing by measurement of sound velocity across the fracture site”, *Surg Gynecol Obste* **107(3)**, 327–332.
- Thomsen, J., Ebbesen, E., and Mosekilde, L. (2002), “Age-related differences between thinning of horizontal and vertical trabeculae in human lumbar bone as assessed by a new computerized method”, *Bone* **31**, 136–142.
- Ulrich, D., van Rietbergen, B., Laib, A., and Ruegsegger, P. (1999), “The ability of three-dimensional structural indices to reflect mechanical aspects of trabecular bone”, *Bone* **25**, 55–60.
- Waters, K. R. and Hoffmeister, B. K. (2005), “Kramers-Kronig analysis of attenuation and dispersion in trabecular bone”, *J Acoust Soc Am* **118**, 3912–20.
- Waters, K. R., Hughes, M. S., Mobley, J., and Miller, J. G. (2003), “Differential forms of the Kramers-Kronig dispersion relations”, *IEEE Trans Ultrason Ferroelectr Freq Control* **50**, 68–76.
- Waters, K. R., Mobley, J., and Miller, J. G. (2005), “Causality-imposed (Kramers-Kronig) relationships between attenuation and dispersion”, *IEEE Trans Ultrason Ferroelectr Freq Control* **52**, 822–823.
- Wear, K. A. (2000), “The effects of frequency-dependent attenuation and dispersion on sound speed measurements: applications in human trabecular bone”, *IEEE Trans Ultrason Ferroelectr Freq Control* **47**, 265–273.
- Wear, K. A. (2005), “The dependencies of phase velocity and dispersion on trabecular thickness and spacing in trabecular bone-mimicking phantoms”, *J Acoust Soc Am* **118**, 1186–1192.

- Wear, K. A. (2007), “Group velocity, phase velocity, and dispersion in human calcaneus in vivo”, J Acoust Soc Am **121**, 2431–37.
- Wear, K. A. (2008), “Mechanisms for attenuation in cancellous-bone-mimicking phantoms”, IEEE Trans Ultrason Ferroelectr Freq Control **55**.
- Wear, K. A., Laib, A., Stuber, A. P., and Reynolds, J. C. (2005), “Comparison of measurements of phase velocity in human calcaneus to Biot theory”, J Acoust Soc Am **117**, 3319–3324.
- Whitehouse, W. J. and Dyson, E. D. (1974), “Scanning electron microscope studies of trabecular bone in the proximal end of the human femur”, J Anat **118(3)**, 417–444.
- WHO (2004), “Prevention and management of osteoporosis”, World Health Organ Tech Rep Ser **921**, 206.
- Williams, J. L. (1992), “Ultrasonic wave propagation in cancellous and cortical bone: prediction of some experimental results by Biot’s theory”, J Acoust Soc Am **91**, 1106–1112.
- Wolff, J. (1986), *The law of bone remodeling* (Springer).

# CHAPTER 3

---

## METHODS OF CONVENTIONAL AND BAYESIAN ANALYSIS

### 3.1 Preface

This chapter details the various analysis methods used in this thesis to determine the ultrasonic properties of cancellous bone. First, we present an overview of how certain ultrasonic properties, such as the phase velocity and attenuation coefficient, are determined through conventional analysis techniques. In order to deal with the complicated waves sometimes observed in trabecular bone, a Bayesian probability method was employed to extract the fundamental ultrasonic properties of the fast and slow waves. The chapter concludes with a discussion of potential complications that can arise as a result of specific features of the experimental apparatus and detailed characteristics of the propagation and detection of diffracting ultrasonic waves.

## 3.2 Background

In many cancellous bone studies with ultrasound, the analysis method used assumes only a single wave is present in the received through-sample signal, or if multiple waves are present, that these waves can be completely separated by time gating. This conventional analysis method is performed in the frequency domain and permits the determination of intrinsic ultrasonic properties of the sample, such as the phase velocity and the attenuation coefficient. Due to the unique structure of trabecular bone, conventional analysis methods applied to cancellous bone data may lead to misleading results for the ultrasonic properties. A Bayesian probability algorithm presented in Section 3.4 may permit the true intrinsic ultrasonic properties of cancellous bone specimens to be determined.

A number of ultrasonic properties are of interest for characterizing a material (like bone) ultrasonically. The phase velocity is one such parameter. If the propagating medium has a phase velocity that varies with frequency, which is the case with most biological tissues, then that medium is said to be dispersive. As indicated in Chapter 2, cancellous bone has been shown to display both positive and negative dispersion.

Another intrinsic ultrasonic property of interest is the attenuation coefficient. The attenuation coefficient is a frequency-dependent measure of the loss in signal amplitude occurring in a sample as a function of distance traveled. The attenuation coefficient of a medium is useful in determining the range of frequencies that can be used to interrogate that medium because ultrasonic signals typically attenuate more rapidly at higher frequencies as well as with increasing sample thickness. In most studies of trabecular bone, the frequencies typ-

ically employed range from 500 kHz to 1 MHz, although some studies present results at frequencies as high as 10 MHz (Hoffmeister *et al.*, 2008; Hoffmeister, 2011). Attenuation properties offer a way to study the structure of a material. Some studies have investigated the anisotropy of the attenuation coefficient and slope of the attenuation coefficient in samples of trabecular bone. These parameters were found to be significantly larger along the trabecular axis than perpendicular to that axis (Glüer *et al.*, 1993; Wear, 2000a). Similar results were found in studies of the fiber structure of hearts (Gibson *et al.*, 2009; Baldwin *et al.*, 2006). More accurate measurements of the attenuation properties of bone, perhaps using the Bayesian formalism, may provide additional insight and information about the structure of trabecular bone and may improve diagnostic capabilities of clinical bone sonometers.

## 3.3 Conventional Data Analysis

### 3.3.1 Broadband Phase Spectroscopy

The formalism used in this thesis was originally developed by Sachse and Pao (1978) and was adapted by Rebecca Trousil, a Laboratory for Ultrasonics alumnus, in her Ph.D. thesis (Trousil, 2002). All of the broadband phase velocity measurements discussed in this thesis were made using the through-transmission method, so the formalism of phase spectroscopy discussed will be based on this approach.

Figure 3.1 shows the two measurements needed for the phase spectroscopy method in the case of a through-transmission experiment. The general complex frequency response at the

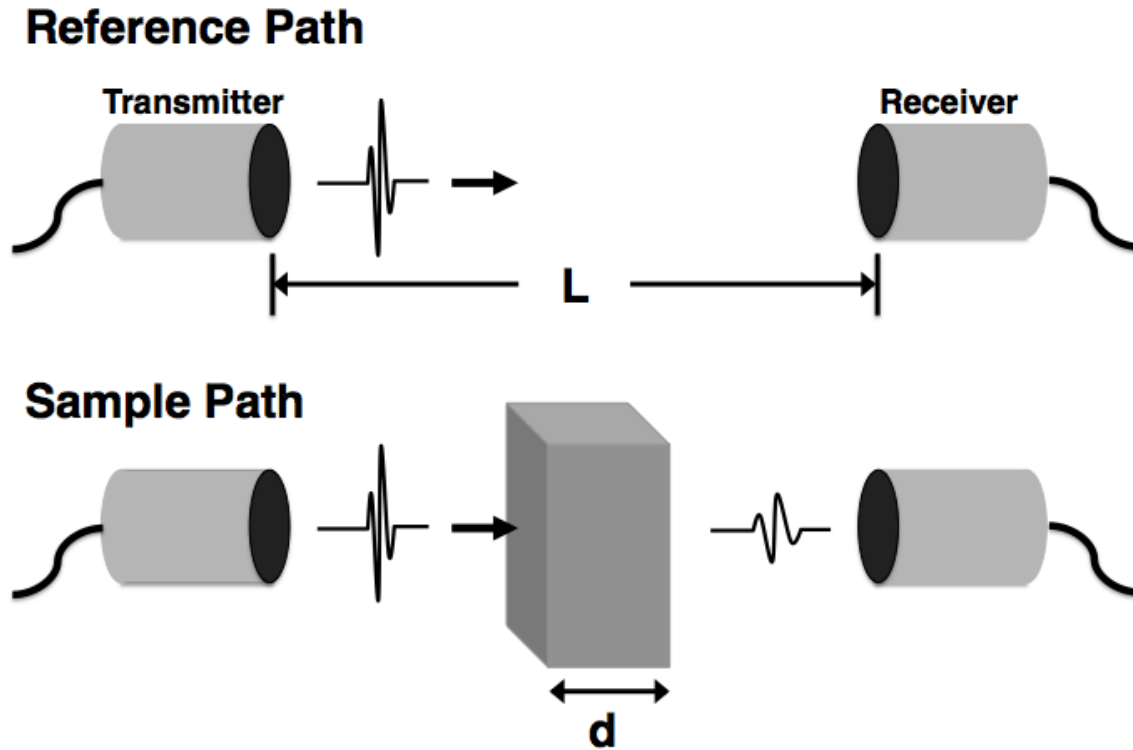


FIGURE 3.1: Experimental set-up for a through-transmission experiment that measures the frequency dependence of the phase velocity. The top panel depicts the reference signal in which the ultrasonic pulse travels a distance  $L$  through water only before being detected. The bottom panel shows the sample signal which travels the same path as the reference except that a sample of thickness  $d$  is inserted between the transducers.



receiving transducer can be expressed as,

$$\tilde{U}(x, \omega) = \aleph(\omega) e^{i[k(\omega)x + i\alpha(\omega)x + \zeta(\omega)]} \quad (3.1)$$

where  $\aleph(\omega)$  is the frequency dependent amplitude,  $k(\omega)$  is the wavenumber,  $\alpha(\omega)$  is the amplitude attenuation coefficient,  $x$  is the propagation distance, and  $\zeta$  is an arbitrary phase factor (Trousil, 2002). The reference trace corresponds to a signal that has traveled a distance  $L$  in the host or reference medium, usually water. The complex frequency response of the reference signal at the receiving transducer can be written as

$$\begin{aligned} \tilde{U}_{ref}(x = L, \omega) &= [\aleph(\omega) e^{-\alpha_{ref}(\omega)L}] \cdot e^{i(k_{ref}(\omega)L + \zeta(\omega))} \\ &= \left| \tilde{U}_{ref}(x = L, \omega) \right| \cdot e^{i\phi_{ref}(\omega)} \end{aligned} \quad (3.2)$$

where  $\left| \tilde{U}_{ref} \right|$  is the magnitude of the complex frequency response and  $\phi_{ref}(\omega)$  is the phase of the complex frequency response of the reference measurement.

The through-sample signal corresponds to a pulse that has traveled the same path as the reference except that a portion of the path has been replaced with a sample of thickness  $d$ . The complex frequency response of the sample measurement at the receiving transducer can be written as

$$\begin{aligned} \tilde{U}_{samp}(x = L, \omega) &= [(T_{h \rightarrow s}^p T_{s \rightarrow h}^p) \aleph(\omega) e^{-\alpha_{ref}(\omega)(L-d) - \alpha_s(\omega)d}] \cdot e^{i(k_{ref}(\omega)(L-d) + k_s(\omega)d + \zeta(\omega))} \\ &= \left| \tilde{U}_{samp}(x = L, \omega) \right| \cdot e^{i\phi_{samp}(\omega)} \end{aligned} \quad (3.3)$$

where  $\left| \tilde{U}_{samp} \right|$  is the magnitude of the complex frequency response and  $\phi_{samp}(\omega)$  is the phase of the complex frequency response of the sample measurement (Trousil, 2002). The pressure amplitude transmission coefficients,  $T_{h \rightarrow s}^p$  and  $T_{s \rightarrow h}^p$  in Equation 3.3 account for the partial

transmission of the incident wave at the boundary between the host medium and the sample ( $h \rightarrow s$ ) and at the boundary between the sample and host medium ( $s \rightarrow h$ ).

The phase velocity can be determined from the phase difference between the reference and the sample measurement. The phase difference can be obtained by subtracting Equation 3.2 from Equation 3.3 to obtain

$$\Delta\phi(\omega) = \phi_{samp}(\omega) - \phi_{ref}(\omega) = \omega d \left( \frac{1}{v_s(\omega)} - \frac{1}{v_h} \right) \quad (3.4)$$

By rearranging the terms in Equation 3.4, an expression for the phase velocity in the sample can be obtained

$$v_s(\omega) = v_h \left( \frac{\omega d}{\omega d + v_h \Delta\phi(\omega)} \right) \quad (3.5)$$

In all the experiments discussed in this thesis, the host medium was water. The phase velocity of the water was calculated using a fifth degree polynomial developed by Marczak that depends on the water temperature (Marczak, 1997). In order to calculate the phase velocity in Equation 3.5, the phase difference,  $\Delta\phi(\omega)$ , must be determined.

### Determining the Experimental Phase Difference

For both the reference measurement and the sample measurement, phase is being accumulated from the instant the transmitting transducer is excited to when the received signal is detected. This phenomena of accumulating phase in the frequency domain as the signal propagates in time can be described by the Fourier Shift Theorem

$$\mathcal{F}[f(t - a)] = e^{-ia\omega} \tilde{F}(\omega) \quad (3.6)$$

where  $a$  is the shift in the time domain,  $\mathcal{F}$  is the Fourier transform, and  $\tilde{F}(\omega)$  is the Fourier transform of  $f(t)$  (Bracewell, 2000). However, the amount of phase accumulated is different between the water measurement and the sample measurement due to replacing a portion of the water path with a sample of thickness  $d$ . The accumulated phase at a specific frequency per distance traveled can be calculated by the wavenumber defined as

$$k(\omega) = \frac{\omega}{v(\omega)} \quad (3.7)$$

where  $\omega$  is the angular frequency and  $v(\omega)$  is the phase velocity. For example, if we consider an experiment with a host medium of water with a phase velocity of 1480 m/s and a plastic sample with a velocity of 2200 m/s at 1 MHz, the corresponding wavenumbers would be  $k_{ref}(1MHz) = 4,243$  rad/m and  $k_{samp}(1MHz) = 2,855$  rad/m, respectively. This calculation indicates that the phase accumulates more slowly in the medium with the higher phase velocity, in this example, the plastic sample. Since the difference in the accumulated phase between the reference signal and the sample signal depends upon the difference in their phase velocities, the phase difference can be used to calculate the phase velocity of the experimentally measured sample.

The total experimental phase associated with the reference signal and the through-sample signal can be expressed as

$$\phi_{ref}(\omega) = (\phi_{shift}^{ref}(\omega) + 2\pi m) + \omega\tau_{delay}^{ref} + \omega\tau_{shift}^{ref} \quad (3.8)$$

$$\phi_{samp}(\omega) = (\phi_{shift}^{samp}(\omega) + 2\pi n) + \omega\tau_{delay}^{samp} + \omega\tau_{shift}^{samp} \quad (3.9)$$

where  $\phi_{shift}$  is the phase of the shifted (or symmetrized) spectrum,  $2\pi m$  and  $2\pi n$  are ambiguities in the shifted reference and sample phase spectra,  $\tau_{delay}$  is the b-delay time, and  $\tau_{shift}$

is the amount of time the signal is shifted. The formalism used here originated with Trousil (2002) and was modified by Benjamin Johnson (2012). The phase difference in Equation 3.4 can be re-written in terms of Equation 3.8 and Equation 3.9 so that

$$\begin{aligned}\Delta\phi(\omega) &= \phi_{samp}(\omega) - \phi_{ref}(\omega) \\ &= \left[ \left( \phi_{shift}^{samp}(\omega) - \phi_{shift}^{ref}(\omega) \right) + 2\pi(m - n) \right] + \omega \left( \tau_{delay}^{samp} - \tau_{delay}^{ref} \right) + \omega \left( \tau_{shift}^{samp} - \tau_{shift}^{ref} \right)\end{aligned}\tag{3.10}$$

where the quantity  $(m - n)$  is known as the phase sheet offset. A description of each component in Equation 3.10 is detailed in the following paragraphs.

The terms  $\tau_{delay}^{samp}$  and  $\tau_{delay}^{ref}$  refer to the trigger delay (b-delay) which informs the oscilloscope to start digitizing the rf signals after some time has elapsed relative to the time of excitation of the transmitting transducer. This permits the signal of interest to be centered on the oscilloscope window and viewed over an expanded time interval. However, the total phase associated with an rf signal must take into account the phase accumulated up to the b-delay time and the phase accumulated within the digitized window.

The phase spectrum associated with an rf signal, termed  $\phi_{shift}$  is obtained from the argument of the Fourier transform of the rf trace,

$$\phi_{shift}(\omega) = \tan^{-1} \left( \frac{\text{Im} [\tilde{U}(\omega)]}{\text{Re} [\tilde{U}(\omega)]} \right)\tag{3.11}$$

The phase calculated in Equation 3.11 is restricted on the interval  $[-\pi, +\pi]$ . This restriction causes the phase spectrum to wrap at its  $\pm\pi$  boundaries, resulting in a phase that rapidly changes with frequency as shown in Figure 3.2. Since this function is a four quadrant inverse tangent, the resulting phase spectrum is ambiguous to integer multiples of  $2\pi$ , which requires

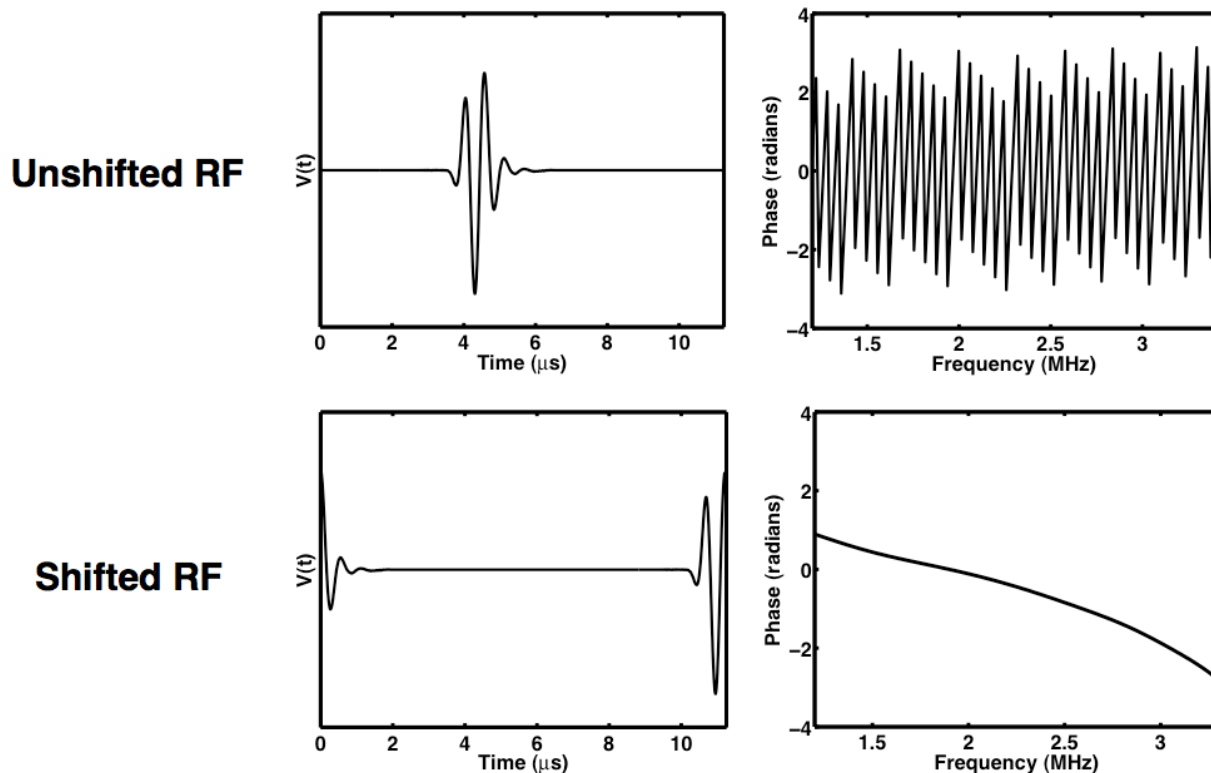


FIGURE 3.2: The effects of shifting the radiofrequency (rf) trace. The top panel shows that if a signal is not shifted (or symmetrized) the phase rapidly changes over the bandwidth. In the bottom panel, the same signal has been shifted using the peak positive criterion, allowing the phase to change more gradually over the bandwidth.

the inclusion of the phase sheet offset in Equation 3.10.

In order to allow the phase spectrum to vary more slowly with frequency, the rf signal is shifted or symmetrized prior to calculating its phase spectrum. This symmetrization reduces the amount of phase wrapping that occurs by distributing the energy in the pulse evenly about the ends of the digitized recording. There are numerous methods for shifting or symmetrizing an rf signal. The approach used in this thesis is to shift the peak positive voltage to the start of the digitized record, wrapping earlier points to the end of the trace. This approach is illustrated in the bottom row of Figure 3.2 along with the corresponding

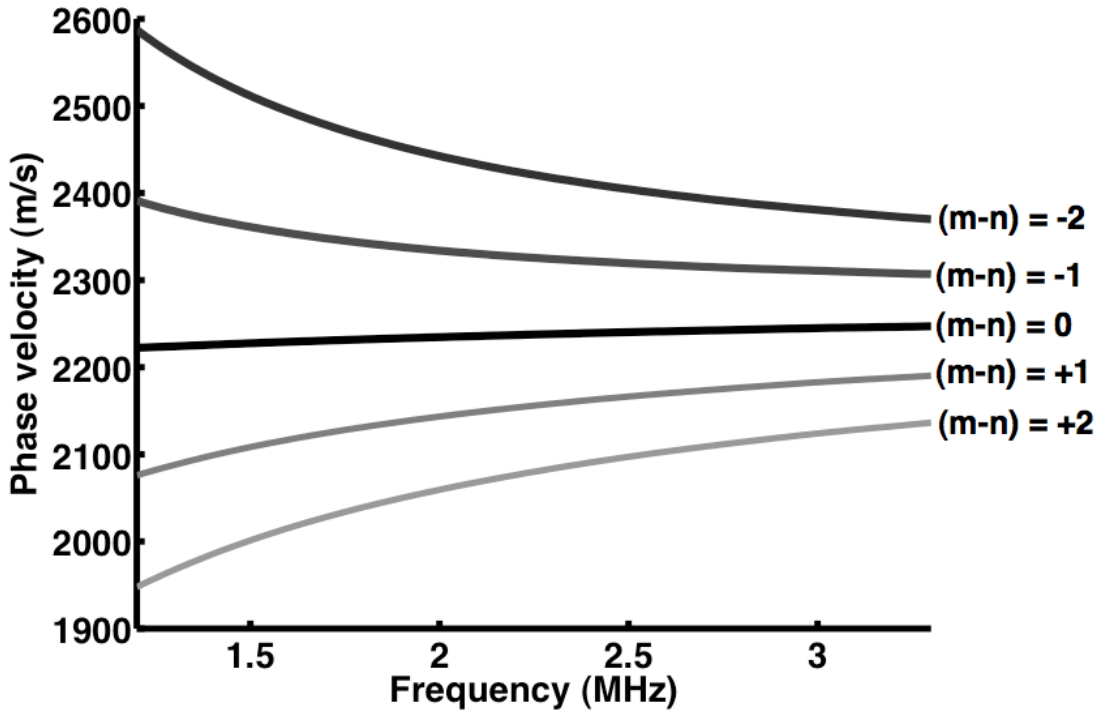


FIGURE 3.3: The effects on the phase velocity results by using different phase sheet offsets  $(m-n)$ . The correct phase sheet is  $(m-n) = 0$ , which produces the least amount of dispersion. By changing the phase sheet offset by one integer the phase velocity as a function of frequency changes quite dramatically.

phase spectrum. The figure demonstrates the significant change in the phase spectra that occur due to shifting the rf signals. The term  $\tau_{shift}$  in Equation 3.10 is the amount of time the rf signals were shifted when performing the symmetrization process. The last term needed to determine the phase difference is the phase sheet offset or the  $(m-n)$  term. In the majority of experiments performed in this Laboratory, the value for  $(m-n)$  is often 0 or  $\pm 1$ . This is true for samples that exhibit modest dispersion over the experimental bandwidth. For studies of cancellous bone, the phase sheet offset may be larger ( $m-n = \pm 2$ ) since dispersions might be greater. The effects of changing the phase sheet offset by one integer are usually quite significant, as illustrated in Figure 3.3.

Two approaches that can be employed to resolve the phase sheet ambiguity are performing narrowband phase velocity measurements or using the Kramers-Kronig relations (Trousil *et al.*, 2001). For most of the studies in this thesis, the Kramers-Kronig relation method was used to determine the correct phase sheet offset. However, as discussed in Chapter 2, the presence of overlapping fast and slow waves in cancellous bone can cause the phase velocity to display apparent negative dispersion.

### **Kramers-Kronig Relations**

The Kramers-Kronig relations were used to determine the correct phase sheet offset for the broadband phase velocity measurements performed on plastic samples in Chapter 7 and on some bone specimens in Chapters 4 and 6. The Kramers-Kronig relations also provided a check on the experimentally measured dispersion based on the connection between the dispersion and the attenuation coefficient in a material. If the attenuation coefficient of a material is known or measured, the dispersion of the phase velocity can be predicted. In media exhibiting linear-with-frequency attenuation coefficients, the predicted dispersion can be obtained from the nearly local Kramers-Kronig relations with one subtraction (Trousil, 2002; Waters *et al.*, 2003, 2005). If a sample has an attenuation coefficient that follows a frequency power law with an exponent greater than 1, then two or more subtractions are necessary to obtain the correct Kramers-Kronig relations (Trousil, 2002; Waters *et al.*, 2000). The plastic samples investigated in this thesis (Chapter 7) all exhibit linear-with-frequency attenuation coefficients; therefore the nearly-local Kramers-Kronig relations with one subtraction were used. The frequencies (500 kHz and 1 MHz) used in the bone studies presented in this

thesis have been shown both in experiment (Chaffai *et al.*, 2000; Jenson *et al.*, 2006) and in simulation (Bossy *et al.*, 2005) to produce linear-with-frequency attenuation coefficients. For frequencies greater than approximately 1.2 MHz, the attenuation coefficient might be better characterized using a power law fit with the exponent greater than 1.

For media with a linear attenuation coefficient of the form

$$\alpha(\omega) = \alpha(\omega_c) + \frac{\beta}{2\pi}(\omega - \omega_c) \quad (3.12)$$

where  $\beta$  is the slope of the amplitude attenuation coefficient and  $\omega_c$  is the angular frequency at the center of the bandwidth, the nearly-local Kramers-Kronig relations with one subtraction were employed to predict the dispersion and to verify the phase sheet offset. The predicted dispersion for the nearly-local Kramers-Kronig relations with one subtraction is approximately given by

$$\frac{1}{v(\omega)} - \frac{1}{v(\omega_0)} = -\frac{2}{\pi} \frac{\beta}{2\pi} \ln(\omega/\omega_0) \quad (3.13)$$

where  $v(\omega)$  is the phase velocity as a function of frequency and  $\omega_0$  is some frequency in the usable bandwidth, generally the center frequency. If the dispersion in the phase velocity is small, then Equation 3.13 can be expanded to first order in the dispersion such that

$$v(\omega) - v(\omega_0) \approx \frac{[v(\omega_0)]^2 \beta}{\pi^2} \ln(\omega/\omega_0) \quad (3.14)$$

The Kramers-Kronig relations do not predict absolute values for the dispersion, just relative differences in the phase velocity. In order to compare the Kramers-Kronig prediction to experimental phase velocity measurements, the phase spectroscopy derived phase velocity at band center was used to set the absolute value of the Kramers-Kronig prediction dispersion



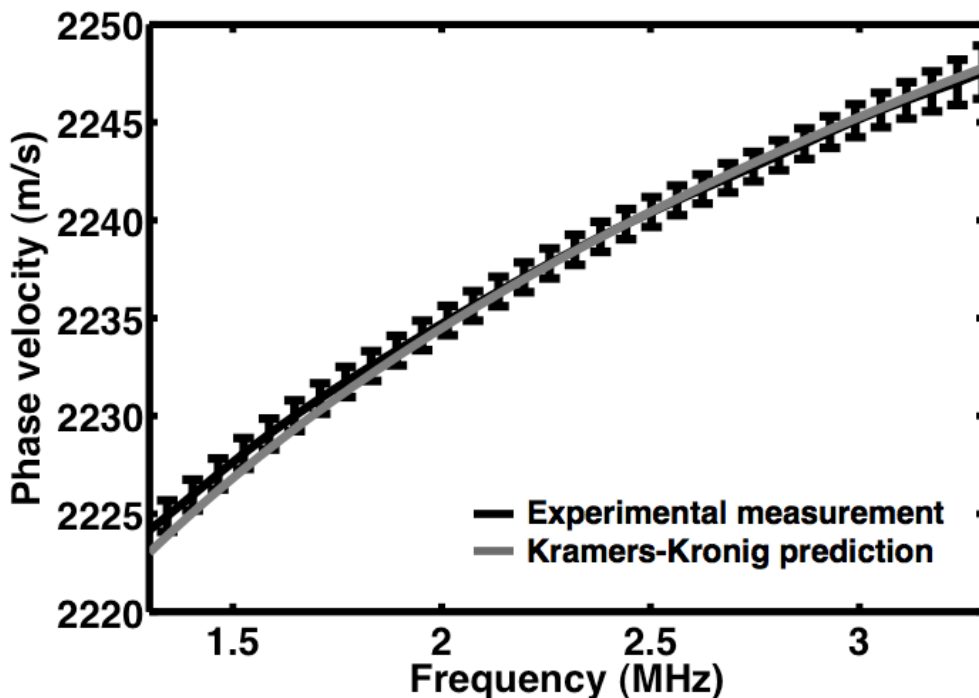


FIGURE 3.4: The phase velocity as determined by phase spectroscopy of the plastic Lexan along with the dispersion prediction by the nearly-local Kramers-Kronig relations with one subtraction.

( $\omega_0 = 2\pi f_c$ ). An example of Kramers-Kronig dispersion prediction along with the phase velocity measured using phase spectroscopy (phase sheet offset = 0) for a sample of Lexan, with an average slope of attenuation  $\beta = 4.6$  dB/cm/MHz and  $v(\omega_0) = 2238$  m/s, is shown in Figure 3.4.

### 3.3.2 Determination of the Attenuation Coefficient

The attenuation properties of a medium can be determined using the same through-transmission measurements acquired for the phase velocity, shown in Figure 3.1. The frequency-dependent attenuation coefficient is determined using the log-spectral subtraction method (Trousil, 2002; Ophir *et al.*, 1984), which compares the signal traveling through

a sample to the signal traveling only through water. The reference (water-only) power spectrum,  $|\tilde{V}_{ref}(f)|^2$ , received by the transducer is given by

$$\left|\tilde{V}_{ref}(f)\right|^2 = \left|\tilde{E}_0(f)\right|^2 \cdot \left[e^{-\alpha_{host}(f) \cdot L}\right]^2 \quad (3.15)$$

where  $|\tilde{E}_0(f)|^2$  represents the frequency-dependent responses of both transducers and the electronics,  $\alpha_{host}(f)$  is the amplitude attenuation coefficient of the reference medium (water for all studies in this thesis), and  $L$  is the distance between the two transducers (Trousil, 2002).

When the sample, of thickness  $d$ , is inserted into the path (Figure 3.1), the received power becomes

$$\left|\tilde{V}_{samp}(f)\right|^2 = \left|\tilde{E}_0(f)\right|^2 \cdot \left[e^{-\alpha_{host}(f) \cdot (L-d)}\right]^2 \cdot \left[e^{-\alpha_{samp}(f) \cdot d}\right]^2 \cdot T_{h \rightarrow s}^I \cdot T_{s \rightarrow h}^I \quad (3.16)$$

where  $\alpha_{samp}(f)$  is the amplitude attenuation coefficient of the sample,  $T_{h \rightarrow s}^I$  is the intensity transmission coefficient at the boundary between the host medium and the sample, and  $T_{s \rightarrow h}^I$  is the intensity transmission coefficient at the interface between the sample and the host medium. Each of the intensity transmission coefficients in Equation 3.16 has the form

$$T_{1 \rightarrow 2}^I = \frac{4 \left| \tilde{Z}_1 \cdot \tilde{Z}_2 \right|}{\left| \tilde{Z}_1 + \tilde{Z}_2 \right|^2} \quad (3.17)$$

where  $\tilde{Z}_1$  and  $\tilde{Z}_2$  are the complex acoustic impedances of the two media (water and sample). In much of our Laboratories' previous work in soft tissues and solids, and in the majority of this thesis, the complex acoustic impedance was approximated as a real quantity

$$\tilde{Z} = \frac{\rho\omega}{k - i\alpha} \approx \rho v \cdot \left[ 1 + \left( \frac{i\alpha}{k} \right) + \left( \frac{i\alpha}{k} \right)^2 + \dots \right] \approx \rho v \quad (3.18)$$

where  $\rho$  is the mass density of the medium and  $v$  is the phase velocity. This approximation can only be implemented when the attenuation coefficient,  $\alpha$ , is small compared to the propagating portion of the complex wave number,  $k$ .

In principle, the system dependent effects, described by  $|\tilde{E}_0(f)|^2$ , can be eliminated by dividing the reference power spectrum by the sample power spectrum yielding

$$\frac{|\tilde{V}_{ref}(f)|^2}{|\tilde{V}_{samp}(f)|^2} = \frac{e^{2d(\alpha_{samp}(f) - \alpha_{host}(f))}}{T_{h \rightarrow s}^I \cdot T_{s \rightarrow h}^I}. \quad (3.19)$$

At the frequencies used in this thesis, the attenuation coefficient of the sample,  $\alpha_{samp}(f)$ , is several orders of magnitude larger than the attenuation coefficient of the host medium (water),  $\alpha_{host}(f)$ . The attenuation coefficient in water is on the order of  $10^{-4}$  Np/cm at 1 MHz (Trousil, 2002; Markham, 1951), whereas the attenuation coefficients of the bone specimens studied in this thesis ranged, on average, from 0.6 to 4.4 Np/cm at 1 MHz. Therefore, for the attenuation measurements presented in this thesis, the attenuation coefficient of water was considered to be negligible and Equation 3.19 could be rewritten as

$$\frac{|\tilde{V}_{ref}(f)|^2}{|\tilde{V}_{samp}(f)|^2} = \frac{e^{2d\alpha_{samp}(f)}}{T_{h \rightarrow s}^I \cdot T_{s \rightarrow h}^I}. \quad (3.20)$$

Equation 3.20 gives the measured signal loss, whereas experimentally, the attenuation coefficient is often expressed logarithmically in units of decibels [dB]. Equation 3.20 can be converted from base- $e$  to base-10 logarithm using the standard logarithm rule

$$\ln a = \ln 10 \cdot \log a \quad (3.21)$$

to give

$$10 \log \left( |\tilde{V}_{ref}(f)|^2 \right) - 10 \log \left( |\tilde{V}_{samp}(f)|^2 \right) = \frac{20}{\ln 10} \cdot [\alpha_{samp}(f) \cdot d] - 10 \log [T_{h \rightarrow s}^I \cdot T_{s \rightarrow h}^I]. \quad (3.22)$$

The natural units of the attenuation coefficient are Np/cm. The factor of  $20/\ln 10$  is a conversion factor between Nepers (base-e) and decibels (base-10) and has the approximate value of 8.686 dB/Np. Equation 3.22 illustrates why the approach to calculating the signal loss is often called "log spectral subtraction", since the two terms on the left side are the reference and through-sample power spectra, respectively. Equation 3.22 can be solved for the parameter of interest,  $\alpha_{samp}(f)$ , in units of dB/cm

$$\alpha_{samp}(f) = \frac{1}{d} \left[ 10 \log \left( |\tilde{V}_{ref}(f)|^2 \right) - 10 \log \left( |\tilde{V}_{samp}(f)|^2 \right) + 10 \log(T_{h \rightarrow s}^I \cdot T_{s \rightarrow h}^I) \right]. \quad (3.23)$$

The attenuation coefficient of the sample,  $\alpha_{samp}(f)$ , in Equation 3.23 can be determined by following the steps illustrated in Figure 3.5. The first step is to calculate the water-path only (reference) power spectrum and the through-sample power spectrum from the acquired reference and sample radiofrequency (rf) signals (top panel of Figure 3.5). Log spectral subtraction of these two power spectra generates the frequency-dependent signal loss shown in the second panel of Figure 3.5. The signal loss contains not only the loss incurred within the sample but also the loss incurred at the interfaces. To obtain the attenuation coefficient, which is the bulk loss per unit length, the insertion loss must be subtracted from the signal loss (panel 3 of Figure 3.5) and the result divided by the sample length,  $d$  (panel 4). The frequency-independent insertion losses (panel 3) can be determined two ways. The first method is using the intensity transmission coefficients, defined in Equation 3.17, and shown as the final term in Equation 3.23. This method requires knowledge of the sample's density and velocity in order to calculate the acoustic impedance of the sample (Equation 3.18). An alternative method for determining the insertion losses is to find the zero-frequency

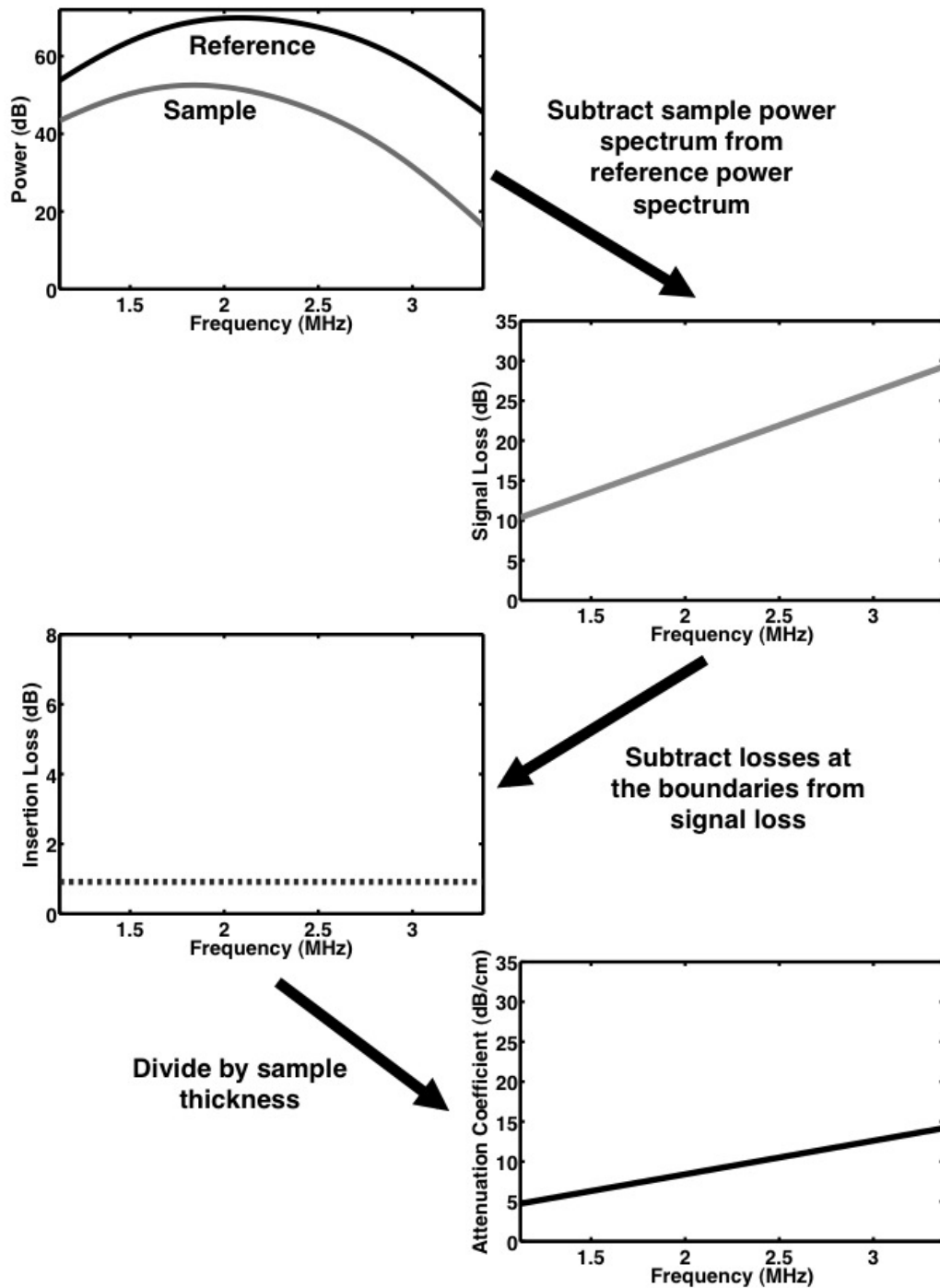


FIGURE 3.5: The steps needed to determine the attenuation coefficient of the sample. The first step is to calculate the power spectra of the reference and sample traces. The signal loss is obtained by the difference between the sample and reference power spectra. Next the insertion losses, or the losses at the boundaries, must be subtracted from the signal loss. The attenuation coefficient is obtained by then dividing the result of the previous step by the sample thickness.

intercept of a least-squares fit to the signal loss versus frequency plot. The vertical offset (at zero frequency) of the signal loss should, in principle, be the total interface loss. Thus, after compensation for these losses, the resulting attenuation coefficient should be zero at zero frequency. With experimental data, this technique does not usually produce reasonable insertion loss values. It has often been observed that the signal loss intercept is a negative value, implying that energy was gained. This can be seen in Figure 3.6 which displays the insertion loss for Lexan predicted by the transmission coefficients (red line) and the insertion loss determined using the zero-frequency intercept of the signal loss versus frequency plot. Diffraction and phase cancellation at the face of the receiving transducer, topics which are discussed later in this chapter, may be possible explanations of why the intercept of the signal loss does not provide a reasonable estimate of the insertion losses. The physics of how the ultrasound beam interacts with the sample at very low frequencies (approaching zero) is difficult to assess. The assumption that the signal loss is approximately linear with frequency may break down as the frequency being used approaches zero (and the wavelength increases).

In studies of cancellous bone, the presence of two waves that often overlap in time, makes determination of the insertion losses using the above methods very difficult or impossible. Typically, the insertion losses are considered to be negligible in comparison to the bulk losses occurring in the bone (McKelvie and Palmer, 1991; Strelitzki and Evans, 1998). Therefore, in the majority of bone studies, the attenuation reported is actually the signal loss or the normalized (by the sample length) signal loss and not the fully compensated attenuation coefficient (Equation 3.23).

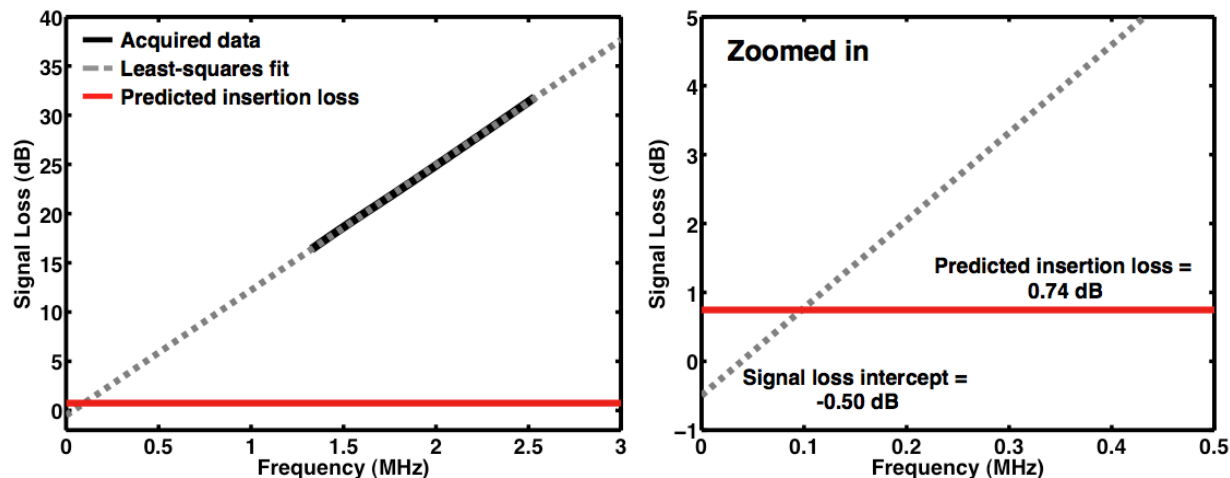


FIGURE 3.6: The insertion losses of Lexan determined using two methods: (1) the intercept of a least-squares fit to the signal loss vs. frequency curve (gray dashed line) and (2) calculation of the transmission coefficients in the last term of Equation 3.23. The solid black line is the experimentally acquired 2.25 MHz Lexan data. The right panel is a zoomed in portion of the left panel and shows that the intercept of the signal loss curve produces a negative insertion loss.

Another parameter of interest to characterize the lossy properties of a sample is the slope of the attenuation,  $\beta$ . In most studies of soft tissue (Goss *et al.*, 1978; Mimbs *et al.*, 1980; Mottley and Miller, 1990; Gibson *et al.*, 2009), the attenuation coefficient rises approximately linearly with frequency

$$\alpha_{samp}(f) = \beta f. \quad (3.24)$$

The slope of the attenuation,  $\beta$ , is considered to be a more robust parameter than the attenuation coefficient because it is less susceptible to potential errors such as those arising from diffraction. The attenuation coefficient in hard tissue, such as bone, is approximately linear only over a more limited range of frequencies than in the case of soft tissue. The attenuation coefficients of bone are typically linear over frequencies ranging from approximately 0.3 MHz to 1.3 MHz (Strelitzki and Evans, 1996; Chaffai *et al.*, 2000; Jenson *et al.*, 2006; Waters and

Hoffmeister, 2005; Barkmann *et al.*, 2008; Wear, 2008). The slope of attenuation ( $\beta$ ) generally reported is the slope of a linear fit to the frequency-dependent signal loss (in contrast to the attenuation coefficient) and is referred to as the "Broadband Ultrasound Attenuation" (BUA) or, if normalized by the sample thickness, the "normalized Broadband Ultrasound Attenuation" (nBUA) (Petley *et al.*, 1995; Langton and Hodgkinson, 1997; Langton and Njeh, 2008).

## 3.4 Bayesian Probability Data Analysis

### 3.4.1 Background

The conventional methods of data analysis detailed in Section 3.3 are useful for data that contain only one wave mode or contain multiple signals that can be separated completely using time gates. For some through-transmission studies on cancellous bone, the fast and slow waves are separated and clearly distinct in the time-domain, thus permitting the use of conventional analysis methods. However, in certain circumstances, the two waves overlap, sometimes significantly, in the time-domain causing difficulties in resolving the individual fast and slow waves (Hosokawa and Otani, 1998; Padilla and Laugier, 2000; Marutyan *et al.*, 2006; Haiat *et al.*, 2008; Anderson *et al.*, 2008). If conventional analysis methods are applied to data containing multiple interfering wave modes, the resulting apparent ultrasonic properties may differ substantially from the ultrasonic properties of the individual fast and slow waves (Marutyan *et al.*, 2006; Anderson *et al.*, 2008), as shown in Figure 3.7, which illustrates the results of processing simulated data. Our Laboratory has shown that the observed anomalous



negative dispersion reported by many laboratories (Strelitzki and Evans, 1996; Droin *et al.*, 1998; Wear, 2000b; Waters and Hoffmeister, 2005; Anderson *et al.*, 2008; Marutyan *et al.*, 2006; Pakula *et al.*, 2009) may result from analyzing interfering fast and slow waves as if only one wave were present (Marutyan *et al.*, 2006; Anderson *et al.*, 2008). Therefore, it appears that an alternative method of analysis needs to be applied to overlapping fast and slow wave data in order to determine the true ultrasonic properties of the bone.

One solution would be to solve the inverse problem: recover the individual properties of the fast and slow waves from acquired mixed-mode data. Our Laboratory proposed a technique that implements Bayesian probability theory to provide estimates of the ultrasonic properties of individual fast and slow waves (Marutyan *et al.*, 2007a,b; Anderson *et al.*, 2010). Subsequently, several other approaches have been investigated to address the inverse problem in studies of cancellous bone (Sebaa *et al.*, 2008; Dencks *et al.*, 2008; Dencks and Schmitz, 2013; Wear, 2010b,a, 2013). The following sections describe the wave propagation model used in the calculations as well as how the Bayesian algorithm calculates estimates of the ultrasonic parameters.

### 3.4.2 Two-mode wave propagation model

Figure 3.8 illustrates the division of an incoming ultrasonic wave into fast wave and slow wave components resulting from propagation through a bone specimen of thickness  $d$ . In the frequency domain, propagation through cancellous bone can be modeled as

$$Output(f) = Input(f)[H_{fast}(f) + H_{slow}(f)] + n \quad (3.25)$$

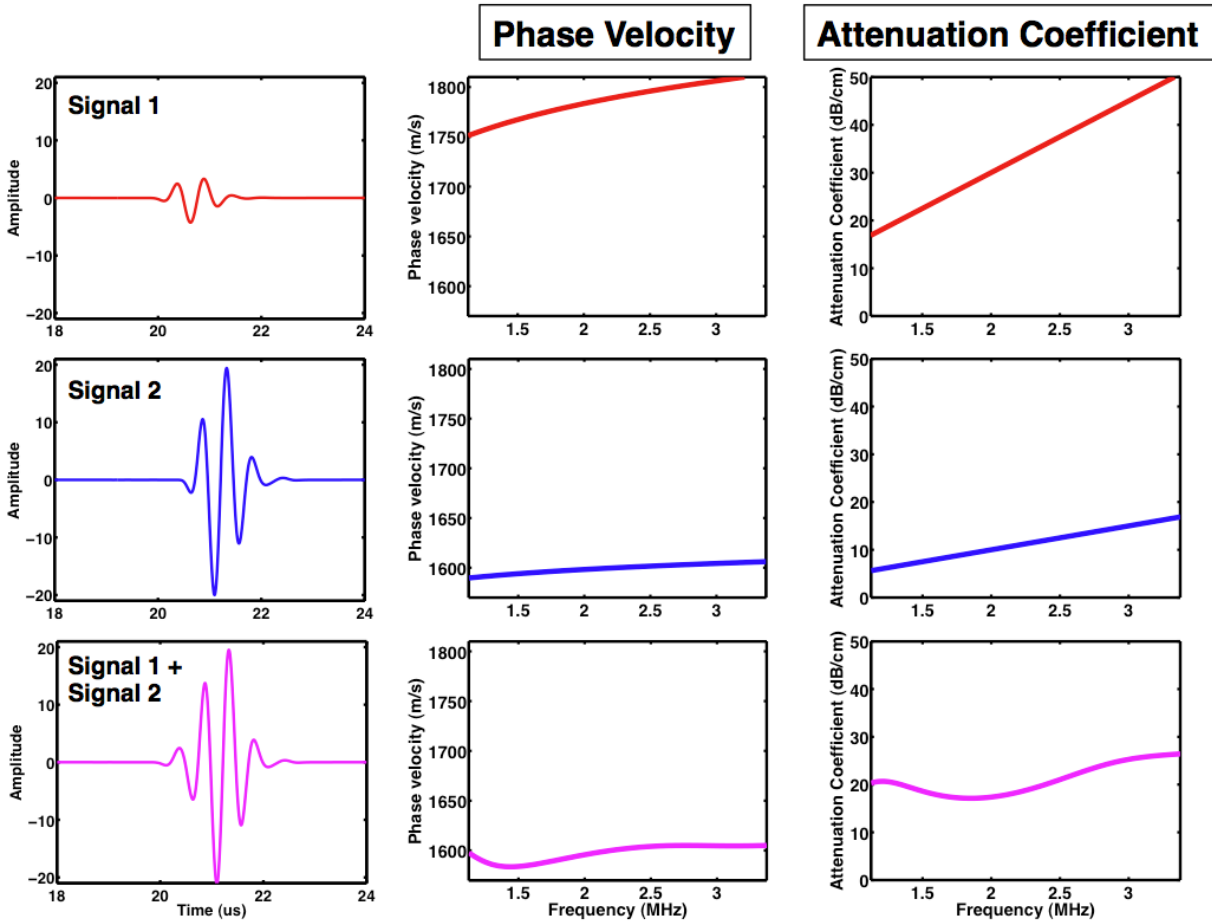


FIGURE 3.7: Effects of performing conventional one-mode analysis on a simulated mixed-mode signal. The top two rows show individual waves and their respective phase velocities and attenuation coefficients. The bottom row shows the mixed-mode signal resulting from adding signal 1 and signal 2 along with the phase velocity and attenuation coefficient obtained from conventional (one-mode) analysis. Both the phase velocity and attenuation coefficient results of the mixed-mode signal display artifacts caused by the interference of the two waves.

## Wave Propagation Model

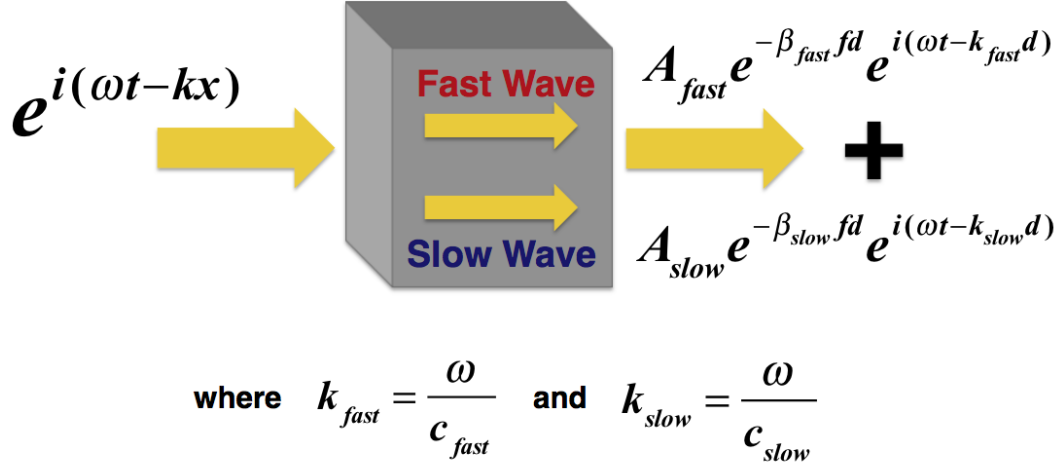


FIGURE 3.8: The two-mode wave propagation model used in the Bayesian probability theory analysis. The incident (input) wave is divided into a fast wave and a slow wave in the bone specimen. The output (mixed-mode) wave is the sum of the fast and slow waves.

where  $Output(f)$  and  $Input(f)$  are the complex Fourier spectra of the model waveform and the transmitted ultrasonic signal, respectively, and  $n$  is an additive noise term. For experimentally acquired data, a reference water-path-only signal was used as a source for  $Input(f)$ . The transfer functions,  $H_{fast}(f)$  and  $H_{slow}(f)$ , in Equation 3.25 for the fast and slow waves are given by

$$H_{fast}(f) = A_{fast} \exp(-\beta_{fast} f d) \exp\left(\frac{i2\pi f d}{c_{fast}(f)}\right) \quad (3.26)$$

$$H_{slow}(f) = A_{slow} \exp(-\beta_{slow} f d) \exp\left(\frac{i2\pi f d}{c_{slow}(f)}\right) \quad (3.27)$$

where  $A_{fast}$  and  $A_{slow}$  are the frequency-independent amplitudes of the two waves,  $\beta_{fast}$  and  $\beta_{slow}$  are the slopes of attenuation,  $d$  is the sample thickness, and  $c_{fast}(f)$  and  $c_{slow}(f)$  are the

phase velocities for the fast and slow waves. The parameters,  $A_{fast}$  and  $A_{slow}$ , are constrained to lie between 0 and 1, indicating that the amplitude of the fast and slow waves must be less than or equal to the amplitude of the reference (water-path-only) signal. In order to satisfy the causality-induced Kramers-Kronig relations, the phase velocities are related to the attenuation coefficients by

$$c_{fast}(f) = c_{fast}(f_0) + [c_{fast}(f_0)]^2 \frac{\beta_{fast}}{\pi^2} \ln\left(\frac{f}{f_0}\right) \quad (3.28)$$

$$c_{slow}(f) = c_{slow}(f_0) + [c_{slow}(f_0)]^2 \frac{\beta_{slow}}{\pi^2} \ln\left(\frac{f}{f_0}\right) \quad (3.29)$$

where  $f_0$  is a reference frequency within the experimental bandwidth, typically the nominal center frequency of the transducer. Based on Equations 3.28 and 3.29, the fast and slow wave phase velocities are required to increase logarithmically with frequency, thus exhibiting positive dispersion.

In Equations 4.2 - 3.29,  $\beta_{fast}$  and  $\beta_{slow}$  are written in natural units of Nepers per length per frequency [e.g. Np/cm/MHz]. Since nBUA is more commonly reported in units of decibels per length per frequency [dB/cm/MHz], nBUA values reported in the remainder of this thesis will be in units of dB/cm/MHz.

### 3.4.3 Bayesian parameter estimation

The Bayesian-based approach used in this thesis parallels closely to methods previously developed and tested by members of this Laboratory (Anderson *et al.*, 2010; Anderson, 2010; Marutyan *et al.*, 2007a,b). All of that work was inspired by the creative contributions of

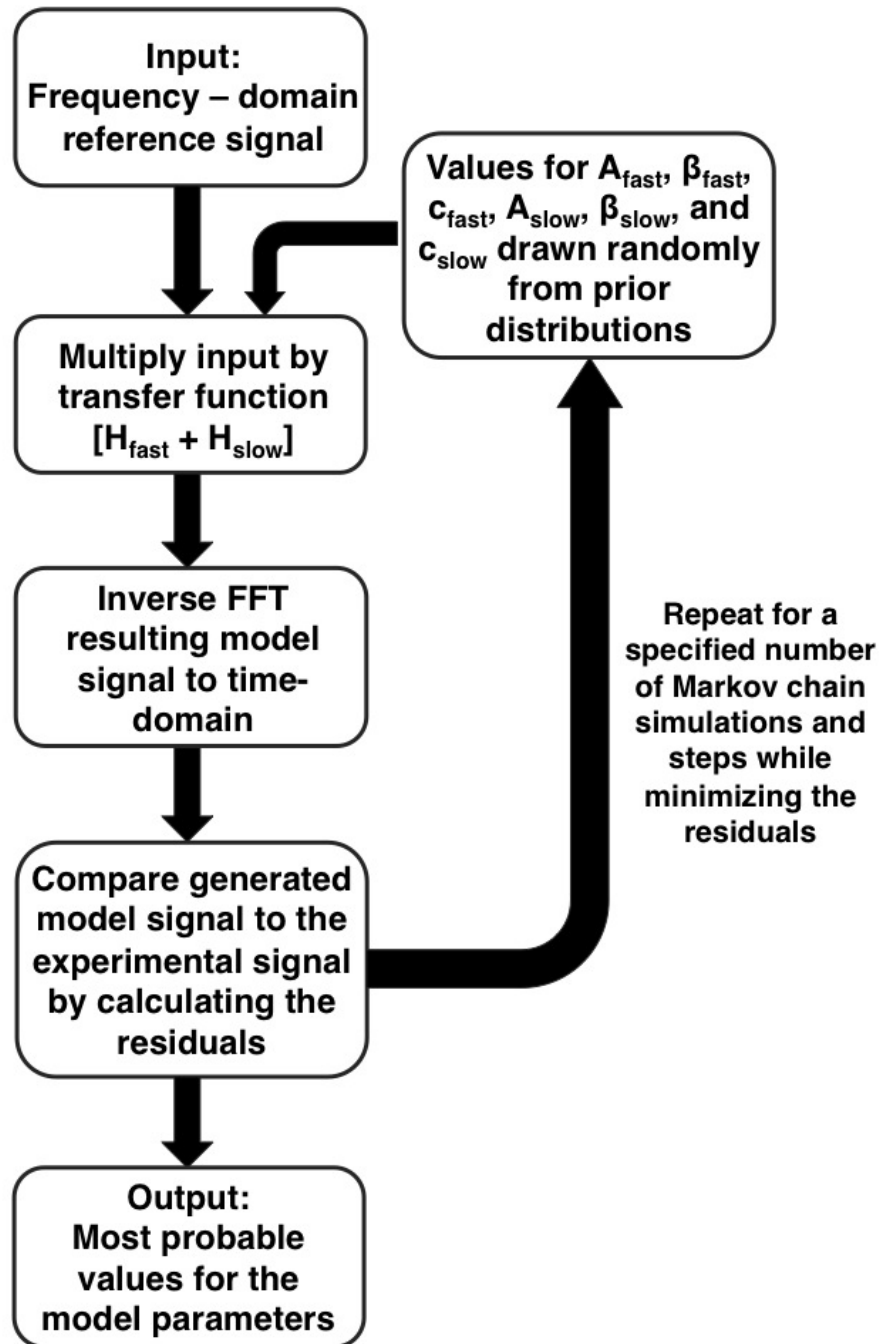


FIGURE 3.9: Schematic illustrating the use of the Bayesian algorithm.

Bretthorst and Jaynes (Jaynes and Bretthorst, 2003; Bretthorst, 2005).

As illustrated in Figure 3.9, Bayesian probability theory can be used to give the most probable estimates for the six propagation parameters ( $A_{fast}$ ,  $A_{slow}$ ,  $\beta_{fast}$ ,  $\beta_{slow}$ ,  $c_{fast}$ ,  $c_{slow}$ ) in the model above. These terms can be represented by a vector  $\Theta = \{A_{fast}, \beta_{fast}, c_{fast}(f_0), A_{slow}, \beta_{slow}, c_{slow}(f_0)\}$ . The *joint posterior probability* for all the parameters,  $\Theta$ , given the experimental data and any prior information is obtained by applying Bayes' Theorem

$$P(\Theta|D, I) = \frac{P(D|\Theta, I)P(\Theta|I)}{P(D, I)} \quad (3.30)$$

where  $D$  is the acquired experimental data, such as the reference and sample signals, and  $I$  is the relevant background information, such as the propagation model. The term  $P(D|\Theta, I)$  is known as the *likelihood*, or the direct probability for the data given the parameters ( $\Theta$ ) and prior information ( $I$ ).  $P(\Theta|I)$  is the *joint prior probability* for the parameters given only background information. The term in the denominator of Equation 3.30 is considered to be a normalization factor.

In the work presented in this thesis, the likelihood function ( $P(D|\Theta, I)$ ) was assigned using a Gaussian prior probability to represent what is known about the noise (Anderson, 2010). The dependence on the standard deviation of this Gaussian was removed using marginalization with a Jeffreys prior (Jeffreys, 1961). The joint prior probability,  $P(\Theta|I)$ , can be factored into the product of the prior probabilities of each individual parameter using the product rule (Cox, 1946) of probability theory

$$P(\Theta|I) = P(A_{fast}|I) \cdot P(\beta_{fast}|I) \cdot P(c_{fast}(f_0)|I) \cdot P(A_{slow}|I) \cdot P(\beta_{slow}|I) \cdot P(c_{slow}(f_0)|I). \quad (3.31)$$

The factorization in Equation 3.31 assumes that the parameters are logically independent -

that is, each prior probability depends only on the parameter of interest. For instance, it is assumed that what is known about  $\beta_{fast}$  does not depend on  $c_{slow}$ . The individual prior probabilities for the six parameters were assigned using bounded Gaussian distributions described by 4 parameters: mean, standard deviation, upper bound and lower bound. The priors are chosen to be general enough such that the results of the parameter estimation are not dependent on the specific values used. The mean is chosen to be the midpoint between the upper and lower bounds, and the standard deviation is chosen to one half of the difference between the upper and lower bounds.

In order to determine the most probable value (posterior probability) for each parameter, a procedure called *marginalization* is applied to the joint posterior probability so that the dependence on the other five parameters is removed. For example, the marginalized posterior probability for  $A_{fast}$  is computed as

$$P(A_{fast}|D, I) = \int \int \int \int \int P(\Theta|D, I) d\beta_{fast} dc_{fast}(f_0) dA_{slow} d\beta_{slow} dc_{slow}(f_0). \quad (3.32)$$

The posterior probabilities for the other parameters can be obtained in a similar way by marginalizing over all the parameters except the one of interest.

Equation 3.32 represents a complicated five-dimensional integral that must be repeated six times, once for each parameter in the model. These multi-dimensional integrals are difficult or impossible to evaluate analytically. Therefore, a Markov chain Monte Carlo simulation with simulated annealing was employed to determine an approximate solution. A Markov chain is a discrete stochastic process in which samples are drawn from a state space, and the current state ( $i$ ) depends only on the previous state ( $i - 1$ ). In the Bayesian

algorithm, a Markov chain is initialized at an arbitrary location in the parameter space set by the prior probability densities. The chain eventually converges to the desired posterior probability density (Anderson, 2010).

The steps within a Markov chain are determined using the Metropolis-Hastings algorithm (Metropolis and Ulam, 1949; Metropolis *et al.*, 1953; Hastings, 1970). This algorithm works by proposing a move within a certain region from the current location. The move to the new location is accepted if the probability at the new location is higher than the probability at the current location. However, even if the proposed location has a smaller probability than the current location, the move is still accepted with probability  $\frac{\text{prob}(\text{newlocation})}{\text{prob}(\text{oldlocation})}$  (Anderson, 2010). Therefore, some downhill moves are allowed, although small downhill moves are more favorable than large downhill moves.

To help prevent Markov chains from becoming trapped on a local maxima, simulated annealing can be introduced to the Bayesian algorithm (Kirkpatrick *et al.*, 1983). This allows the chains to explore a series of intermediate probability densities for a sufficient number of Metropolis-Hastings steps. An advantage of simulated annealing is that it can be easily parallelized, thus allowing for multiple independent Markov chains to be run simultaneously and in parallel (Anderson, 2010). The use of multiple Markov chains provides another safeguard against local minimum because low-probability chains can be "killed" and replaced by higher-probability chains.

Further details on Bayesian probability theory are given by Jaynes and Bretthorst (2003), Sivia and Skilling (2006), Bretthorst (2005), and the doctoral thesis of Christian Anderson (2010).



## 3.5 Comparison of conventional and Bayesian methods of analysis

Conventional and Bayesian methods were discussed above as possible techniques to analyze data from cancellous bone. Although the two methods evaluate similar parameters, there are fundamental differences between the two methods that require consideration. Conventional analysis is carried out entirely in the frequency-domain, whereas the Bayesian analysis does the comparison of the model-generated wave and the experimental wave in the time-domain.

Both conventional and Bayesian analysis methods measure the phase velocity of the sample. Conventional methods, using phase spectroscopy, give the phase velocity over the entire usable bandwidth. In contrast, the Bayesian estimation technique gives the phase velocity at a specific frequency,  $f_0$ , which is usually chosen to be the center frequency of the usable bandwidth. The phase velocity at other frequencies can be determined using the Kramers-Kronig relations (Equations 3.28- 3.29), which can be applied separately for both the fast and slow waves.

Similarly, both methods of analysis give values of  $\beta$ . As discussed above,  $\beta$  is properly defined as the slope of the attenuation coefficient plotted as a function of frequency, which has had the insertion losses removed. However, in most studies of bone, the reported  $\beta$  or nBUA value is actually the slope of the signal loss, which still includes the loss at the boundaries. In spite of this, if the insertion losses are frequency-independent, the slopes of the attenuation coefficient and signal loss are equal. Insertion losses are dependent on the relative acoustic

impedances at the boundary. As indicated in Equation 3.18, impedances (and consequently insertion losses) can be frequency dependent, but are approximately independent of frequency if the ratio of  $\alpha/k$  is sufficiently small. Because the Bayesian method performs the comparison of the model-generated wave and the experimental wave in the time-domain, the estimated values for  $\beta_{fast}$  and  $\beta_{slow}$  may be influenced by the estimation of the  $A_{fast}$  or  $A_{slow}$  parameters, since they also contribute to the overall loss of the signal.

Perhaps the most challenging parameters to interpret in the Bayesian method are the fast and slow wave amplitudes,  $A_{fast}$  and  $A_{slow}$ . It is assumed that these parameters account for the frequency-independent (and distance-independent) losses, in contrast to the term  $\exp(-\beta fd)$  which accounts for the frequency and distance-dependent losses. In the case of a one-mode signal, the  $A$  parameter should be equivalent to the (two surface) transmission losses and therefore can be compared to the insertion losses calculated with conventional methods using Equation 3.17. However, in the case of two-mode propagation, these amplitude terms contain information about the distribution of the incident energy into the two wave modes in addition to information about the insertion losses. The fact that both the insertion losses and the distribution of energy occur at the same location - the boundary - adds to the complexity of the problem (Hoffman *et al.*, 2012). When an incident pulse hits the boundary between the water and the specimen, there will be three resulting waves. The reflected wave contains information corresponding to the insertion losses. There will also be two transmitted waves, a fast wave with amplitude  $A_{fast}$  and a slow wave with amplitude  $A_{slow}$ . Since some of the incident waves energy is lost to the reflected wave, it is difficult to determine a simple relationship between  $A_{fast}$  and  $A_{slow}$  or even to interpret the

individual values of  $A_{fast}$  and  $A_{slow}$  (Hoffman *et al.*, 2012). It is also possible that  $A_{fast}$  and  $A_{slow}$  also include contributions from diffraction and phase cancellation at the receiving transducer (Anderson *et al.*, 2010). Since diffraction and phase cancellation are dependent on frequency, the assumption that  $A_{fast}$  and  $A_{slow}$  are frequency-independent might prove inaccurate. Given all of these complicating factors, it is difficult to predict the expected values of  $A_{fast}$  and  $A_{slow}$  in two-mode systems.

### 3.6 Other potential complicating factors

In addition to the difficulties caused by two overlapping wave modes, there are other complicating factors that are not addressed in the conventional analysis method and are not directly accounted for in the propagation model used in the Bayesian analysis method. Perhaps the two largest potential factors are diffraction and phase cancellation at the face of a piezoelectric receiving transducer (Bauer *et al.*, 2008, 2009). Both of these effects could introduce systematic errors, which could then influence the estimates of the ultrasonic parameters, especially those involved in the signal loss ( $A_{fast}$ ,  $A_{slow}$ ,  $\beta_{fast}$ ,  $\beta_{slow}$ ) (Anderson, 2010). The sample thickness dependence observed in bone data (Chapter 6) and in plastic phantom data (Chapter 7) presented in this thesis may be, in part, due to one or both of these effects. The Bayesian analysis method may be more sensitive to diffraction and phase cancellation effects than the conventional method. The Bayesian method performs the comparison of the model-generated wave and the experimental wave in the time-domain, in contrast to the case for conventional analysis which processes the data in the frequency

domain. In the Bayesian approach, the estimated values for  $\beta_{fast}$  and  $\beta_{slow}$  may be influenced by the estimation of the  $A_{fast}$  or  $A_{slow}$  parameters, whereas in the conventional approach the value of  $\beta$  is not influenced by the determination of the insertion losses. The effects of diffraction on both conventional and Bayesian results will be discussed further in Chapter 7.

## Bibliography

- Anderson, C. (2010), “Physics of ultrasonic wave propagation in bone and heart characterized using Bayesian parameter estimation”, Ph.D. thesis, Washington University in St. Louis.
- Anderson, C., Bauer, A. Q., Holland, M., Pakula, M., Laugier, P., Bretthorst, G. L., and Miller, J. G. (2010), “Inverse problems in cancellous bone: Estimation of the ultrasonic properties of fast and slow waves using Bayesian probability theory”, *J Acoust Soc Am* **128**, 2940–2948.
- Anderson, C., Marutyan, K., Holland, M., Wear, K. A., and Miller, J. G. (2008), “Interference between wave modes may contribute to the apparent negative dispersion observed in cancellous bone”, *J Acoust Soc Am* **124**, 1781–1789.
- Baldwin, S., Marutyan, K., Yang, M., Wallace, K., Holland, M., and Miller, J. (2006), “Measurements of the anisotropy of ultrasonic attenuation in freshly excised myocardium”, *J Acoust Soc Am* **119**, 3130–3139.
- Barkmann, R., Laugier, P., Moser, U., Dencks, S., Klausner, M., Padilla, F., Haiat, G., Heller, M., and Glüer, C. (2008), “In vivo measurements of ultrasound transmission through the human proximal femur”, *Ultrasound Med and Biol* **34**, 1186–90.
- Bauer, A. Q., Anderson, C. C., Holland, M. R., and Miller, J. G. (2008), “Measurement artifacts in sonometry of cancellous bone: The relative impact of phase cancellation and interference on measurements of phase-distorting phantoms”, *IEEE International Ultrasonics Symposium Proceedings*, 137–141.
- Bauer, A. Q., Anderson, C. C., Holland, M. R., and Miller, J. G. (2009), “Bone sonometry: Reducing phase aberration to improve estimates of broadband ultrasonic attenuation”, *J Acoust Soc Am* **125**, 522–529.
- Bossy, E., Padilla, F., Peyrin, F., and Laugier, P. (2005), “Three-dimensional simulation of ultrasound propagation through trabecular bone structures measured by synchrotron microtomography”, *Phys Med Biol* **50**, 5545–5556.
- Bracewell, R. (2000), *The Fourier Transform and its Applications* (McGraw-Hill), 3rd edition.
- Bretthorst, G. L. (2005), “Exponential parameter estimation (in NMR) using Bayesian probability theory”, *Concepts Magn Reson* **27**, 55–63.
- Chaffai, S., Padilla, F., Berger, G., and Laugier, P. (2000), “In vitro measurement of the frequency-dependent attenuation in cancellous bone between 0.2 and 2 MHz”, *J Acoust Soc Am* **108**(3), 1281–1289.

- Cox, R. T. (1946), “Probability, frequency, and reasonable expectation”, *Am J Phys* **14**, 1–13.
- Dencks, S., Barkmann, R., Padilla, F., Laugier, P., Schmitz, G., and Glüer, C. (2008), “Model-based estimation of quantitative ultrasound variables at the proximal femur”, *IEEE Trans Ultrason Ferroelectr Freq Control* **55(6)**, 1304–1315.
- Dencks, S. and Schmitz, G. (2013), “Estimation of multipath transmission parameters for quantitative ultrasound measurements of bone”, *IEEE Trans Ultrason Ferroelectr Freq Control* **60(9)**, 1884–1895.
- Droin, P., Berger, G., and Laugier, P. (1998), “Velocity dispersion of acoustic waves in cancellous bone”, *IEEE Trans Ultrason Ferroelectr Freq Control* **45**, 581–592.
- Gibson, A., Singh, G., Hoffman, J., Ludomirsky, A., and Holland, M. (2009), “Measurements of ultrasonic attenuation properties of midgestational fetal pig hearts”, *Ultrasound in Med and Biol* **35(2)**, 319–328.
- Glüer, C., Wu, C., and Genant, H. (1993), “Broadband ultrasound attenuation signals depend on trabecular orientation: An in vitro study”, *Osteoporosis Int.* **3**, 185–191.
- Goss, S. A., Johnston, R. L., and Dunn, F. (1978), “Comprehensive compilation of empirical ultrasonic properties of mammalian tissues”, *J Acoust Soc Am* **64**, 423–457.
- Haiat, G., Padilla, F., Peyrin, F., and Laugier, P. (2008), “Fast wave ultrasonic propagation in trabecular bone: numerical study of the influence of porosity and structural anisotropy”, *J Acoust Soc Am* **123**, 1694–1705.
- Hastings, W. (1970), “Monte Carlo sampling methods using Markov chains and their applications”, *Biometrika* **57**, 97–109.
- Hoffman, J., Nelson, A., Holland, M., and Miller, J. (2012), “Cancellous bone fast and slow waves obtained with Bayesian probability theory correlate with porosity from computed tomography”, *J Acoust Soc Am* **132(3)**, 1830–1837.
- Hoffmeister, B. K. (2011), “Frequency dependence of apparent ultrasonic backscatter from human cancellous bone”, *Phys Med Biol* **56(3)**, 667–683.
- Hoffmeister, B. K., Johnson, D. P., Janeski, J. A., Keedy, D. A., Steinert, B. W., Viano, A. M., and Kaste, S. C. (2008), “Ultrasonic characterization of human cancellous bone in vitro using three different apparent backscatter parameters in the frequency range 0.6 - 15.0 MHz”, *IEEE Trans Ultrason Ferroelectr Freq Control* **55(7)**, 1442–1452.
- Hosokawa, A. and Otani, T. (1998), “Acoustic anisotropy in bovine cancellous bone”, *J Acoust Soc Am* **103**, 2718–2722.
- Jaynes, E. and Bretthorst, G. (2003), *Probability theory: The logic of science* (Cambridge University Press, Cambridge).

- Jeffreys, H. (1961), *Theory of Probability* (Oxford Univ Press).
- Jenson, F., Padilla, F., Bousson, V., Bergot, C., Laredo, J. D., and Laugier, P. (2006), “In vitro ultrasonic characterization of human cancellous femoral bone using transmission and backscatter measurements: Relationships to bone mineral density”, *J Acoust Soc Am* **119**, 654–663.
- Johnson, B. (2012), “Ultrasonic characterization of shear thickening suspensions”, Ph.D. thesis, Washington University in St. Louis.
- Kirkpatrick, S., Jr, C. G., and Vecchi, M. (1983), “Optimatization by simulated annealing”, *Science* **220**, 671–680.
- Langton, C. and Hodgskinson, R. (1997), “The in vitro measurement of ultrasound in cancellous bone”, *Stud Health Technol Inform* **40**, 175–199.
- Langton, C. and Njeh, C. (2008), “The measurement of broadband ultrasonic attenuation in cancellous bone—a review of the science and technology”, *IEEE Trans Ultrason Ferroelectr Freq Control* **55**, 1546–1554.
- Marczak, W. (1997), “Water as a standard in the measurements of speed of sound in liquids”, *J Acoust Soc Am* **102**, 2776–2779.
- Markham, J. (1951), “Absorption of sound in fluids”, *Review of Modern Physics* **23**, 353–411.
- Marutyan, K., Anderson, C., Wear, K. A., Holland, M., Miller, J. G., and Bretthorst, G. L. (2007a), “Parameter estimation in ultrasonic measurements on trabecular bone”, *AIP Conference Proceedings* **954**, 329–336.
- Marutyan, K., Bretthorst, G. L., and Miller, J. G. (2007b), “Bayesian estimatiion of the underlying bone properties from mixed fast and slow mode ultrasonic signals”, *J Acoust Soc Am* **121**, EL8–15.
- Marutyan, K., Holland, M., and Miller, J. (2006), “Anomalous negative dispersion in bone can result from the interference of fast and slow waves”, *J Acoust Soc Am* **120**, EL55–61.
- McKelvie, M. and Palmer, S. (1991), “The interaction of ultrasound with cancellous bone”, *Phys Med Biol* **36**, 1331–1340.
- Metropolis, N., Rosenbluth, A., Rosenbluth, M., Teller, A., and Teller, E. (1953), “Equation of state calculations by fast computing machines”, *J Chem Phys* **21**, 1087–1092.
- Metropolis, N. and Ulam, S. (1949), “The Monte Carlo method”, *J Am Stat Assoc* **44**, 335–341.

- Mimbs, J. W., O'Donnell, M., Bauwens, D., Miller, J. W., and Sobel, B. E. (1980), "The dependence of ultrasonic attenuation and backscatter on collagen content in dog and rabbit hearts", *Circ Res* **47**, 49–58.
- Mottley, J. G. and Miller, J. G. (1990), "Anisotropy of the ultrasonic attenuation in soft tissues: measurements in vitro", *J Acoust Soc Am* **88**, 1203–1210.
- Ophir, J., Shawker, T., Maklad, H., Miller, J., Flax, S., Narayana, P., and Jones, J. (1984), "Attenuation estimation in reflection: Progress and prospects", *Ultrasonic Imaging* **6**, 349–395.
- Padilla, F. and Laugier, P. (2000), "Phase and group velocities of fast and slow compressional waves in trabecular bone", *J Acoust Soc Am* **108**, 1949–1952.
- Pakula, M., Padilla, F., and Laugier, P. (2009), "Influence of the filling fluid on frequency-dependent velocity and attenuation in cancellous bone between 0.35 and 2.5 MHz", *J Acoust Soc Am* **126**, 3301–3310.
- Petley, G., Robins, P., and Aindow, J. (1995), "Broadband ultrasonic attenuation: are current measurement techniques inherently inaccurate?", *Br J Radiol* **68**, 1212–1214.
- Sachse, W. and Pao, Y. (1978), "On the determination of phase and group velocities of dispersive waves in solids", *Journal of Applied Physics* **49**, 4320.
- Sebaa, N., Fellah, Z., Fellah, M., Ogam, E., Mitri, F., Depollier, C., and Lauriks, W. (2008), "Application of the Biot model to ultrasound in bone: inverse problem", *IEEE Trans Ultrason Ferroelectr Freq Control* **55**, 1516–1523.
- Sivia, D. and Skilling, J. (2006), *Data analysis: A Bayesian tutorial* (Oxford Univ Press, New York).
- Strelitzki, R. and Evans, J. (1996), "An investigation of the measurement of broadband ultrasonic attenuation in trabecular bone", *Ultrasonics* **34**, 785–791.
- Strelitzki, R. and Evans, J. (1998), "Diffraction and interface losses in broadband ultrasound attenuation measurements of the calcaneum", *Physiol Meas* **19**, 197–204.
- Trousil, R. (2002), "Ultrasonic propagation in inhomogeneous media: Toward quantitative ultrasonic imaging", Ph.D. thesis, Washington University in St. Louis.
- Trousil, R., Waters, K., and Miller, J. (2001), "Experimental validation of the use of the Kramers-Kronig relations to eliminate the phase sheet ambiguity in broadband phase spectroscopy", *J Acoust Soc Am* **109**(2236-2243).
- Waters, K. and Hoffmeister, B. K. (2005), "Kramers-Kronig analysis of attenuation and dispersion in trabecular bone", *J Acoust Soc Am* **118**, 3912–3920.



- Waters, K., Hughes, M., Mobley, J., Brandenburger, G. H., and Miller, J. G. (2000), “On the applicability of Kramers-Kronig relations for ultrasonic attenuation obeying a frequency power law”, *J Acoust Soc Am* **108**, 556–563.
- Waters, K., Hughes, M., Mobley, J., and Miller, J. (2003), “Differential forms of the Kramers-Kronig dispersion relations”, *IEEE Trans Ultrason Ferroelectr Freq Control* **50(68-76)**.
- Waters, K., Mobley, J., and Miller, J. G. (2005), “Causality-imposed (Kramers-Kronig) relationships between attenuation and dispersion”, *IEEE Trans Ultrason Ferroelectr Freq Control* **52**, 822–833.
- Wear, K. A. (2000a), “Anisotropy of ultrasonic backscatter and attenuation from human calcaneus: Implications for relative roles of absorption and scattering in determining attenuation”, *J Acoust Soc Am* **107(6)**, 3474–3479.
- Wear, K. A. (2000b), “Measurements of phase velocity and group velocity in human calcaneus”, *Ultrasound Med and Biol* **26**, 641–646.
- Wear, K. A. (2008), “The effect of phase cancellation on estimates of broadband ultrasound attenuation and backscatter coefficient in human calcaneus in vitro”, *IEEE Trans Ultrason Ferroelectr Freq Control* **55**, 384–390.
- Wear, K. A. (2010a), “Cancellous bone analysis with modified least squares Prony’s method and chirp filter: Phantom experiments and simulation”, *J Acoust Soc Am* **128**, 2191–2203.
- Wear, K. A. (2010b), “Decomposition of two-component ultrasound pulses in cancellous bone using modified least squares Prony’s method - phantom experiment and simulation”, *Ultrasound Med and Biol* **36**, 276–287.
- Wear, K. A. (2013), “Estimation of fast and slow wave properties in cancellous bone using Prony’s method and curve fitting”, *J Acoust Soc Am* **133**, 2490–2501.

# CHAPTER 4

---

## EFFECTS OF INTERFERING FAST AND SLOW WAVES ON THE ULTRASONIC PROPERTIES OF HUMAN CALCANEAL BONE

### 4.1 Preface

This Chapter details the methods and results of ultrasonic measurements made on human calcaneal (heel) bone specimens. Phase velocity and apparent attenuation properties of the bone specimens obtained from assuming one wave mode are compared to those results obtained from a Bayesian two wave mode technique. Micro-computed tomography was also performed on the samples to assess microstructural information. It was investigated whether the Bayesian-derived ultrasonic parameters correlate with the clinically-relevant microCT parameters. These results are presented in the peer-reviewed journal article, “Cancellous bone fast and slow waves obtained with Bayesian probability theory correlate with porosity

from computed tomography” by Joseph J. Hoffman, Amber M. (Nelson) Groopman, Mark R. Holland, and James G. Miller and published in *The Journal of the Acoustical Society of America*, Vol. 132, No. 3, pp. 1830-37 and in the conference proceeding, ”Single mode analysis appears to overestimate the attenuation of human calcaneal bone based on Bayesian-derived fast and slow wave mode analysis” by Amber M. (Nelson) Groopman, Joseph J. Hoffman, Mark R. Holland, and James G. Miller for the 2012 *IEEE Ultrasonics Symposium*, pp. 1015-18.

## 4.2 Introduction

It is well known that cancellous bone can support the propagation of two compressional wave modes, referred to as the fast wave and the slow wave. Depending on the experimental situation, these two wave modes can overlap substantially in the time-domain. Analysis of this interfering two-mode signal can lead to misleading results of the bone’s ultrasonic properties (Marutyan *et al.*, 2006; Anderson *et al.*, 2008; Bauer *et al.*, 2008). To ensure that the true ultrasonic properties of the cancellous bone are determined, the fast and slow waves should be separated and analyzed individually. We have previously demonstrated an approach utilizing Bayesian probability theory that is capable of isolating the fast and slow waves, even in cases of extreme overlap and interference (Marutyan *et al.*, 2007). This Bayesian technique has proven successful at separating the two wave modes in experimental data from both plastic phantoms (Anderson *et al.*, 2010) and from cancellous bone (Nelson *et al.*, 2011).

One significant determinant of fast and slow wave separation or overlap in the time domain is the angle of ultrasonic insonification. Previous studies have shown that for parallel insonification or insonification along the primary direction of the trabeculae there are often distinct fast and slow waves (Hosokawa and Otani, 1997, 1998). This means that these waves can be separated using time gates and conventional methods of analysis. However, for perpendicular insonification there often appears to be only one wave present in the received time domain signal. Clinical bone sonometry systems applied to the heel involve propagation perpendicular to the predominant trabecular orientation and these systems measure quantitative ultrasound parameters assuming one wave.

There were three objectives for this study. The first objective was to isolate and identify fast and slow waves in the case of perpendicular insonification of the calcaneus (heel bone). The second objective was to compare directly the results of one-mode analysis and two-mode (Bayesian) analysis. This comparison was designed to quantify the effects arising from the presence of, and potential interference of, two waves on ultrasonic measurements of phase velocity and broadband ultrasound attenuation. The third objective was to compare the Bayesian-derived fast and slow wave ultrasonic properties to anatomical data acquired by microCT (Hoffman *et al.*, 2012).

## 4.3 Methods

### 4.3.1 Calcaneal sample preparation

Eight human calcaneal samples obtained from cadavers were prepared by sawing off the cortical edges resulting in approximately rectangular specimens of only trabecular bone. India ink was used to mark the medial face of the samples. The dimensions of the samples were measured using digital calipers at five locations in each dimension. The thicknesses of the samples, in the medial-lateral direction, ranged from 8.09 mm to 15.45 mm and are listed in Table 4.1. The samples were defatted by soaking them for approximately 48 hours in a 1:1 solution of ethyl alcohol and acetone and then rinsing with a water jet (Ding *et al.*, 1997). The samples were then dried in a vacuum desiccator. The process of defatting resulted in a loss of approximately 20-50% of the initial mass. Apparent mass densities of the defatted specimens were determined by dividing the mass of the sample by the mean volume and can be found in Table 4.1.

### 4.3.2 MicroCT measurements

Three-dimensional trabecular bone microstructure was measured by micro-computed tomography (SCANCO Medical vivaCT 40, Wayne, PA). The volume-of-interest (VOI) used for the microstructural analysis included approximately 95% of the total sample volume. The system was configured to have a spatial resolution of 17.5  $\mu\text{m}$  in all three dimensions. A grayscale threshold was chosen to be used for all of the scans. The threshold determines what is categorized as bone (white) and what is categorized as not bone (black). If the threshold

TABLE 4.1: Physical characteristics of the human calcaneal samples. The thickness measurements listed are for the medial-lateral direction and are the mean plus or minus one standard deviation of five measurements. The apparent mass density was calculated from the mass and the mean volume. The bone volume fraction (BV/TV) was determined by microCT measurements.

Sample	Thickness (mm)	Apparent Density (g/cm <sup>3</sup> )	BV/TV
B-1	11.52 ± 0.18	0.22	0.086
B-2	11.74 ± 0.22	0.50	0.171
B-3	11.36 ± 0.26	0.49	0.213
B-4	8.09 ± 0.52	0.47	0.198
B-5	15.45 ± 0.55	0.35	0.162
B-6	12.68 ± 0.15	0.48	0.165
B-7	12.44 ± 0.81	0.14	0.059
B-8	11.52 ± 0.40	0.24	0.116

is set too low, bone structures may appear much thicker than in the original, unsegmented image. However, if the threshold is set too high, some bone structure might be missed or thinned compared to the unsegmented image. Figure 4.1 shows the region of interest (ROI) used for segmentation and the effects of thresholding on the eight calcaneal samples. From these segmented and thresholded images, automated distance transformation algorithms were used to calculate the following parameters: bone volume fraction (BV/TV), trabecular number (Tb.N), trabecular thickness (Tb.Th), trabecular spacing (Tb.Sp), structural model index (SMI), and the connective density (Conn. D). Table 4.2 gives brief descriptions of these structural parameters.

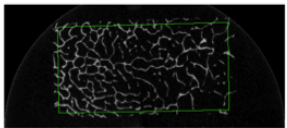
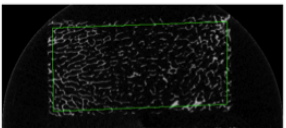
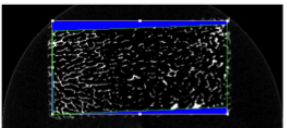
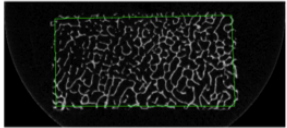
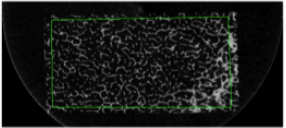
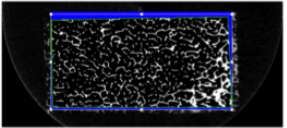
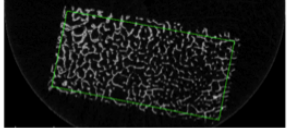
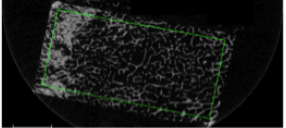
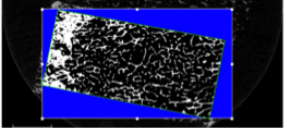
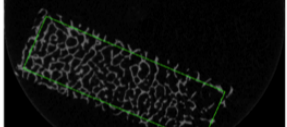
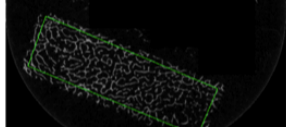
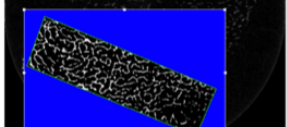
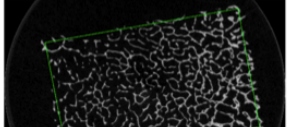
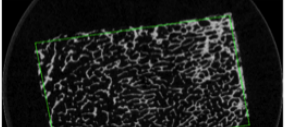
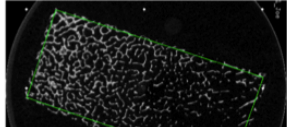
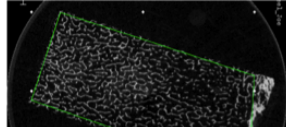
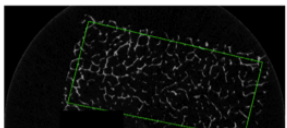
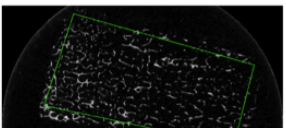
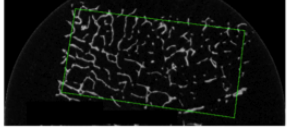
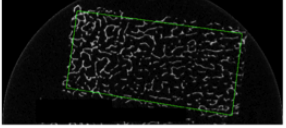
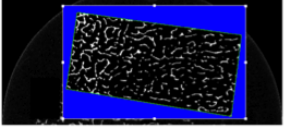
Sample	First slice of VOI	Last slice of VOI	Last slice with threshold applied
B-1			
B-2			
B-3			
B-4			
B-5			Image unavailable
B-6			Image unavailable
B-7			Image unavailable
B-8			

FIGURE 4.1: MicroCT images of the eight human calcaneal samples studied. The first column shows the first slice in the volume of interest (VOI). The second column shows the last slice in the VOI. The third column shows the last slice in the VOI after the threshold has been applied (white = bone, black = not bone). The green boxes represent the region of interest segmented for the measurements of bone histomorphometry in each slice.

TABLE 4.2: Definitions and descriptions of the trabecular bone microstructural parameters obtained from microCT.

Abbreviation	Variable	Description	Units
BV/TV	Bone volume fraction	Ratio of the segmented bone volume to the total volume of the ROI	%
Tb. N	Trabecular number	Measure of the average number of trabeculae per unit length	1/mm
Tb. Th	Trabecular thickness	Mean thickness of trabeculae	mm
Tb. Sp	Trabecular spacing	Mean distance between trabeculae	mm
SMI	Structure model index	Indicator of the structure of the trabeculae: SMI = 0 for parallel plates and SMI = 3 for cylindrical rods	
Conn. D	Connective density	Measure of the degree of connectivity of trabeculae normalized by the total volume (TV)	1/mm <sup>3</sup>

### 4.3.3 Ultrasonic measurements

Data were acquired in a water tank at room temperature ( $T = 21.1 \pm 0.1$  C) using a matched pair of 1.125 inch diameter, 1.5 inch focal length, broadband transducers (Panametrics v391, Waltham, MA) nominally centered at 500 kHz in a through-transmission arrangement. The two transducers were separated by approximately 76 mm (3 inches) or twice the focal length. One hour prior to ultrasonic testing, the samples were degassed underwater in a desiccator to remove any air trapped inside the samples. Since the specimens were small and not all the same size, custom sample holders were constructed from high density styrofoam as shown in Figure 4.2. The calcaneal samples were placed on a motion controller located halfway between the transducers and were insonified with the ultrasonic beam in the mediolateral direction, which is the same orientation used in clinical heel bone sonometers. The excitation signal was a 500 kHz center frequency, single-cycle sine wave





FIGURE 4.2: Sample holder consisting of a custom-cut piece of high density styrofoam fit into a Delrin frame. The Delrin frame was attached to a computer-controlled motion controller. Photograph by Amber Groopman.

burst with a peak-to-peak amplitude of 400 mV from a pulse/function generator (HP 8116A, Palo Alto, CA). Before being sent to the transmit transducer, the signal was amplified by a 50 dB gain radiofrequency (rf) power amplifier (ENI 240L, Rochester, NY). Received signals were first low-pass filtered (1.6 MHz) then amplified by a preamplifier (Panametrics 5676, Waltham, MA) before being digitized using an 8-bit Tektronix oscilloscope (TDS 5052B, Beaverton, OR). The time-domain traces were digitized at a rate of 50 MS/s (20ns/pt) and temporally averaged 128 times. Radiofrequency data were collected at 9 individual sites in the middle of each sample, as shown in Figure 4.3. These sites covered an 8 mm by 8 mm grid with 4 mm spacing between data sites. The 4 mm spacing was chosen to correspond to the theoretical 6 dB down beam width, which ensures that the sites are spatially independent. The radiofrequency data acquired from the calcaneal samples along with reference (water path only) time-domain traces were used as inputs into a Bayesian probability algorithm

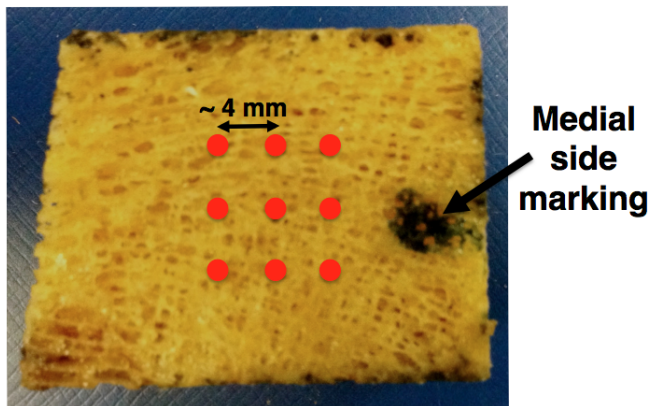


FIGURE 4.3: Bone specimen with raster scan locations. The spacing between sites was approximately 4 mm. Photograph by Amber Groopman.

that estimated the ultrasonic parameters of the separated fast and slow waves.

#### 4.3.4 Bayesian parameter estimation

In this study, Bayesian probability theory was implemented to estimate a total of six ultrasonic parameters: three for the fast wave ( $A_{fast}$ ,  $\beta_{fast}$ ,  $c_{fast}(f)$ ) and three for the slow wave ( $A_{slow}$ ,  $\beta_{slow}$ ,  $c_{slow}(f)$ ). These six parameters come from a model that represents the received sample signal as the sum of a fast wave and a slow wave. The details of the ultrasonic wave propagation model can be found in Chapter 3.

In the frequency domain, ultrasonic data through cancellous bone can be modeled as

$$Output(f) = Input(f)[H_{fast}(f) + H_{slow}(f)] \quad (4.1)$$

where  $Input(f)$  and  $Output(f)$  are the complex Fourier spectra of the transmitted signal and the received sample signal, respectively. In this study, a reference water path only signal was used for  $Input(f)$ .  $H_{fast}(f)$  and  $H_{slow}(f)$  are the transfer functions for the fast and slow

TABLE 4.3: Prior probability distributions for each model parameter. The means and standard deviations define Gaussian distributions that are bounded by the minimum and maximum values.

	$A_{fast}$	$A_{slow}$	$\beta_{fast}$ (dB/cm/MHz)	$\beta_{slow}$	$c_{fast}(500 \text{ kHz})$	$c_{slow}(500 \text{ kHz})$ (m/s)
Minimum	0	0	0	0	1500	1300
Mean	0.5	0.5	21.7	21.7	1750	1500
Maximum	1.0	1.0	43.3	43.3	2000	1700
Std. Dev.	0.5	0.5	21.7	21.7	250	200

waves. The transfer function for the fast wave is given by

$$H_{fast}(f) = A_{fast} \exp(-\beta_{fast} f d) \exp\left(\frac{i 2\pi f d}{c_{fast}(f)}\right) \quad (4.2)$$

where  $A_{fast}$  is a frequency-independent loss term,  $\beta_{fast}$  is the slope of attenuation for the fast wave,  $d$  is the sample thickness, and  $c_{fast}(f)$  is the phase velocity for the fast wave. The transfer function for the slow wave,  $H_{slow}(f)$ , has the same form as Eq. 4.2; the subscript  $A_{fast}$  is replaced with  $A_{slow}$ . In order to satisfy the causality-induced Kramers-Kronig relations, the phase velocities were required to increase logarithmically with frequency, thus exhibiting positive dispersion.

For the Bayesian parameter estimation, the prior probabilities for each of the six parameters were assigned to be bounded Gaussian distributions as shown in Table 4.3. The posterior probability density functions for each of the parameters are five dimensional integrals. They were approximated using a Markov chain Monte Carlo simulation with simulated annealing.

### 4.3.5 Data Analysis

The same method of data analysis was applied to both the unseparated sample wave, which likely consists of interfering fast and slow waves, and the Bayesian-separated fast wave and slow wave.

Phase velocities were calculated using a phase spectroscopy technique, which determines the phase velocity in a sample by comparing the phases of the Fourier transforms of a reference and a through-sample signal (Trousil, 2002). The frequency dependent phase velocity of the sample was obtained from

$$c_s(f) = c_w \left[ \frac{2\pi f d}{2\pi f d + c_w \Delta\phi(f)} \right] \quad (4.3)$$

where  $c_w$  is the speed of sound in water and  $\phi(f)$  is the difference in phase between the sample and reference spectra. The phase velocities of the unseparated sample wave ( $c_{samp}(f)$ ), the individual fast wave ( $c_{fast}(f)$ ), and the individual slow wave ( $c_{slow}(f)$ ) were determined for all 72 sites (9 sites per sample) studied.

The attenuation coefficient, in units of dB/cm, was determined by performing a log-spectral subtraction technique of the form,

$$\alpha(f) = \frac{10 \log \left( \left| \tilde{V}_w(f) \right|^2 \right) - 10 \log \left( \left| \tilde{V}_s(f) \right|^2 \right) + 10 \log [T_{h \rightarrow s}^I \cdot T_{s \rightarrow h}^I]}{d} \quad (4.4)$$

where  $\left| \tilde{V}_w(f) \right|^2$  and  $\left| \tilde{V}_s(f) \right|^2$  are the power spectra of the reference and through-sample signals, and  $T_{h \rightarrow s}^I$  and  $T_{s \rightarrow h}^I$  are the intensity transmission coefficients for the front wall and back wall boundaries, respectively (Trousil, 2002). The insertion losses at the boundaries between the water and sample (i.e., the third term in Equation 4.4) were neglected since the

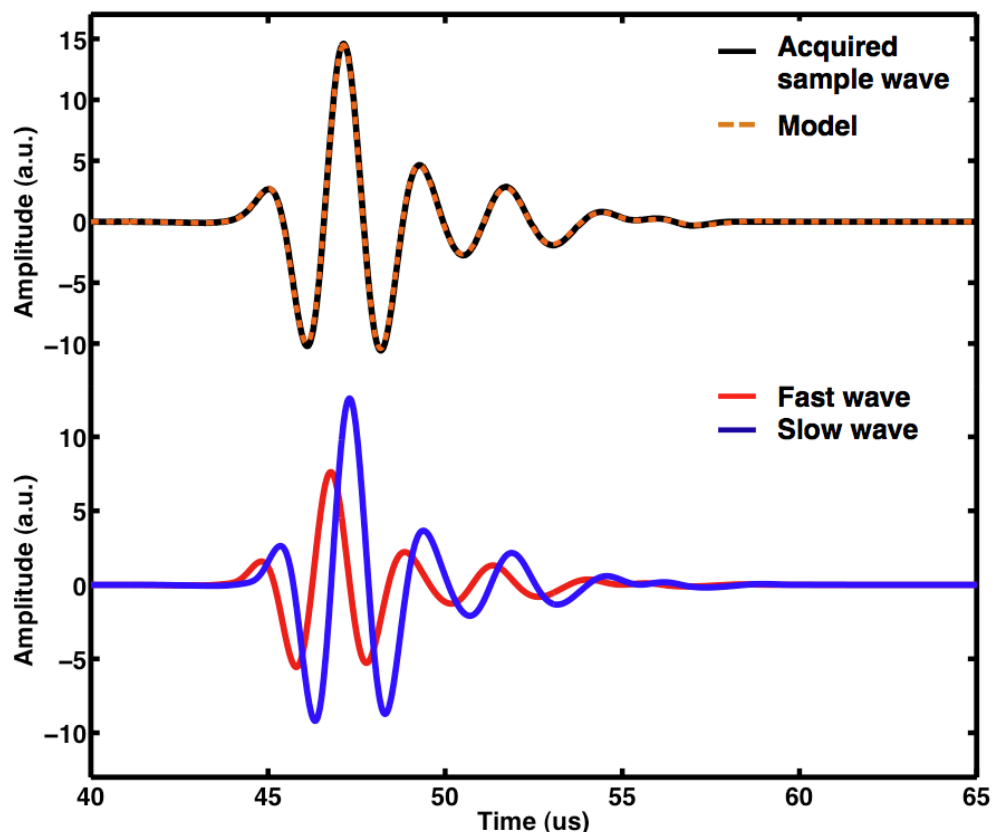


FIGURE 4.4: Top panel: The acquired sample radiofrequency data (solid black line) along with the model generated with the parameters estimated by the Bayesian algorithm (dashed orange line). Bottom panel: The individual fast wave (red line) and slow wave (blue line) that comprise the model waveform shown in the top panel.

estimated interface losses for the samples in this study were less than 0.5 dB, which agrees with the values found in the literature (McKelvie and Palmer, 1991; Strelitzki and Evans, 1998). The normalized slope of attenuation or broadband ultrasound attenuation (nBUA) was determined by performing a linear fit of the attenuation coefficient over the bandwidth from 350 to 630 kHz (the -6 dB bandwidth).

## 4.4 Results

For all the sites interrogated, the Bayesian two-mode algorithm converged on a set of parameters that produced a model wave that was similar to the acquired signal traveling through the specimen. Radiofrequency (rf) data acquired from one representative site is shown in the top panel of Figure 4.4. The model constructed from the parameters estimated using the Bayesian probability technique is overlaid for comparison. To quantify the quality of agreement between the model and the data, the coefficient of variation (CV) of the root-mean-square-deviation (RMSD) was calculated for each spatial site and was defined as

$$CV(RMSD) = \frac{RMSD}{\overline{x_{data}}} = \frac{\sqrt{\frac{\sum_{i=1}^{i=n} (x_{data,i} - x_{model,i})^2}{n}}}{\overline{x_{data}}} \quad (4.5)$$

where  $\overline{x_{data}}$  is the mean of the observed data and  $n$  is the number of data points. The  $CV(RMSD)$  was calculated for the data over a 22  $\mu$ s window. For the eight samples, the  $CV(RMSD)$  ranged from 5.1% to 14.2% with an average value of 8.9%. These values indicate satisfactory agreement between the data and models. The separated fast wave and slow wave modes that make up the model waveform are displayed in the bottom panel of Figure 4.4. As seen in this figure, the fast and slow waves overlapped substantially, with an approximate 90 degree phase shift between the two waves. A similar trend was seen in the signals from the other bone specimens.

### 4.4.1 Phase velocity

Phase velocity analysis applied to the unseparated sample wave revealed that 40 out of 72 total sites displayed negative dispersion as shown in Figure 4.5. In each of the eight samples,

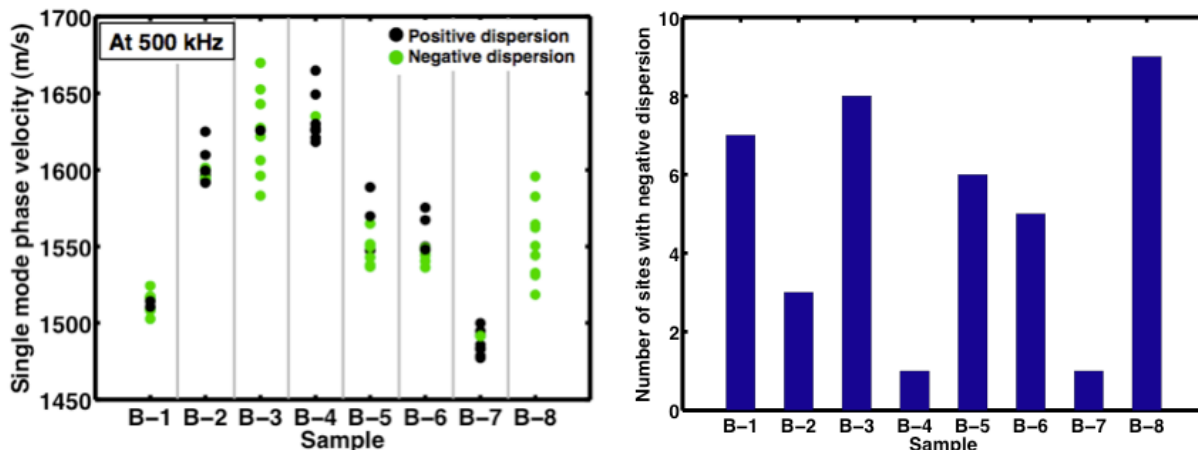


FIGURE 4.5: Left: The phase velocity and dispersion of the 72 sites investigated (9 sites per sample). The black circles represent sites with positive dispersion and the green circles represent sites displaying negative dispersion. Right: The number (out of 9 possible) sites in each sample that displayed negative dispersion using single mode analysis.

at least one of the nine sites interrogated displayed negative dispersion. This appearance of negative dispersion, which is in conflict with the causality-imposed Kramers-Kronig relations, may indicate that there are two waves present in the received sample signal, as reported in previous studies from our laboratory (Anderson *et al.*, 2010). The average magnitude of dispersion ranged from  $-77$  m/s/MHz to  $+29$  m/s/MHz. There was no apparent correlation between the bone volume fraction of the sample and the sample's average magnitude of dispersion. The mean phase velocity at 500 kHz over all eight samples was  $1565 \pm 52$  m/s (mean  $\pm$  SD) for the unseparated sample waves.

Phase velocity analysis of the separated fast and slow waves showed that these waves exhibited positive dispersion, as required by the model. Figure 4.6 shows an example of the frequency dependence of the phase velocity obtained from two-mode analysis. The fast and slow wave phase velocity results for all 72 sites are shown in Figure 4.7. The mean phase

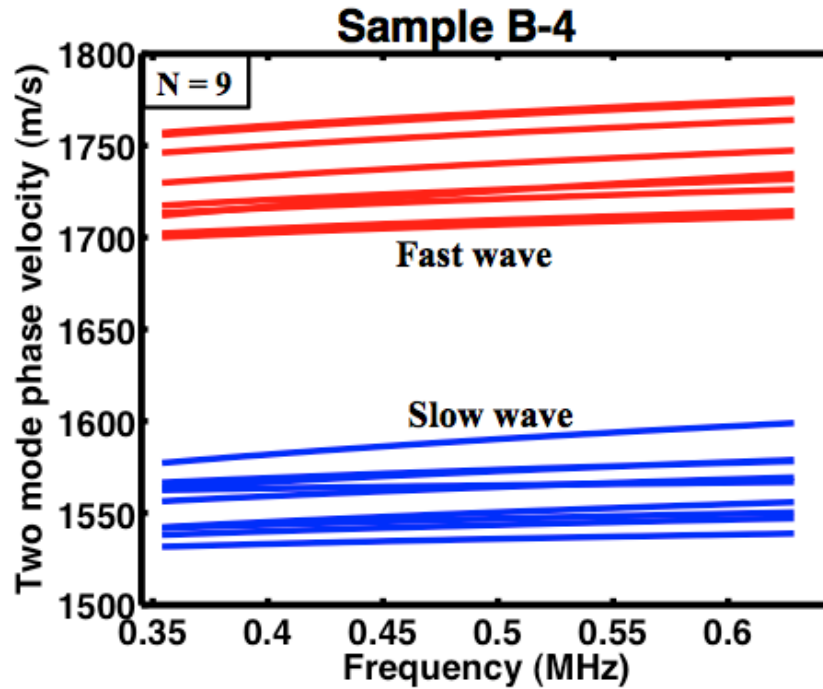


FIGURE 4.6: The fast and slow wave phase velocities ( $N=9$  sites) as a function of frequency for bone sample B-4. The red lines represent the fast wave and the blue lines represent the slow wave. Both fast and slow wave phase velocities display positive dispersion as required by the model.

velocities at 500 kHz over all eight samples were  $1645 \pm 68$  m/s and  $1523 \pm 40$  m/s for the fast and slow waves, respectively. Figure 4.8 shows the phase velocity at 500 kHz averaged over nine sites for the sample wave, the individual fast wave, and the individual slow wave for all eight specimens. The phase velocity obtained from the one-mode analysis of the sample wave always lay between the fast and slow wave phase velocities estimated by the two-mode Bayesian algorithm.



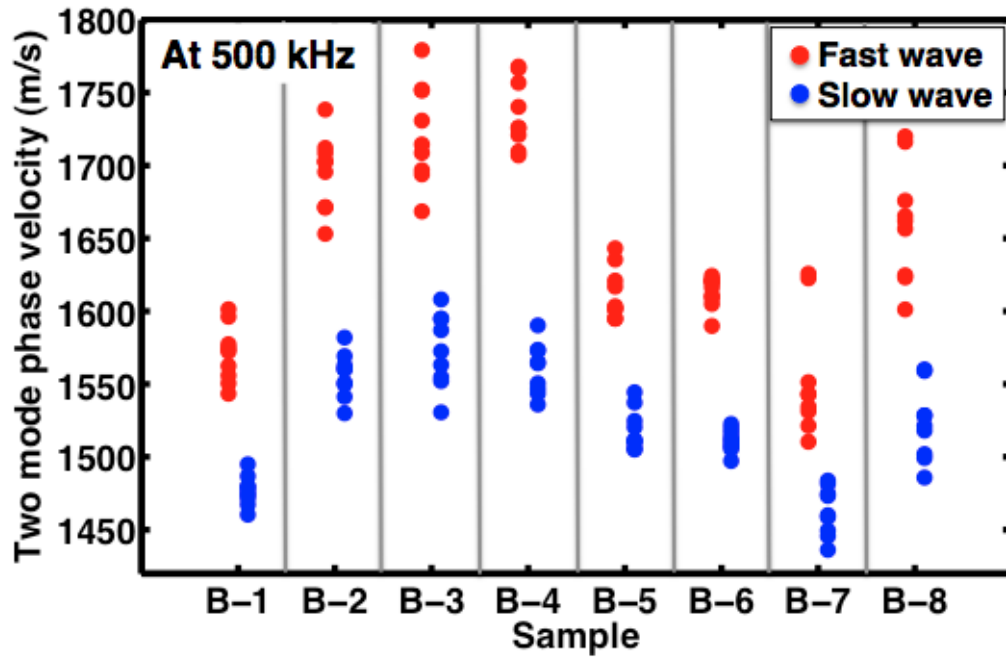


FIGURE 4.7: The fast and slow wave phase velocities for all sites (N=72). The red circles represent the fast wave and the blue circles represent the slow wave.

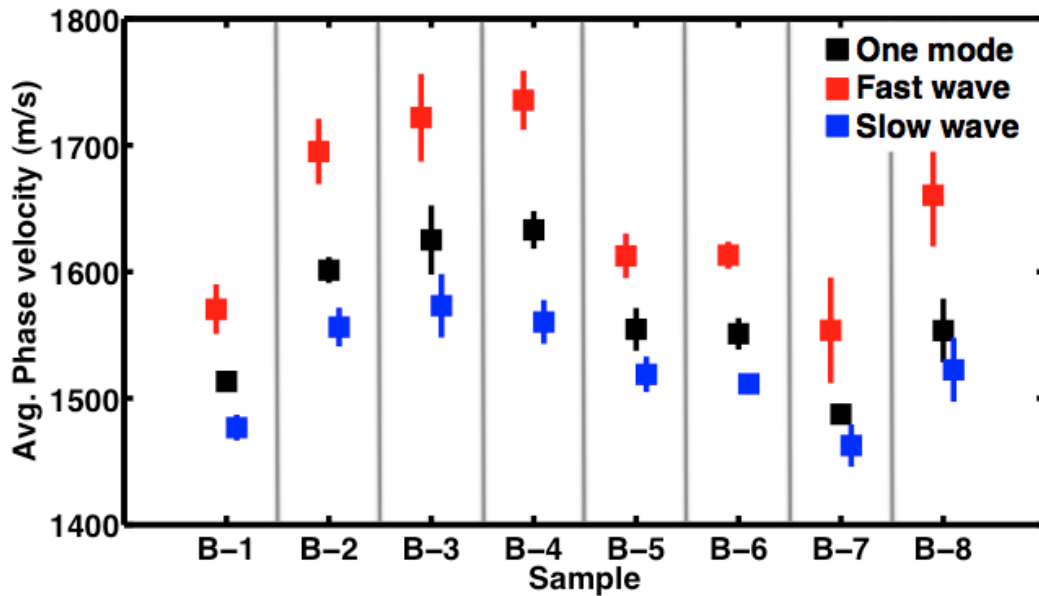


FIGURE 4.8: The average ( $\pm$  SD) phase velocity at 500 kHz over nine central sites of the fast wave (red squares), slow wave (blue squares), and the unseparated sample wave (black squares).

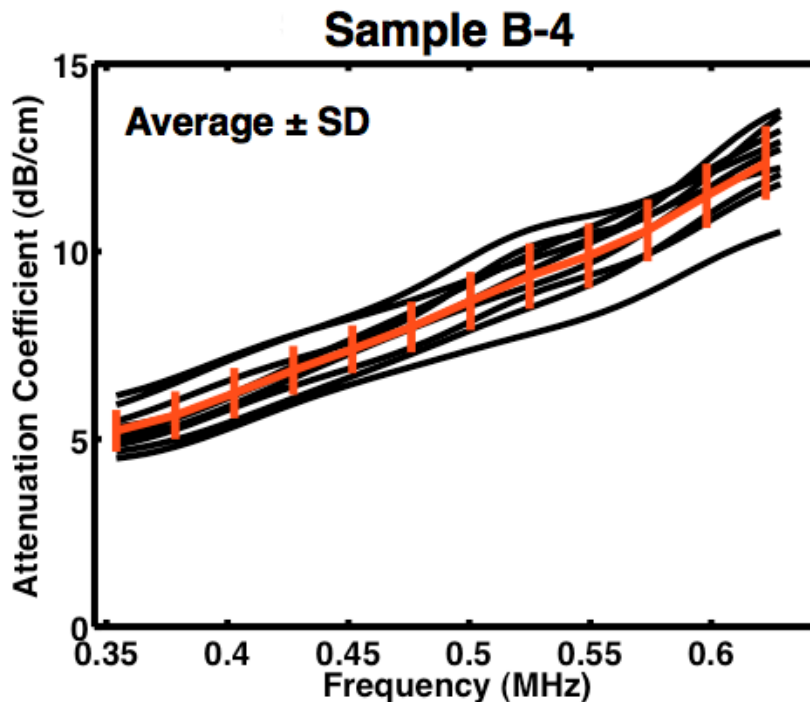


FIGURE 4.9: The one mode attenuation coefficient as a function of frequency for bone sample B-4. The black lines are the attenuation coefficients at each spatial site and the orange line is the average  $\pm$  one SD. For all 9 sites, the attenuation coefficients were approximately linear with frequency.

#### 4.4.2 Broadband ultrasound attenuation (nBUA)

At all 72 sites interrogated, the attenuation coefficient of the unseparated sample wave increased approximately linearly over the bandwidth. Figure 4.9 shows the attenuation coefficients at each of the nine sites interrogated from sample B-4, as well as the average attenuation coefficient. The average attenuation coefficients as a function of frequency obtained from the one mode analysis are displayed in Figure 4.10 for all eight samples. The slope of the attenuation coefficient, also known as the normalized broadband ultrasound attenuation (nBUA), was determined by a least squares fit over the usable bandwidth. The mean nBUA over all eight samples for the unseparated sample waves was  $19.3 \pm 8.2$  dB/cm/MHz.

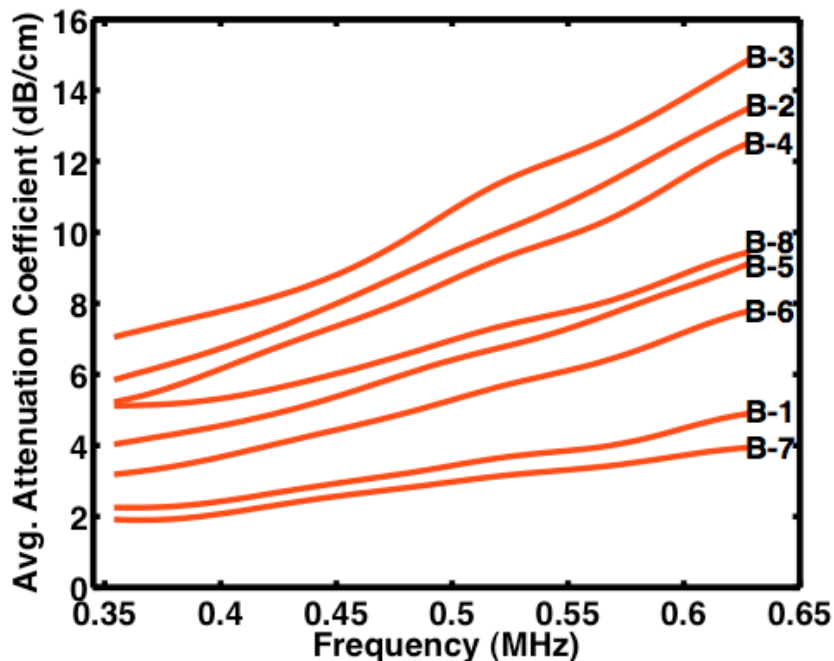


FIGURE 4.10: The average ( $N=9$ ) attenuation coefficients obtained from one mode analysis for each of the eight bone samples.

The attenuation coefficient curves for both the fast and slow waves were also linear with frequency. As illustrated in Figure 4.11, the attenuation coefficients of the fast and slow waves had similar values. This was not necessarily expected because the fast wave attenuation is often larger than the slow wave attenuation. However, the samples investigated in this study had high porosities and therefore relatively less hard tissue to attenuate the signal. The propagation direction (along the predominant trabecular axis) might also be playing a role in why the attenuation coefficients of the fast and slow waves have comparable values.

The fast and slow wave normalized broadband ultrasound attenuations (nBUA) for all 72 sites are shown in Figure 4.12. This figure illustrates the substantial heterogeneity of the bone samples; there is a large variation in nBUA values from site to site within a single sample. The mean nBUA over all eight samples for the fast and slow waves were  $5.6 \pm 4.0$

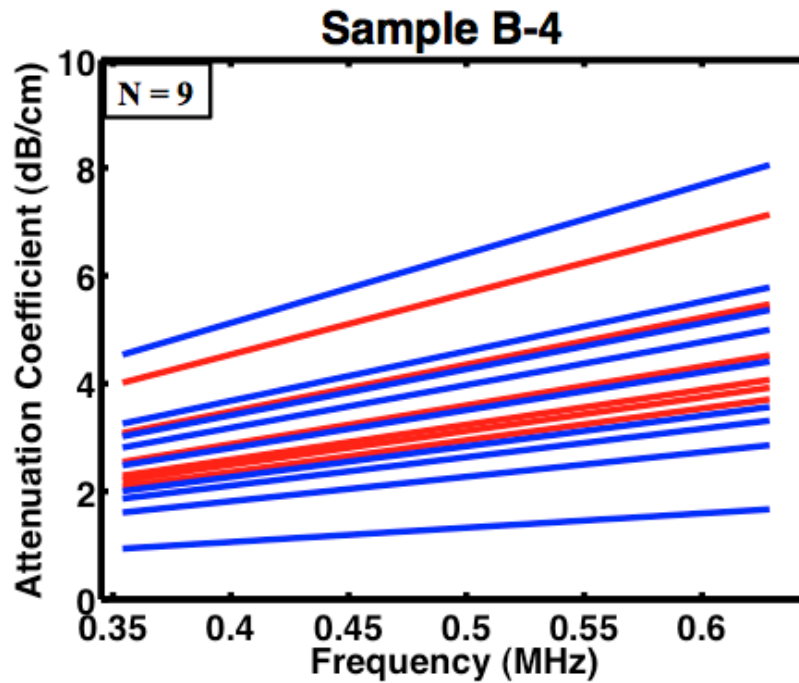


FIGURE 4.11: The fast and slow wave attenuation coefficients ( $N=9$  sites) as functions of frequency for bone sample B-4. The red lines represent the fast wave and the blue lines represent the slow wave. Both fast and slow wave attenuation coefficients were linear with frequency and displayed similar values.

dB/cm/MHz and  $4.1 \pm 3.0$  dB/cm/MHz, respectively. For some samples, specifically samples B-1 and B-8, the slopes of attenuation for the fast and slow waves were approximately zero. A possible explanation for these very small nBUA values is that both of these samples have high porosities (91% and 88% respectively) thus the losses in the sample are small. An alternative explanation is that there is truly only one wave present. Figure 4.13 compares the average normalized slope of attenuation for the fast and slow waves to the average slope of attenuation for the unseparated sample wave. The nBUA obtained from the one-mode analysis of the sample wave was consistently larger than the nBUAs from either the fast waves or slow waves.

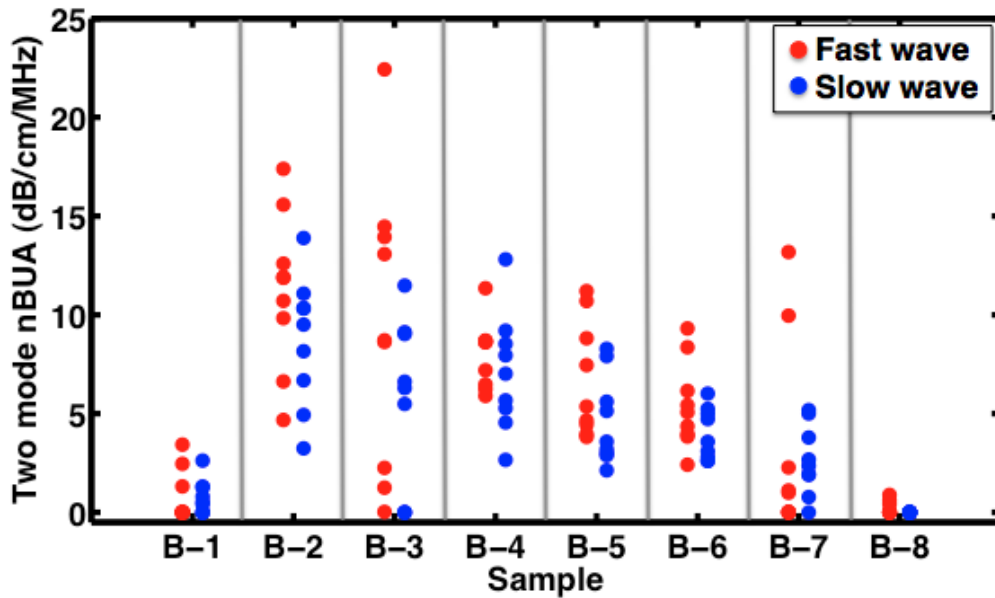


FIGURE 4.12: The nBUA values for the fast and slow waves at all 72 sites. The red circles represent the fast wave and the blue circles represent the slow wave.

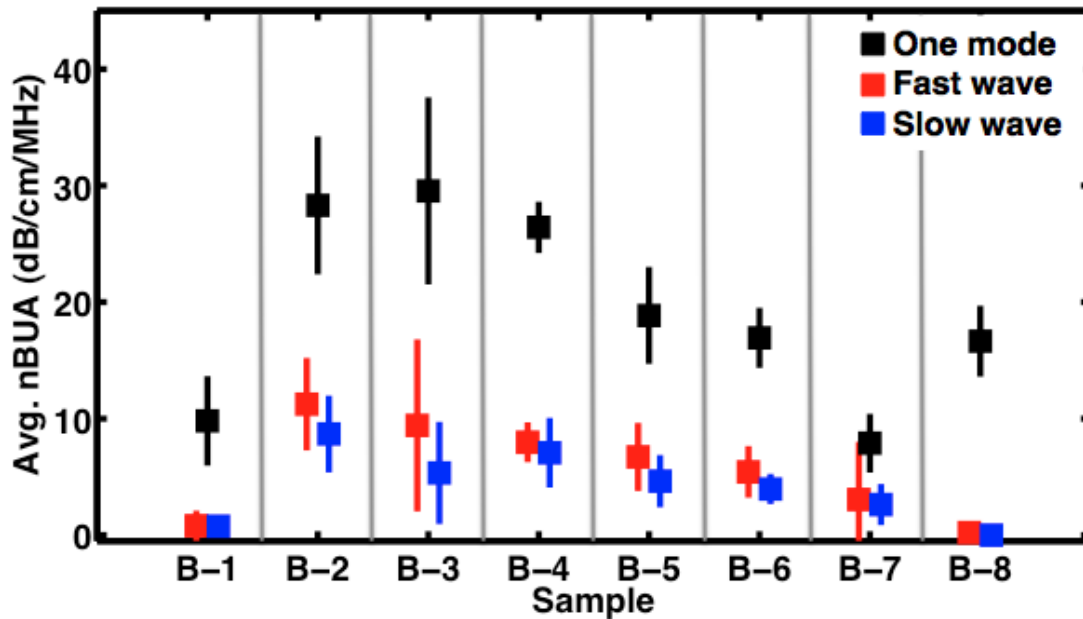


FIGURE 4.13: The average normalized slope of attenuation over nine central sites of the fast wave (red squares), slow wave (blue squares), and the unseparated sample wave (black squares).

TABLE 4.4: Pearson’s correlation coefficients between the Bayesian parameters and the bone sample’s structural parameters. Porosity is defined as  $(1-BV/TV)$ . Negative values imply an inverse relationship.

Bayesian Parameter	Porosity	Tb.Sp	Tb.N	Conn. D	SMI
$c_{fast}$	-0.85	-0.70	0.70	0.52	-0.87
$c_{slow}$	-0.93	-0.80	0.79	0.61	-0.90
$\beta_{fast}$	-0.80	-0.93	0.93	0.73	-0.64
$\beta_{slow}$	-0.72	-0.86	0.85	0.61	-0.61
$A_{fast}$	-0.54	-0.71	0.66	0.57	-0.40
$A_{slow}$	0.66	0.41	-0.39	-0.36	0.70

### 4.4.3 Correlation with structural parameters

The mean  $\pm$  SD porosity of the eight samples was  $0.85 \pm 0.05$ . Table 4.4 shows the Pearson’s correlation coefficients between the estimated Bayesian parameters and the microarchitectural parameters determined by microCT. Figure 4.14 shows the correlation plots of the six Bayesian parameters with the porosity determined by microCT. The structural model index (SMI) values, which can range from 0 for parallel plate architecture to 3 for cylindrical rod architecture, had a mean of 1.43, suggesting that the bone samples had almost equal amounts of plate-like and rod-like structures. The best predictor of the fast and slow wave speeds was porosity or  $(1-BV/TV)$ . The best predictors of the slopes of attenuation(nBUA) for the fast and slow waves were trabecular spacing (Tb.Sp) and trabecular number (Tb.N). Trabecular spacing and trabecular number were highly correlated with  $R^2 = 0.99$ , thus the Pearson’s correlation coefficients for these two parameters with the Bayesian

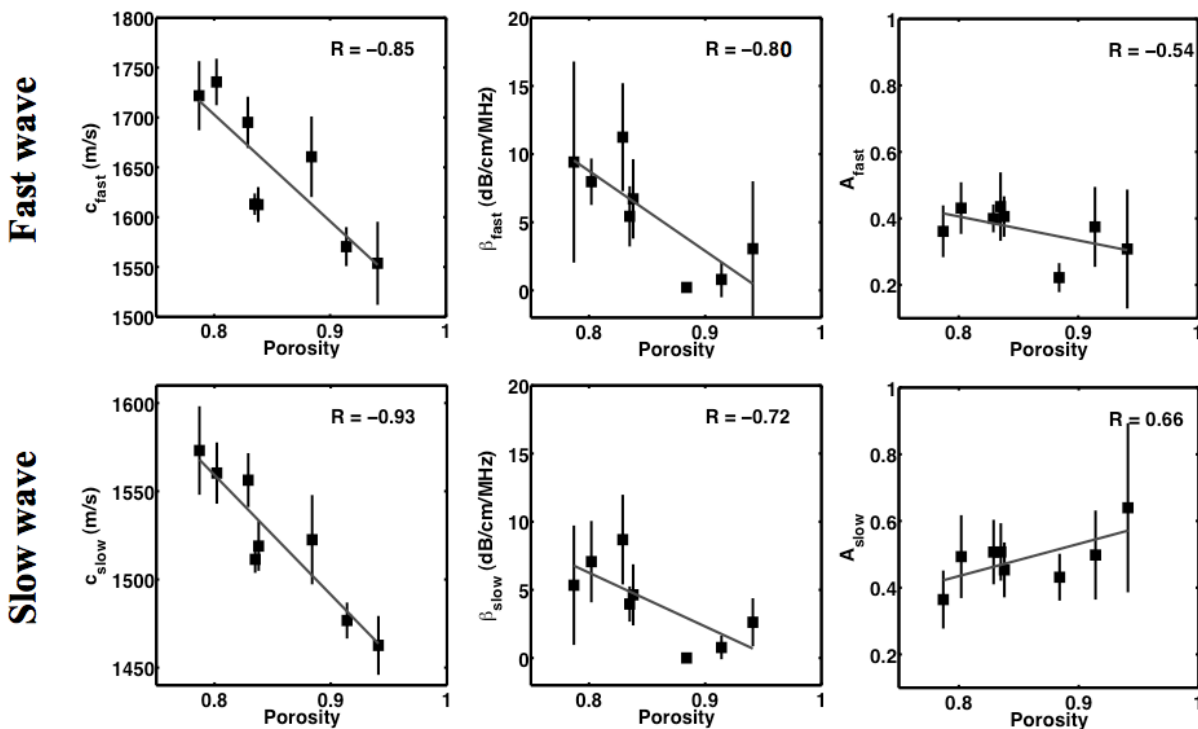


FIGURE 4.14: The Bayesian-derived parameters plotted against sample porosity. The top plots show the three fast wave parameters and the bottom plots show the three slow wave parameters. Porosity was determined by microCT. Each value shown is the mean of nine independent sites plus or minus one standard deviation.

parameters would be expected to be almost identical. The best predictor for the ratio of  $A_{fast}$  to  $A_{slow}$ , which may provide a good measure of how the incident energy is divided between the two modes, was trabecular spacing (Tb.Sp).

## 4.5 Discussion

Regarding the comparison of one mode versus two mode analyses, the results of this study showed two significant features: a phase velocity for the single mode that lay between the fast and slow wave velocities and a broadband ultrasound attenuation for the single

mode that was much greater than the broadband ultrasound attenuation values associated with either the fast or slow waves. This suggests that the phase velocity from the one mode analysis is a mixture of the fast and slow wave velocities. To explore this hypothesis, the one mode phase velocity was taken to be a weighted sum of the fast and slow wave phase velocities,

$$c_{samp} = A * c_{fast} + B * c_{slow}. \quad (4.6)$$

The coefficients,  $A$  and  $B$ , in Equation 4.6 were determined by a linear best fit to a plot of  $c_{samp}/c_{fast}$  vs.  $c_{slow}/c_{fast}$ . From this linear fit, it was determined that  $A = 0.25$  and  $B = 0.75$ . Thus, on average, the phase velocity of the unseparated signal contains approximately 75% of the slow wave velocity and 25% of the fast wave velocity. Figure 4.15 shows the predicted one mode phase velocity using Equation 4.6 and the one mode phase velocity determined by phase spectroscopy.

The overestimation of the nBUA value for the single mode appeared to be due to the significant interference of the fast and slow waves in the time-domain. The interference between these two wave modes was unintentionally being perceived as true signal loss occurring within the bulk of the sample. Additionally, the conventional one mode analysis did not take into account insertion losses (the losses at the boundaries of the sample). Therefore, all of the loss must be accounted for in the slope of attenuation (nBUA) term. In contrast, the Bayesian parameters,  $A_{fast}$  and  $A_{slow}$ , included the losses at the boundaries as well as how the initial wave energy was divided between the two waves propagating in the sample. However, as stated earlier in Section 4.3.5, the insertion losses estimated for the specimens studied in this chapter were negligible in comparison to the losses occurring within the samples.



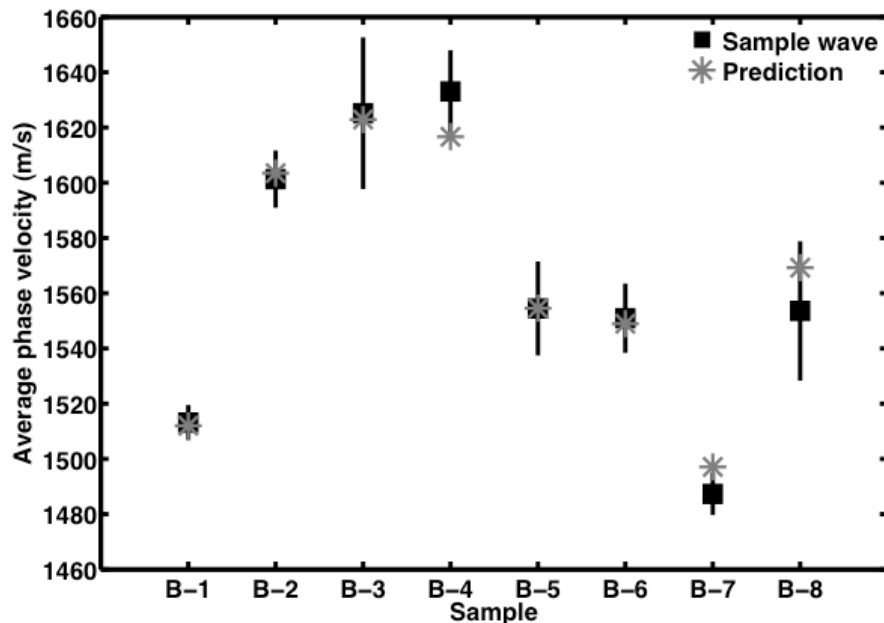


FIGURE 4.15: The average phase velocity using one mode (phase-spectroscopy) analysis (black squares) and the predicted one mode phase velocity (gray asterisks) using the weighted sum of fast and slow wave velocities found in Eq. 4.6.

The dependences of the Bayesian ultrasonic parameters ( $c_{fast}$ ,  $c_{slow}$ ,  $\beta_{fast}$ ,  $\beta_{slow}$ ,  $A_{fast}/A_{slow}$ ) on the microarchitectural parameters were consistent with those previously reported (Chaffai *et al.*, 2002; Nicholson *et al.*, 2001; Wear *et al.*, 2012). The correlation coefficients between  $\beta_{fast}$  and porosity ( $r = -0.80$ ) and  $\beta_{slow}$  and porosity ( $r = -0.72$ ) were slightly lower than those reported for single-mode nBUA versus BV/TV by Nicholson *et al.* (2001), 0.86, Chaffai *et al.* (2002), 0.88, and Wear *et al.* (2012), 0.85. However, the correlation coefficients for  $c_{fast}$  and porosity ( $r = -0.85$ ) and  $c_{slow}$  and porosity ( $r = -0.93$ ) were similar to those reported for single-mode phase velocity versus BV/TV by Nicholson *et al.* (2001), 0.86, Chaffai *et al.* (2002), 0.90, and Wear *et al.* (2012), 0.81. Differences in the correlation coefficients between the present study and previous studies may arise as a result of the fact that these previous studies were using the phase velocity and the slope of attenuation (nBUA) from an assumed

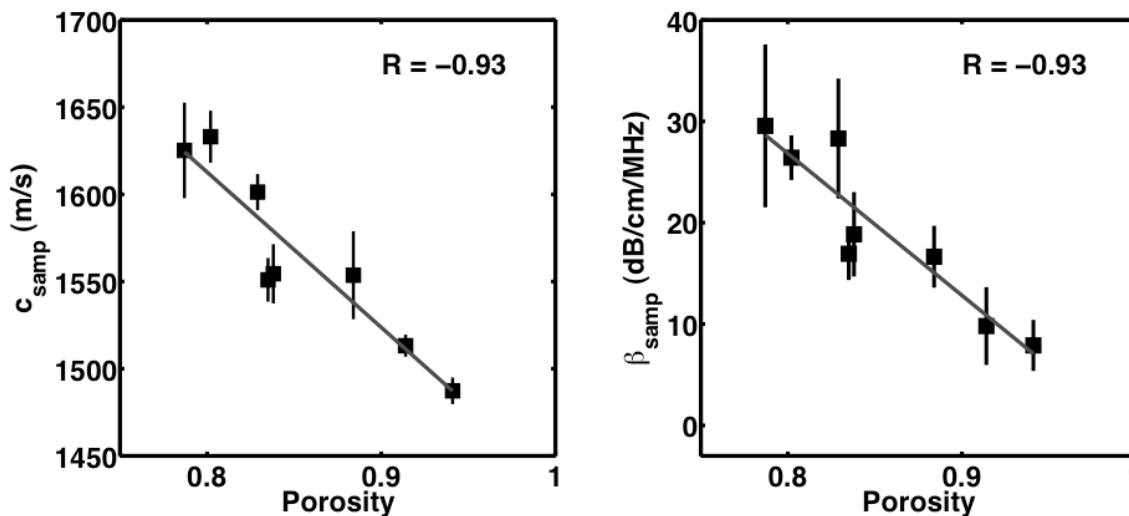


FIGURE 4.16: The phase velocities and normalized slopes of attenuation (nBUA) obtained from one mode analysis plotted versus porosity. Porosity was determined by microCT. Each point is the mean plus or minus one standard deviation of nine spatial sites.

single wave, whereas in the current study the analysis was performed assuming two waves are present. In order to investigate if the two-mode Bayesian parameters provided improved correlations to clinically meaningful structural parameters, the results of the one mode analysis were plotted as functions of porosity as shown in Figure 4.16. The phase velocity and nBUA results obtained from one mode analysis both correlated well with porosity ( $R = 0.93$ ) and actually correlated better than any one of the Bayesian parameters. Although this was unexpected, it may not be entirely surprising. With the assumptions that only a single wave is present, the resulting values for the speed and the nBUA are presumably some combination of the individual fast and slow wave speeds and nBUAs, respectively. This may imply that the one mode results contain more information than any one Bayesian parameter. However, it may be possible to combine the Bayesian parameters in such a way to improve the correlations with the structural parameters, such as porosity.

To justify the assumption of a two-mode model, a comparison was carried out to determine if the two-mode model fit the experimental data better than the one-mode model. For this portion of the study, a Bayesian one-mode model was applied to the data using three parameters ( $A_{one}$ ,  $\beta_{one}$ ,  $c_{one}$ ) instead of the six parameters ( $c_{fast}$ ,  $c_{slow}$ ,  $\beta_{fast}$ ,  $\beta_{slow}$ ,  $A_{fast}$ ,  $A_{slow}$ ) in the two-mode model. For all 72 sites investigated, the two-mode model produced a smaller coefficient of variation (CV) of the root-mean-square-deviation (RMSD) than the one-mode Bayesian model. This result might be expected because the number of adjustable parameters was changed from 6 to 3.

The results from the one-mode Bayesian analysis were compared to the results obtained from conventional (one-mode) analysis. The phase velocity,  $c_{one}$ , obtained from the one-mode Bayesian algorithm agreed well with the velocities obtained from the conventional one-mode analysis ( $R^2 = 1.0$ ), with an average percent difference of  $0.18 \pm 0.11$  m/s. The nBUA values,  $\beta_{one}$ , obtained from the one-mode Bayesian technique also correlated well ( $R^2 = 0.93$ ) with the nBUA values determined from the conventional one-mode analysis, however the actual values differed. The nBUA values obtained from the one-mode Bayesian technique were consistently smaller than those obtained from conventional one-mode analysis. The mean difference in  $\beta$  between the two methods,  $\Delta\beta$ , was  $7.3 \pm 3.1$  dB/cm/MHz for all 72 sites. Figure 4.17 shows the average differences in  $\beta$  between the conventional one-mode analysis and the Bayesian one-mode analysis. As shown in the right panel of Figure 4.17, the differences between the nBUA values obtained with the two methods of one-mode analysis (Bayesian and conventional) were quite large for lower bone porosities and then decreased as porosity increased. This trend with porosity held true even when  $A_{one}$  was set to equal one

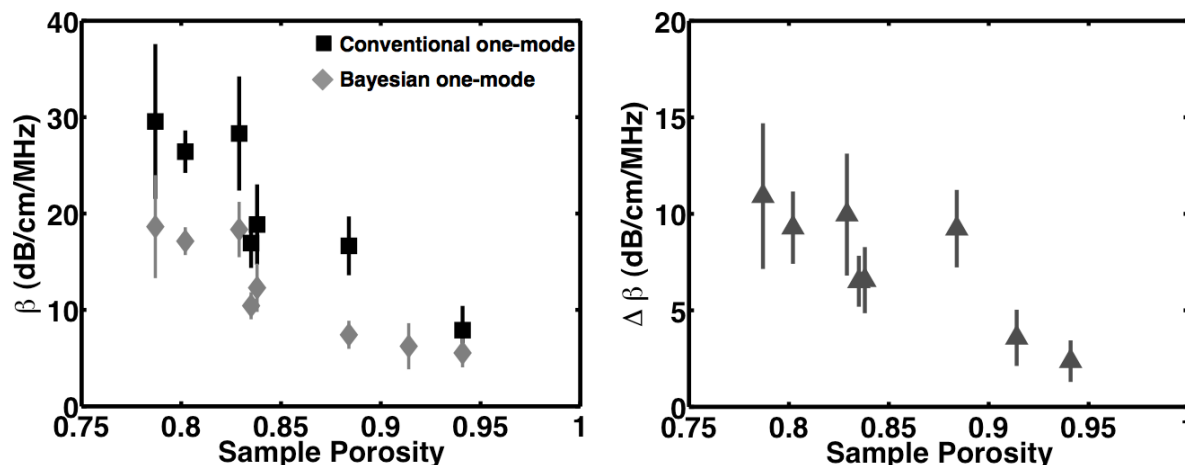


FIGURE 4.17: Left: The average ( $N = 9$ )  $\pm$  one standard deviation nBUA values obtained from the one-mode conventional analysis (black squares) and from the one-mode Bayesian analysis (gray diamonds) as a function of sample porosity. Right: The mean difference in  $\beta$ ,  $\Delta\beta$ , between conventional one-mode analysis and Bayesian one-mode analysis (shown in the left panel) plotted versus sample porosity.

in the Bayesian one-mode model, which was more consistent with conventional one-mode analysis where the insertion losses were considered negligible. The discrepancy between conventional and Bayesian nBUA values also occur in other studies presented later in this thesis (Chapters 6 and 7).

To investigate the reproducibility of the two-mode Bayesian algorithm, all 72 sites were run through the algorithm five times using the same priors as shown in Table 4.3. In order to quantify the reproducibility, the relative standard deviation (RSD) given by

$$RSD(\%) = \frac{\theta}{\bar{x}} \times 100 \quad (4.7)$$

was calculated for each spatial site. Table 4.5 gives the mean RSD ( $N = 9$ ) of each Bayesian parameter for all eight samples. For four out of the six Bayesian parameters ( $A_{fast}$ ,  $A_{slow}$ ,  $c_{fast}$ , and  $c_{slow}$ ), the RSD was less than 2.5% for all the samples, which suggests that the Bayesian algorithm is robust and reproducible. However, for some of the samples,  $\beta_{fast}$  and

TABLE 4.5: The mean (over 9 sites) relative standard deviation (RSD)  $\pm$  SD of the six Bayesian parameters for the eight calcaneal samples studied. The RSD was calculated after running all 72 sites through the Bayesian algorithm five times.

Sample	Mean relative standard deviation (RSD) %					
	$\mathbf{c}_{fast}$	$\mathbf{c}_{slow}$	$\mathbf{\beta}_{fast}$	$\mathbf{\beta}_{slow}$	$\mathbf{A}_{fast}$	$\mathbf{A}_{slow}$
<b>B-1</b>	0.02 $\pm$ 0.03	0.01 $\pm$ 0.01	29.7 $\pm$ 27.5	59.3 $\pm$ 50.3	0.61 $\pm$ 0.88	0.52 $\pm$ 0.79
<b>B-2</b>	0.01 $\pm$ 0.00	0.00 $\pm$ 0.00	0.43 $\pm$ 0.37	0.23 $\pm$ 0.21	0.27 $\pm$ 0.11	0.22 $\pm$ 0.13
<b>B-3</b>	0.01 $\pm$ 0.01	0.00 $\pm$ 0.00	3.28 $\pm$ 5.73	31.2 $\pm$ 48.4	0.33 $\pm$ 0.15	0.25 $\pm$ 0.11
<b>B-4</b>	0.08 $\pm$ 0.09	0.04 $\pm$ 0.04	3.05 $\pm$ 3.85	2.23 $\pm$ 3.29	1.62 $\pm$ 1.81	1.65 $\pm$ 1.94
<b>B-5</b>	0.03 $\pm$ 0.02	0.01 $\pm$ 0.01	1.67 $\pm$ 1.56	1.20 $\pm$ 1.32	1.07 $\pm$ 0.92	1.00 $\pm$ 0.86
<b>B-6</b>	0.07 $\pm$ 0.07	0.03 $\pm$ 0.03	3.28 $\pm$ 2.38	1.85 $\pm$ 1.65	2.14 $\pm$ 2.15	2.03 $\pm$ 2.74
<b>B-7</b>	0.06 $\pm$ 0.05	0.04 $\pm$ 0.06	27.1 $\pm$ 28.1	9.38 $\pm$ 17.5	2.43 $\pm$ 2.47	2.09 $\pm$ 2.59
<b>B-8</b>	0.01 $\pm$ 0.00	0.00 $\pm$ 0.00	59.9 $\pm$ 46.5	90.4 $\pm$ 29.2	0.19 $\pm$ 0.11	0.09 $\pm$ 0.03

$\beta_{slow}$  had RSD values greater than 20%. This high degree of variation was associated with values of  $\beta$  very close to zero.

## 4.6 Conclusions

The results of this study show that fast and slow waves identified by the Bayesian method have properties that correlate with microstructural parameters, such as porosity. Results also show that the Bayesian technique can separate the fast and slow waves even in cases of significant temporal overlap. In light of potential artifacts caused by interfering fast and slow waves, analyses performed on segregated fast and slow waves might represent a useful step toward deriving additional diagnostically useful information from bone sonometry.

## **4.7 Acknowledgments**

Thanks to Tarpit Patel for his help in taking the microCT measurements and to Dan Loesche for his help in acquiring the bone tissue specimens. This study was supported, in part, by NIH Grant R01-AR057433 and NIAMS grant P30AR057235.

## Bibliography

- Anderson, C. C., Bauer, A. Q., Holland, M. R., Pakula, M., Laugier, P., Bretthorst, G. L., and Miller, J. G. (2010), “Inverse problems in cancellous bone: Estimation of the ultrasonic properties of fast and slow waves using Bayesian probability theory”, *J Acoust Soc Am* **128**(5), 2940–2948.
- Anderson, C. C., Marutyan, K. R., Holland, M. R., Wear, K. A., and Miller, J. G. (2008), “Interference between wave modes may contribute to the apparent negative dispersion observed in cancellous bone”, *J Acoust Soc Am* **124**(3), 1781–1789.
- Bauer, A. Q., Marutyan, K. R., Holland, M. R., and Miller, J. G. (2008), “Negative dispersion in bone: The role of interference in measurements of the apparent phase velocity of two temporally overlapping signals”, *J Acoust Soc Am* **123**(4), 2407–2414.
- Chaffai, S., Peyrin, F., Nuzzo, S., Porcher, R., Berger, G., and Laugier, P. (2002), “Ultrasonic characterization of human cancellous bone using transmission and backscatter measurements: relationships to density and microstructure”, *Bone* **30**, 229–237.
- Ding, M., Dalstra, M., Danielson, C., Kabel, J., Hvid, I., and Linde, F. (1997), “Age variations in the properties of human tibial trabecular bone”, *J Bone Joint Surg Br* **79**, 995–1002.
- Hoffman, J., Nelson, A., Holland, M., and Miller, J. (2012), “Cancellous bone fast and slow waves obtained with Bayesian probability theory correlate with porosity from computed tomography”, *J Acoust Soc Am* **132**(3), 1830–1837.
- Hosokawa, A. and Otani, T. (1997), “Ultrasonic wave propagation in bovine cancellous bone”, *J Acoust Soc Am* **101**(1), 558–562.
- Hosokawa, A. and Otani, T. (1998), “Acoustic anisotropy in bovine cancellous bone”, *J Acoust Soc Am* **103**(5), 2718–2722.
- Marutyan, K. R., Bretthorst, G. L., and Miller, J. G. (2007), “Bayesian estimation of the underlying bone properties from mixed fast and slow mode ultrasonic signals”, *J Acoust Soc Am* **121**(1), EL8–EL15.
- Marutyan, K. R., Holland, M. R., and Miller, J. G. (2006), “Anomalous negative dispersion in bone can result from the interference of fast and slow waves”, *J Acoust Soc Am* **120**(5), EL55–EL61.
- McKelvie, M. and Palmer, S. (1991), “The interaction of ultrasound with cancellous bone”, *Phys Med Biol* **36**, 1331–1340.
- Nelson, A., Hoffman, J., Anderson, C., Holland, M., Nagatani, Y., Mizuno, K., Matsukawa, M., and Miller, J. (2011), “Determining attenuation properties of interfering fast and slow ultrasonic waves in cancellous bone”, *J Acoust Soc Am* **130**, 2233–2240.

- Nicholson, P., Muller, R., Cheng, S., Ruegsegger, P., Van Der, P., Dequeker, J., and Boonen, S. (2001), “Quantitative ultrasound and trabecular architecture in the human calcaneus”, *J Bone Miner Res* **16**, 1886–1892.
- Strelitzki, R. and Evans, J. (1998), “Diffraction and interface losses in broadband ultrasound attenuation measurements of the calcaneum”, *Physiol Meas.* **19**, 197–204.
- Trousil, R. (2002), “Ultrasonic propagation in inhomogeneous media: Toward quantitative ultrasonic imaging”, Ph.D. thesis, Washington University in St. Louis.
- Wear, K., Nagaraja, S., Dreher, M., and Gibson, S. (2012), “Relationships of quantitative ultrasound parameters with cancellous bone microstructure in human calcaneus in vitro”, *J Acoust Soc Am* **131**, 1605–1612.



# CHAPTER 5

---

## SIMULATION OF THE EFFECTS OF OVERLAPPING FAST AND SLOW WAVES ON THE APPARENT ATTENUATION OF CANCELLOUS BONE

### 5.1 Preface

This chapter is based on the peer-reviewed journal article "Determining attenuation properties of interfering fast and slow ultrasonic waves in cancellous bone" by Amber M. (Nelson) Groopman, Joseph J. Hoffman, Christian C. Anderson, Mark R. Holland, Yoshiki Nagatani, Katsunori Mizuno, Mami Matsukawa, and James G. Miller and published in *The Journal of the Acoustical Society of America*, Vol. 130, No. 4, pp. 2233-40.

## 5.2 Abstract

Previous studies have shown that interference between fast waves and slow waves can lead to observed negative dispersion in cancellous bone. In this study, the effects of overlapping fast and slow waves on measurements of the apparent attenuation as a function of propagation distance are investigated along with methods of analysis used to determine the attenuation properties. Two methods are applied to simulated data that were generated based on experimentally acquired signals taken from a bovine specimen. The first method uses a time-domain approach that was dictated by constraints imposed by the partial overlap of fast and slow waves. The second method uses a frequency-domain log-spectral subtraction technique on the separated fast and slow waves. Applying the time-domain analysis to the broadband data yields apparent attenuation behavior that appears to be larger in the early stages of propagation and decreases as the wave travels deeper. In contrast, performing frequency-domain analysis on the separated fast waves and slow waves results in attenuation coefficients that are independent of propagation distance. Results suggest that features arising from the analysis of overlapping two-mode data may represent an alternate explanation for the previously reported apparent dependence on propagation distance of the attenuation coefficient of cancellous bone.

## 5.3 Introduction

Although dual-energy X-ray absorptiometry (DXA) is the current gold standard for diagnosing osteoporosis, quantitative ultrasound represents an approach for evaluating the

quality of cancellous bone that has the potential for determining the likelihood of osteoporosis (Hans and Krieg, 2008; Laugier, 2008; Frost *et al.*, 2001). In Japan, ultrasonic screening for osteoporosis is recommended by the government and is included in the publicly funded annual health check. Cancellous bone is a porous material consisting of a matrix of solid trabeculae filled with soft bone marrow. The heterogenous structure of cancellous bone can result in the propagation of complicated ultrasonic waveforms that obfuscate measurements and make the interpretation of results difficult.

Cancellous bone is known to support the propagation of two compressional wave modes, often referred to as fast waves and slow waves (Hosokawa, 2010; Hosokawa and Otani, 1998, 1997; Mizuno *et al.*, 2009; Haiat *et al.*, 2008; Cardoso *et al.*, 2003; Padilla and Laugier, 2000). In some experimental situations, the two waves are separated in the time-domain data, whereas in other circumstances the two waves substantially overlap and may appear as only a single wave. The degree to which the fast waves and slow waves overlap depends on a number of factors including porosity, structural anisotropy, ultrasonic path length, and the angle of insonification relative to the predominant trabecular orientation (Hosokawa and Otani, 1998; Haiat *et al.*, 2008; Mizuno *et al.*, 2008; Lee and Choi, 2007).

When the fast waves and slow waves are clearly distinct and separated in time in the radiofrequency data, each mode can be analyzed individually to obtain intrinsic ultrasonic properties such as the attenuation coefficient and phase velocity. However, under circumstances in which there is overlap between the two wave modes, conventional analysis methods may suggest potentially misleading material properties. Previous studies have demonstrated that interfering fast wave and slow wave modes can account for the apparent negative dis-

---

persion sometimes observed in measurements of cancellous bone (Anderson *et al.*, 2011; Marutyan *et al.*, 2006b; Anderson *et al.*, 2008; Marutyan *et al.*, 2006a; Bauer *et al.*, 2008). This apparent negative dispersion arises when conventional phase spectroscopy analysis of two overlapping waves is performed as if only one wave were present. Sometimes the presence of an additional wave is not apparent in the RF signal.

One objective of the current study was to examine the effects of interfering fast and slow waves on the determination of the attenuation properties of cancellous bone. A second objective was to investigate the influence of the choice of methods employed to extract the attenuation properties.

## 5.4 Methods

In this study, two methods for determining the attenuation properties as a function of propagation distance were applied to the same simulated data to permit a comparison of the relative advantages and disadvantages of the two methods of analysis. The two methods of analysis include a previously reported time-domain technique (Nagatani *et al.*, 2008) and a frequency-domain technique performed on separated fast and slow waves. Details of these methods of analysis are presented later in this section.

### 5.4.1 Generating simulated ultrasonic waves

The experimental observations that provided the basis for the simulated data employed in this study were reported in a manuscript by Nagatani *et al.*(2008). In that study, through-

transmission measurements were conducted on a 20 x 20 x 15 mm sample from a bovine femoral head, which was immersed in degassed water. Planar PVDF transmitting and receiving transducers were separated by 60 mm. The transmitter was excited by a single cycle of a 1 MHz sinusoid. The direction of wave propagation was parallel to the predominant bone axis. To investigate whether the fast wave attenuation properties were influenced by the thickness of the sample and thus the propagation distance, in that earlier study the specimen was gradually shortened from 15 mm to 6 mm in steps of 1 mm by removing bone tissue from one end of the sample.

In the present work, signals presented in that previous study were employed in conjunction with a model that explicitly accounts for the presence of fast and slow wave modes (Anderson *et al.*, 2008, 2010). The ultrasonic propagation through bone was modeled as

$$Output(f) = Input(f)[H_{fast}(f) + H_{slow}(f)] \quad (5.1)$$

where  $Output(f)$  and  $Input(f)$  are the complex Fourier spectra of the received mixed mode waveform and the incident waveform, respectively, and  $H_{fast}(f)$  and  $H_{slow}(f)$  are the transfer functions for the fast and slow waves. In this study, the input wave was taken as the reference water-path only signal from the Nagatani *et al.* paper, which is shown in panel(a) of Figure 7 of that paper (Nagatani *et al.*, 2008). The transfer functions for the individual fast and

slow waves are given by

$$H_{fast}(f) = A_{fast} \exp(-\beta_{fast} f d) \exp\left(\frac{i 2\pi f d}{c_{fast}(f)}\right) \quad (5.2a)$$

$$H_{slow}(f) = A_{slow} \exp(-\beta_{slow} f d) \exp\left(\frac{i 2\pi f d}{c_{slow}(f)}\right) \quad (5.2b)$$

in which  $A_{fast}$  and  $A_{slow}$  are frequency-independent signal loss parameters,  $\beta_{fast}$  and  $\beta_{slow}$  are the slopes of attenuation for the fast and slow waves,  $d$  is the sample thickness, and  $c_{fast}(f)$  and  $c_{slow}(f)$  are the phase velocities for the fast and slow waves. The phase velocities of the fast and slow waves were required to satisfy the Kramers-Kronig relations for media exhibiting linear-with-frequency attenuation coefficients (Waters and Hoffmeister, 2005; Bauer *et al.*, 2007; O'Donnell *et al.*, 1978, 1981; Waters *et al.*, 2005, 2000), thus having the following form

$$c_{fast}(f) = c_{fast}(f_0) + [c_{fast}(f_0)]^2 \frac{\beta_{fast}}{\pi^2} \ln\left(\frac{f}{f_0}\right) \quad (5.3a)$$

$$c_{slow}(f) = c_{slow}(f_0) + [c_{slow}(f_0)]^2 \frac{\beta_{slow}}{\pi^2} \ln\left(\frac{f}{f_0}\right) \quad (5.3b)$$

where  $f_0$  is a reference frequency taken from within the experimental bandwidth, usually at or near midband. In our calculations,  $f_0$  was set at 1 MHz, which was the frequency of the excitation pulse.

The parameters in Equations 5.2 - 5.3 ( $A_{fast}$ ,  $A_{slow}$ ,  $\beta_{fast}$ ,  $\beta_{slow}$ ,  $c_{fast}(f_0)$ ,  $c_{slow}(f_0)$ ) were estimated using Bayesian probability theory applied to the reference water-only signal and the sample signal traveling through 9 mm of bone from the Nagatani *et al.* paper(2008)

TABLE 5.1: The values used for the six parameters in the propagation model. This set of parameter values was used because it maximized the posterior probability of the model.

	Parameters					
	$A_{fast}$	$A_{slow}$	$\beta_{fast}$ (dB/cm/MHz)	$\beta_{slow}$	$c_{fast}(1 \text{ MHz})$ (m/s)	$c_{slow}(1 \text{ MHz})$
Bayesian estimate	1.00	0.13	49.2	7.1	1933	1475

(panels (a) and (b) from Figure 7, respectively). More detailed explanations of Bayesian parameter estimation can be found in Anderson *et al.*(2010), Bretthorst (2005), and Marutyan *et al.*(2007). The values of the six parameters used in the propagation model above are given in Table 5.1. Once these six parameters were known, the individual fast and slow waves could be generated for each sample thickness  $d$ , which was varied from 6 mm to 15 mm in 1 mm increments.

### 5.4.2 Methods of analysis of attenuation properties

The two analysis methods discussed in this section were applied to the simulated data generated using the propagation model above.

#### ***Time-domain analysis of unseparated wave***

The method of analysis used in this section is described in the Nagatani *et al.* paper (2008). Its use was suggested by the limitations imposed by the overlapping wave modes. In this time-domain technique, the amplitudes of the first peak of the received signal, which are assumed to correspond to the fast waves, are compared for a series of sample thicknesses.

The apparent attenuation value,  $\alpha_{time}$ , of the fast wave is defined by

$$\alpha_{time} = \frac{20 \log \left( \frac{V_n}{V_{n+1}} \right)}{\Delta d} \quad (5.4)$$

where  $V_n$  and  $V_{n+1}$  are the amplitudes of the first arriving peaks in the received RF waveforms. The indices  $n$  and  $n + 1$  correspond to successive sample thicknesses differing by  $\Delta d = 1mm$ . This analysis method was employed to determine the apparent attenuation of the fast waves, but not the slow waves. This choice was made because the amplitudes of the slow waves were sometimes affected by interference from the fast waves, thus leading to meaningless determination of the attenuation of the slow waves (Nagatani *et al.*, 2008).

### **Frequency-domain analysis of separated fast waves and slow waves**

The frequency-domain method of determining the attenuation coefficient of a sample (dB/cm) is carried out by performing a log-spectral subtraction technique (Ophir *et al.*, 1984; Baldwin *et al.*, 2006),

$$\alpha(f) = \frac{10 \log \left( \left| \tilde{V}_n(f) \right|^2 \right) - 10 \log \left( \left| \tilde{V}_{n+1}(f) \right|^2 \right)}{\Delta d} \quad (5.5)$$

where  $|\tilde{V}_n(f)|$  and  $|\tilde{V}_{n+1}(f)|$  are the magnitudes of the Fourier transforms of the received signals when the sample has a thickness corresponding to length indices  $n$  and  $n + 1$ , respectively, and  $\Delta d = 1mm$ . Typically, a through-sample power spectrum is subtracted from a water-only reference power spectrum. In the present study, to apply this frequency-domain analysis method in a fashion analogous to that used in the time-domain analysis method described above, differences between spectra at thickness indices  $n$  and  $n + 1$  were analyzed.



Determining the attenuation coefficient using the difference of two through-sample power spectra eliminated the need for compensating for the insertion losses at the boundaries.

In this method, Equation 5.5 was applied to the isolated fast wave signal and the isolated slow wave signal. This method of analysis is expected to yield the attenuation coefficient of only the fast wave, free from artifacts caused by interference with the slow wave, and visa versa. The attenuation coefficients corresponding to the fast wave and the slow wave will be referred to as  $\alpha_{fast}(f)$  and  $\alpha_{slow}(f)$ , respectively.

## 5.5 Results

### 5.5.1 Simulated ultrasonic waves

Simulated ultrasonic data were generated using the model in Equations 5.1-5.3 for sample thicknesses ranging in 1 mm steps from 6 mm to 15 mm. Examples of the simulated sample waveforms along with the input reference waveform from the Nagatani et al. paper (2008) are shown in Figure 5.1. Fast and slow waves can be observed in all of the sample traces. As the sample thickness and thus propagation distance were increased, the fast wave was highly attenuated relative to the slow wave.

### 5.5.2 Time-domain analysis results of unseparated wave

The attenuation value  $\alpha_{time}$  of the fast wave at specific propagation distances within the sample was determined from the peak amplitudes of fast waves that had traversed different sample thicknesses 6, 7, 8,...,15 mm. Figure 5.2 shows the attenuation  $\alpha_{time}$  of the fast wave

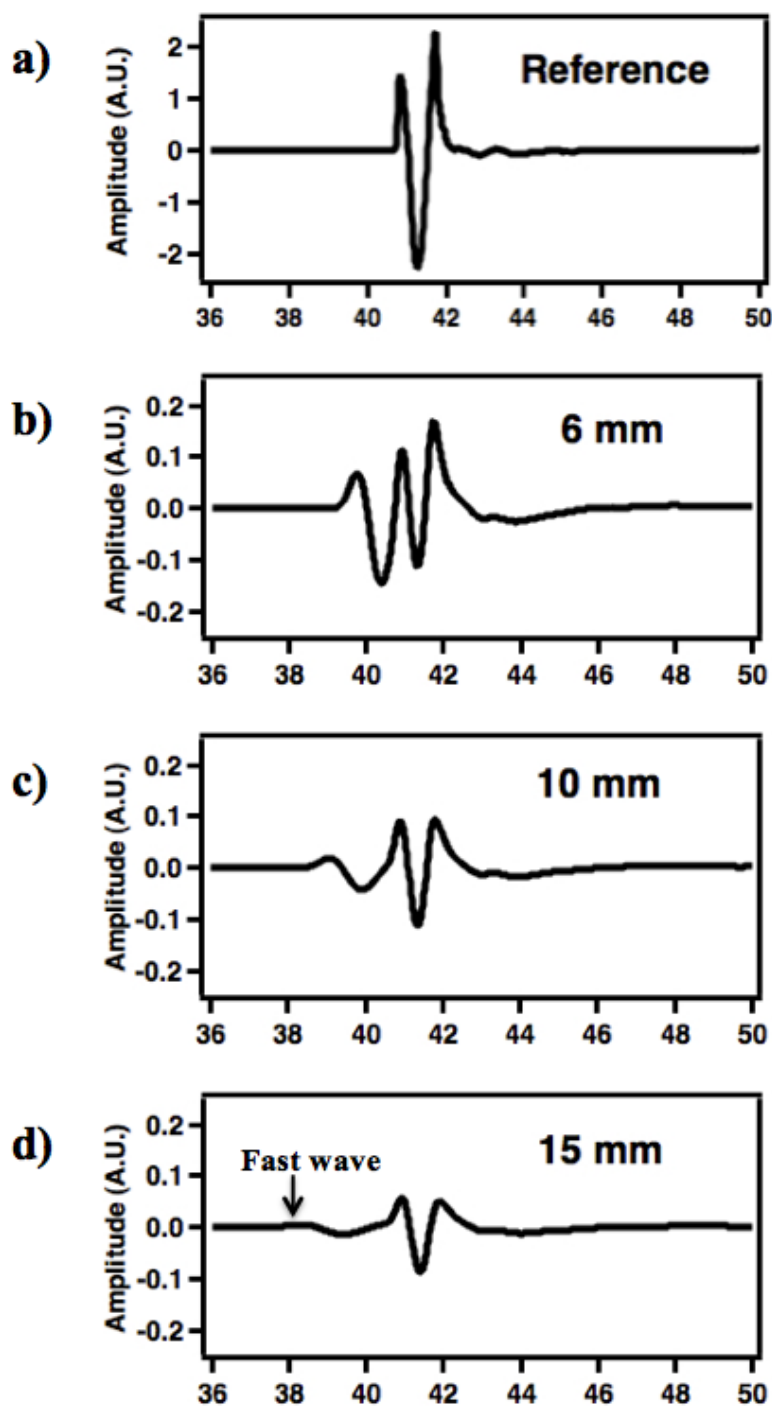


FIGURE 5.1: (a) Reference (water-path only) waveform. Simulated sample waveforms traveling through (b) 6 mm, (c) 10 mm and (d) 15 mm of sample.

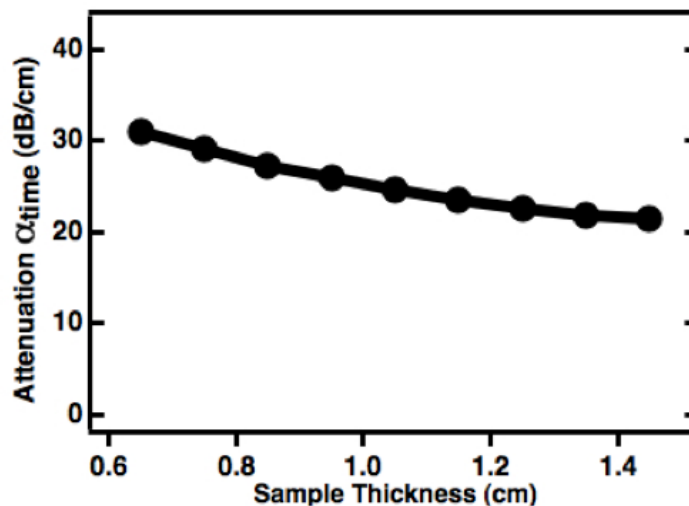


FIGURE 5.2: The dependence of the attenuation,  $\alpha_{time}$ , of the fast wave on propagation distance using the time-domain analysis method.

as a function of propagation distance. Similar to the results reported in the Nagatani *et al.* paper (2008), the results depicted in Figure 5.2 show that the attenuation of the fast wave appears to be larger at the beginning of propagation and then gradually smaller as the wave travels farther into the sample.

### 5.5.3 Frequency-domain analysis results of separated fast waves and slow waves

The propagation model and Bayesian probability theory analysis used in this study permitted the separation of the sample waveform into fast waves and slow waves. Representative examples of the individual fast waves and slow waves obtained from sample waveforms that have propagated through 6 mm, 10 mm, and 15 mm of sample are shown in Figure 5.3. The fast waves, identified as those arriving earlier in time, have lower amplitudes than the slow waves.

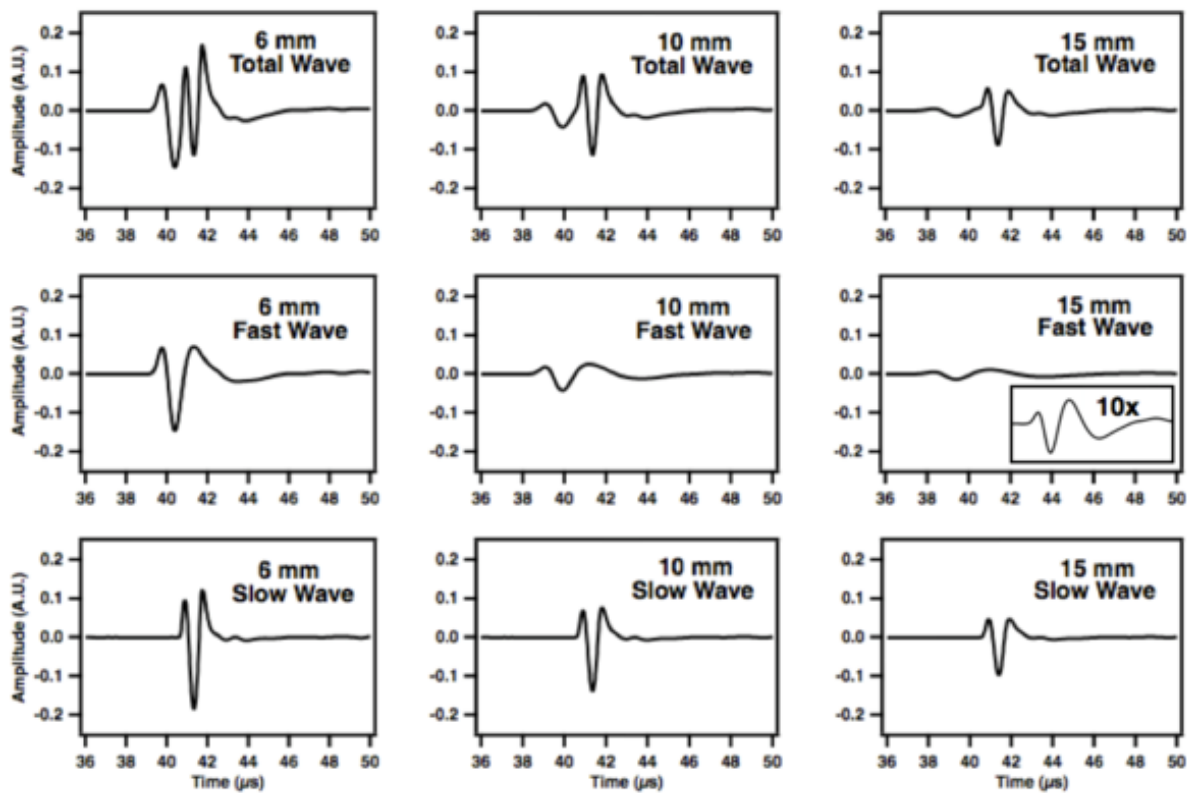


FIGURE 5.3: The top panels show the sample waveform comprised of overlapping fast and slow waves for sample thicknesses of 6 mm, 10 mm, and 15 mm, respectively. The middle and bottom panels display the individual fast waves and individual slow waves, respectively, for the three sample thicknesses.

For this method of analysis, the individual fast waves and slow waves were used in the log-spectral subtraction technique expressed in Equation 5.5. Separating the fast and slow waves permits determination of the fast wave's attenuation coefficient without introducing interference artifacts from the slow wave. Similarly, the slow wave's attenuation coefficient can be determined free from interference effects introduced by the fast wave. Performing the frequency domain analysis on the separated waveforms is essentially an inversion of the process used to simulate them from the values produced by the Bayesian parameter estimation. For this reason, it is guaranteed that this method will recover the attenuation coefficients used to initially simulate the waves. Furthermore, these attenuation coefficients cannot vary with distance. Figure 5.4 shows that, as required, the attenuation coefficient at 1 MHz of the fast wave,  $\alpha_{fast}(f = 1 \text{ MHz})$ , and the attenuation coefficient at 1 MHz of the slow wave,  $\alpha_{slow}(f = 1 \text{ MHz})$ , as a function of sample thickness display no dependence on the propagation distance, and that the numerical values of  $\alpha_{fast}(f = 1 \text{ MHz})$  and  $\alpha_{slow}(f = 1 \text{ MHz})$  are consistent with those used as input to the simulations. This result, though only a consistency check on the method, stands in contrast to the time-domain analysis shown above that seems to indicate a propagation distance dependence of the attenuation, despite the fact that the analyzed signals were simulated to have a strictly constant-with-propagation-distance attenuation coefficient.

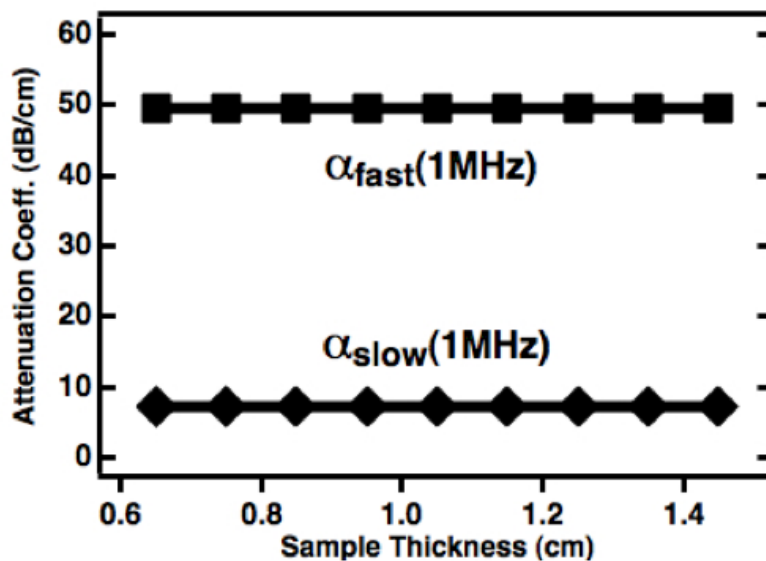


FIGURE 5.4: The attenuation coefficient of the separated fast wave,  $\alpha_{fast}(f)$ , and slow wave,  $\alpha_{slow}(f)$ , at 1 MHz as a function of propagation distance.

## 5.6 Discussion

Cancellous bone can support the generation and propagation of two compressional wave modes, fast waves and slow waves. Depending on factors, such as sample length and relative velocities of the fast and slow waves, these two wave modes can overlap substantially and therefore interfere in the time-domain signal. Analysis of these overlapping waveforms can lead to unexpected conclusions. Conventional phase spectroscopy analysis performed on mixed mode signals as if only one wave were present can yield apparent negative dispersion (Marutyan *et al.*, 2006a; Anderson *et al.*, 2008; Bauer *et al.*, 2008). Previous work has demonstrated, however, that when decomposed, the fast wave and slow wave each exhibit positive dispersion as required by the causality-induced Kramers-Kronig relations (Anderson *et al.*, 2010; Marutyan *et al.*, 2007). Negative dispersion has been measured not only in trabecular bone (Haiat *et al.*, 2006; Strelitzki and Evans, 1996; Wear, 2001, 2000; Droin

*et al.*, 1998) and cortical bone (Haiat *et al.*, 2008) *in vitro* but also in trabecular bone-mimicking phantoms (Lee and Choi, 2007; Wear, 2005). Several models have been proposed that predict negative dispersion including multilayer models (Wear, 2001, 2007), multiple scattering models (Haiat *et al.*, 2008), and independent scattering models (Haiat and Naili, 2011). The objective of this study was to investigate the potential value of separating the fast waves and slow waves for determining the attenuation properties of cancellous bone and to compare the results of time-domain and frequency-domain methods for the analysis of attenuation.

In this study, two methods of analysis were investigated using the same simulated cancellous bone data. The time-domain analysis method applied to the mixed-mode signal yielded a fast wave attenuation that started high at the beginning of propagation and then decreased as the wave traveled farther into the sample. However, the waves had been simulated with a strictly constant-with-propagation-distance attenuation coefficient. The frequency-domain analysis method applied to the separated fast waves and slow waves that made up that mixed-mode signal, recovered the attenuation coefficients of both wave modes and did not introduce a dependence on the propagation distance. This finding demonstrates that application of time-domain based analysis to determine the attenuation properties of mixed mode waves can introduce an apparent dependence of the properties on propagation distance.

The ability to separate the fast and slow waves permits application of frequency-domain methods. If the separation is performed and the resulting waves are analyzed in the frequency domain, the known attenuation coefficients can be recovered. Figure 5.5 demonstrates that performing either these steps in isolation can introduce an apparent dependence on propaga-

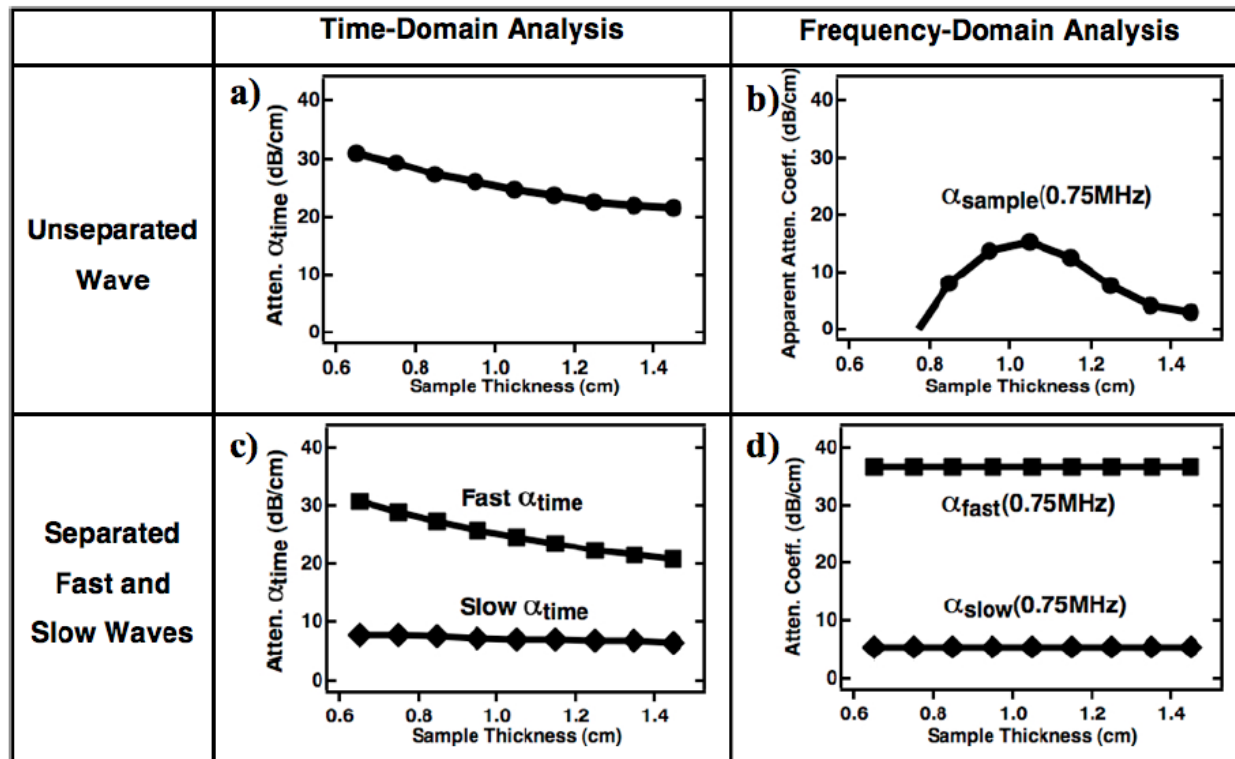


FIGURE 5.5: The attenuation behavior as a function of sample thickness results when applying, panel (a): the time-domain method to the unseparated fast wave, panel (b): log-spectral subtraction to the entire sample wave, consisting of overlapping wave modes, panel (c): the time-domain method to the individual fast wave and slow wave, and panel (d): log-spectral subtraction to the separated fast wave and slow wave.

tion distance. As illustrated, frequency-domain analysis of the unseparated wave (Fig. 5.5, panel (b)) and time-domain analysis of the separated waves (Fig. 5.5, panel (c)) both result in variable-with-distance apparent attenuation.

When the time-domain method was applied to the individual separated fast waves and slow waves, the attenuation of the fast wave,  $\alpha_{time}^{fast}$ , and the attenuation of the slow wave,  $\alpha_{time}^{slow}$ , both showed a dependence on sample thickness (Fig. 5.5, panel (c)). This phenomenon results from estimating the attenuation from the time-domain amplitude of a broadband pulse. In the current system, a 1 MHz center-frequency, broadband pulse was used as the



input signal. Typically, the attenuation coefficient for both fast and slow waves increases with frequency in the range of interest. As a result, early in the propagation, the higher frequency components of the broadband signal are reduced more rapidly than the lower frequency signals, thus resulting in a signal exhibiting proportionally more of the lower frequency components. These lower frequency components are attenuated less with distance than the higher frequencies, resulting in a perceived attenuation coefficient that appears to decrease with distance. (Because of the shift to lower frequency components, to permit a better comparison with the time-domain analysis results, in Figure 5.5 the frequency-domain attenuation coefficients for both the unseparated wave (panel (b)) and the separated fast and slow waves (panel (d)) are shown for  $f = 0.75$  MHz rather than  $f = 1$  MHz. In panel (b) the values of  $\alpha_{sample}$  (0.75 MHz) are negative below sample thicknesses of 0.8 cm due to interference between the fast and slow waves.)

The frequency-domain analysis method properly accounts for the broadband nature of the data; however, applying this method to the mixed-mode sample waveform still yields an apparent attenuation coefficient that depends on the thickness of the sample (Fig. 5.5, panel (b)). This effect, observed previously in bone mimicking phantoms (Bauer *et al.*, 2008, 2007), appears to be a result of interference between the fast and slow waves being perceived as attenuation. Figure 5.6 shows the apparent attenuation coefficient of the combined wave for three propagation distances, along with the known attenuation coefficients for the fast and slow wave. Panel (a) shows that when the signals have propagated a short distance, there is substantial interference between the two waves and a resulting anomalous attenuation coefficient. By the time the signals propagate to 10 mm (panel (b)) and 15 mm (panel (c)),

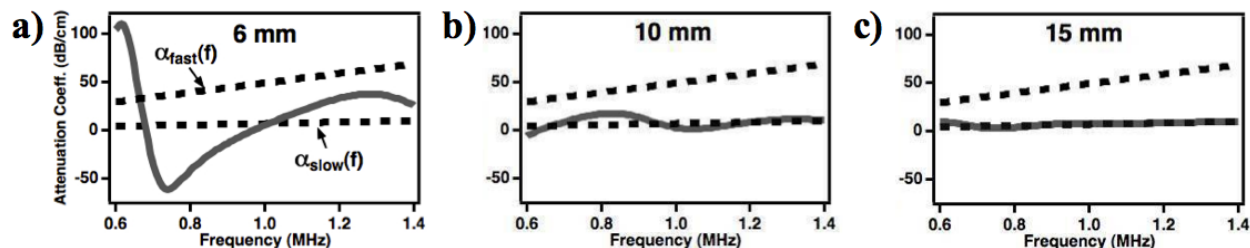


FIGURE 5.6: The attenuation coefficients determined using the frequency-domain technique for the entire sample wave (solid line) and the separated fast and slow waves (dashed lines) for three propagation distances: 6 mm (panel a), 10 mm (panel b), and 15 mm (panel c).

the fast wave has been attenuated more than the slow wave, so the attenuation coefficient of the combined wave approaches the slow wave value. As illustrated in Figure 5.4, the underlying attenuation coefficient of each mode can be obtained if separated fast waves and slow waves are available.

The results presented above might provide insight into the interpretation of the recent study by Nagatani *et al.*(2008). That previous work showed that the attenuation properties of cancellous bone appear to vary substantially on the scale of millimeters. The current work attempts to demonstrate that in a simulated sample with constant attenuation properties, apparent variation with sample thickness can be introduced by the analysis methods. The nature and scale of the variation with depth reported by Nagatani *et al.* may not be fully accounted for by the effects originating from use of time-domain analysis, but gaining a complete understanding of this complicated system will likely require isolation of these effects.

As described previously, the complicated trabecular structure of cancellous bone could potentially be an alternative or additional cause for the previously reported apparent decrease with distance of the attenuation coefficient (Nagatani *et al.*, 2008). The substantially higher

speed of sound within the trabeculae (approximately 3500 m/s) relative to the lower speed of sound in the intervening marrow (approximately 1470 m/s) (Laugier, 1999) causes the portions of the propagating signal that travel through the hard bone to advance much more quickly than the signal that propagates primarily through the interstitial marrow. When these faster signals have propagated only a short distance through the sample (relative to the pertinent scales determined by the trabecular spacing and by the wavelength of the sound), their phase fronts might be significantly misaligned. As a result, signals from a relatively large (compared to the wavelength) phase sensitive receiving aperture (real or simulated) would be subject to phase cancellation artifacts at its face (Busse and Miller, 1981a,b). This phase cancellation represents irretrievable loss of information that would appear as apparent attenuation. Similar examples of phase cancellation appearing as apparent attenuation in bone have been reported previously (Petley *et al.*, 1995; Langton and Subhan, 2001; Bauer *et al.*, 2007, 2008; Wear, 2007, 2008; Cheng *et al.*, 2011).

In the context of this attenuation explanation, if the fast wave is permitted to propagate farther into the sample, the phase front will tend towards realignment as the randomness induced by the trabeculae averages out over this longer path (Nagatani *et al.*, 2008). A phase sensitive receiver placed at the end of such a longer propagation path will be subject to less phase cancellation, and therefore less perceived attenuation. This phenomenon is described more fully in Nagatani *et al.* (2008) and is demonstrated in Figure 10 of that paper.

This phenomenon potentially complicates the interpretation of signals propagated through cancellous bone. However, because it is intrinsically linked to the size and spacing of trabeculae, this effect might ultimately be exploited to infer from apparent attenuation mea-

measurements the relevant length scales of the sample under investigation. Knowledge of these length scales might then be used to estimate clinically useful parameters such as the porosity and bone volume per total volume (BV/TV).

If the mixed-mode signal cannot be decomposed into its individual wave modes, then both the time-domain method and the frequency-domain method might introduce an apparent dependence on distance of the attenuation properties that is not representative of the underlying structure. Therefore, the ability to separate the fast waves and slow waves is of considerable importance. Bayesian probability theory is one method for determining the individual properties of the interfering wave modes (Anderson *et al.*, 2010; Marutyan *et al.*, 2007), but in principle any method that can isolate the two waves could be applied. Wear, for example, recently demonstrated that the modified least squares Prony's method was also able to decompose a mixed-mode signal and yield accurate estimates of its ultrasonic properties (Wear, 2010a,b).

The results of this study show that overlapping fast waves and slow waves can complicate the determination of the attenuation properties of cancellous bone. Specifically, the subtleties introduced by certain analysis methods applied to these temporally overlapped waves might represent, in part, an alternative explanation for the previously observed dependence on propagation distance of the attenuation properties of cancellous bone. Frequency domain analysis performed on the separated fast and slow waves was shown to be the least susceptible to such artifacts.

## **5.7 Acknowledgments**

This study was supported by NIH Grant R01-AR057433.

## Bibliography

- Anderson, C. C., Bauer, A. Q., Holland, M. R., Pakula, M., Laugier, P., Bretthorst, G. L., and Miller, J. G. (2010), “Inverse problems in cancellous bone: Estimation of the ultrasonic properties of fast and slow waves using Bayesian probability theory”, *J Acoust Soc Am* **128**(5), 2940–2948.
- Anderson, C. C., Bauer, A. Q., Marutyan, K. R., Holland, M. R., Pakula, M., Bretthorst, G. L., Laugier, P., and Miller, J. G. (2011), “Phase Velocity of Cancellous Bone: Negative Dispersion Arising from Fast and Slow Waves, Interference, Diffraction, and Phase Cancellation at Piezoelectric Receiving Elements”, in “Bone Quantitative Ultrasound”, , edited by Laugier, P. and Haiat, G. (Springer, Netherlands), 319–330, 978-94-007-0017-8.
- Anderson, C. C., Marutyan, K. R., Holland, M. R., Wear, K. A., and Miller, J. G. (2008), “Interference between wave modes may contribute to the apparent negative dispersion observed in cancellous bone”, *J Acoust Soc Am* **124**(3), 1781–1789.
- Baldwin, S. L., Marutyan, K. R., Yang, M., Wallace, K. D., Holland, M. R., and Miller, J. G. (2006), “Measurements of the anisotropy of ultrasonic attenuation in freshly excised myocardium”, *J Acoust Soc Am* **119**, 3130–3139.
- Bauer, A. Q., Marutyan, K. R., Holland, M. R., and Miller, J. G. (2007), “Is the Kramers-Kronig relationship between ultrasonic attenuation and dispersion maintained in the presence of apparent losses due to phase cancellation?”, *J Acoust Soc Am* **122**, 222–228.
- Bauer, A. Q., Marutyan, K. R., Holland, M. R., and Miller, J. G. (2008), “Negative dispersion in bone: The role of interference in measurements of the apparent phase velocity of two temporally overlapping signals”, *J Acoust Soc Am* **123**(4), 2407–2414.
- Bretthorst, G. L., Hutton, W. C., Garbow, J. R., and Ackerman, J. J. H. (2005), “Exponential parameter estimation (in NMR) using Bayesian probability theory”, *Concepts Magn Reson* **27A**, 55–63.
- Busse, L. and Miller, J. G. (1981a), “Detection of spatially nonuniform ultrasonic radiation with phase sensitive (piezoelectric) and phase insensitive (acoustoelectric) receivers”, *J Acoust Soc Am* **70**(5), 1377–1386.
- Busse, L. and Miller, J. G. (1981b), “Response characteristics of a finite aperture, phase insensitive ultrasonic receiver based upon the acoustoelectric effect”, *J Acoust Soc Am* **70**(5), 1370–1376.
- Cardoso, L., Teboul, F., Sedel, L., Oddou, C., and Meunier, A. (2003), “In vitro acoustic waves propagation in human and bovine cancellous bone”, *J Bone Miner Res* **18**(10), 1803–12.

- Cheng, J., Serra-Hsu, F., Tian, Y., Lin, W., and Qin, Y. (2011), “Effects of phase cancellation and receiver aperture size on broadband ultrasonic attenuation for trabecular bone in vitro”, *Ultrasound in Med and Biol* **37(12)**, 2116–2125.
- Droin, P., Berger, G., and Laugier, P. (1998), “Velocity dispersion of acoustic waves in cancellous bone”, *IEEE Trans Ultrason Ferroelectr Freq Control* **45(3)**, 581–592, 0885-3010.
- Frost, M. L., Blake, G. M., and Fogelman, I. (2001), “Quantitative ultrasound and bone mineral density are equally strongly associated with risk factors factors for osteoporosis”, *J Bone Miner Res* **16(2)**, 406–16.
- Haiat, G., Lhemery, A., Renaud, F., Padilla, F., Laugier, P., and Naili, S. (2008), “Velocity dispersion in trabecular bone: Influence of multiple scattering and of absorption”, *J Acoust Soc Am* **124(6)**, 4047–4058.
- Haiat, G. and Naili, S. (2011), “Independent scattering model and velocity dispersion in trabecular bone: comparison with a multiple scattering model”, *Biomech Model Mechanobiol* **10**, 95–108.
- Haiat, G., Padilla, F., Cleveland, R., and Laugier, P. (2006), “Effects of frequency-dependent attenuation and velocity dispersion on in vitro ultrasound velocity measurements in intact human femur specimens”, *IEEE Trans Ultrason Ferroelectr Freq Control* **53**, 39–51.
- Hans, D. and Krieg, M. A. (2008), “The clinical use of quantitative ultrasound (QUS) in the detection and management of osteoporosis”, *IEEE Trans Ultrason Ferroelectr Freq Control* **55(7)**, 1529–1538, 0885-3010.
- Hosokawa, A. (2010), “Effect of porosity distribution in the propagation direction on ultrasound waves through cancellous bone”, *IEEE Trans Ultrason Ferroelectr Freq Control* **57(6)**, 1320–1328.
- Hosokawa, A. and Otani, T. (1997), “Ultrasonic wave propagation in bovine cancellous bone”, *J Acoust Soc Am* **101(1)**, 558–562.
- Hosokawa, A. and Otani, T. (1998), “Acoustic anisotropy in bovine cancellous bone”, *J Acoust Soc Am* **103(5)**, 2718–2722.
- Langton, C. M. and Subhan, M. (2001), “Computer and experimental simulation of a cortical end-plate phase cancellation artifact in the measurement of BUA at the calcaneus”, *Physiol Meas* **22**, 581–587.
- Laugier, P. (1999), “The basic physics of ultrasound”, in “Quantitative Ultrasound: Assessment of osteoporosis and bone status”, , edited by Njeh, C. F., Hans, D., Fuerst, T., Glüer, C. C., and Genant, H. K. (Martin Dunitz Ltd, London), 56.

- Laugier, P. (2008), “Instrumentation for in vivo ultrasonic characterization of bone strength”, *IEEE Trans Ultrason Ferroelectr Freq Control* **55(6)**, 1179–1196, 0885-3010.
- Lee, K. I. and Choi, M. J. (2007), “Phase velocity and normalized broadband ultrasonic attenuation in polyacetal cuboid bone-mimicking phantoms”, *J Acoust Soc Am* **121**, EL263–EL269.
- Marutyan, K. R., Holland, M. R., and Miller, J. G. (2006a), “Anomalous negative dispersion in bone can result from the interference of fast and slow waves”, *J Acoust Soc Am* **120(5)**, EL55–EL61.
- Marutyan, K. R., Holland, M. R., and Miller, J. G. (2006b), “Evidence that the Negative Dispersion in Bone Results from Interference Between Fast and Slow Modes Each with Positive Dispersion”, in “IEEE Ultras Symp”, 17–20.
- Marutyan, K. R., L., B. G., and Miller, J. G. (2007), “Bayesian estimation of the underlying bone properties from mixed fast and slow mode ultrasonic signals”, *J Acoust Soc Am* **121(1)**, EL8–EL15.
- Mizuno, K., Matsukawa, M., Otani, T., Laugier, P., and Padilla, F. (2009), “Propagation of two longitudinal waves in human cancellous bone: An in vitro study”, *J Acoust Soc Am* **125(5)**, 3460–3466.
- Mizuno, K., Matsukawa, M., Otani, T., Takada, M., Isao, M., and Tsujimoto, T. (2008), “Effects of structural anisotropy of cancellous bone on speed of ultrasonic fast waves in the bovine femur”, *IEEE Trans Ultrason Ferroelectr Freq Control* **55(7)**, 1480–1487, 0885-3010.
- Nagatani, Y., Mizuno, K., Saeki, T., Matsukawa, M., Sakaguchi, T., and Hosoi, H. (2008), “Numerical and experimental study on the wave attenuation in bone - FDTD simulation of ultrasound propagation in cancellous bone”, *Ultrasonics* **48**, 607–612.
- O’Donnell, M., Jaynes, E., and Miller, J. G. (1978), “General relationships between ultrasonic attenuation and dispersion”, *J Acoust Soc Am* **63**, 1935–1937.
- O’Donnell, M., Jaynes, E., and Miller, J. G. (1981), “Kramers-Kronig relationship between ultrasonic attenuation and phase velocity”, *J Acoust Soc Am* **69**, 696–701.
- Ophir, J., Shawker, T., Maklad, H., Miller, J., Flax, S., Narayana, P., and Jones, J. (1984), “Attenuation estimation in reflection: Progress and prospects”, *Ultrasonic Imaging* **6**, 349–395.
- Padilla, F. and Laugier, P. (2000), “Phase and group velocities of fast and slow compressional waves in trabecular bone”, *J Acoust Soc Am* **108**, 1949–1952.
- Petley, G. W., Robins, P. A., and Aindow, J. D. (1995), “Broadband ultrasonic attenuation: Are current measurement techniques inherently inaccurate?”, *Br J Radiol* **68**, 1212–1214.



- Strelitzki, R. and Evans, J. (1996), “On the measurement of the velocity of ultrasound in the os calcis using short pulses”, *Eur J Ultrasound* **4**, 205–213.
- Waters, K. R. and Hoffmeister, B. K. (2005), “Kramers-Kronig analysis of attenuation and dispersion in trabecular bone”, *J Acoust Soc Am* **118**, 3912–3920.
- Waters, K. R., Hughes, M. S., Mobley, J., Brandenburger, G. H., and Miller, J. G. (2000), “On the applicability of Kramers-Kronig relations for ultrasonic attenuation obeying a frequency power law”, *J Acoust Soc Am* **108**, 556–563.
- Waters, K. R., Mobley, J., and Miller, J. G. (2005), “Causality-imposed (Kramers-Kronig) relationships between attenuation and dispersion”, *IEEE Trans Ultrason Ferroelectr Freq Control* **52**, 822–823.
- Wear, K. A. (2000), “Measurements of phase velocity and group velocity in human calcaneus”, *Ultrasound in Med and Biol* **26**, 641–646.
- Wear, K. A. (2001), “A stratified model to predict dispersion in trabecular bone”, *IEEE Trans Ultrason Ferroelectr Freq Control* **48**, 1079–1083.
- Wear, K. A. (2005), “The dependencies of phase velocity and dispersion on trabecular thickness and spacing in trabecular bone-mimicking phantoms”, *J Acoust Soc Am* **118**, 1186–1192.
- Wear, K. A. (2007), “Group velocity, phase velocity, and dispersion in human calcaneus in vivo”, *J Acoust Soc Am* **121**(4), 2431–2437.
- Wear, K. A. (2008), “The effect of phase cancellation on estimates of broadband ultrasound attenuation and backscatter coefficient in human calcaneus in vitro”, *IEEE Trans Ultrason Ferroelectr Freq Control* **55**, 384–390.
- Wear, K. A. (2010a), “Cancellous bone analysis with modified least squares Prony’s method and chirp filter: Phantom experiments and simulation”, *J Acoust Soc Am* **128**(4), 2191–2203.
- Wear, K. A. (2010b), “Decomposition of two-component ultrasound pulses in cancellous bone using modified least squares Prony method-Phantom experiment and simulation”, *Ultrasound in Med and Biol* **36**(2), 276–287.

# CHAPTER 6

---

## STUDY OF SYSTEMATICALLY SHORTENED EQUINE CANCELLOUS BONE

### 6.1 Introduction

The material presented in this chapter makes use of a powerful approach introduced by Professor Mami Matsukawa and her co-investigators at Doshisha University in Kyoto, Japan. The approach pioneered by Dr. Matsukawa consists of systematically shortening a carefully prepared bone specimen, with ultrasonic data acquired at each sample length. Professor Mami Matsukawa and her co-investigators prepared the bone specimen and acquired the data used in this investigation.

The bone specimen investigated, which was of unusually high bone volume fraction (BV/TV), was obtained from the radius of a horse. The relatively high bone volume fraction resulted in a rather large separation between the fast wave and slow wave velocities. This, in turn, permitted investigation with both conventional and Bayesian techniques for a wide

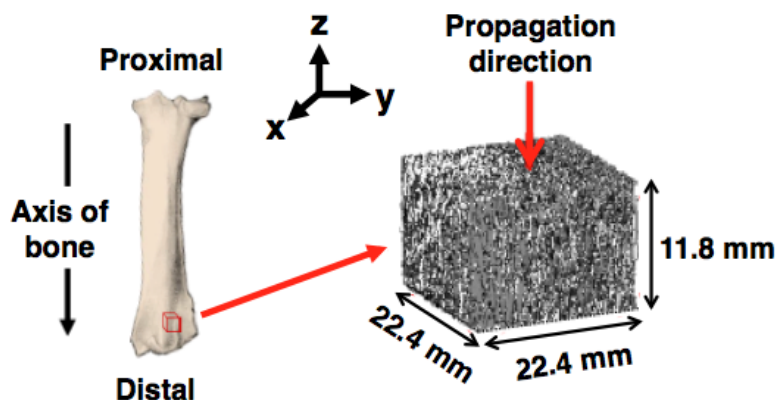


FIGURE 6.1: The equine trabecular specimen was obtained from the distal end of the left radius. The ultrasonic signal was propagated along the main bone axis, which is the predominant trabecular orientation. Adapted from Fujita *et al.* (2013).

range of sample thicknesses.

## 6.2 Methods

### 6.2.1 Data acquisition

The following sample preparation and ultrasonic measurements were performed at Doshisha University in Kyoto, Japan by Dr. Mami Matsukawa's group. A rectangular cancellous bone specimen, approximately 22.4 mm x 22.4 mm x 11.8 mm in size, was extracted from the left radius of a 36 month old horse as shown in Figure 6.1. The sample was defatted using a water pick. Micro-CT, with a spatial resolution of 41  $\mu\text{m}$ , was performed on the sample to obtain measurements of the bone volume fraction (BV/TV).

For the ultrasonic measurements, the sample was immersed in a room temperature tank filled with degassed water. The sample itself was placed in an "acoustic tube" as shown

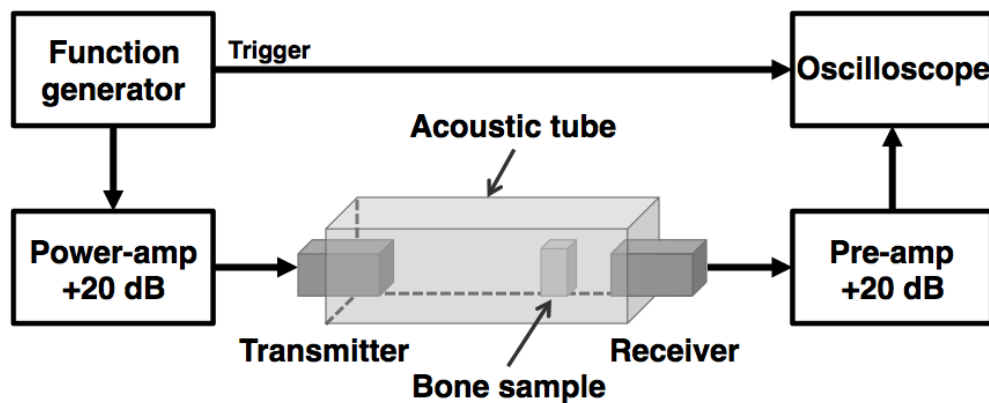


FIGURE 6.2: Through-transmission arrangement for the ultrasonic measurements. For each sample thickness, the bone sample was placed in an acoustic tube approximately 75 mm from the transmitting transducer. The two rectangular PVDF transducers were separated by a distance of 100 mm. Figure adapted from Fujita *et al.* (2013).

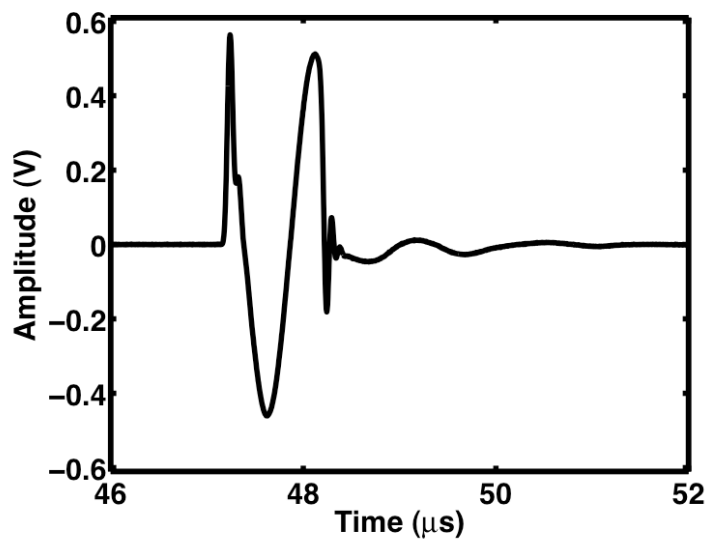


FIGURE 6.3: Water-path-only reference signal with a center frequency of 1 MHz.

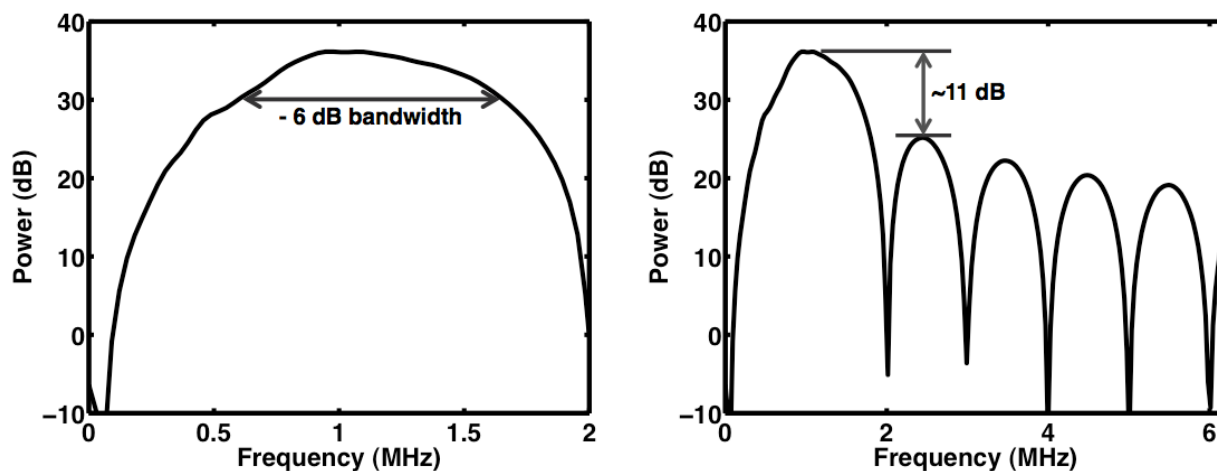


FIGURE 6.4: Power spectrum of the reference signal shown in Figure 6.3. Left: The power spectrum around 1 MHz, the center frequency of the transducer. Right: The same power spectrum over a wider frequency range. As is evident from the figure, the reference trace contained high levels of the harmonic frequencies.

in Figure 6.2. The walls of the acoustic tube were covered by polystyrene to prevent the ultrasonic waves from reflecting off the acoustic tube. A pair of planar, wideband polyvinylidene fluoride (PVDF) transducers, with an active area of 15 mm x 15 mm, were used to investigate the sample. The transducers were separated by a distance of 100 mm, with the front surface of the sample positioned at 75 mm from the transmitting transducer. The transmitter was excited by a single cycle of a 1 MHz sinusoidal pulse with a peak-to-peak amplitude of 5 V generated by a function generator and then amplified by 20 dB using a power amplifier. Figure 6.3 shows the water-path-only reference signal and Figure 6.4 shows the power spectrum of the reference signal. The received signal, after passing through the sample, was first amplified by a 20 dB preamplifier and then digitized with an oscilloscope. This process was repeated as the equine sample was shortened from 11.8 mm down to 0.5 mm in 0.5 mm increments, for a total of 24 data sets. At each step, the sample was ground

down using a polishing machine.

The received signals that traveled through each of the sample thicknesses are shown in Figure 6.5. Separated fast and slow waves are clearly evident at the larger sample thicknesses, ranging from 11.8 mm to 6 mm. Samples thinner than approximately 6 mm produced a sample signal that had either overlapping fast and slow waves or that appeared to be only one wave. The effects of sample thickness on the presence of fast and slow waves are more clearly observed in Figure 6.6, in which the slow wave was normalized to unit amplitude for each trace.

### 6.2.2 Data analysis

Data analysis was carried out in the Laboratory for Ultrasonics at Washington University in Saint Louis. Bayesian parameter estimation analysis and conventional analysis, both described in more detail in Chapter 3, were applied to the data acquired at specific sample lengths.

#### Bayesian parameter estimation analysis

The Bayesian probability method was performed on the 24 data sets acquired at sample lengths ranging from 11.8 mm to 0.5 mm. The six fast and slow wave ultrasonic parameters,  $A_{fast}$ ,  $A_{slow}$ ,  $\beta_{fast}$ ,  $\beta_{slow}$ ,  $c_{fast}(f_0)$ ,  $c_{slow}(f_0)$ , were estimated using the wave propagation model detailed in Section 3.4.2. For the Bayesian parameter estimation, the prior probabilities for each of the six parameters were assigned to be bounded Gaussian distributions as shown in Table 6.1 and  $f_0$  was set to 1 MHz, the center frequency of the transmitted signal.

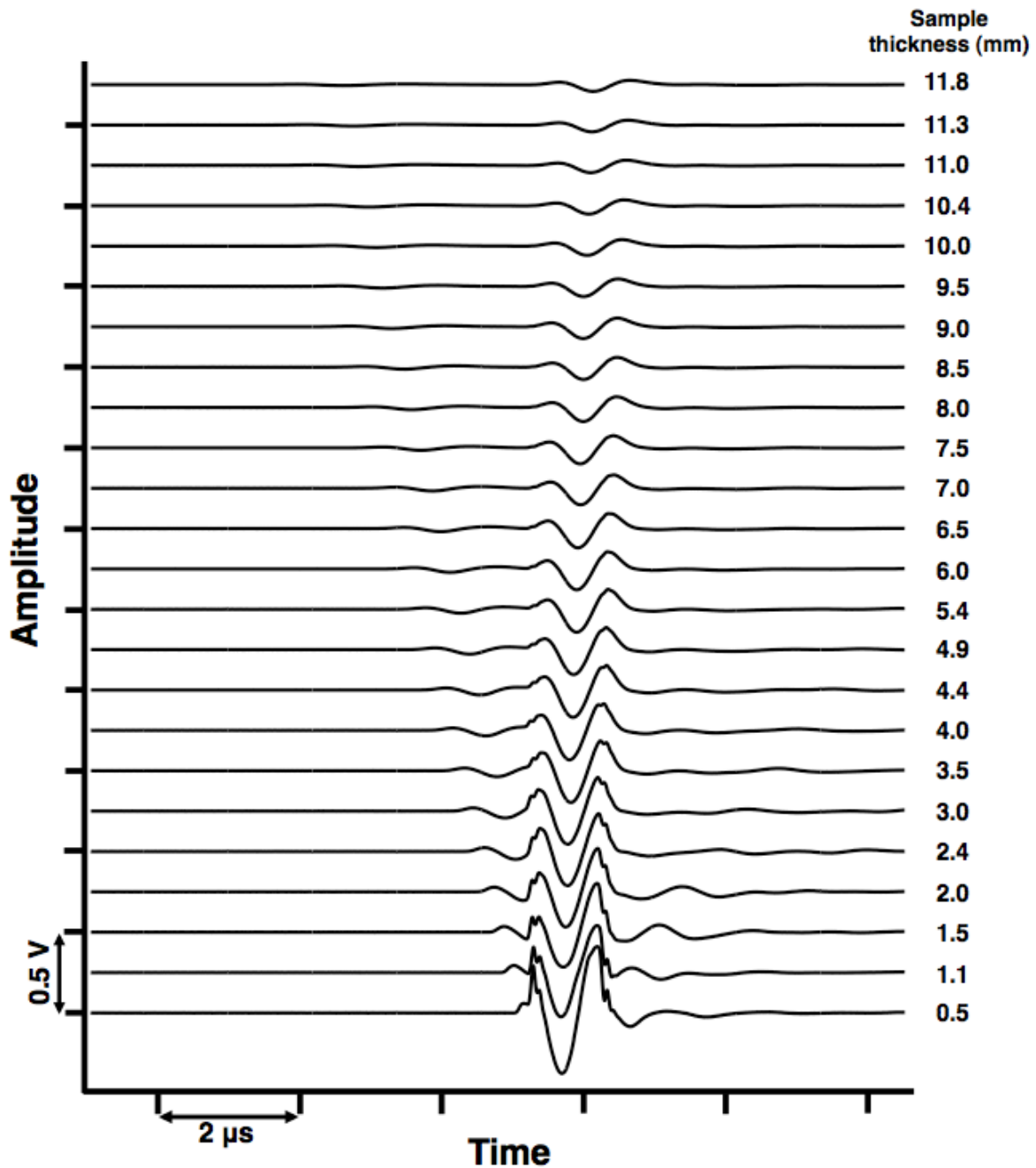


FIGURE 6.5: Acquired experimental data on the equine sample at 24 different lengths. As the sample thickness decreased, the originally separated fast and slow waves became more overlapped until the received signal appeared to contain only a single wave.

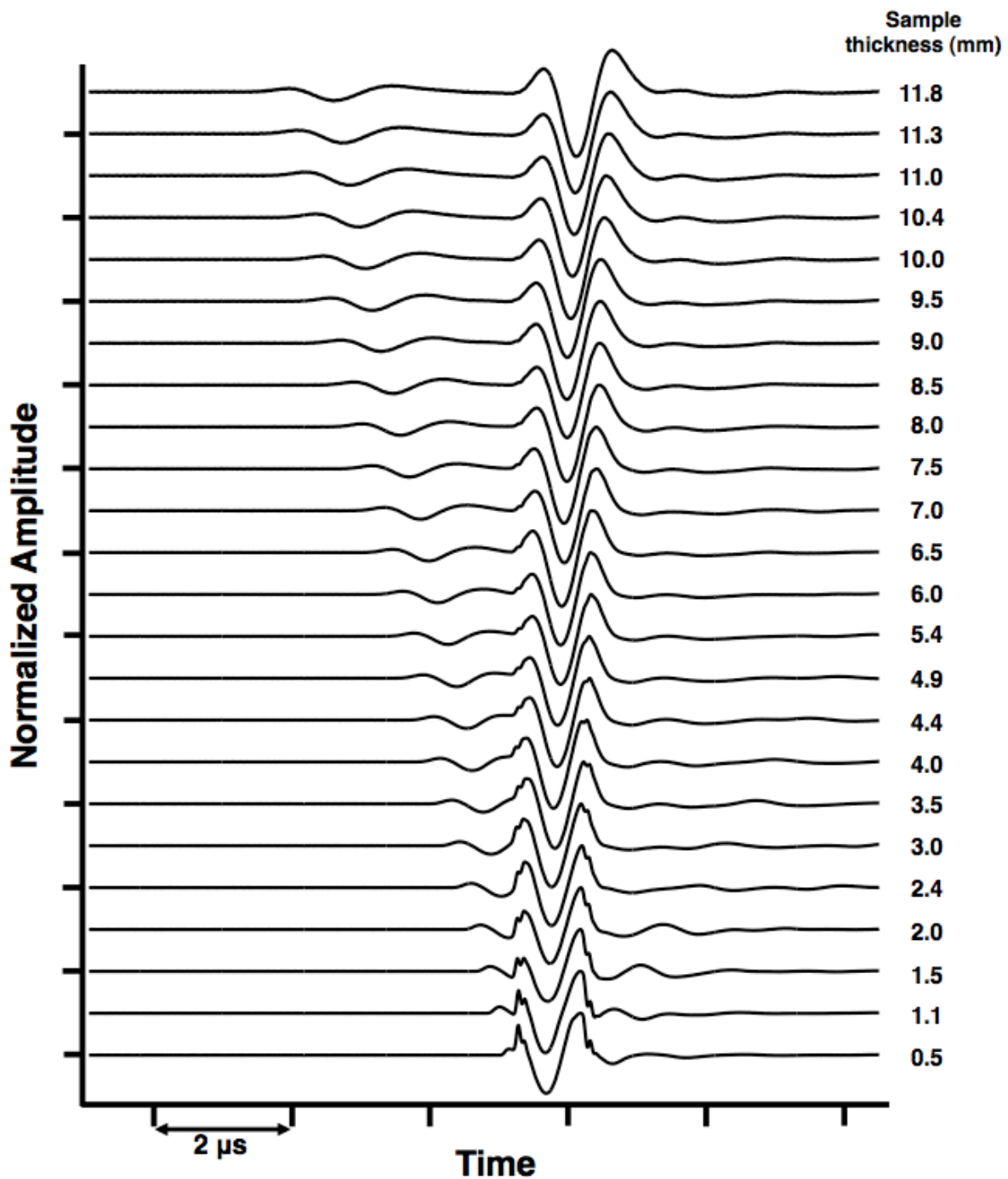


FIGURE 6.6: The received signals shown in Figure 6.5 with the maximum voltage normalized to unity for each thickness. This normalization permitted the fast waves present in the longer sample lengths to be visible. As the sample thickness decreased, the location of the fast wave moved closer to the location of the slow wave. The slow wave also shifted to earlier times as the sample thickness changed.



TABLE 6.1: Prior probability distributions for each model parameter. The means and standard deviations define Gaussian distributions that are bounded by the minimum and maximum values.

	$A_{fast}$	$A_{slow}$	$\beta_{fast}$ (dB/cm/MHz)	$\beta_{slow}$ (dB/cm/MHz)	$c_{fast}$ (1 MHz) (m/s)	$c_{slow}$ (1 MHz) (m/s)
Minimum	0	0	0	0	1500	1300
Mean	0.5	0.5	25	25	2000	1500
Maximum	1.0	1.0	50	50	2500	1700
Std. Dev.	0.5	0.5	25	25	500	200

### Conventional analysis

Conventional analysis was performed on the sample lengths that were sufficiently long as to permit enough separation of the fast and slow waves so that time-domain gating could be carried out effectively. A 90% Tukey window, shown in Figure 6.7, was used to time-gate the received sample signals into individual fast and slow waves for sample thickness from 6.0 mm to 11.8 mm, a total of 13 lengths. A Tukey window is a rectangular window with sinusoidal tapering on either end. It is referred to as a 90% Tukey window because the central 90% of the window is equal to unity.

In this analysis, the individually windowed fast and slow waves were compared to a reference signal obtained by recording a signal traveling only through water, as shown in Figure 6.3. The phase velocities were determined using the phase spectroscopy methods detailed in Section 3.3.1. In order to determine the attenuation coefficients of the fast and slow waves as detailed in Section 3.3.2, the insertion losses for the fast and slow waves, respectively, were taken into account. The insertion losses were estimated by determining

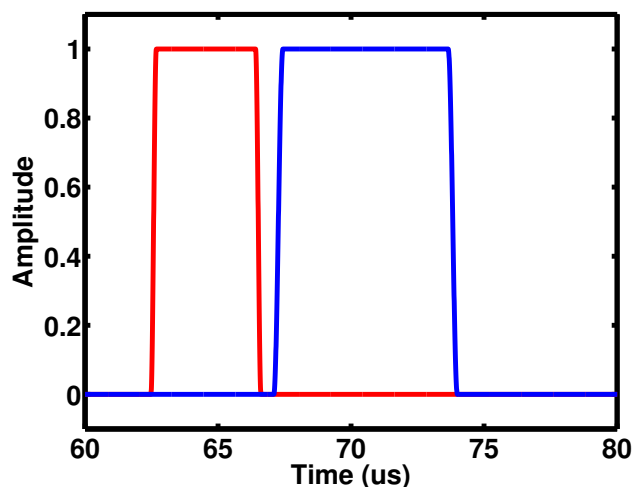


FIGURE 6.7: Representative 90% Tukey windows used to separate the fast waves (red) and the slow waves (blue). The specific windows plotted were for sample length  $d = 11.8$  mm. Window lengths varied depending on the degree of separation of the fast and slow waves and the systematic variation in frequency of the fast and slow waves.

the zero-frequency intercepts of the signal loss versus frequency curves, as illustrated in Figure 6.8. The fast and slow wave impedances are unknown. Therefore the intensity transmission coefficients of the fast and slow waves can not be determined independently. The average ( $\pm$  one standard deviation) insertion losses of the fast and slow waves for sample thickness ranging from 6.0 mm to 11.8 mm are shown in Figure 6.9. The normalized broadband ultrasound attenuations (nBUA) of the fast and slow waves were determined by the slope of a linear fit of the attenuation coefficient over the bandwidth 0.58 - 1.25 MHz.

### Estimation of apparent frequency

In Fujita *et al.* (2013), the apparent frequencies of the fast waves and slow waves at each sample length were determined using time intervals of peaks and zero-crossings in the time-domain signals. As discussed in Chapter 5, time domain analysis methods may be

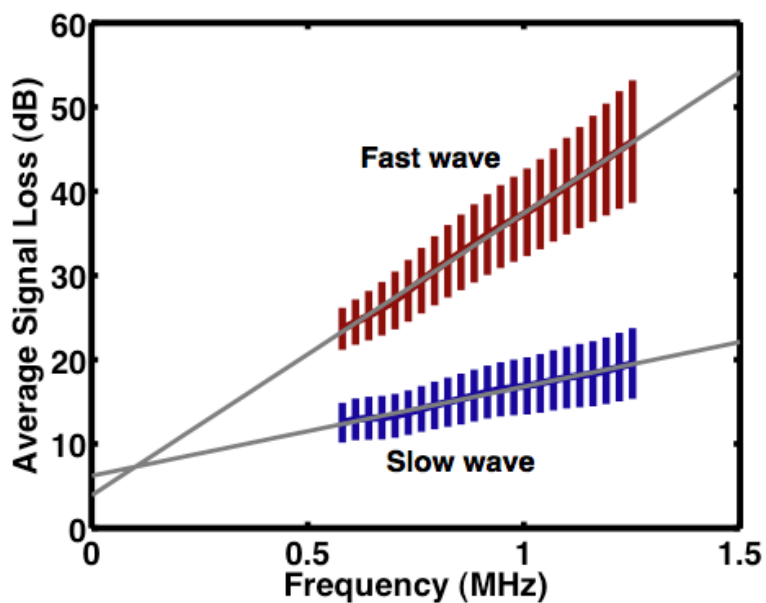


FIGURE 6.8: Average  $\pm$  one standard deviation signal loss of the fast waves (red) and slow waves (blue) over 13 sample lengths ranging from  $d = 6.0$  mm to 11.8 mm. The gray lines are the linear fits over the usable bandwidth. In principle, the zero - frequency intercepts of the gray lines represent the insertion losses of the fast and slow waves.

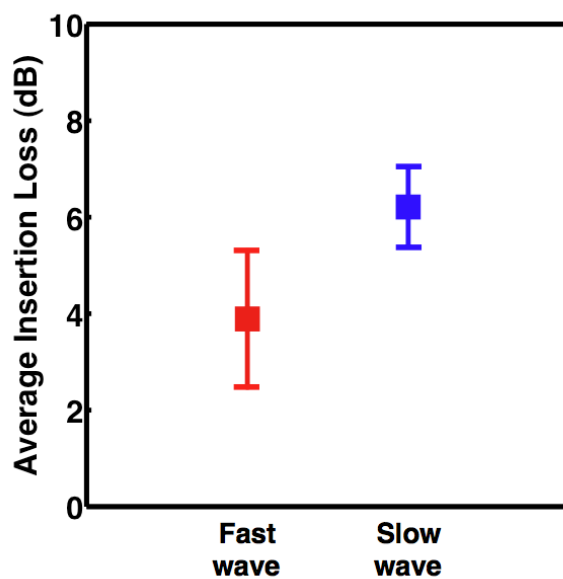


FIGURE 6.9: The average ( $N = 13$ )  $\pm$  one standard deviation insertion loss for the fast and slow waves as determined by the zero-frequency intercepts of the signal loss curves, as shown in Figure 6.8, for sample thicknesses from 6.0 mm to 11.8 mm.

inappropriate for broadband ultrasonic wave propagation. In contrast, the Bayesian methods recovered the individual fast and slow waves permitting the apparent frequencies of the fast and slow waves to be determined using frequency-domain methods. The Bayesian-separated fast and slow waves at each sample length were Fast Fourier Transformed so that the centroid of the linear power spectrum of the fast and slow waves were used to determine the shifted center frequencies. (The centroid or center-of-mass was employed rather than the maximum value because the majority of the spectra were either asymmetric or contained multiple peaks of similar amplitude.)

The experimental spectral shifts in frequency of the fast and slow waves were compared to the spectral shifts predicted by Ophir and Jaeger (1982). When a wideband ultrasonic pulse propagates through a lossy medium whose attenuation coefficient increases with increasing frequency, the higher frequency components will be attenuated more than lower frequency components. This results in a downshift in the center frequency of the received power spectrum. In the case of a linear-with-frequency attenuation coefficient or  $f = 1$  dependence, the spectral shift is given by

$$\Delta f = f_0 - f_c = 2\beta d\sigma^2 \quad (6.1)$$

where  $f_0$  is the center frequency of the reference signal,  $f_c$  is the downshifted center frequency,  $\beta$  is the slope of the attenuation coefficient (nBUA),  $d$  is the propagation distance, and  $\sigma^2$  is the variance of the spectrum of the transmitted pulse. To determine a value for the variance,  $\sigma^2$ , Ophir and Jaeger (1982) state the relationship between the half amplitude bandwidth

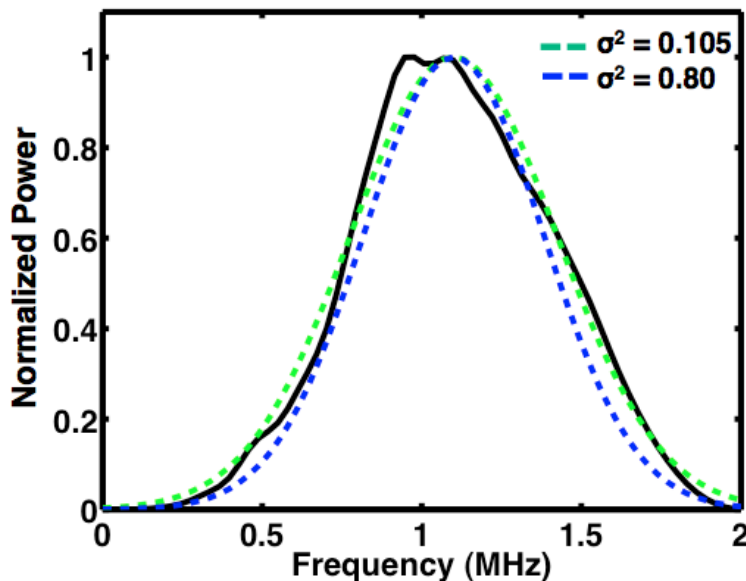


FIGURE 6.10: Fits to the reference power spectrum (black) of Gaussians with  $\sigma^2 = 0.105$   $\text{MHz}^2$  (green) and  $\sigma^2 = 0.08$   $\text{MHz}^2$  (blue).

and the variance of a Gaussian spectrum as

$$\exp \left[ -\frac{(f - f_0)^2}{2\sigma^2} \right] = 1/2. \quad (6.2)$$

Equation 6.2 can be solved for  $f_{l,h}$ , the low and high frequencies for which the amplitude of the spectrum is 1/2, resulting in

$$f_{l,h} = f_0 \pm 1.18\sigma. \quad (6.3)$$

The best Gaussian fit to the reference power spectrum yielded a variance of  $\sigma^2 = 0.105$   $\text{MHz}^2$ . However, it was observed that the experimental spectral shifts of the fast and slow waves were better fit by the predicted spectral shift when  $\sigma^2 = 0.08$   $\text{MHz}^2$ . The Gaussian curves with  $\sigma^2 = 0.105$   $\text{MHz}^2$  and with  $\sigma^2 = 0.08$   $\text{MHz}^2$  along with the reference power spectrum are shown in Figure 6.10. The predicted spectral shifts for the fast and slow waves, shown in Figure 6.11, were determined using Equation 6.1 with  $\sigma^2 = 0.08$   $\text{MHz}^2$ ,  $d$  the sample

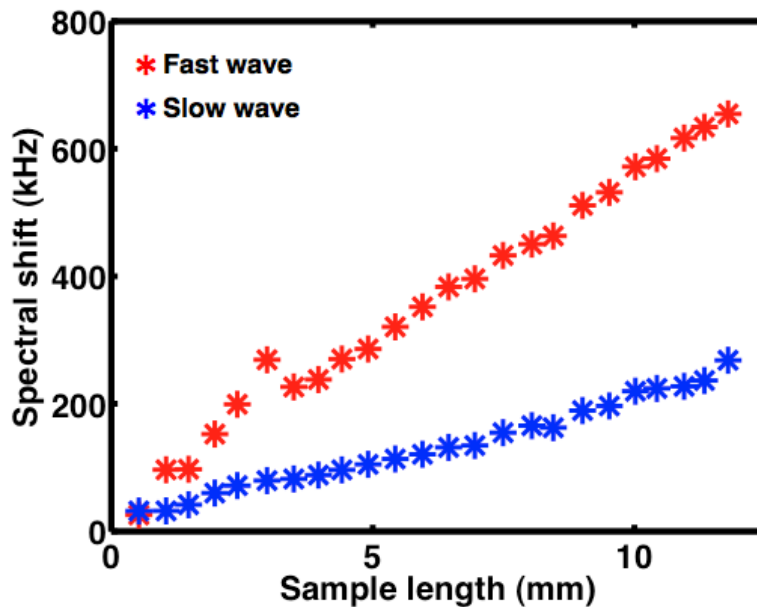


FIGURE 6.11: The downshifts in the center frequency of the fast and slow waves as determined by Equation 6.1.

thickness, and  $\beta$  the Bayesian-derived nBUA.

### Estimation of segmental attenuation

Fujita *et al.* (2013) also reported the apparent attenuation of the fast and slow waves using a segmental approach identical to that employed by Nagatani *et al.*, which was discussed in Chapter 5. This segmental time-domain method for determining the apparent attenuation uses the peak amplitudes of the fast and slow waves for successive sample thickness and defines the attenuation as

$$\alpha_{time} = \frac{20 \log \left( \frac{V_n}{V_{n+1}} \right)}{\Delta d}. \quad (6.4)$$

where  $V_n$  and  $V_{n+1}$  are the amplitudes of the peaks in the received RF waveforms. The indices  $n$  and  $n + 1$  correspond to successive sample thicknesses differing by  $\Delta d = 0.5$  mm.

An analysis similar to that performed in Section 5.4.2, was carried out on the Bayesian-

separated fast and slow waves obtained at each sample thickness. This analysis method is a combination of the conventional analysis detailed above (because it occurs in the frequency-domain) and the Fujita *et al.* (2013) time-domain attenuation analysis (because it compares the loss at successive sample thicknesses). Equation 6.5 gives what will be referred to as the segmental attenuation coefficient

$$\alpha_{seg}(f) = \frac{10 \log \left( \left| \tilde{V}_n(f) \right|^2 \right) - 10 \log \left( \left| \tilde{V}_{n+1}(f) \right|^2 \right)}{\Delta d} \quad (6.5)$$

where  $|\tilde{V}_n(f)|$  and  $|\tilde{V}_{n+1}(f)|$  are the magnitudes of the Fourier transforms of the Bayesian fast or slow waves when the sample has a thickness corresponding to length indices  $n$  and  $n + 1$ , respectively. For the initial analysis  $\Delta d = 0.5$  mm (in subsequent work, values of  $\Delta d$  were systematically increased). Figure 6.12 illustrates the difference between the conventional (bulk) analysis, which uses a water-path-only signal as a reference, and the segmental analysis, which uses a through-sample signal at a different sample thickness as a reference. This segmental method has both advantages and disadvantages. The main advantage is that the insertion losses do not need to be known because the sample signals at two different lengths should have approximately the same insertion losses and thus cancel. Other advantages to the segmental attenuation approach include providing information about local inhomogeneities and potentially being less susceptible to diffraction effects. Some disadvantages include larger fractional errors from any uncertainties in the path lengths ( $\Delta d$ ) as well as very limited clinical utility .

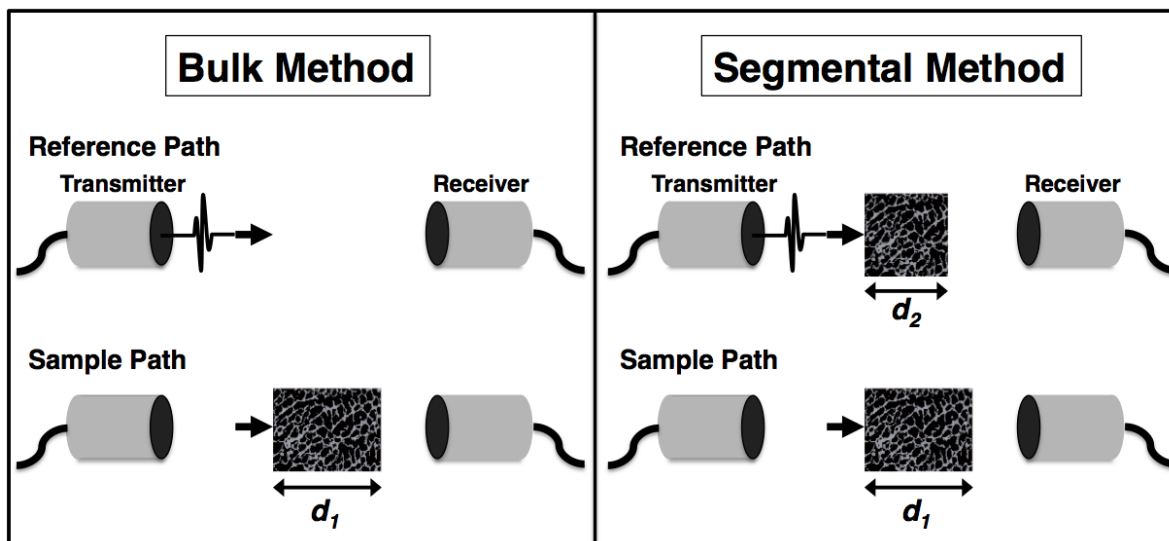


FIGURE 6.12: Left: The bulk attenuation method referred to as conventional analysis in this thesis. In the bulk method the sample trace is compared to a water-path-only reference trace. In this method, the resulting attenuation is the loss in the whole sample of thickness  $d_1$ . Right: The segmental attenuation method, in which the signal at sample thickness  $d_1$  is compared to a signal at a sample thickness of  $d_2$ . In the segmental method, the resulting attenuation is the loss in the sample thickness  $d_1-d_2$ .

## 6.3 Results

### 6.3.1 Results of Bayesian parameter estimation

In order to illustrate the results of Bayesian analysis, the experimental data and the models constructed from Bayesian parameter estimation are shown in Figure 6.13 for four selected sample thicknesses. For a sample thickness of 1.1 mm, only one wave was apparent. For a thickness of 4.0 mm, the fast and slow waves were significantly overlapped. For a sample thickness of 7.0 mm, the fast and slow waves were just barely separated. For a thickness of 11.0 mm, the fast and slow waves were completely separated. The residuals, the difference between the experimental trace and the model trace, are shown in the middle panel of each subplot, and were scaled to be consistent with the overall amplitude of the



experimental signal. Table 6.2 gives the coefficient of variation (CV) of the root-mean-square-deviation (RMSD), given by Equation 4.5, for the Bayesian-constructed model and the data. As is evident in Figure 6.13 and Table 6.2, the Bayesian algorithm provided a better fit to the signals from the thicker samples than the signals obtained from the thinner samples. However, even for the thinner samples, in which the fast and slow waves were significantly overlapped, the Bayesian algorithm still produced model fits that were in good agreement with the data.

The average results of the Bayesian probability analysis for the six model parameters over sample thickness  $d = 3.5$  mm to 11.8 mm are shown in Figures 6.14 - 6.16. Samples shorter than  $d = 3.5$  mm were not included in the averages. As will be seen in later analysis shown in Figures 6.28, 6.30, and 6.34, there was significant variability in the Bayesian estimates of the six model parameters for samples thinner than 3.5 mm.

Figure 6.14 displays the average fast and slow wave phase velocities at 1 MHz determined by Bayesian parameter estimation over 18 sample thickness ( $d = 3.5$  mm to 11.8 mm). The average fast wave velocity, shown in Table 6.3, was  $2409.7 \pm 17.0$  m/s which is consistent with previously reported values. The average slow wave velocity was  $1402.0 \pm 2.7$  m/s. This velocity is lower than the velocity of the 1 MHz ultrasonic signal in water, which was approximately 1489 m/s. The significant difference in velocity between the fast wave and slow wave allowed the two waves to achieve separation in the time-domain even for relatively small sample lengths. This is in contrast to the human heel study detailed in Chapter 4 where the fast and slow wave velocities differed by only 120 m/s on average for similar sample thicknesses.

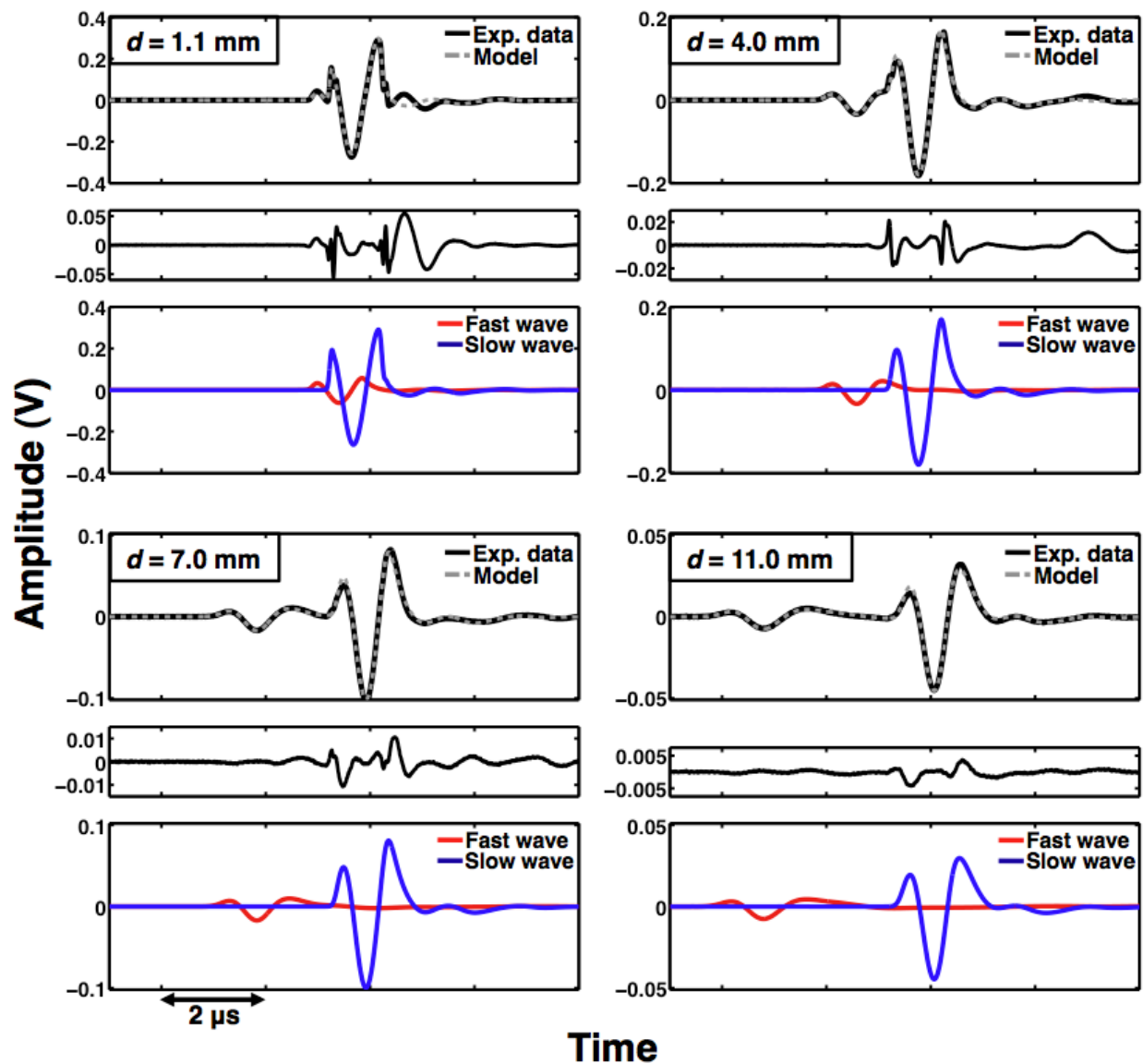


FIGURE 6.13: Model results constructed using the parameters estimated from Bayesian probability theory for four representative thicknesses of the equine sample. For each sample thickness: the top panel shows the experimental data along with the model constructed from the Bayesian estimates, the middle panel shows the residual or difference between the data and model, and the bottom panel shows the individual fast and slow waves that make up the model signal. In each panel, the vertical scale was adjusted to facilitate visualizing the signals.

TABLE 6.2: Goodness-of-fit of the Bayesian-derived model to the experimentally acquired signals. The coefficient of variation (CV) of the root-mean-square-deviation (RMSD), shown in Equation 5.5, was determined to quantify the fit of the model generated by the Bayesian estimated parameters to the experimental data.

Sample thickness (mm)	CV(RMSD) ( %)
11.8	12.7
11.3	17.9
11.0	18.8
10.4	17.6
10.0	16.1
9.5	19.0
9.0	18.0
8.5	22.4
8.0	19.4
7.5	17.4
7.0	21.5
6.5	18.4
6.0	20.6
5.4	22.0
4.9	22.5
4.4	22.6
4.0	24.6
3.5	26.7
3.0	29.1
2.4	37.6
2.0	43.9
1.5	57.9
1.1	54.3
0.5	32.4

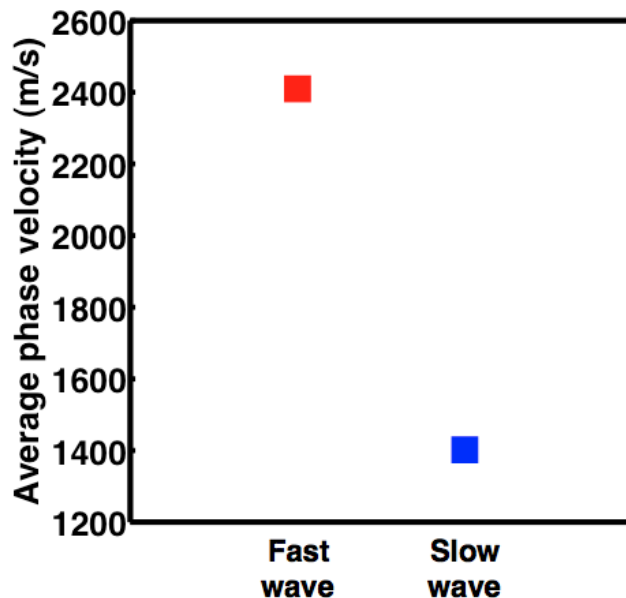


FIGURE 6.14: The average value  $\pm$  one standard deviation over sample lengths  $d = 3.5$  mm to 11.8 mm ( $N = 18$ ) of  $c_{fast}$  and  $c_{slow}$  as estimated by Bayesian methods. The error bars are too small to be seen.

The average fast wave nBUA over 18 sample thicknesses ( $d = 3.5$  mm to 11.8 mm) was  $31.4 \pm 1.4$  dB/cm/MHz and the average slow wave nBUA was  $11.5 \pm 0.6$  dB/cm/MHz, as shown in Figure 6.15 and Table 6.3. It is typically reported that the fast wave has a larger nBUA than the slow wave since it is thought that the fast wave travels mainly through the bony trabeculae, which is more attenuating than the water or marrow filling the porous areas.

The average model parameters  $A_{fast}$  and  $A_{slow}$  over sample thicknesses  $d = 3.5$  mm to 11.8 mm ( $N = 18$ ) are shown in Figure 6.16. The mean values for  $A_{fast}$  and  $A_{slow}$ , in Table 6.3, were  $0.36 \pm 0.04$  and  $0.52 \pm 0.10$ , respectively. A value of  $A = 1$  means that the total input signal is transmitted into and out of the sample with no reflection losses at either boundary. If  $A_{fast}$  and  $A_{slow}$  are purely insertion losses then these results imply that more

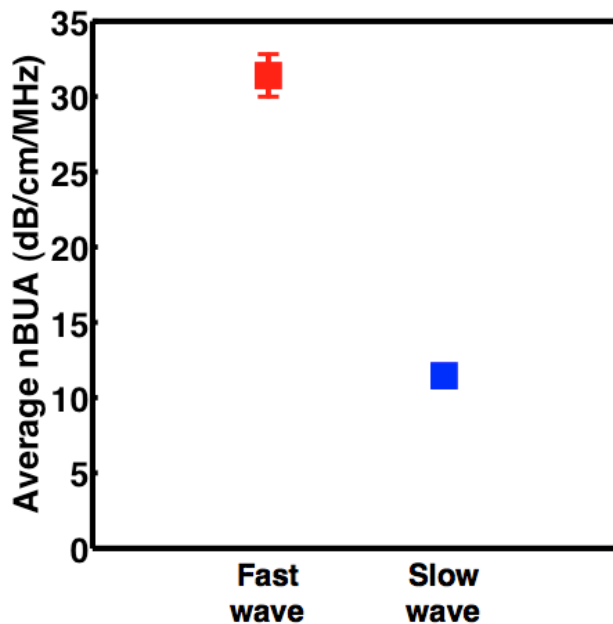


FIGURE 6.15: The average values  $\pm$  one standard deviation over sample lengths  $d = 3.5$  mm to 11.8 mm ( $N = 18$ ) of  $\beta_{fast}$  and  $\beta_{slow}$  as estimated by Bayesian methods. The error bars for the slow wave nBUA are too small to be seen.

signal is transmitted through the boundaries for the slow waves than for the fast waves.

### 6.3.2 Results of conventional analysis

The phase velocities as a function of frequency for the windowed fast waves and slow waves over sample lengths  $d = 6.0$  mm to 11.8 mm ( $N=13$ ) are shown in Figure 6.17. All of the phase velocities exhibited positive dispersion, which implies a good separation of the waves using time gates. If, when time gated, a signal contained parts of both fast and slow waves, then the signal might have displayed negative dispersion when analyzed conventionally. The average fast wave velocity, shown in Table 6.4, was  $2412.2 \pm 11.8$  m/s and the average slow wave velocity was  $1404.8 \pm 1.1$  m/s. These average values for the fast and slow wave phase velocities using conventional phase spectroscopy agreed well with those obtained using the

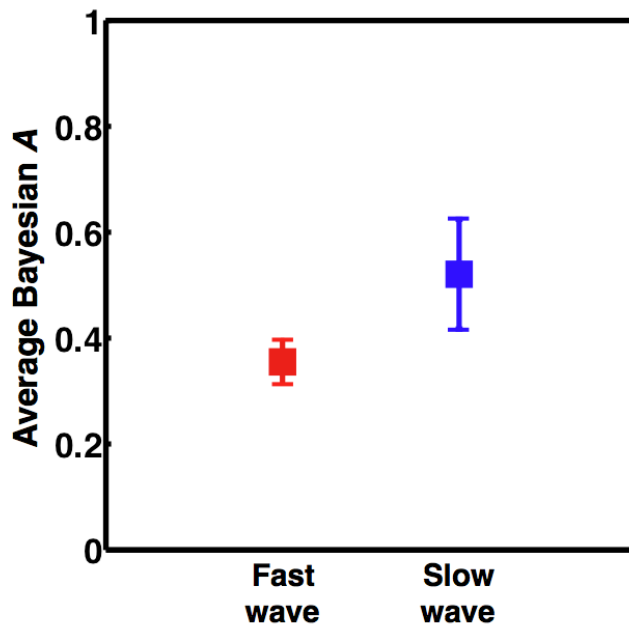


FIGURE 6.16: The average value  $\pm$  one standard deviation over sample lengths  $d = 3.5$  mm to 11.8 mm ( $N = 18$ ) of  $A_{fast}$  and  $A_{slow}$  as estimated by Bayesian methods.

Bayesian analysis method. The average difference in the phase velocity at 1 MHz between conventional and Bayesian methods was  $6.1 \pm 3.8$  m/s for the fast wave and  $1.5 \pm 0.9$  m/s for the slow wave.

The attenuation coefficients of the fast waves and slow waves for sample lengths from  $d = 6.0$  mm to  $d = 11.8$  mm are shown in Figure 6.19. All of the attenuation coefficients showed approximately a linear dependence with frequency over the bandwidth, which is demarcated by the vertical dashed lines in Figure 6.19. The average slopes of the attenuation coefficient (nBUA) over that bandwidth are shown in Figure 6.20 for the fast and slow waves. The average fast wave nBUA, shown in Table 6.4, was  $37.7 \pm 1.4$  dB/cm/MHz and the average slow wave nBUA was  $11.8 \pm 0.6$  dB/cm/MHz. The average value for  $\beta_{slow}$  using conventional methods was in good agreement with that estimated by Bayesian methods, Table 6.3, whereas

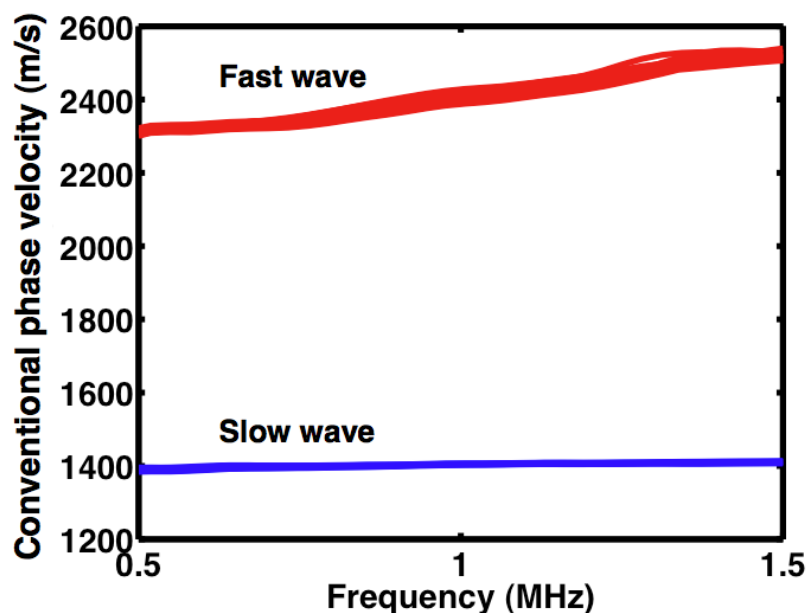


FIGURE 6.17: Phase velocities as a function of frequency for the fast waves (red) and the slow waves (blue) as determined by conventional analysis methods for sample thicknesses  $d = 6.0$  mm to 11.8 mm ( $N = 13$ ).

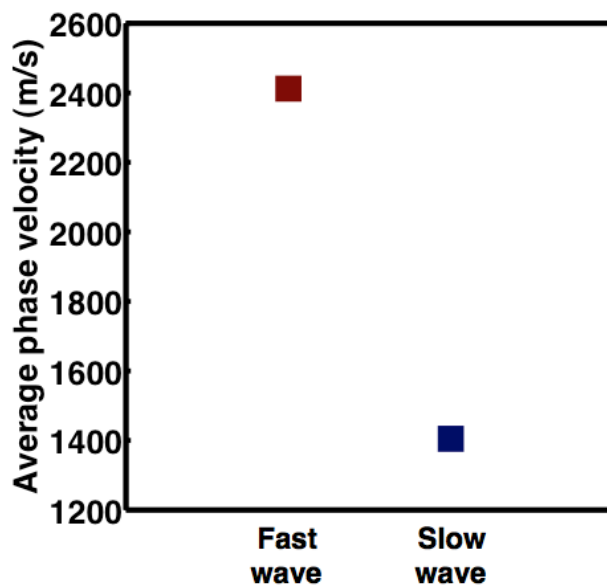


FIGURE 6.18: Average ( $\pm$  one standard deviation) phase velocities at 1 MHz of the fast waves (left) and the slow waves (right) as determined by conventional analysis methods over sample thicknesses  $d = 6.0$  mm to 11.8 mm ( $N = 13$ ). The error bars are too small to be seen on this scale.

TABLE 6.3: The mean and standard deviation of the parameters estimated using the Bayesian algorithm for sample thicknesses from 3.5 mm to 11.8 mm ( $N = 18$ ). The values for sample thicknesses under 3.5 mm were not included due to large variabilities and uncertainties.

Bayesian parameters	Mean value	Standard deviation
$c_{fast}$ (m/s)	2409.7	17.0
$c_{slow}$ (m/s)	1402.0	2.7
$\beta_{fast}$ (dB/cm/MHz)	31.4	1.4
$\beta_{slow}$ (dB/cm/MHz)	11.5	0.6
$A_{fast}$	0.36	0.04
$A_{slow}$	0.52	0.10

the average values for  $\beta_{fast}$  agreed only moderately well.

The parameters  $A_{fast}$  and  $A_{slow}$  for conventional analysis were obtained from the insertion loss (IL) values determined by the zero-frequency intercepts of the signal loss. This conversion assumes that the Bayesian  $A_{fast}$  and  $A_{slow}$  parameters are primarily determined by the losses at the boundaries between the sample and the reference medium,

$$IL[dB] = 20 \log(A). \quad (6.6)$$

The average conventional insertion losses for the fast wave,  $A_{fast}$ , and slow wave,  $A_{slow}$ , are shown in Figure 6.21 for sample lengths  $d = 6.0$  mm to 11.8 mm ( $N=13$ ). The average values for  $A_{fast}$  and  $A_{slow}$  were  $0.65 \pm 0.11$  and  $0.49 \pm 0.05$ , respectively. The results of conventional analysis for  $A_{fast}$  and  $A_{slow}$  exhibited a trend opposite to that seen in the Bayesian estimates. For the conventional analysis,  $A_{fast}$  was larger than  $A_{slow}$ , implying that more of the initial signal is transmitted through both boundaries for the fast wave than for the slow wave.



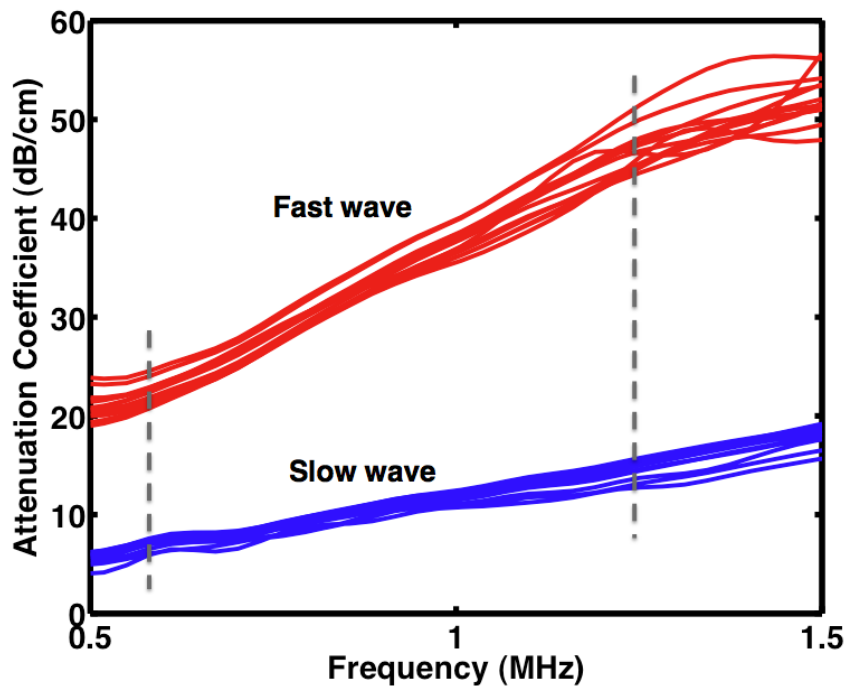


FIGURE 6.19: Attenuation coefficients of the fast waves (red) and slow waves (blue) as determined by conventional analysis. The vertical dashed lines show the low and high frequencies of the bandwidth. The slopes of the linear fit between those dashed lines are the nBUA values for the fast and slow waves.

### 6.3.3 Results of apparent frequency

The apparent frequency of the fast and slow waves as determined by the centroids of the Bayesian-separated fast and slow waves are shown as a function of sample length in Figure 6.22. The fast waves exhibited a rapid downshift in center frequency from the original center frequency of  $f_0 = 1$  MHz with longer sample lengths. At the longest sample length ( $d = 11.8$  mm), the downshifted center frequency of the fast wave was 507 kHz, which is approximately half the center frequency of the reference signal. The slow waves also displayed a downshifted center frequency, although not as significant as the fast wave. At the longest sample thickness, the center frequency of the slow wave was approximately 814 kHz.

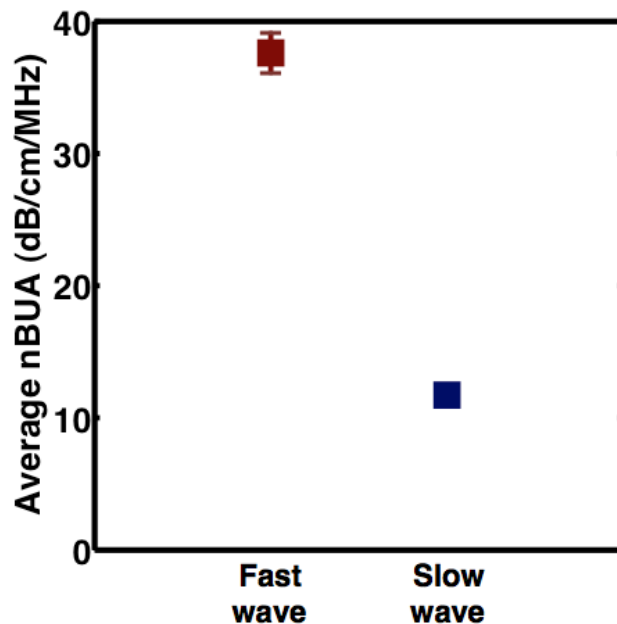


FIGURE 6.20: Average ( $\pm$  one standard deviation) slopes of the attenuation coefficients (nBUA) of the fast waves (left) and slow waves (right) as determined using conventional analysis methods over sample thicknesses  $d = 6.0$  mm to 11.8 mm ( $N = 13$ ).

In Figure 6.23, the results of the (frequency-domain) centroid frequencies were compared to both the (time-domain) apparent frequencies reported by Fujita *et al.* (2013) and the predicted center frequencies,  $f_c$  determined by Equation 6.1 along with the spectral shifts shown in Figure 6.11. The downshifted center frequencies determined by the centroid agree very well with the predicted frequencies calculated using Equation 6.1. There was even good agreement between the two experimentally determined apparent frequencies, even though one was done in the frequency-domain and one was done in the time-domain. This good agreement may imply that for specific parameters, time-domain methods may produce reasonably accurate estimates and could be beneficial in clinical settings where time constraints prohibit more involved frequency-domain methods. It should also be noted that the results from Fujita *et al.* (2013) may not be from the same sample as that studied in this chapter.

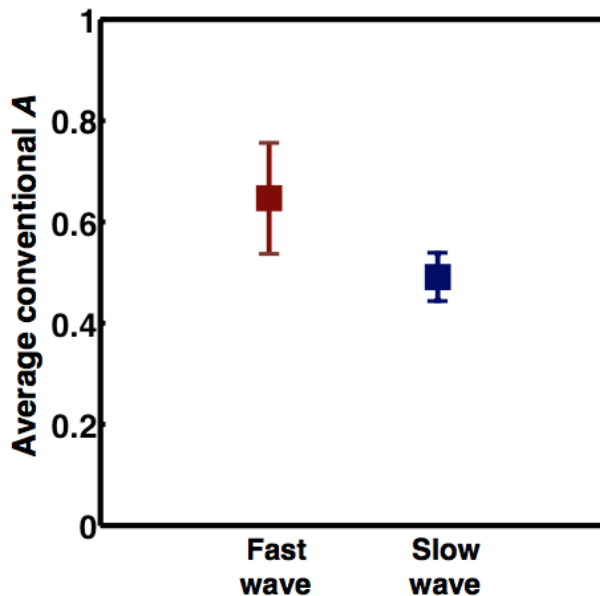


FIGURE 6.21: Average values of  $A_{fast}$  and  $A_{slow}$  determined using conventional methods over sample thickness  $d = 6.0$  mm to 11.8 mm ( $N = 13$ ).  $A_{fast}$  and  $A_{slow}$  were determined using the insertion loss values shown in Figure 6.9.

### 6.3.4 Results of segmental attenuation

The segmental attenuation coefficients at 1 MHz of the fast and slow waves are shown in Figure 6.24 and Figure 6.25, respectively, along with the time-domain attenuation results reported in Fujita *et al.* (2013). For both the fast and slow waves, the segmental attenuation varied dramatically with sample length position. These segmental attenuation coefficients are the losses occurring within a piece of the sample that is only 0.5 mm thick. These large variations in the segmental attenuation might be due to actual inhomogeneities in the bone sample but may be artifacts caused by uncertainties in the sample lengths. Estimating attenuation in very thin samples is also quite challenging. The average segmental attenuation coefficient at 1 MHz for the fast wave was  $28.8 \pm 10.8$  dB/cm for the frequency-domain method (over  $N = 23$  sample segments) and was  $26.7 \pm 11.0$  dB/cm for the time-domain

TABLE 6.4: The mean and standard deviation of the parameters determined using conventional analysis methods for sample thicknesses from 6.0 mm to 11.8 mm.

Conventional parameters	Mean value	Standard deviation
$c_{fast}(1 \text{ MHz})(\text{m/s})$	2412.2	11.8
$c_{slow}(1 \text{ MHz})(\text{m/s})$	1404.8	1.1
$\beta_{fast}(\text{dB/cm/MHz})$	37.7	1.4
$\beta_{slow}(\text{dB/cm/MHz})$	11.8	0.6
$A_{fast}$	0.65	0.11
$A_{slow}$	0.49	0.05

method (over  $N = 13$  sample segments). The average segmental attenuation coefficient at 1 MHz for the slow wave was  $19.0 \pm 8.3$  dB/cm for the frequency-domain method and was  $28.8 \pm 12.6$  dB/cm for the time-domain method as shown in Figure 6.25.

The segmental attenuation coefficients were also determined for combinations of  $\Delta d = 2$  mm, 4 mm, 6 mm, 8 mm, 10 mm, and 11 mm. The  $\Delta d = 11$  mm segmental attenuation coefficients compared the longest and the shortest sample lengths. Figure 6.26 shows the segmental attenuation coefficient at 1 MHz for the combinations of  $\Delta d$  values listed above. For both the fast and slow waves, the segmental attenuation coefficients were more consistent for larger values of  $\Delta d$ . In spite of this, the average within any one  $\Delta d$  produced a value for the attenuation coefficient that was in good agreement with the segmental attenuation coefficient averaged over all  $\Delta ds$ . This was also true for the slope of the segmental attenuation coefficient (segmental nBUA), shown in Figure 6.27.

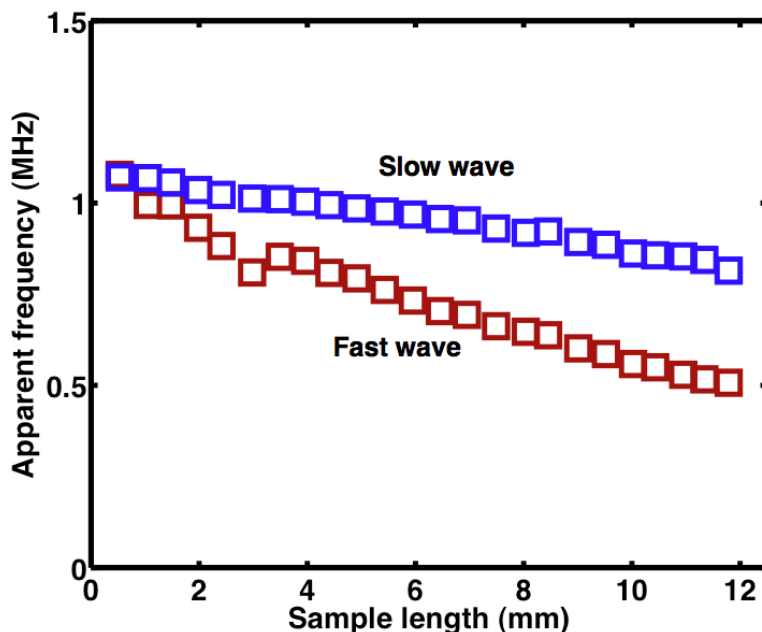


FIGURE 6.22: The shifting center frequencies of the fast and slow waves as a function of sample length. The center frequencies were determined by calculating the centroid of the Bayesian-separated fast and slow waves.

### 6.3.5 Trends with sample thickness

Results presented thus far indicate reasonable consistency among several methods of data analysis, including substantial agreement between Bayesian-derived results and those obtained over the more limited range for which conventional analysis can be applied. Even though trabecular bone is not a homogenous material, it was anticipated that each of the six model parameters ( $c_{fast}$ ,  $c_{slow}$ ,  $\beta_{fast}$ ,  $c_{slow}$ ,  $A_{fast}$ ,  $A_{fast}$ ) would be consistent over all sample lengths, that is distance-independent. Furthermore, this trabecular bone specimen had a relatively consistent bone volume fraction throughout the sample, as is shown in Table 6.5.

Results showed Bayesian methods permitted reliable measurements down to sample lengths as small as 3.5 mm whereas conventional analysis methods could not be used for

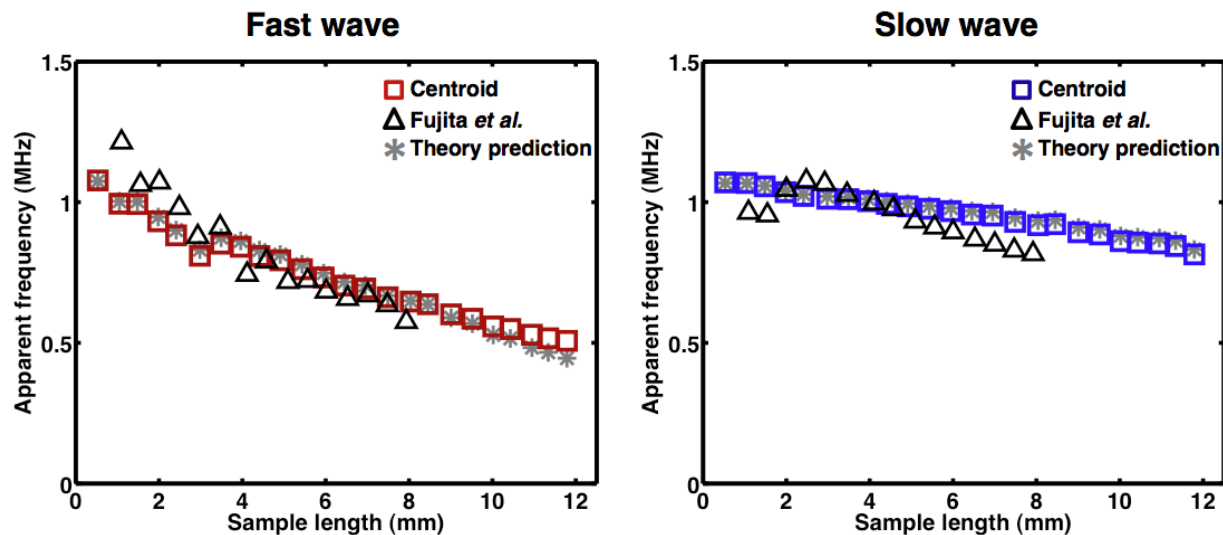


FIGURE 6.23: Comparison of the apparent frequencies of the fast waves and the slow waves using three different methods. The squares show the shifting center frequencies of the two waves using the (frequency-domain) centroid of the Bayesian-separated fast and slow waves. The black triangles are results presented in Fujita *et al.* using time intervals. The gray stars represent the predicted center frequency determined using Equation 6.1.

lengths less than 6.0 mm. However, even Bayesian methods produced somewhat variable results for sample lengths less than 3.5 mm, as will be seen in Figures 6.28, 6.30, and 6.34.

Shorter sample lengths present obvious challenges. At shorter lengths there is less actual sample being interrogated by the ultrasonic signal. It was shown in Chapter 4 that the Bayesian algorithm was able to determine, with quite good reproducibility, estimates of the six model parameters for almost completely overlapped fast and slow waves, so presumably the Bayesian approach was not responsible for the observed variability at very short sample lengths. Another potential explanation is the presence of higher frequency components in the original water-only reference signal. As is evident in Figure 6.6, for the received signals at sample thickness under  $d = 3.5$  mm, these high frequency components are still prominent, perhaps causing the Bayesian algorithm difficulty in fitting the data. Due to the variability

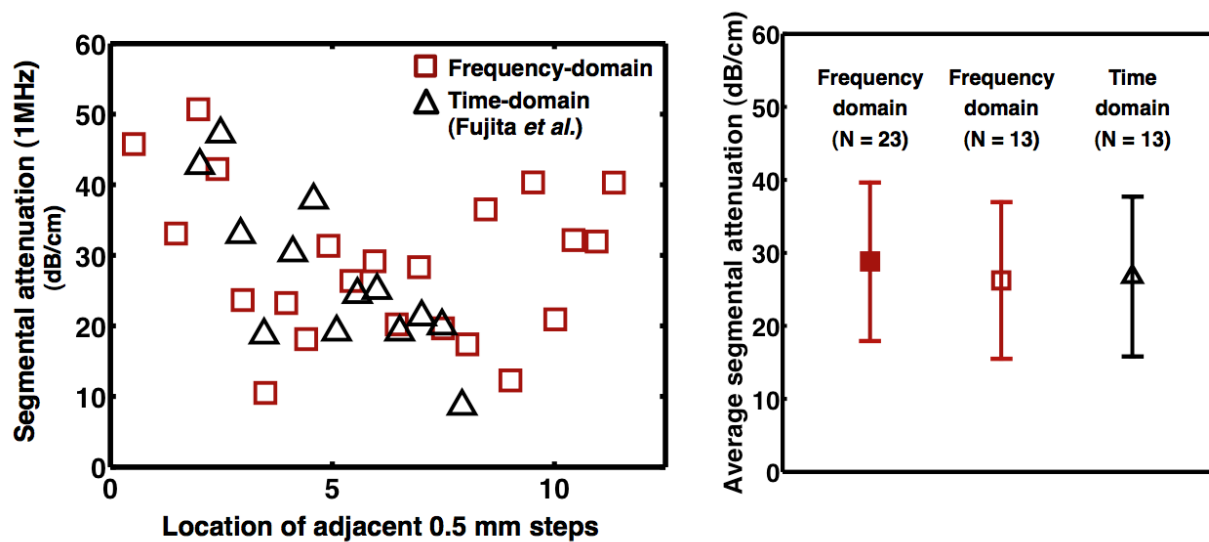


FIGURE 6.24: Left: Segmental attenuation coefficients of the fast waves at each adjacent 0.5 mm step. The attenuation coefficients shown are for  $\Delta d = 0.5$  mm. The squares represent the segmental attenuation coefficient using the frequency-domain method from Equation 6.5. The triangles show the results from Fujita *et al.* (2013), which determined segmental attenuation coefficients using time-domain methods in Equation 6.4. Right: Average values of the segmental attenuation coefficients of the fast waves for the time-domain method (open triangle) and the frequency-domain method over all sample lengths ( $N = 23$ ) (solid square) and over similar lengths used in the time domain method ( $N = 13$ ) (open square).

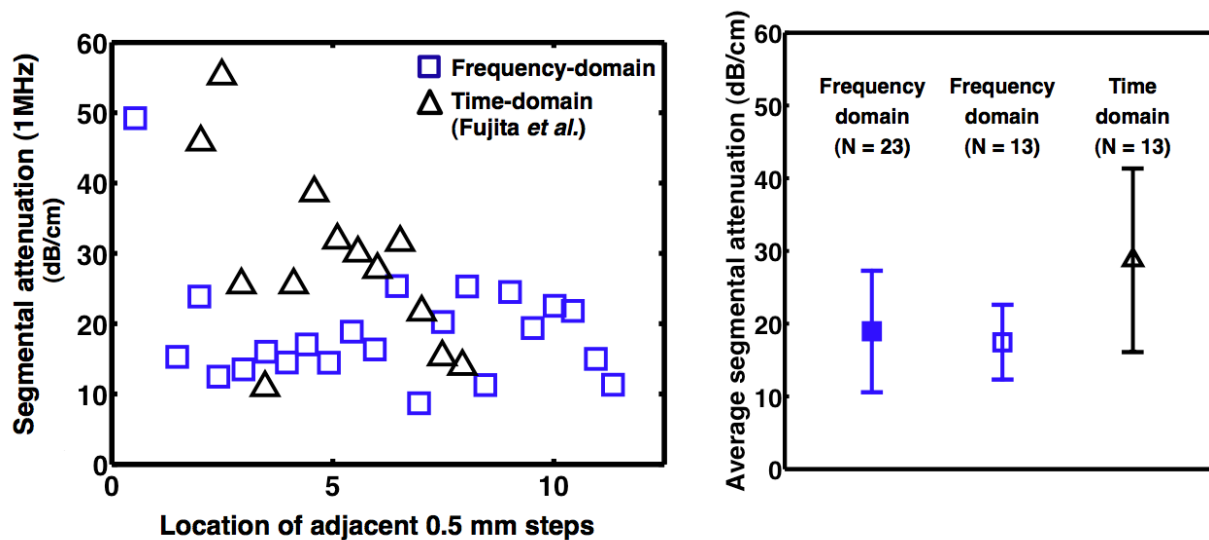


FIGURE 6.25: Left: Segmental attenuation coefficients of the slow waves at each adjacent 0.5 mm step. The attenuation coefficients shown are for  $\Delta d = 0.5$  mm. The squares represent the segmental attenuation coefficient using the frequency-domain method from Equation 6.5. The triangles show the results from Fujita *et al.* (2013), which determined segmental attenuation coefficients using time-domain methods in Equation 6.4. Right: Average values of the segmental attenuation coefficients of the slow waves for the time-domain method (open triangle) and the frequency-domain method over all sample lengths ( $N = 23$ ) (solid square) and over similar lengths used in the time domain method ( $N = 13$ ) (open square).

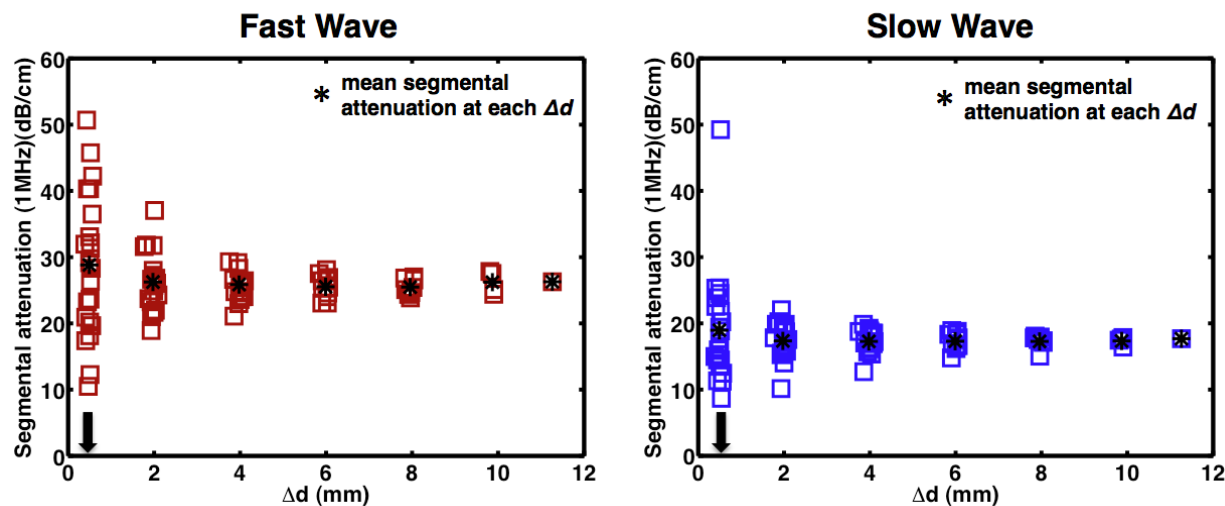


FIGURE 6.26: Segmental attenuation coefficients at 1 MHz of the fast waves (left) and slow waves (right) for  $\Delta d = 0.5$  mm, 2 mm, 4 mm, 6 mm, 8 mm, 10 mm, and 11 mm. The black stars show the mean attenuation coefficient at 1 MHz for each value of  $\Delta d$ . As the thickness,  $\Delta d$ , of the segment increases, the estimate of the attenuation coefficient appears to improve.



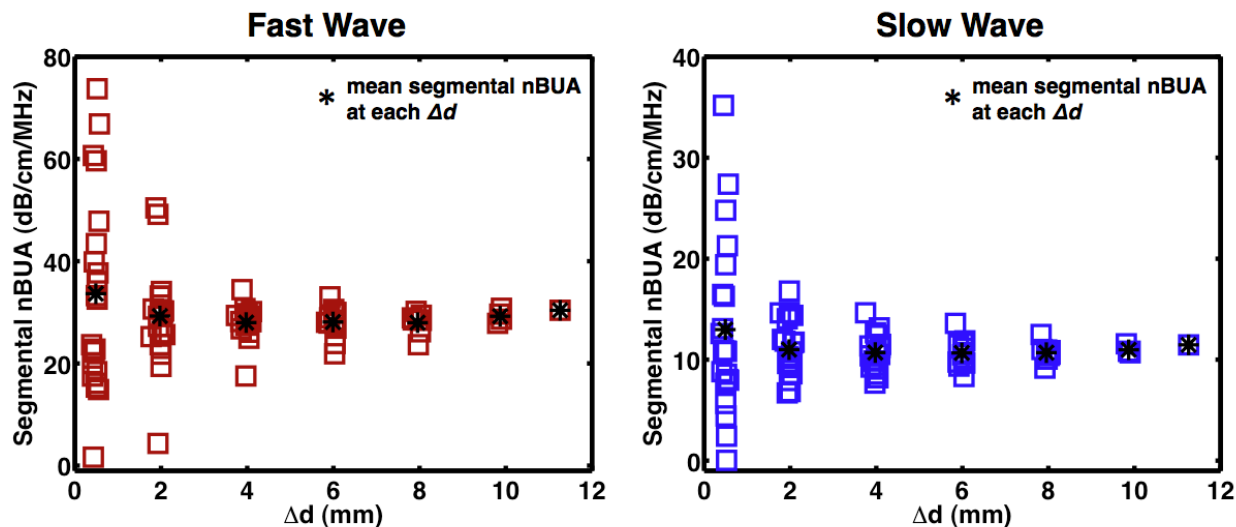


FIGURE 6.27: Segmental slopes of the attenuation coefficient (nBUA) of the fast waves (left) and slow waves (right) for  $\Delta d = 0.5$  mm, 2 mm, 4 mm, 6 mm, 8 mm, 10 mm, and 11 mm. The black stars show the mean nBUA for each value of  $\Delta d$ . As the thickness,  $\Delta d$ , of the segment increases, the estimate of the nBUA appears to improve. Note the change in scale for the slow wave nBUA.

in the results for sample lengths under 3.5 mm, only the results for sample lengths greater than that were included in the results presented in Figures 6.14, 6.15, and 6.16.

In addition to the variability observed for sample thicknesses less than 3.5 mm, an unanticipated systematic variation with sample length was also observed. Figure 6.28 displays the fast and slow wave phase velocities at 1 MHz determined by Bayesian parameter estimation for each sample thickness, from  $d = 0.5$  mm to 11.8 mm. The fast wave velocities appeared to show a systematic dependence on sample thickness. The fast wave velocities increased slightly, changing by approximately 6.1 m/s/mm over sample lengths  $d = 3.5$  mm to 11.8 mm. In contrast, the slow wave phase velocities exhibited a more constant behavior, increasing by only 0.82 m/s/mm over the same range of sample lengths. The phase velocity results as a function of sample thickness from  $d = 6.0$  mm to 11.8 mm for both conventional analysis

TABLE 6.5: Bone volume fraction (BV/TV) for various positions in the trabecular bone specimen. Position 1- 3 mm was located at the distal end of the specimen, which is where the ultrasonic signal entered. Position 9 - 11 mm was at the proximal end of the specimen, from which the sample was shortened.

Position	1-3 mm	3-5 mm	5-7 mm	7-9 mm	9-11 mm
BV/TV	39.4%	38.9%	37.7%	37.5%	37.3%

and Bayesian analysis are shown in Figure 6.29. The fast wave phase velocities obtained by conventional analysis also increased with sample length, and the slow wave phase velocities also stayed relatively constant. Thus, the Bayesian method of analysis and conventional method of analysis agree very well in both the values of the phase velocities and the small, but systematic trends with sample length.

Figure 6.30 shows the results of Bayesian estimation for  $A_{fast}$  and  $A_{slow}$  as a function of all sample lengths ( $d = 0.5$  mm to 11.8 mm). It is clear that  $A_{fast}$  and  $A_{slow}$  both exhibited systematic dependencies on sample thickness. In contrast to the phase velocities,  $A_{slow}$  showed significantly more dependence on sample length than  $A_{fast}$ . As discussed in Section 3.5, in principle  $A_{fast}$  and  $A_{slow}$  account for insertion losses and the distribution of energy between the fast and slow wave modes. In view of the unexpected sample length dependencies,  $A_{fast}$  and  $A_{slow}$  might also be sensitive to potential diffraction (Xu and Kaufman, 1993; Kaufman *et al.*, 1995) and phase cancellation effects (Bauer *et al.*, 2008, 2009). As a function of sample length,  $A_{fast}$  increased by approximately 0.01 per mm of sample while  $A_{slow}$  decreased by 0.04 per mm of sample. At  $d = 3.5$  mm,  $A_{fast}$  equaled 0.29 and

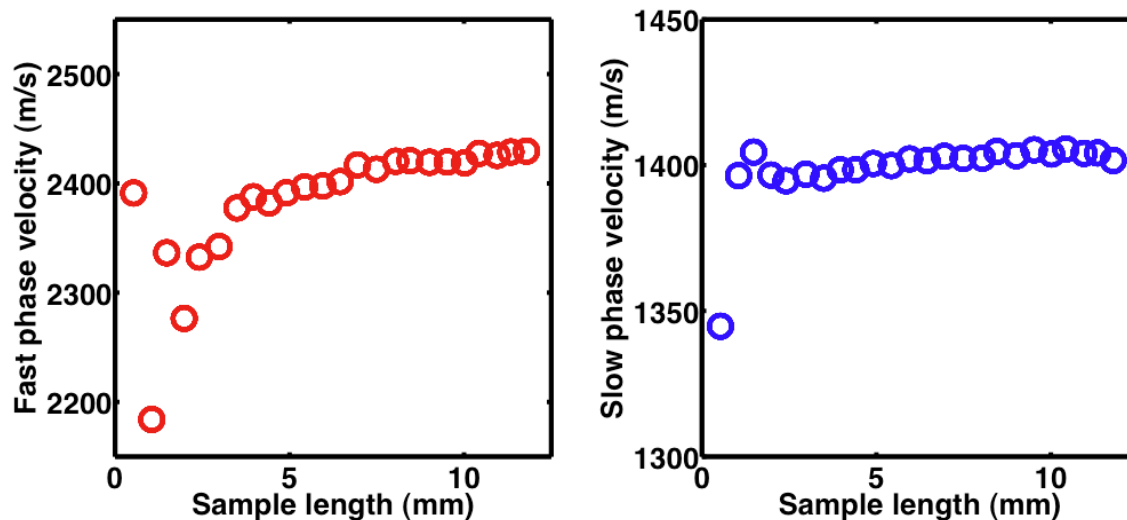


FIGURE 6.28: Bayesian estimation of the fast wave (right) and slow wave (left) phase velocities at 1 MHz as a function of sample thickness over all sample lengths,  $d = 0.5$  mm to 11.8 mm ( $N = 24$ ).

at  $d = 11.8$  mm,  $A_{fast}$  equaled 0.39, corresponding to an absolute change of 2.57 dB. For the slow wave, at  $d = 3.5$  mm,  $A_{slow}$  equaled 0.71 and at  $d = 11.8$  mm,  $A_{slow}$  equaled 0.46, corresponding to an absolute change of 3.77 dB.

Values for  $A_{fast}$  and  $A_{slow}$  using conventional analysis were determined from Equation 6.6 along with the insertion loss values at each sample length, which are shown in Figure 6.31.  $A_{fast}$  determined from conventional analysis showed a strong sample length dependence, increasing by 0.05 per mm of sample.  $A_{slow}$  determined from conventional analysis also displayed a sample length dependence, although it was not as large as that in  $A_{fast}$ , decreasing by 0.02 per mm of sample. At  $d = 6.0$  mm,  $A_{fast}$  equaled 0.55 and at  $d = 11.8$  mm,  $A_{fast}$  equaled 0.87, corresponding to an absolute change of 3.98 dB. For the slow wave, at  $d = 6.0$  mm,  $A_{slow}$  equaled 0.54 and at  $d = 11.8$  mm,  $A_{slow}$  equaled 0.45, corresponding to an absolute change of 1.58 dB. Comparisons of the results for  $A_{fast}$  and  $A_{slow}$  between conventional and

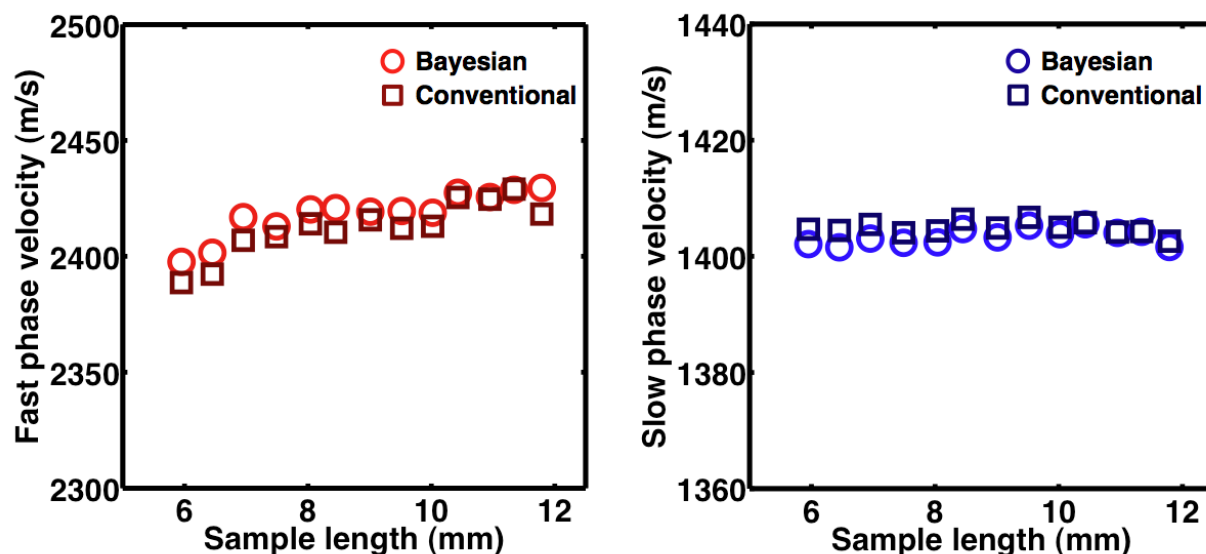


FIGURE 6.29: Comparison of the phase velocities at 1 MHz obtained by conventional (phase-spectroscopy) methods (squares) and by Bayesian probability methods (circles) for the fast wave (left) and the slow wave (right) at sample thicknesses  $d = 6.0$  mm to 11.8 mm ( $N = 13$ ).

Bayesian analysis techniques are shown in Figure 6.32. Bayesian and conventional analysis results of  $A_{slow}$  agreed remarkably well, with both methods displaying the fact that  $A_{slow}$  has a systematic dependence with sample length. For  $A_{fast}$ , the two methods did not agree as well but did show the same trend with sample length. Conventional analysis produced  $A_{fast}$  values that were more strongly dependent on sample length than those estimated by Bayesian methodology.

Another parameter of interest was the relative amplitude ratio of the fast and slow waves, or  $A_{fast}/A_{slow}$ . In Figure 6.33, the ratio of  $A_{fast}$  to  $A_{slow}$  for both Bayesian and conventional analysis is plotted against sample length for  $d = 6.0$  mm to 11.8 mm. The dependence on sample thickness was very evident for  $A_{fast}/A_{slow}$  using either method of analysis. The ratio  $A_{fast}/A_{slow}$  determined by Bayesian methods increased by 0.07 per mm, whereas the

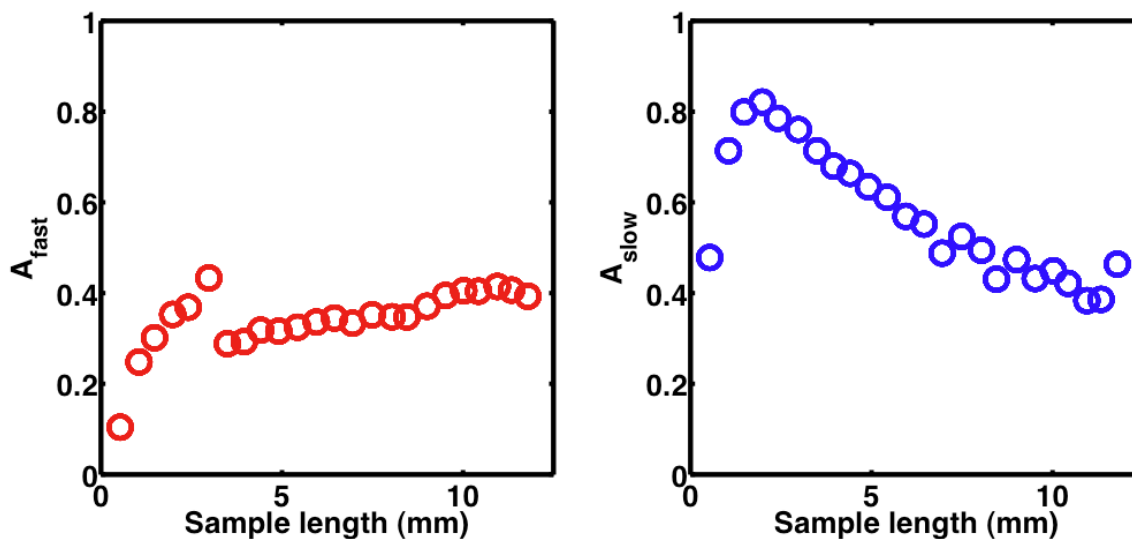


FIGURE 6.30: Bayesian estimation of  $A_{fast}$  and  $A_{slow}$  as a function of sample thickness, ranging from  $d = 0.5$  mm to 3.5 mm ( $N = 24$ ).

conventionally-determined  $A_{fast}/A_{slow}$  increased by 0.15 per mm.

Figure 6.34 shows the results of Bayesian estimation for  $\beta_{fast}$  and  $\beta_{slow}$  as a function of sample length, for  $d = 0.5$  mm to 11.8 mm. The normalized broadband ultrasound attenuation (nBUA) for the fast and slow waves displayed some sample-length dependence, even though these parameters were expected to be distance-independent. For sample lengths from 3.5 mm to 11.8 mm, the fast wave nBUA values decreased by 0.42 dB/cm/MHz per mm of sample whereas the slow wave nBUA values decreased by only 0.04 dB/cm/MHz per mm of sample.

Figure 6.35 shows the comparison of the slopes of the attenuation coefficients (nBUA) among three analysis methods: conventional, Bayesian, and segmental. The segmental slope of attenuation shown in the figure was obtained by taking the average of the mean nBUA values at each  $\Delta d$  from Figure 6.27. The mean segmental nBUA agreed well with the

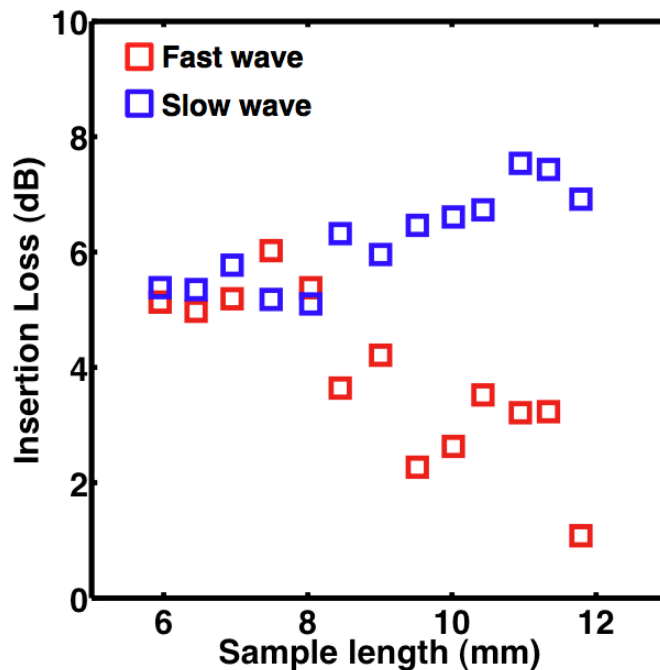


FIGURE 6.31: Insertion losses for the fast and slow waves as determined by the zero-frequency intercepts of the signal loss using conventional analysis methods, for sample thicknesses from 6.0 mm to 11.8 mm ( $N = 13$ ).

Bayesian estimated nBUA for both fast and slow waves. This would be expected because the segmental analysis was performed on the Bayesian-derived fast and slow waves. For the slow wave, the conventional nBUA agreed with the Bayesian and segmental nBUA values. Both conventional and Bayesian analyses produced slow wave nBUA values that increased with increasing sample length. The opposite trend was observed for the fast wave nBUA. Conventional and Bayesian analyses produced fast waves nBUA values that decreased with increasing sample length, although the conventional values were on average  $6.8 \pm 1.2$  dB/cm/MHz larger than the Bayesian values. The reason for this difference between the Bayesian and conventional fast wave nBUA values is unclear. However, if the effects of both the frequency-independent losses ( $A_{fast}$  and  $A_{slow}$ ) and the frequency-dependent losses ( $\beta_{fast}$

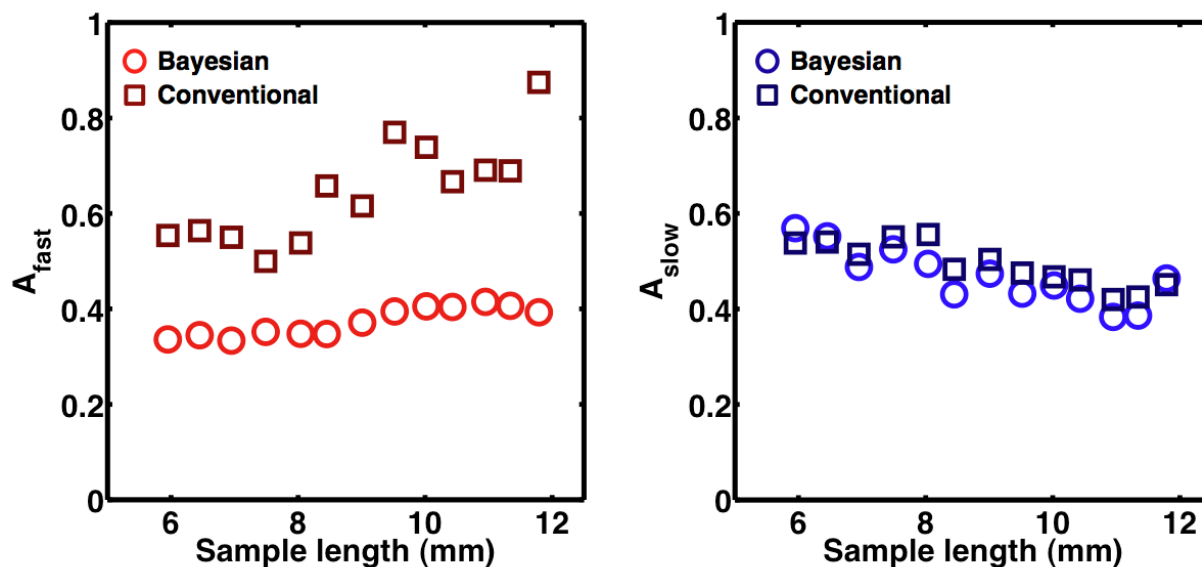


FIGURE 6.32: Comparison of the  $A_{fast}$  and  $A_{slow}$  obtained by conventional methods (squares) and by Bayesian probability methods (circles) at sample lengths ranging from  $d = 6.0$  mm to 11.8 mm ( $N = 13$ ).

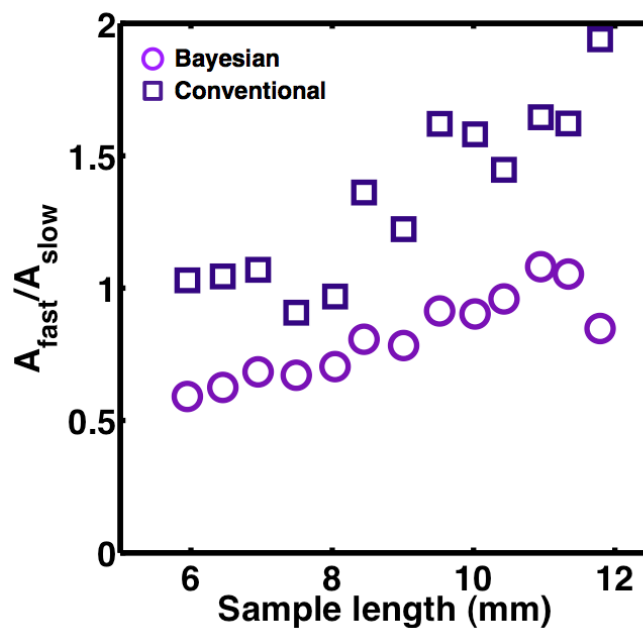


FIGURE 6.33: The ratio of  $A_{fast}$  to  $A_{slow}$  as a function of sample thickness ( $d = 6.0$  mm to 11.8 mm) for both Bayesian (circles) and conventional (squares) analysis.

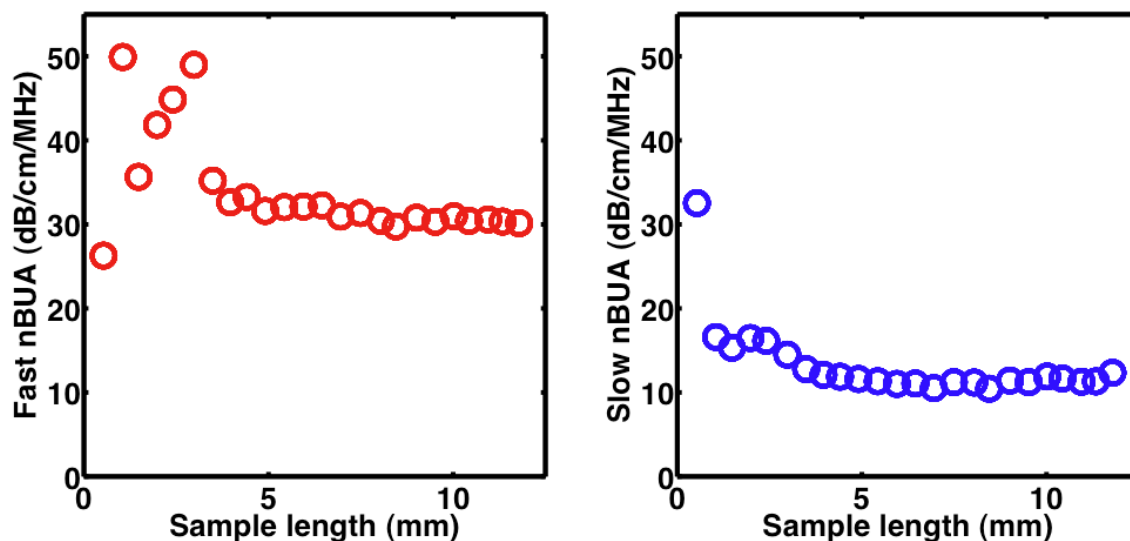


FIGURE 6.34: Bayesian estimation of the fast wave (right) and slow wave (left) normalized broadband ultrasound attenuation (nBUA) as a function of sample thickness.

and  $\beta_{slow}$ ) are taken into account by considering

$$A \exp[-\beta f_0 d] \quad (6.7)$$

for both the fast and slow waves, it appears that the two analysis methods are relatively consistent with each other, as shown in Figure 6.36. In Equation 6.7 and for Figure 6.36,  $f_0$  was set to 1 MHz. Based on these results, it is apparent that there is a trade-off between the  $A$  terms, where  $A = 1$  means no loss, and the  $\beta$  terms when accounting for the total loss. Although the  $\beta_{fast}$  obtained conventionally was larger than that obtained with Bayesian analysis, the conventionally-obtained  $A_{fast}$  was also larger than the Bayesian-derived  $A_{fast}$ , thus producing an overall loss similar to that found with Bayesian methods.



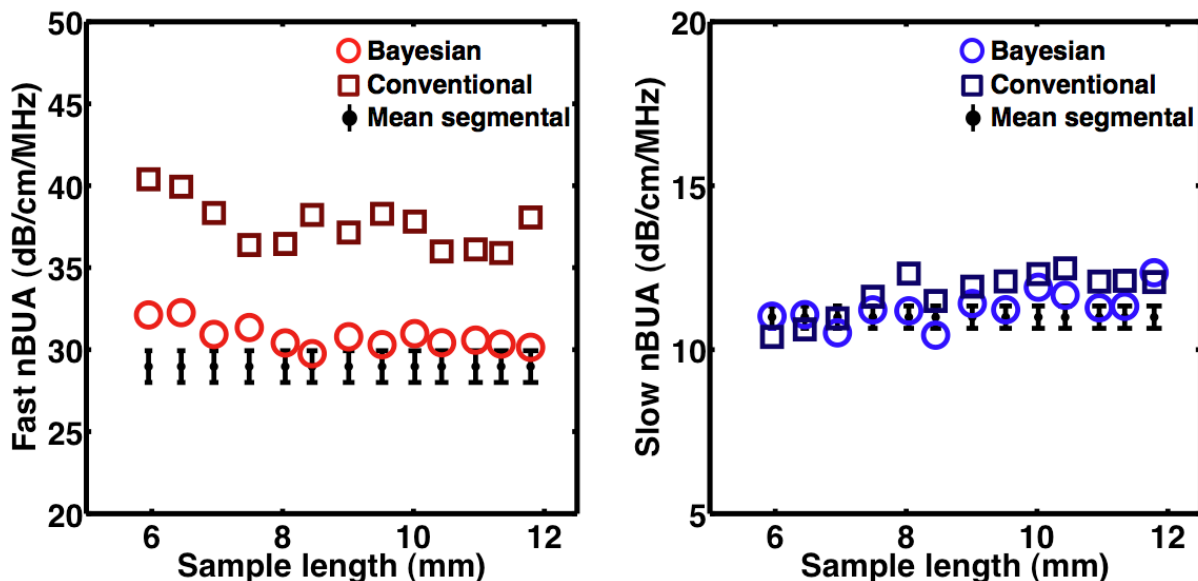


FIGURE 6.35: Comparison of  $\beta_{fast}$  (right) and  $\beta_{slow}$  (left) obtained by using three techniques: (1) conventional method (squares), (2) Bayesian probability method (circles), and (3) segmental (frequency-domain) method (solid dots) at sample thickness ranging from  $d = 6.0$  mm to 11.8 mm. The segmental fast and slow nBUA values shown here are the mean ( $\pm$  one standard deviation) segmental nBUA over all values of  $\Delta d$  as shown in Figure 6.27.

## 6.4 Discussion and Conclusions

It was shown in Chapter 5 that frequency-domain analysis of broadband data provides an effective method for the determination of the attenuation and phase velocity of trabecular bone. However, in many experimental situations with cancellous bone, the conventional (frequency-domain) analysis methods also cannot be employed due to the strong overlap of fast and slow waves. In the study presented in this chapter, conventional analysis could not be used for sample lengths under 6.0 mm. In contrast, Bayesian probability methods were able to estimate the fast and slow waves ultrasonic parameters for all sample lengths. For sample lengths that were sufficiently long as to permit both conventional and Bayesian analysis, both techniques yielded comparable values.

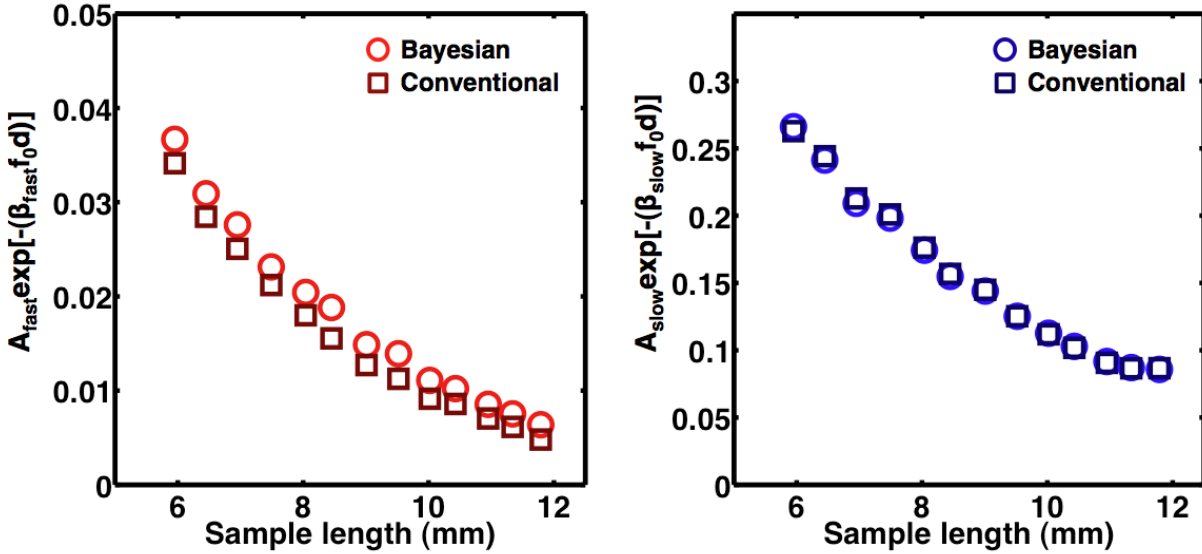


FIGURE 6.36: The prefactor of the received amplitude (at 1 MHz) of the fast waves (left) and slow waves (right) as determined by conventional (squares) and Bayesian (circles) analysis methods. The prefactor of received amplitude at 1 MHz is determined by Equation 6.7.

In a homogeneous medium, all six ultrasonic parameters ( $c_{fast}$ ,  $c_{slow}$ ,  $\beta_{fast}$ ,  $\beta_{slow}$ ,  $A_{fast}$ ,  $A_{slow}$ ) should be constant with sample thickness because they are intrinsic properties of the material. Although some variation is to be expected because trabecular bone is heterogeneous, relatively small, systematic changes with sample length were observed. Possible contributions for the systematic dependences on sample length include diffraction effects, phase cancellation at the face of the finite aperture phase-sensitive receiving transducer, and other experimental factors not included in the Bayesian analysis model.

Even though the ultrasonic parameters displayed a modest sample length dependence, these variations are not likely to influence clinical applications. Compared to the site-to-site variations in phase velocity and nBUA observed in the human heel measurements of Chapter 4, the relatively small, systematic variation with sample thickness is not likely to be clinically significant.

## **6.5 Acknowledgments**

The equine bone data analyzed in this Chapter were acquired in the laboratory of Professor Mami Matsukawa at Doshisha University in Kyoto, Japan. We are grateful to Professor Matsukawa and her colleagues for providing us this excellent data set.

## Bibliography

- Bauer, A. Q., Anderson, C. C., Holland, M. R., and Miller, J. G. (2009), “Bone sonometry: Reducing phase aberration to improve estimates of broadband ultrasonic attenuation”, *J Acoust Soc Am* **125(1)**, 522–529.
- Bauer, A. Q., Marutyan, K. R., Holland, M. R., and Miller, J. G. (2008), “Negative dispersion in bone: The role of interference in measurements of the apparent phase velocity of two temporally overlapping signals”, *J Acoust Soc Am* **123(4)**, 2407–2414.
- Fujita, F., Mizuno, K., and Matsukawa, M. (2013), “An experimental study on the ultrasonic wave propagation in cancellous bone: Waveform changes during propagation”, *J Acoust Soc Am* **134(6)**, 4775–4781.
- Kaufman, J., Xu, W., Chiabrera, A., and Siffert, R. (1995), “Diffraction effects in insertion mode estimation of ultrasonic group velocity”, *IEEE Trans Ultrason Ferroelectr Freq Control* **42(2)**, 232–242.
- Ophir, J. and Jaeger, P. (1982), “Spectral shifts of ultrasonic propagation through media with nonlinear dispersive attenuation”, *Ultrasonic Imaging* **4**, 282–289.
- Xu, W. and Kaufman, J. (1993), “Diffraction correction methods for insertion ultrasound attenuation estimation”, *IEEE Trans Biomed Eng* **40(6)**, 563–570.

# CHAPTER 7

---

## EXPLORING UNEXPECTED SAMPLE THICKNESS-DEPENDENCE USING PLASTIC PHANTOMS

### 7.1 Preface

This chapter outlines the work completed in an attempt to explain the sample length dependence of the ultrasonic parameters observed in measurements of equine bone presented in Chapter 6.

### 7.2 Plastics

In order to determine the cause of the sample thickness-dependence observed in the Bayesian and conventionally derived ultrasonic parameters from the equine bone sample, similar measurements were taken on bone-mimicking plastic phantoms. The plastic phan-

toms used in this chapter were all constructed from Lexan<sup>TM</sup>, a material that has been previously been measured in our Laboratory. Plastic phantoms were used in these studies rather than other materials or bone in order to simplify the propagation model and to limit the number of variables to be determined. In homogeneous plastics, there is only one longitudinal wave mode propagating and the properties of the material, such as velocity, attenuation, and insertion losses, are known from previous studies.

In applying Bayesian probability theory, as described in Section 3.4, to the data acquired from the plastic phantoms presented in this chapter, the wave propagation model used in the Bayesian analysis was altered slightly to allow for only one wave to propagate. This was accomplished by setting  $A_{fast} = 0$ , thereby eliminating the fast wave. Therefore, the three parameters that were estimated by the Bayesian algorithm for the plastic phantom studies were  $A_{slow}$ ,  $\beta_{slow}$ , and  $c_{slow}$ .

### 7.3 Initial plastic phantom studies

In response to the unexpected sample thickness dependence observed in the ultrasonic parameters determined with both conventional and Bayesian analysis methods, measurements were carried out on three circular (3 inch diameter) Lexan<sup>TM</sup> phantoms with thicknesses of approximately 9.5 mm, 19 mm, and 38 mm. Each sample was approximately double the thickness of the previous sample. This was expected to produce predicted bulk losses that doubled for each doubling of thickness, but not affect the surfaces losses. The three Lexan<sup>TM</sup> phantoms were measured with a matched pair of 1 MHz nominal center frequency

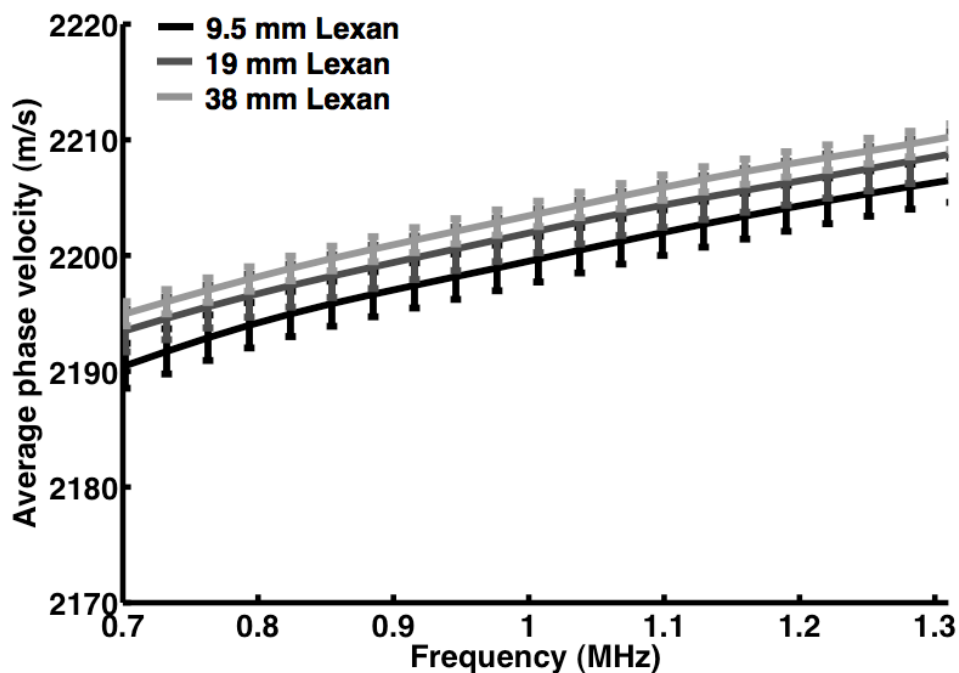


FIGURE 7.1: The average ( $N = 5$ ) phase velocity using conventional phase spectroscopy methods for the three Lexan<sup>TM</sup> samples ( $d = 9.5$  mm, 19 mm, and 38 mm). The error bars represent plus or minus one standard deviation.

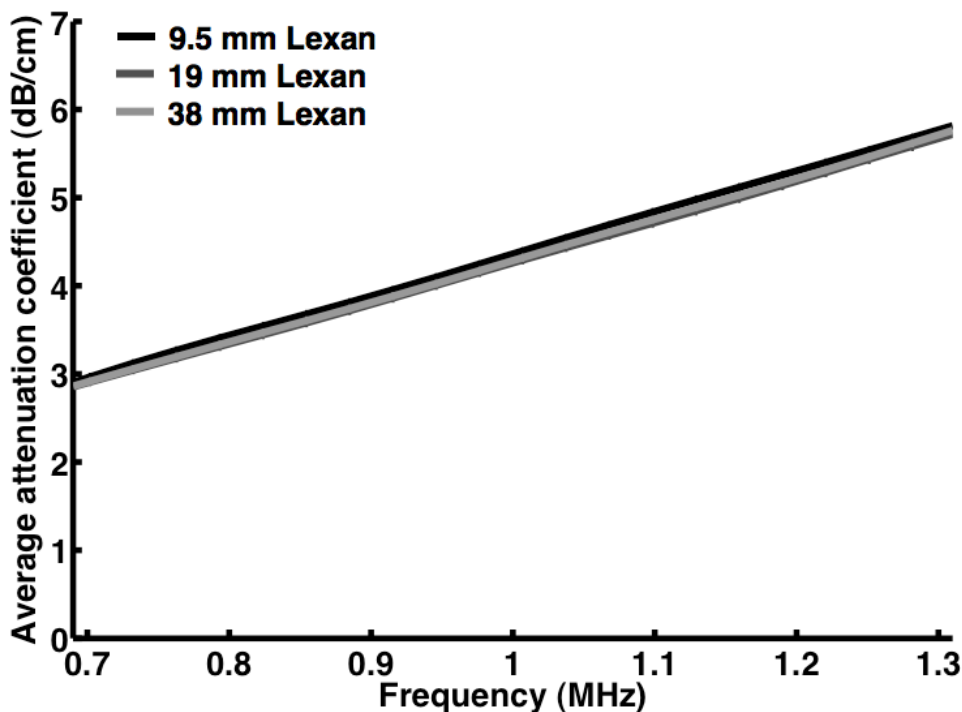


FIGURE 7.2: The average ( $N = 5$ ) attenuation coefficient using conventional analysis methods for the three Lexan<sup>TM</sup> samples ( $d = 9.5$  mm, 19 mm, and 38 mm). The error bars represent plus or minus one standard deviation and are too small to be seen.

focused transducers (0.5 inch diameter, 4 inch focus) in a through-transmission arrangement. Measurements were acquired at five spatial locations on each Lexan<sup>TM</sup> phantom.

The data were analyzed using both conventional and Bayesian analysis methods as discussed in Chapter 3. The average phase velocities determined using conventional phase spectroscopy were consistent among the three thicknesses of Lexan<sup>TM</sup>, only differing by approximately 2 m/s for each doubling of sample thickness, as shown in Figure 7.1. Consistent results for the average attenuation coefficients for the three Lexan<sup>TM</sup> phantoms were also observed, as seen in Figure 7.2.

Bayesian analysis generated model waveforms that fit the experimental data extremely well. The average (of 5 spatial sites per sample) Bayesian estimates for phase velocity ( $c$ ),



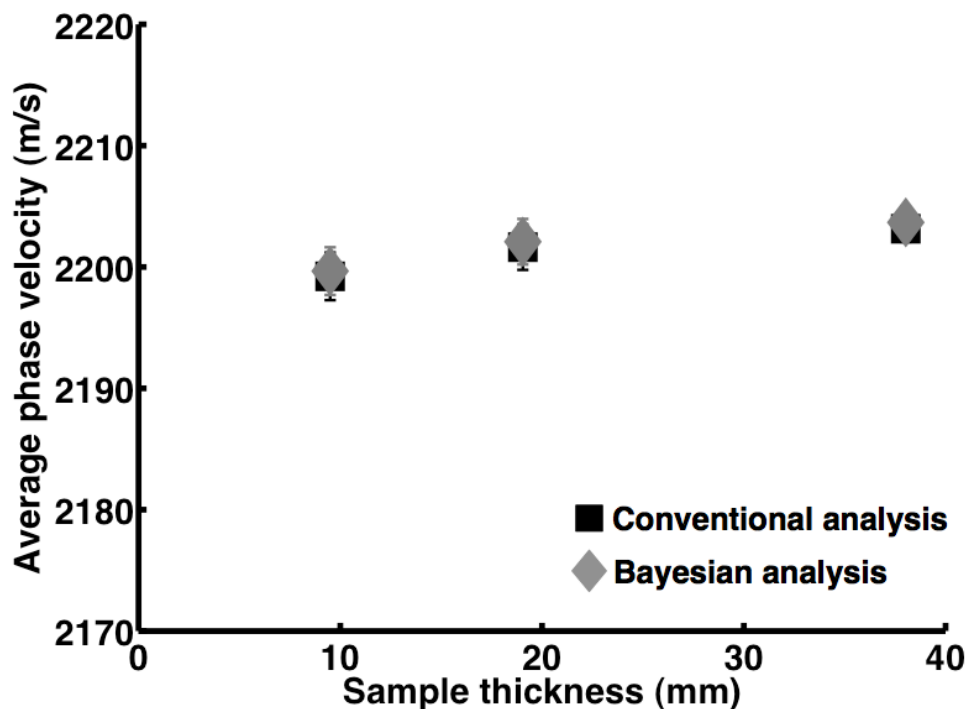


FIGURE 7.3: Comparison of the average ( $N = 5$ ) phase velocity (at 1 MHz) obtained using conventional analysis (black squares) and Bayesian analysis (gray diamonds) for three thicknesses of Lexan<sup>TM</sup>. The error bars represent plus or minus one standard deviation.

slope of attenuation ( $\beta$ ), and transmission coefficient-related term ( $A$ ) are shown in Figures 7.3 - 7.5 as a function of sample thickness, along with the results determined using conventional methods. The phase velocities at 1 MHz were approximately identical for conventional and Bayesian analysis. This was in contrast with the results obtained for nBUA and  $A$ . As shown in Figure 7.4, the slope of attenuation determined by the Bayesian algorithm systematically decreased with increasing sample length, whereas the conventionally-derived nBUA was slightly more constant among the sample lengths. A similar situation was observed for the transmission coefficient-related  $A$  term (Figure 7.5). The predicted transmission coefficient-related  $A$  term (conventional analysis) was determined using the

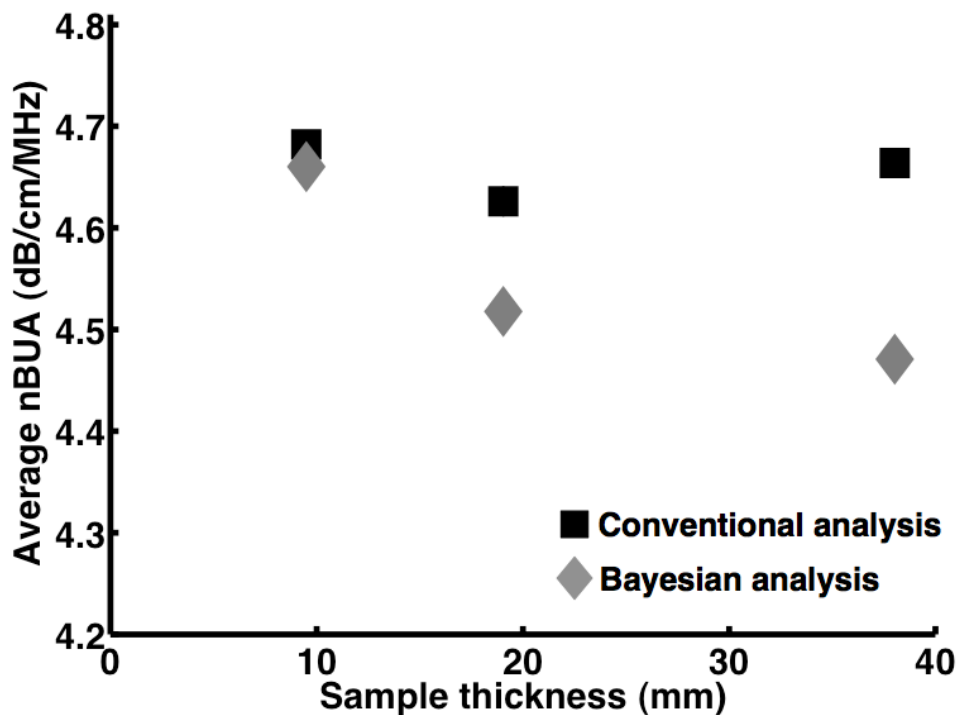


FIGURE 7.4: Comparison of the average ( $N = 5$ ) slope of attenuation (nBUA) obtained using conventional analysis (black squares) and Bayesian analysis (gray diamonds) for three thicknesses of Lexan<sup>TM</sup>. The error bars represent plus or minus one standard deviation and are too small to be seen.

impedance difference between water and Lexan<sup>TM</sup>, and had an average value of 0.92, which corresponded to total surface losses of 0.75 dB. The transmission coefficient-related terms determined using Bayesian analysis systematically increased with increasing sample thickness. For the thickest Lexan<sup>TM</sup> phantom ( $d = 38$  mm), the Bayesian transmission coefficient-related  $A$  term was 1.0, which corresponds to no surface losses. This was surprising because the Bayesian-derived nBUA was smallest for the thickest Lexan<sup>TM</sup> phantom, implying there was less total (surface + bulk) loss for the thickest Lexan<sup>TM</sup> sample.

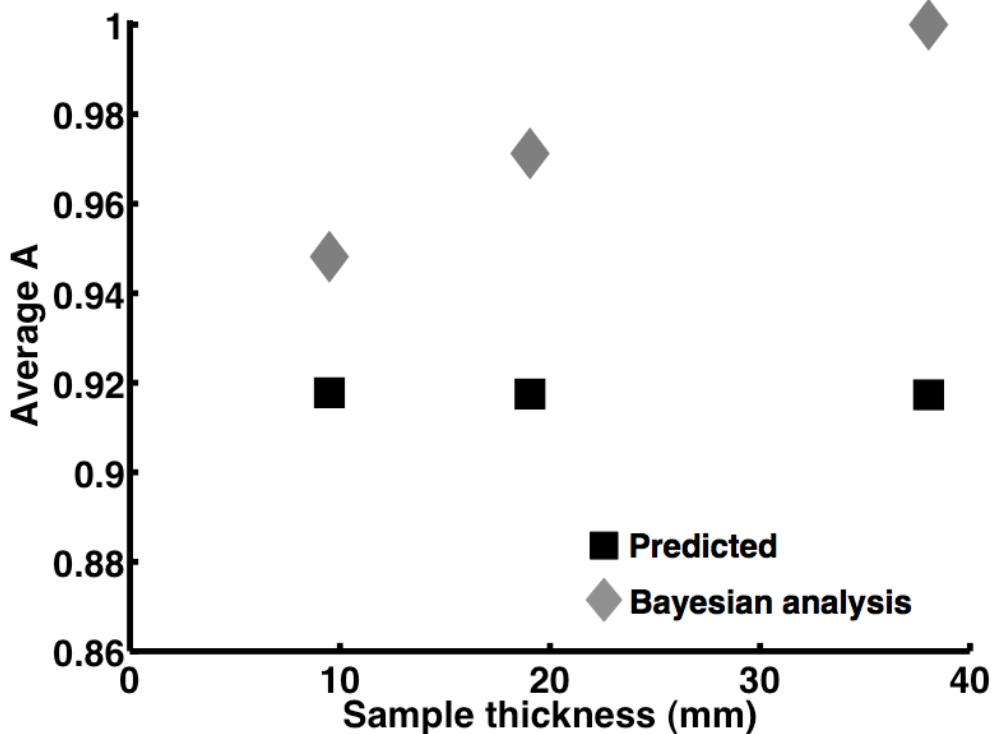


FIGURE 7.5: Comparison of the average ( $N = 5$ ) predicted transmission coefficient-related terms (black squares) and the average Bayesian-estimated  $A$  terms (gray diamonds) for three thicknesses of Lexan<sup>TM</sup>. The error bars represent plus or minus one standard deviation and are too small to be seen.

### 7.3.1 Checking dependences of the parameters in the Bayesian model

We first wanted to verify was that the Bayesian algorithm was estimating the parameters in a predictable manner, and also to check for any unexpected dependences of the parameters on each other. All of the following tests were carried out using the data acquired on the three Lexan<sup>TM</sup> phantoms discussed above.

TABLE 7.1: Results of the Bayesian algorithm when a sample signal from the 9.5 mm thick Lexan<sup>TM</sup> sample was artificially modified so that its amplitude was half and one quarter of the original amplitude.

Amplitude	$A$	$\beta$ (dB/cm/MHz)
Original	0.95	4.66
0.5x	0.47	4.66
0.25x	0.24	4.67

### Amplitude test

One sample trace from each of the three Lexan<sup>TM</sup> samples was digitally modified to produce a signal with half the original amplitude and another signal was produced with a quarter of the original amplitude. These modified sample signals along with the unmodified reference (water-path-only) signals were processed with the Bayesian algorithm. As expected, the estimate for  $\beta$  did not change but the estimate for  $A$  changed proportionally to the change in amplitude, as shown in Table 7.1 for the 9.5 mm Lexan<sup>TM</sup> sample. The value of  $\beta$  was not expected to change because an overall decrease in amplitude does not affect the frequency components or shape of the signal.

### Sample length test

One input to the Bayesian algorithm is the thickness of the samples being studied. In this test, the sample thickness input into the Bayesian algorithm was varied (artificially) to investigate how the parameters  $A$  and  $\beta$  were affected. We expected that the parameter  $A$  should remain unchanged since it should not depend on sample thickness, but that  $\beta$  should

TABLE 7.2: Results of the Bayesian algorithm on a signal from the 9.5 mm thick Lexan<sup>TM</sup> sample when the sample thickness input into the Bayesian algorithm was changed from the original thickness  $d$  to  $2*d$  and to  $4*d$ . Neither the sample nor reference signals were modified before being input into the Bayesian algorithm.

Sample thickness	$A$	$\beta$ (dB/cm/MHz)
Original $d$ (9.5 mm)	0.95	4.66
$2*d$ (19 mm)	0.95	2.33
$4*d$ (38 mm)	0.95	1.16

change inverse proportionally to the change in sample thickness. One trace from each of the three Lexan<sup>TM</sup> samples was processed with the Bayesian algorithm with the input sample thickness set to three different values: the original length  $d$ ,  $2*d$ , and  $4*d$ . The results, as shown for the 9.5 mm Lexan<sup>TM</sup> sample in Table 7.2, were consistent with our predictions.

### Additional Bayesian tests

Next we wanted to explore whether the Bayesian algorithm would correctly recover one of the parameters if the remaining parameters were constrained to be the values determined using conventional analysis, as listed in Table 7.3. For example, if the parameters  $A$ ,  $\beta$ , and  $c$  were all set to the conventional analysis results, could the Bayesian algorithm correctly recover the sample thickness  $d$ ? Since conventional and Bayesian analysis produced different values for these three parameters, it was not necessarily expected that the Bayesian algorithm would recover the correct sample thickness if the other parameters were set to the conventional analysis values. Although  $d$  is not usually an adjustable parameter, the algorithm can be modified easily to permit the sample thickness to be a searchable parameter. As shown in

TABLE 7.3: Input values of the three parameters in the Bayesian algorithm for the tests listed in Table 7.4. These values were determined by conventional analysis methods performed on the data from the three Lexan<sup>TM</sup> phantoms.

<b>Parameter</b>	<b>Input value for Bayesian algorithm</b>
$A$	0.92
$\beta$	4.66 dB/cm/MHz
$c$	2200 m/s

Table 7.4, the Bayesian algorithm was able to correctly estimate the sample thickness of the three Lexan<sup>TM</sup> phantoms. However, the model waveforms generated by these simulations did not fit the experimental signals as well as those generated when allowing the Bayesian algorithm to estimate all of the parameters. It was found that the residuals from the tests constraining  $A$ ,  $\beta$ , and  $c$  were 3 -10 times larger than the residuals from the tests allowing  $A$ ,  $\beta$ , and  $c$  to be adjustable. This may imply that the Bayesian algorithm does a better job at fitting the rf data than conventional analysis. The other tests that were performed are listed in Table 7.4 along with their respective results. Other tests were performed are as listed in Table 7.4, with the outcomes summarized in the column labelled "Result".

### 7.3.2 Noise levels

Another concern was the effect of noise in the estimation of the parameters by the Bayesian algorithm. The received signals are typically zero-padded prior to analysis to increase the frequency resolution, but values of zero cause problems in the Bayesian code (Kay and Marple, 1981). Therefore, a small amount of random noise is added to the refer-

TABLE 7.4: The tests performed on the Bayesian algorithm using data from the three Lexan<sup>TM</sup> phantoms. For these tests, some of the parameters were set to be the value determined by conventional analysis (listed in Table 7.3) and investigating how that affected the Bayesian estimate of the remaining parameter(s).

Set constant	Find	Result
$A, \beta,$ and $c$	$d$	Bayesian algorithm recovered correct sample thickness $d$ .
$\beta, c, d$	$A$	Bayesian estimate of $A$ became worse (more sample thickness dependence).
$A, c, d$	$\beta$	Estimates of $\beta$ smaller (by 0.21 – 0.29 dB/cm/MHz) when compared to unconstrained Bayesian runs.
$\beta, c$	$d$ and $A$	Bayesian algorithm correctly estimated sample thickness $d$ , but the estimates of $A$ became worse.

TABLE 7.5: Results of the Bayesian algorithm on a signal from the 9.5 mm thick Lexan<sup>TM</sup> sample with four different levels of added random noise.

Noise level	$A$	$\beta$ (dB/cm/MHz)	$c$ (m/s)
Initial	0.95	4.66	2200
25x	0.94	4.60	2200
50x	0.95	4.67	2200
100x	0.97	4.83	2200

ence and sample signals before they are processed by the Bayesian algorithm. The added random noise eliminates these issues. In this study, added noise levels were varied from the initial level to 100 times the initial level in steps of 25 (total of 4 noise levels). The initial level of added random noise depended on the peak-to-peak amplitude of the sample signal. This was done on one sample signal from each of the three Lexan<sup>TM</sup> samples. The noise level of the reference signal was left unchanged. Figure 7.6 shows a sample signal from the 9.5 mm Lexan<sup>TM</sup> sample with the four levels of added random noise.

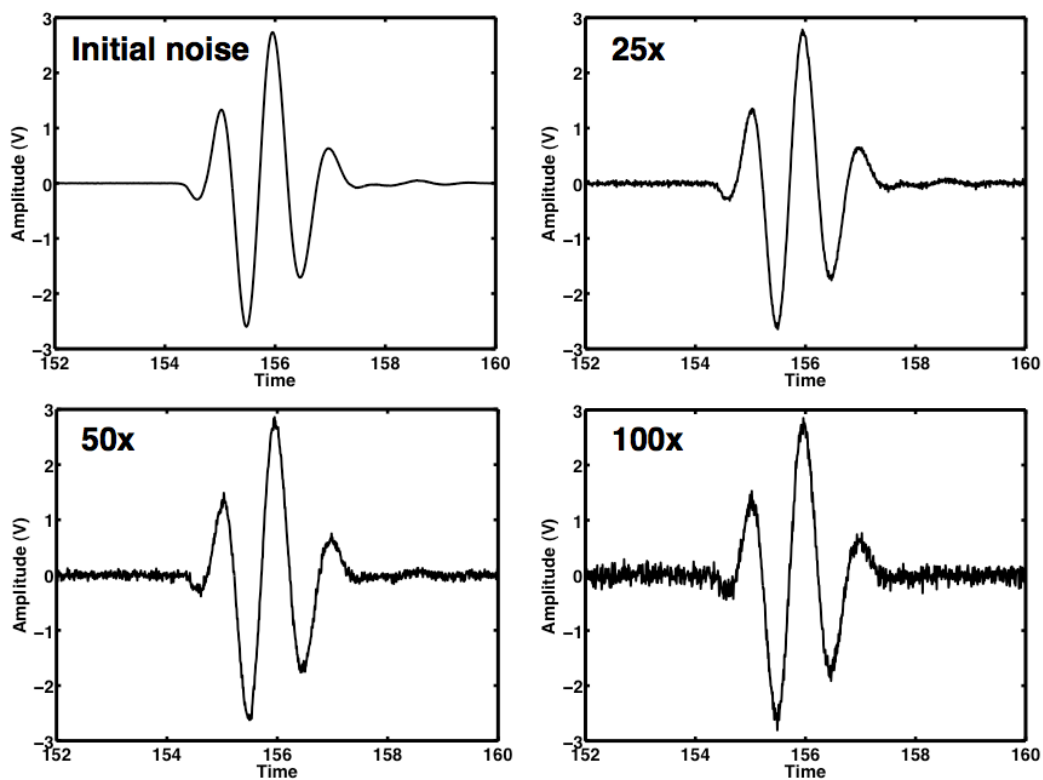


FIGURE 7.6: Sample signals from the 9.5 mm Lexan<sup>TM</sup> sample with four different levels of added random noise.



Table 7.5 shows the results of the Bayesian algorithm for the 9.5 mm thick Lexan<sup>TM</sup> phantom. Overall the parameters are stable for all levels of random noise although this begins to break down for the 100x the initial noise level. Similar results were observed for the 19 mm and the 38 mm thick Lexan<sup>TM</sup> samples. It is possible that if the signal-to-noise ratio is low, that the Bayesian may have more difficulty determining estimates of the Bayesian parameters. Anderson *et al.*(2010) found that as signal-to-noise ratio decreased, the peaks of the marginal posterior probability distributions for each Bayesian parameter do not change significantly, but the widths of these distributions do increase, indicating less confidence in the parameter value.

### 7.3.3 Removing Kramers-Kronig requirement

In the propagation model used in the Bayesian algorithm, the fast and slow wave phase velocities are forced to increase logarithmically with frequency by assuming that the nearly-local form of the Kramers-Kronig relations are valid for the fast and slow waves. This form of the Kramers-Kronig relations requires that the attenuation coefficient is linear with frequency. To ensure that this restriction on the velocity was not causing the observed sample-thickness dependence, the Kramers-Kronig requirement was removed from the Bayesian code. This caused each frequency present in the signal to travel at the same velocity (the velocity at the center frequency). One trace from each of the three Lexan<sup>TM</sup> phantoms was run through the Bayesian algorithm without the Kramers-Kronig requirement.

The Bayesian algorithm without the Kramers-Kronig requirement yielded slightly different estimates for the parameters  $A$  and  $\beta$  than the original (with Kramers-Kronig) Bayesian

TABLE 7.6: Results of the Bayesian algorithm with and without the Kramers-Kronig (KK) requirement on one trace from each of the three Lexan<sup>TM</sup> phantoms.

Sample thickness (mm)		$A$	$\beta$ (dB/cm/MHz)	$c$ (1 MHz) (m/s)
9.5 mm	with KK	0.95	4.66	2200
	without KK	0.96	4.77	2201
19 mm	with KK	0.97	4.52	2202
	without KK	0.99	4.64	2202
38 mm	with KK	1.00	4.47	2204
	without KK	1.00	4.52	2202

algorithm, as shown in Table 7.6, but there was still an unexpected sample-thickness dependence. In comparison to the Kramers-Kronig version of the Bayesian method, the non-KK Bayesian method estimated slightly larger values of  $A$ , slightly larger values for  $\beta$ , and the same values for speed. A comparison of the residuals showed that the inclusion of the Kramers-Kronig requirement significantly improved the model fit to the experimental data because it takes into account dispersion.

### 7.3.4 Explicitly defining $A$

The frequency independent terms  $A_{fast}$  and  $A_{slow}$  in our original propagation model account for transmission of the signal from the surrounding medium (which for laboratory-based immersion studies would be water) into the cancellous bone and subsequently back out of the bone into the surrounding medium. Presumably the initially one-mode signal propagates as a two-mode compressional signal in the cancellous bone. In analogy with the simpler problem of transmission at a boundary between media that each support only a single

compressional mode, the assumption is that characteristic impedances provide an approach that accounts for the fraction of the incoming pressure (or stress) and particle velocity (or time rate of change of strain) transmitted from the host medium into the cancellous bone.

It was hypothesized that by explicitly specifying the functional forms of the transmission coefficients at the entry and exit surfaces, additional information that might further characterize bone structure could be obtained, as well as potentially reduce the sample thickness dependence. As shown below, this extension of the propagation model leads directly to the introduction of fast wave and slow wave effective mass densities,  $\rho_{fast}$  and  $\rho_{slow}$ .

Our original propagation model, discussed in Section 3.4.2, explicitly identifies the phase velocities  $c_{fast}$  and  $c_{slow}$ , slopes of attenuation  $\beta_{fast}$  and  $\beta_{slow}$ , and the frequency independent signal loss prefactors  $A_{fast}$  and  $A_{slow}$ .

$$Output(f) = Input(f) \left[ A_{fast} \exp(-\beta_{fast}fd) \exp\left(\frac{i2\pi fd}{c_{fast}(f)}\right) + A_{slow} \exp(-\beta_{slow}fd) \exp\left(\frac{i2\pi fd}{c_{slow}(f)}\right) \right] \quad (7.1)$$

where  $Output(f)$  and  $Input(f)$  are the complex Fourier spectra of the received waveform and the incident waveform, respectively, and  $d$  is the sample thickness.

This study attempted to enhance this model by accounting for transmission into and out of water-immersed cancellous bone specimens, resulting in an explicit dependence of  $A_{fast}$  and  $A_{slow}$  on the complex impedances  $Z_{fast}$  and  $Z_{slow}$ :

$$A_{fast} = \left[ \frac{2Z_{ref}}{Z_{ref} + Z_{fast}} \right] \left[ \frac{2Z_{fast}}{Z_{fast} + Z_{ref}} \right] \quad (7.2)$$

and

$$A_{slow} = \left[ \frac{2Z_{ref}}{Z_{ref} + Z_{slow}} \right] \left[ \frac{2Z_{slow}}{Z_{slow} + Z_{ref}} \right] \quad (7.3)$$

where  $Z_{fast}$  and  $Z_{slow}$  are of the form

$$Z_{fast} = \frac{\rho_{fast}c_{fast}}{1 + \left(\frac{\alpha_{fast}}{k_{fast}}\right)^2} \left[ 1 + i\frac{\alpha_{fast}}{k_{fast}} \right] \quad (7.4)$$

and

$$Z_{slow} = \frac{\rho_{slow}c_{slow}}{1 + \left(\frac{\alpha_{slow}}{k_{slow}}\right)^2} \left[ 1 + i\frac{\alpha_{slow}}{k_{slow}} \right] \quad (7.5)$$

where  $\alpha$  is the attenuation coefficient expressed in inverse distance units,  $k$  is the wave number also in inverse distance, and  $\rho_{fast}$  and  $\rho_{slow}$  are the effective mass densities of the fast wave and slow wave, respectively. In Equations 7.2 and 7.3 for  $A_{fast}$  and  $A_{slow}$ , the first term in the product represents the particle velocity transmission coefficient for the front (water to bone) surface and the second term in the product represents the corresponding quantity for the back (bone to water) surface.

As illustrated in Figure 7.7, although the transmission coefficients for pressure and for particle velocity differ, the product of the front surface (water to bone) and back surface (bone to water) transmission coefficients are identical whether one is considering either pressure or particle velocity.

The newly updated Bayesian model, with the  $A$  terms rewritten as Equations 7.2 and 7.3, was tested on the data acquired from the three thicknesses of Lexan<sup>TM</sup>. This permitted us to determine if the newly updated Bayesian algorithm estimated a different transmission coefficient than that estimated using the Bayesian model with the  $A$  terms not explicitly defined. Additionally, because the mass density of Lexan<sup>TM</sup> can be measured experimentally,

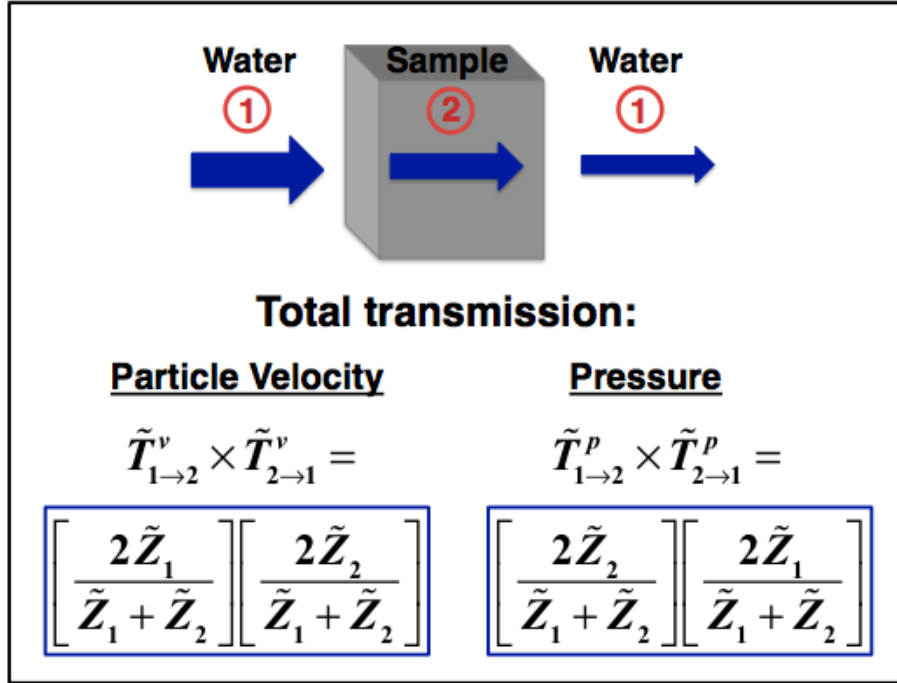


FIGURE 7.7: The total transmission coefficients, accounting for both the front and back surfaces, for pressure and for particle velocity.

the mass density estimated by this updated propagation model should provide a check on whether this redefinition of  $A$  is satisfactory.

It was determined for Lexan<sup>TM</sup> (and for the heel bone samples in Chapter 4), that the complex impedances given by Equations 7.4 and 7.5 could each be simplified to  $Z = \rho c$  since  $\alpha/k$  was sufficiently small compared to one. In the case of Lexan<sup>TM</sup>, where  $\beta = 5.4\text{e-}5$  Np/m/Hz (4.7 dB/cm/MHz) and  $c = 2200$  m/s:

$$\frac{\alpha}{k} = \frac{\beta c}{2\pi} = 0.019 \quad (7.6)$$

For all five sites on each of the three Lexan<sup>TM</sup> samples, the enhanced model yielded results identical to those of the original model for phase velocity, slope of attenuation  $\beta$ , and transmission coefficient-related term  $A$ . The estimated mass density  $\rho$  obtained from the

TABLE 7.7: The measured mass density and the Bayesian-estimated mass density of the three Lexan<sup>TM</sup> samples.

Sample thickness (mm)	Measured mass density (kg/m <sup>3</sup> )	Bayesian estimated mass density (kg/m <sup>3</sup> )
9.5 mm	1217	1072 ± 2
19 mm	1216	949 ± 7
38 mm	1218	673 ± 1

enhanced model did not agree with the experimentally measured mass density of the Lexan<sup>TM</sup> samples, and displayed a significant sample-thickness dependence. It was determined that the modified Bayesian model attempted to keep the same  $A$  term as the original model even though it was redefined in terms of mass densities and speeds. Since the velocity,  $c$ , was also essentially fixed, then the only other adjustable parameter was the density  $\rho$ , thus leading to unrealistic density values. Another issue was that the resulting transmission coefficient-related term ( $A$ ) was not very sensitive to  $\rho$ . Figure 7.8 displays the transmission coefficient  $A$  as a function of  $\rho$  determined using Equation 7.3 with  $c_{slow} = 2200$  m/s,  $c_{ref} = 1486$  m/s, and  $\rho_{ref} = 1000$  kg/m<sup>3</sup>. This graph illustrates two concerns:(1) there is not a unique  $\rho$  for a given  $A$  value (2) for some regions, a large change in density  $\rho$  only leads to modest changes in  $A$ . Therefore, if the modified Bayesian model attempts to achieve the same  $A$  value as the original model, and the value is only a little off from the true transmission coefficient, the Bayesian-estimated mass density may be a very poor estimate of the true mass density.

Since the density of the Lexan<sup>TM</sup> samples were known ( $\rho_{actual} \approx 1200$  kg/m<sup>3</sup>), the data were reprocessed using the modified Bayesian model with the mass density parameter limited to values between 1000 - 2000 kg/m<sup>3</sup> (in these units, water is 1000 kg/m<sup>3</sup>). For all of these

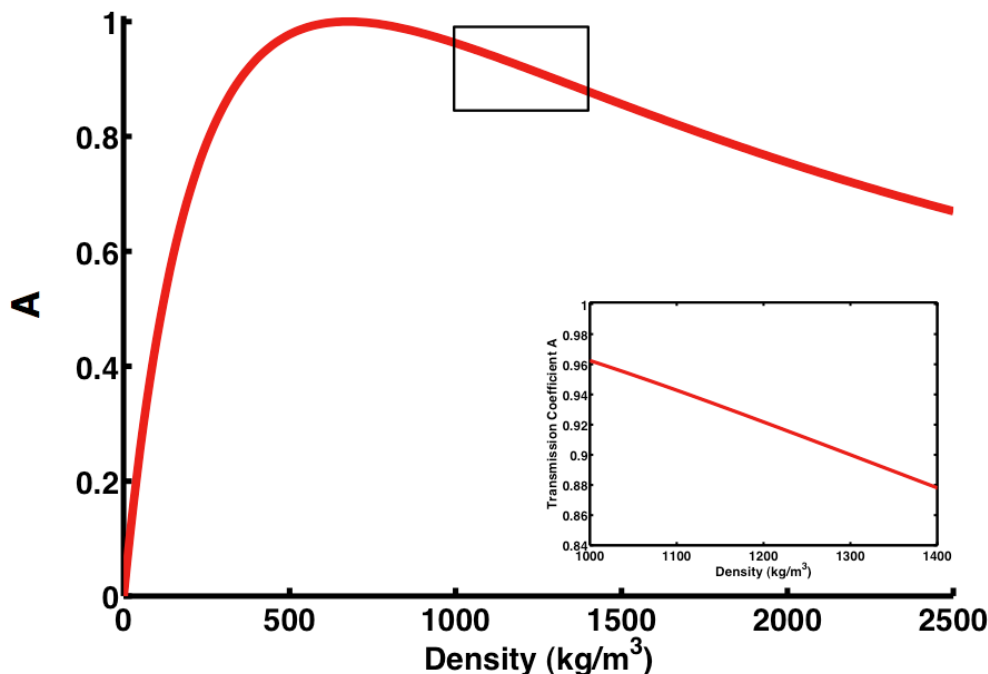


FIGURE 7.8: Plot of the transmission coefficient-related term  $A$  as a function of mass density  $\rho$  determined using Equation 7.3 with  $c_{slow} = 2200$  m/s,  $c_{ref} = 1486$  m/s, and  $\rho_{ref} = 1000$  kg/m<sup>3</sup>. The inset is zoomed in around the actual density of Lexan<sup>TM</sup> ( $\rho \approx 1200$  kg/m<sup>3</sup>).

runs, the modified Bayesian algorithm estimated the mass density to be 1000 kg/m<sup>3</sup>, the minimum amount allowed.

### 7.3.5 Checking for nonlinearities

Another possible explanation for the observed sample-thickness dependence was the presence of nonlinear propagation effects. Water itself is a nonlinear medium, and in our experiments there can be relatively long path lengths of water that the signal must travel between the two transducers. In nonlinear propagation, energy at a frequency,  $f$  may be "promoted" to the higher harmonics ( $2f$ ,  $3f$ , etc.) (Wallace, 2001). The effects of nonlinear propagation can be difficult to measure since attenuation usually increases with frequency,

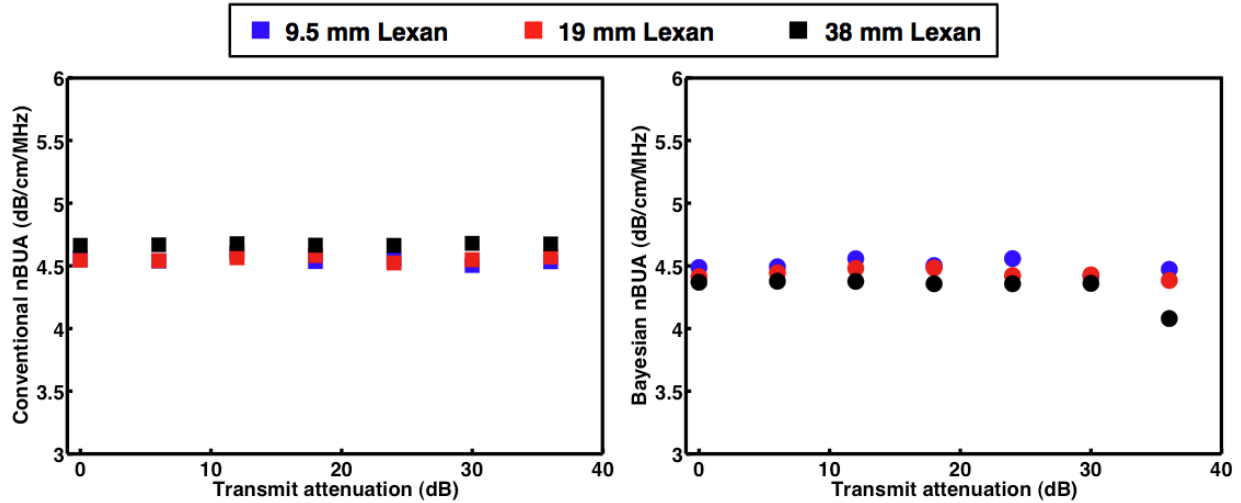


FIGURE 7.9: Left: Results of the slope of attenuation using conventional analysis for varying driving voltages (input attenuations) on the three Lexan<sup>TM</sup> phantoms. Right: The results of the slope of attenuation using Bayesian analysis for varying driving voltages. The approximately constant  $\beta$  with driving voltage suggest that there are no nonlinear propagation effects.

thus the energy promoted to higher frequencies are "killed off" in the sample and not seen at the receiving transducer.

To determine if nonlinear propagation effects were occurring, the three Lexan<sup>TM</sup> phantoms ( $d = 9.5, 19, \text{ and } 38 \text{ mm}$ ) were remeasured using the same experimental set-up but systematically varying the driving voltage. The original driving voltage (to the transmitter) was set to approximately 60 V. Click-stop attenuators, on the transmit side, were then increased in steps of 6 dB from 0 until the signal fell into the noise for each of the three Lexan<sup>TM</sup> samples. The slope of attenuation,  $\beta$ , was determined with conventional analysis and with Bayesian analysis.

Figure 7.9 shows the results for  $\beta$  as a function of driving voltage (input attenuation) using both conventional and Bayesian analysis. The results suggested that there were no effects from nonlinear propagation. If there had been nonlinearities, the value of  $\beta$  would have



increased at low transmit attenuations (that is, high drive voltages). The slope of attenuation estimated by the Bayesian algorithm started to decrease at transmit attenuations greater than 36 dB, presumably due to low signal-to-noise ratios.

### 7.3.6 Introducing quadratic attenuation term

The original propagation model used in the Bayesian algorithm assumes that the attenuation within the sample is linear with frequency,  $\alpha = \beta f$ . This assumption might be valid only for specific samples and over specific frequency ranges. If the attenuation coefficient has a slight curvature, then trying to fit it with a line may result in an overestimation or underestimation of the true attenuation depending on the curvature. In order to account for any not-linear-with-frequency dependence of the attenuation coefficient, the loss term in the propagation model used in the Bayesian algorithm was modified to include a quadratic attenuation term,

$$Ae^{-\beta fd} \rightarrow Ae^{-(\beta f + \gamma f^2)d} \quad (7.7)$$

Although the modified attenuation term in Equation 7.7 does account for any curvature present in the attenuation coefficient as a function of frequency, it is not the most realistic form for experimental data which is only reliable over a certain (limited) bandwidth. It also assumes knowledge of the attenuation at zero frequency, which is not valid for most experiments. Therefore, it made more physical sense to expand the attenuation coefficient around the center frequency,  $f_0$ ,

$$Ae^{-[\alpha_0 + \beta(f-f_0) + \gamma(f-f_0)^2]d} \quad (7.8)$$

TABLE 7.8: Bayesian analysis results using the propagation model with the additional quadratic attenuation term (Eq. 7.8) for the three Lexan<sup>TM</sup> phantoms. The original Bayesian estimates for  $A$ ,  $\beta$ , and  $c$  are also shown for comparison.

Parameter	Propagation Model	9.5 mm Lexan	19 mm Lexan	38 mm Lexan
$A$	Original	$0.95 \pm 0.00$	$0.97 \pm 0.00$	$1.00 \pm 0.00$
	Quadratic Attenuation	$0.57 \pm 0.00$	$0.36 \pm 0.00$	$0.14 \pm 0.00$
$\beta$ (dB/cm/MHz)	Original	$4.66 \pm 0.00$	$4.52 \pm 0.01$	$4.47 \pm 0.00$
	Quadratic Attenuation	$4.66 \pm 0.00$	$4.53 \pm 0.01$	$4.52 \pm 0.00$
$c$ (1 MHz) (m/s)	Original	$2200 \pm 2$	$2202 \pm 2$	$2204 \pm 1$
	Quadratic Attenuation	$2200 \pm 2$	$2202 \pm 2$	$2204 \pm 1$
$\gamma$ (dB/cm <sup>2</sup> /MHz <sup>2</sup> )	Original	-	-	-
	Quadratic Attenuation	$0.03 \pm 0.01$	$0.15 \pm 0.01$	$0.00 \pm 0.00$

where  $\alpha_0 = \alpha(f_0)$ .

The modified propagation model with the expanded quadratic attenuation term in conjunction with the Bayesian algorithm was applied to the data from the three Lexan<sup>TM</sup> phantoms ( $d = 9.5$  mm, 19 mm, and 38 mm). With this version of the propagation model, the adjustable parameters to be estimated by the Bayesian algorithm include the original three parameters  $A$ ,  $\beta$ , and  $c$  plus two additional parameters,  $\alpha_0$  and  $\gamma$ .

The results of the Bayesian analysis with the additional quadratic attenuation term for the three Lexan<sup>TM</sup> phantoms are shown in Table 7.8. The Bayesian estimates for  $\beta$  and  $c$  were very similar to those obtained with the original Bayesian algorithm (only linear-with-frequency attenuation). However, the estimates for  $A$  varied significantly from the original Bayesian algorithm. Additionally, the estimates for the parameter,  $\alpha_0$ , are not shown in the Table because the Bayesian algorithm did not appear to be capable of sampling the parameter space for it. The posterior probability distributions for  $\alpha_0$  ended up being the same as the prior probability distributions. It was determined that the Bayesian algorithm

was combining the two frequency-independent losses in the propagation model into one parameter, thus minimizing the number of adjustable parameters. Therefore, the  $A$  value given by the propagation model with the quadratic attenuation term ( $A_{quad}$ ) was actually

$$A_{quad} = A_{original}e^{-\alpha_0 d} = A_{original}e^{-\beta f_0 d}. \quad (7.9)$$

This can be verified by looking at the values for the 9.5 mm sample of Lexan<sup>TM</sup> in Table 7.8 and using Equation 7.9.

$$\begin{aligned} A_{quad} &= A_{original}e^{-\beta f_0 d} \\ &= 0.95e^{-0.536 \text{ Np/cmMHz} * 1 \text{ MHz} * 0.95 \text{ cm}} = 0.95 * 0.60 \\ &= 0.57 \end{aligned} \quad (7.10)$$

Similar results were verified for the 19 mm and the 38 mm thick Lexan<sup>TM</sup> samples. This explained why the Bayesian algorithm appeared not to estimate a value for  $\alpha_0$ .

## 7.4 Systematic shortening of Lexan<sup>TM</sup> sample

In order to study more thoroughly the sample-thickness dependence observed in the equine sample discussed in Chapter 6, a Lexan<sup>TM</sup> phantom of approximately the same dimensions as the equine specimen was measured while systematically decreasing the thickness of the sample. A piece of Lexan<sup>TM</sup> was machined to have a square face with dimensions of 22 mm x 22 mm and a starting thickness of 30 mm. These are similar (face) dimensions to those of the equine specimen. Measurements were acquired using both 1 MHz and 2.25 MHz nominal center frequency transducers arranged in a through-transmission configuration

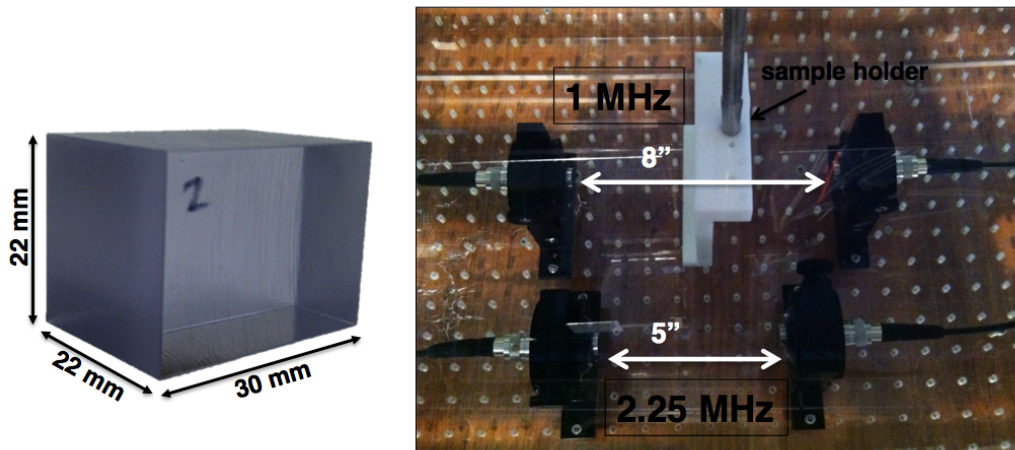


FIGURE 7.10: Left: Lexan<sup>TM</sup> sample with approximately the same (face) dimensions as the equine sample studied in Chapter 6. This Lexan<sup>TM</sup> phantom was gradually shortened from 30 mm down to 10.5 mm in increments of approximately 2 mm. Right: The experimental configuration used on the Lexan<sup>TM</sup> sample. Measurements were taken using both 1 MHz and 2.25 MHz transducers although only the 2.25 MHz data is presented in this thesis.

as shown in Figure 7.10. The sample was attached to a motion-controller permitting the sample to be moved in the y-z plane and permitting measurements at four spatial locations for each sample thickness. The Lexan<sup>TM</sup> phantom was gradually shortened from 30 mm down to 10.5 mm in increments of approximately 2 mm ( $N = 11$  sample thicknesses) using a fly cutter. After each cut, the cut face was polished smooth using sandpaper and oil, and the new thickness was measured using digital calipers. The Lexan<sup>TM</sup> sample was shortened only to 10 mm, in contrast to the 0.5 mm for the equine sample, due to the constraints of the cutting system

For this study, only the results of the 2.25 MHz measurements will be presented. The 1 MHz data yielded not-linear-with-frequency attenuation coefficients and not smoothly varying (with frequency) phase velocities. It was hypothesized that the beam width of the 1 MHz transducers may have been large enough in comparison to the size of the face

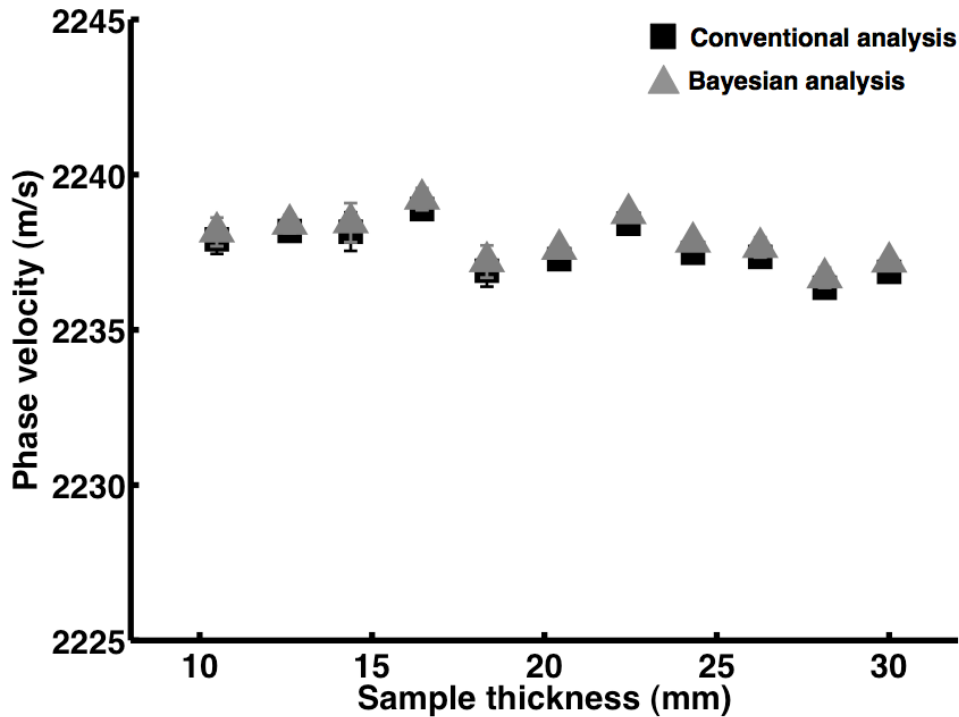


FIGURE 7.11: The average ( $N = 4$ ) phase velocity at 2.25 MHz as a function of the 11 thicknesses of Lexan<sup>TM</sup> using conventional analysis (black squares) and Bayesian analysis (gray triangles). The error bars represent plus or minus one standard deviation.

of the sample that a portion of the beam may have gone around the sample, producing the distortions observed. The theoretical beam diameter at -6 dB down for the 1 MHz transducers used in the study was calculated to be approximately 12 mm. Although this theoretical beam diameter is smaller than the sample face, the actual beam diameter is much larger when the energies below -6 dB are considered.

The data acquired from each of the 11 sample thicknesses were analyzed using both conventional and Bayesian analysis. The phase velocities and dispersions determined using conventional phase spectroscopy agreed well with the Kramers-Kronig predictions and displayed no systematic sample thickness dependence (Figure 7.11). The phase velocities estimated using the Bayesian algorithm were in very good agreement with the conventional

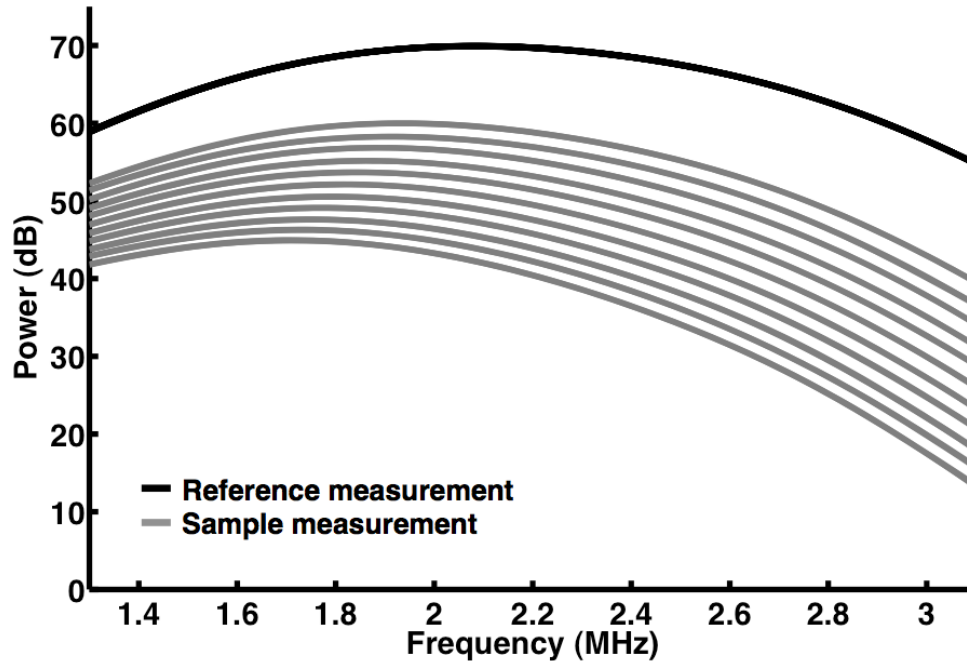


FIGURE 7.12: Power spectra of the reference measurements (black line) and the sample measurements (gray line) acquired for each of the 11 thicknesses of the Lexan<sup>TM</sup> sample using the 2.25 MHz transducers. For each sample thickness, four spatial locations on the sample were measured.

results as shown in Figure 7.11.

The power spectra of the reference measurements and the sample measurements for each of the 11 thicknesses are shown in Figure 7.12. This figure displays the systematic increase in power of the sample signal as the sample is gradually shortened. The average (over four spatial sites) attenuation coefficients, determined using conventional analysis, for the 11 thicknesses of the Lexan<sup>TM</sup> sample are shown in Figure 7.13. Based on this figure, the attenuation coefficients for the various sample thicknesses are quite similar. However, when the attenuation coefficients at the center frequency (2.25 MHz) were plotted as a function of sample thickness, it was observed that the attenuation coefficients decreased slightly but systematically as the sample thickness increased (Figure 7.14). This small but

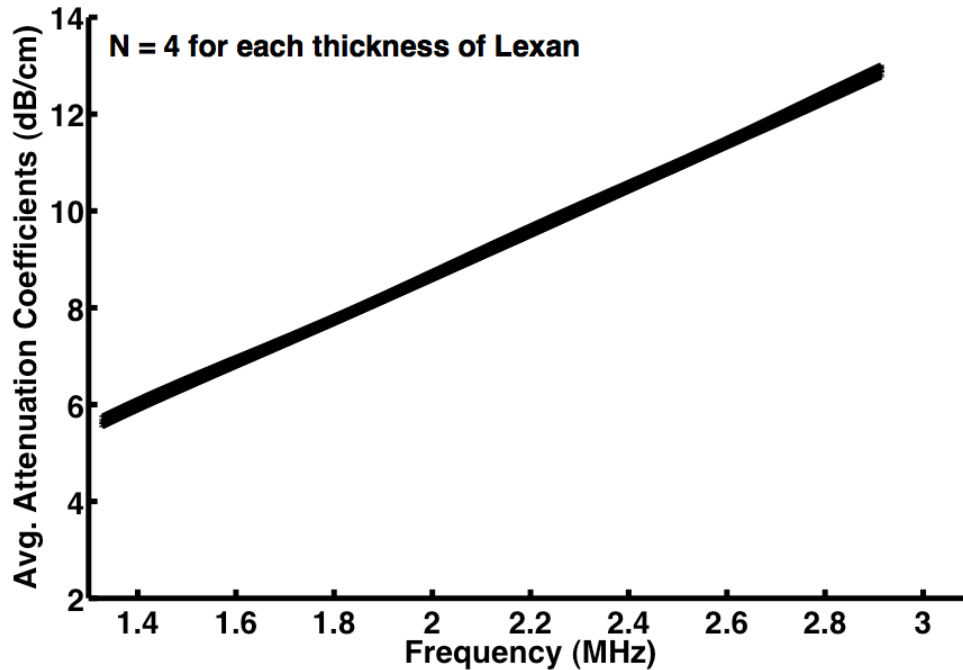


FIGURE 7.13: The average attenuation coefficients for each of the 11 thicknesses of Lexan<sup>TM</sup>. For each thickness of the plastic phantom, four spatial locations were measured. The error bars on each of the 11 attenuation coefficients are too small to be seen.

systematic variation of the attenuation coefficient is unexpected and unexplained. Perhaps it is a consequence of diffraction effects as will be discussed later in Section 7.8.

In contrast to the attenuation coefficient at 2.25 MHz, the slope of attenuation (nBUA) obtained using conventional analysis displayed no sample thickness dependence as shown in Figure 7.15. Over all 11 sample thicknesses, the average conventional nBUA was  $4.51 \pm 0.01$  dB/cm/MHz. On the other hand, Bayesian analysis estimated the slope of attenuation to be, on average,  $4.40 \pm 0.03$  dB/cm/MHz. The Bayesian-estimated nBUA also displayed a slight systematic sample-thickness dependence, as shown in Figure 7.15. The Bayesian nBUA of 4.36 dB/cm/MHz at a sample thickness of 30 mm increased to 4.45 dB/cm/MHz at a sample thickness of 10.5 mm.

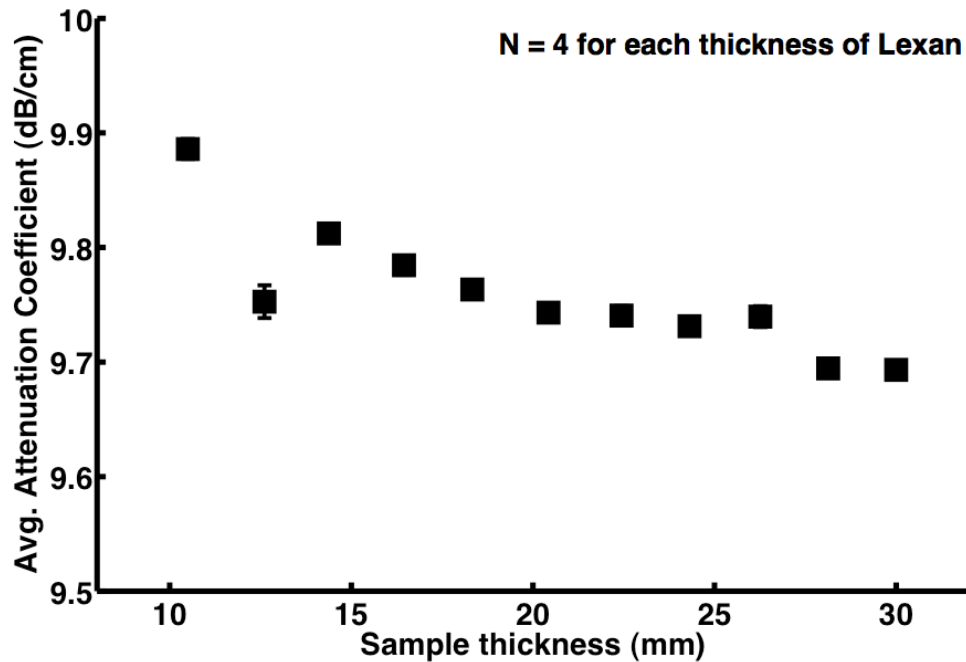


FIGURE 7.14: The average attenuation coefficients ( $N = 4$ ) at 2.25 MHz for each of the 11 thicknesses of Lexan<sup>TM</sup>. The error bars represent plus or minus one standard deviation and are too small to be seen on most of the measurements.

A similar trend was observed for the transmission coefficient-related  $A$  terms. The predicted conventional transmission coefficients determined using the impedance difference between water and Lexan<sup>TM</sup> were, as expected, to be constant as a function of sample thickness (Figure 7.16). In contrast, the Bayesian-estimated  $A$  terms increased systematically towards 1 (no loss at surfaces) as the sample thickness increased. This trend was even more pronounced if the transmission coefficient-related terms were determined using the zero-frequency intercept of the signal loss versus frequency graph. Using that approach, the  $A$  terms increased linearly with sample thickness and even surpassed a value of one, which implies energy is gained instead of lost at the surfaces.

In an effort to account for all the experimental variables that were present in the equine



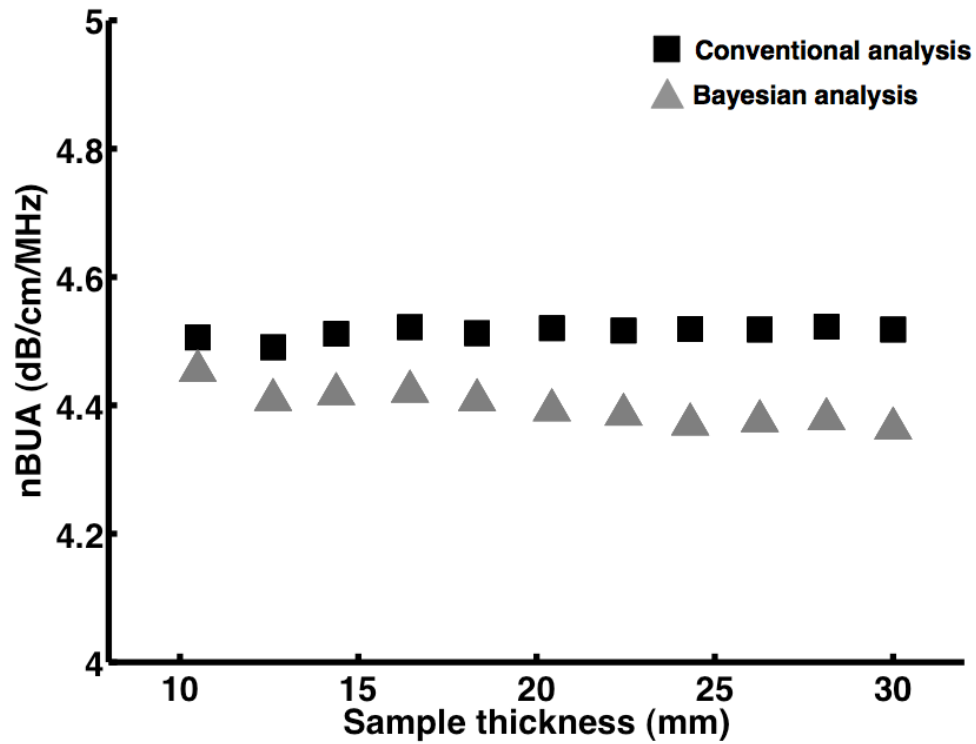


FIGURE 7.15: The average slope of attenuation ( $N = 4$ ) as a function of the 11 thicknesses of Lexan<sup>TM</sup> using conventional analysis (black squares) and Bayesian analysis (gray triangles). The error bars are too small to be seen on this scale.

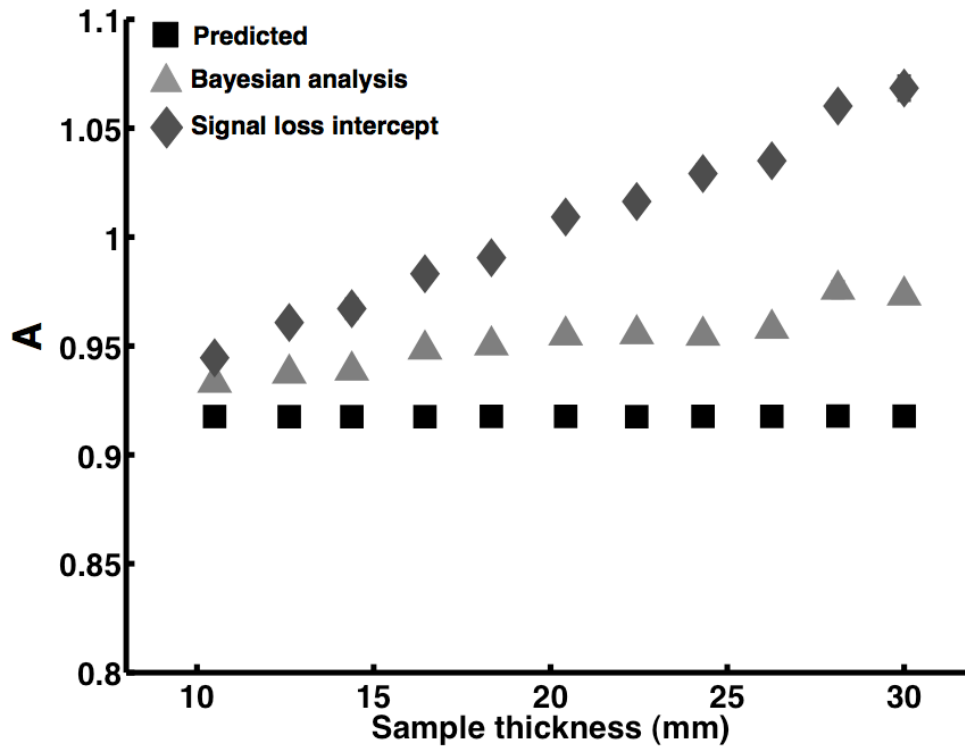


FIGURE 7.16: The average ( $N = 4$ ) transmission coefficient-related terms as a function of the 11 thicknesses of Lexan<sup>TM</sup> using Bayesian analysis (gray triangles) and the signal loss intercept (gray diamonds). The predicted values for  $A$  are represented by black squares. The error bars represent plus or minus one standard deviation.

bone study, a similar Lexan<sup>TM</sup> phantom (with dimensions 22 mm x 22 mm x 30 mm) was sent to Professor Mami Matsukawa's laboratory in Japan. The Lexan<sup>TM</sup> sample was measured in the same acoustic tube apparatus as the equine specimen, thereby permitting us to determine if the experimental set-up introduced any additional effects. The Matsukawa laboratory performed measurements on the Lexan<sup>TM</sup> sample at 0.7, 1, and 2 MHz for sample thicknesses ranging from 20 mm down to 6 mm in approximately 2 mm increments ( $N = 8$ ). The data was sent back to the Laboratory for Ultrasonics for analysis using both conventional and Bayesian methods.

The data acquired from the laboratory of Professor Matsukawa were consistent, in some ways, with the data taken in our Laboratory on a similar Lexan<sup>TM</sup> sample. The data from both laboratories had average attenuation coefficients that were consistent with each other, as shown in Figure 7.17. However, some of the data from our Japanese collaborators displayed large amounts of random variation with sample thickness that may have overshadowed any potential systematic dependence on sample thickness. One example of such data is the phase velocity at 2 MHz as a function of sample thickness. The phase velocities of the Matsukawa-lab data varied from 2187 m/s to 2230 m/s for different thicknesses of the same sample. In contrast, the phase velocities measured by our laboratory for a similar Lexan<sup>TM</sup> sample varied by less than 1 m/s over a wider range of the sample thicknesses.

### 7.4.1 Frequency filtering

As discussed in Chapter 3, conventional analysis methods are performed in the frequency domain over a limited range of frequencies, typically the -6 dB or -10 dB down bandwidth.

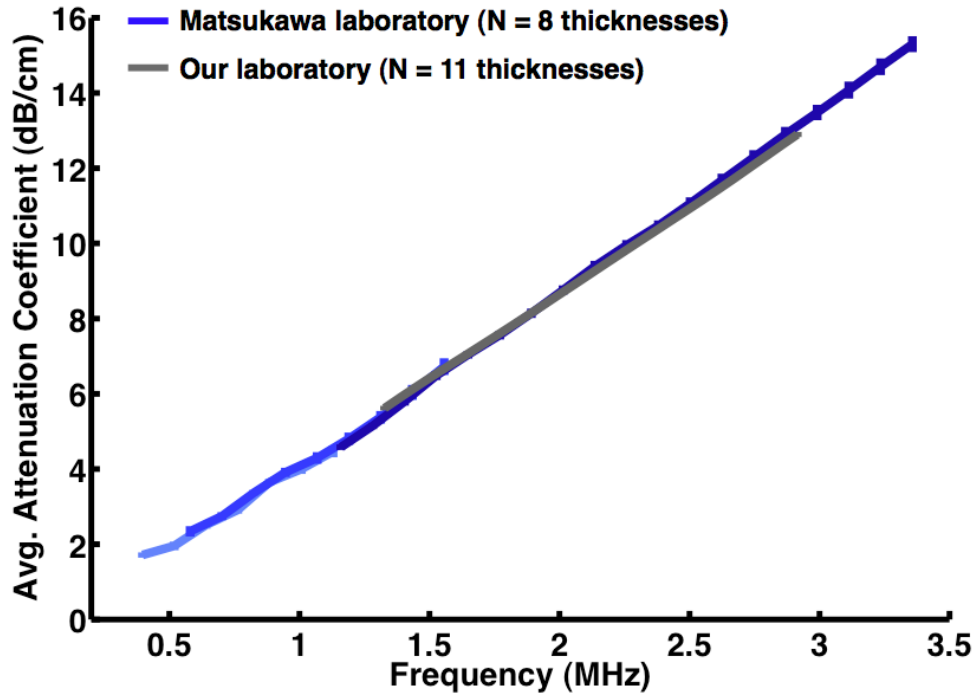


FIGURE 7.17: Comparison of the average attenuation coefficient of a systematically shortened Lexan<sup>TM</sup> phantom measured by the laboratory of Mami Matsukawa (blue) and by our laboratory (gray). Conventional analysis was performed by our laboratory on both sets of data. The Matsukawa laboratory acquired data on the Lexan<sup>TM</sup> sample at 0.7, 1, and 2 MHz. Our laboratory acquired data at 2.25 MHz. The error bars represent plus or minus one standard deviation.

In contrast, the Bayesian algorithm determines the best model parameters by trying to fit the time-domain signal. This time-domain signal may contain frequencies outside the bandwidth used in the conventional analysis. It was hypothesized that by restricting the frequencies present in the reference and sample signals input into the Bayesian algorithm to those frequencies used in the conventional analysis, the Bayesian estimates for nBUA and the transmission coefficients might be more constant as a function of sample thickness.

For this study, a Butterworth filter was chosen. An example of a low-pass Butterworth filter of various orders ( $n$ ) is illustrated in Figure 7.18 with a cutoff frequency of 4 MHz. At

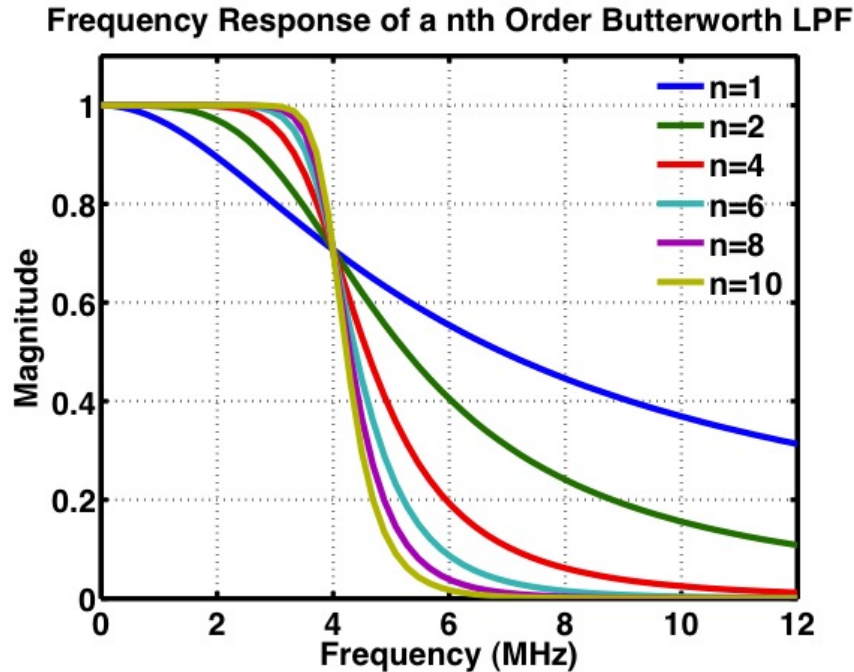


FIGURE 7.18: Illustration of a low-pass Butterworth filter with a cutoff frequency of 4 MHz and with an order ranging from  $n = 1$  to  $n = 10$ .

the cutoff frequency, the filter attenuates the input power by half or 3 dB, which corresponds to a 0.707 decrease in amplitude. The order,  $n$ , of the filter determines the amount of additional attenuation for frequencies higher than the cutoff frequency. For a first order ( $n = 1$ ) Butterworth filter, the signal amplitude is reduced by half (or the power by 6 dB) every time the frequency doubles (goes up one octave). For higher order filters, the power rolloff is  $6n$  dB per octave.

Bandpass Butterworth filters were applied to the data acquired on the systematically shortened Lexan<sup>TM</sup> samples measured by both our laboratory and by the Matsukawa laboratory. The shortened Lexan<sup>TM</sup> data set taken by Professor Matsukawa's laboratory were very useful for this study, due to the significant presence of higher frequency components in the reference signals as shown in Figure 7.19. The power spectra of the reference signals from

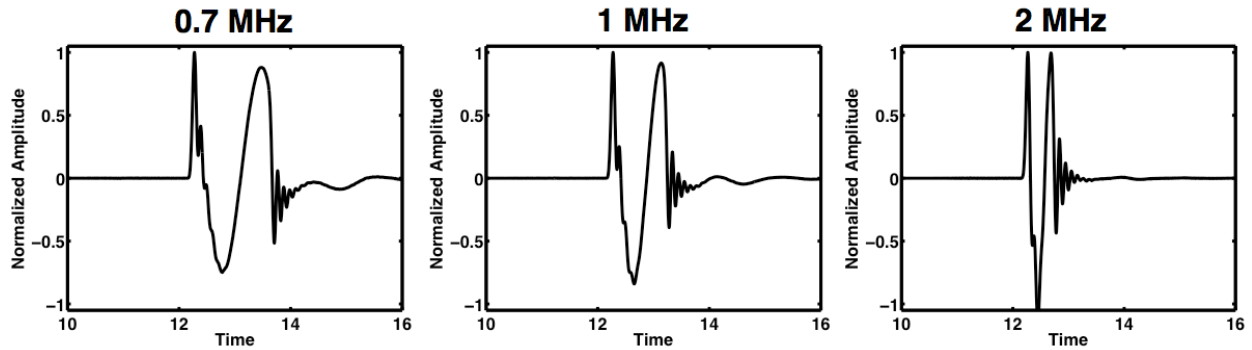


FIGURE 7.19: Reference (water-path only) radiofrequency signals acquired by Mami Matsukawa’s laboratory for the three sets of transducers with center frequencies of approximately 0.7 MHz, 1 MHz, and 2 MHz. These signals showed evidence of higher frequency components.

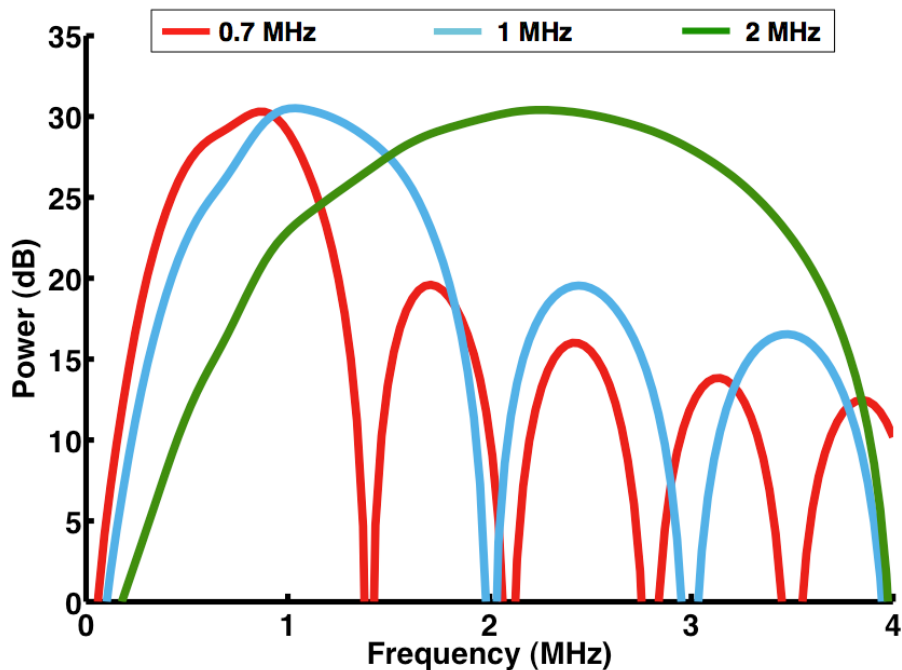


FIGURE 7.20: The power spectra of the three reference signals shown in Figure 7.19 for the shortened Lexa data acquired by Professor Mami Matsukawa’s laboratory using transducers with center frequencies of 0.7 MHz, 1 MHz, and 2 MHz. For all three transducer sets, the reference signal contained significant amounts of higher frequency components that were only 10 to 15 decibels lower than the main frequency lobe.

TABLE 7.9: Bandpass Butterworth filters applied to the data from the shortened Lexan<sup>TM</sup> sample measured in our laboratory.

	<b>Low cutoff frequency (MHz)</b>	<b>High cutoff frequency (MHz)</b>	<b>Filter Order (<math>n</math>)</b>
<b>Butterworth filter 1</b>	1.2	3.5	$n = 4, 8$
<b>Butterworth filter 2</b>	0.8	4.5	$n = 4, 8, 12$

TABLE 7.10: Bandpass Butterworth filters applied to the shortened Lexan<sup>TM</sup> sample measured by the laboratory headed by Professor Mami Matsukawa.

<b>Center frequency (MHz)</b>	<b>Conventional Bandwidth (MHz)</b>	<b>Butterworth filter bandwidth 1 (MHz) order <math>n = 6</math></b>	<b>Butterworth filter bandwidth 2 (MHz) order <math>n = 10</math></b>
<b>0.7</b>	0.40 – 1.16	0.3 – 1.4	0.1 – 1.9
<b>1</b>	0.58 – 1.65	0.5 – 1.9	0.3 – 2.4
<b>2</b>	1.16 – 3.36	1.05 – 3.60	0.7 – 4.2

the three frequencies (0.7 MHz, 1 MHz, and 2 MHz) used in the Matsukawa measurements, shown in Figure 7.20, contain lobes of the higher harmonics that are only 10-15 decibels down from the main lobe at the center frequency. Therefore, the application of bandpass frequency filters to this data set should show more of an effect than filtering the data from our laboratory.

The specifications of the bandpass Butterworth filters applied to the shortened Lexan<sup>TM</sup> data from our laboratory and from Professor Matsukawa's laboratory are displayed in Tables 7.9 and 7.10, respectively. A representative example of the effects of applying a Butterworth filter on a reference signal and power spectrum are shown in Figure 7.21 for the 2 MHz signal acquired by Professor Matsukawa's laboratory. The filters were applied to both

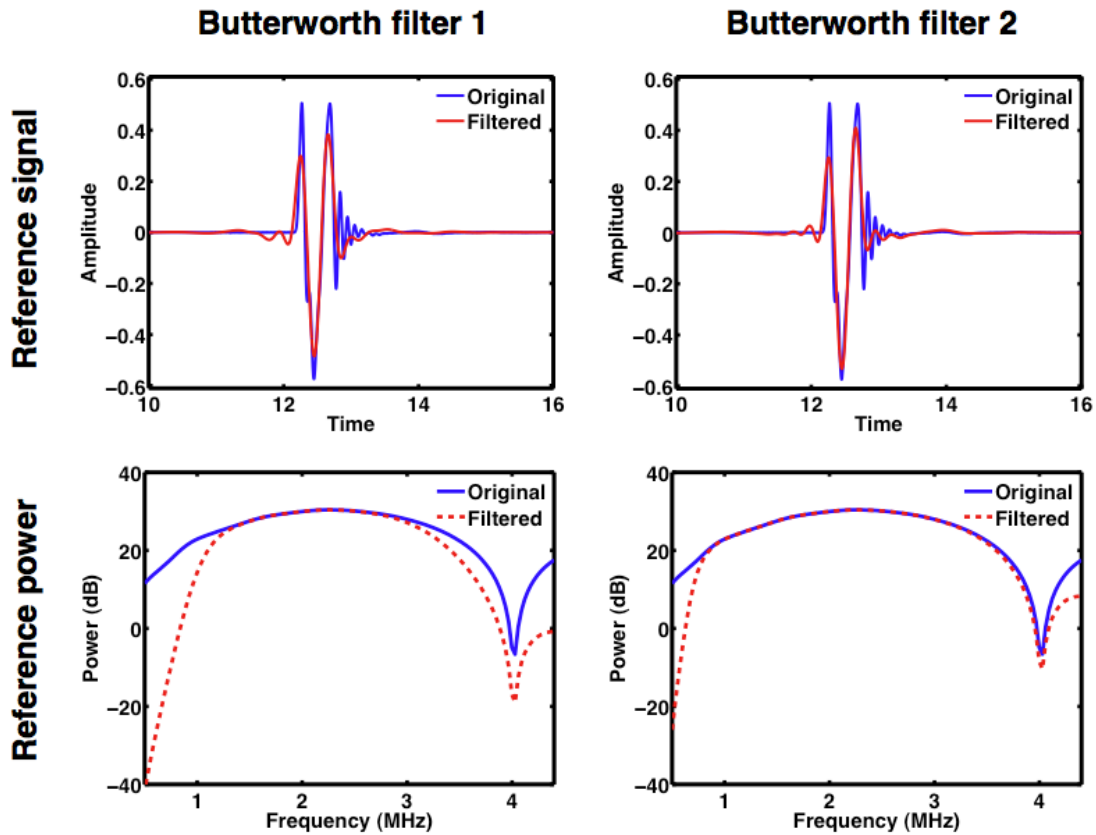


FIGURE 7.21: The effects of applying two different bandpass Butterworth filters to the 2 MHz reference signal and power spectrum acquired by Professory Matsukawa’s laboratory. The original (unfiltered) signals and power spectra are shown in blue while the filtered rf signals and power spectra are shown in red. The specifications of the two Butterworth filters are listed in Table 7.10.

the reference and sample signals before they were input into the Bayesian algorithm.

For both data sets (our laboratory’s and Professor Matsukawa’s laboratory), frequency filtering produced no change in the phase velocity estimations determined by Bayesian analysis. Frequency filtering produced a slight, but insignificant improvement in the Bayesian-estimated nBUA (less sample thickness dependence) in our Lexan<sup>TM</sup> data and in the 0.7 MHz and 1 MHz Lexan<sup>TM</sup> data from our Japanese collaborators. There was no difference between the filtered and unfiltered Bayesian estimated nBUA for the 2 MHz Lexan<sup>TM</sup> data



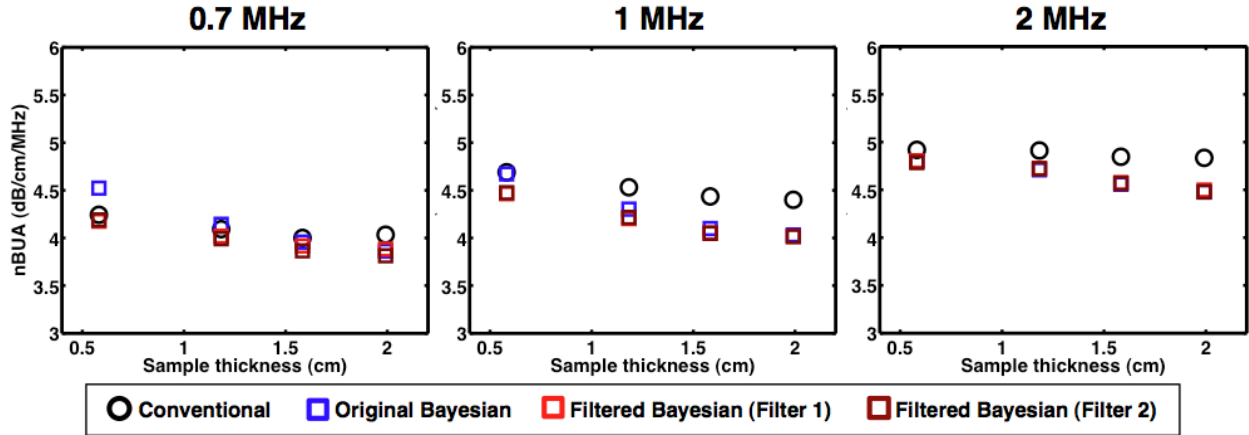


FIGURE 7.22: Comparison of the slopes of attenuation (nBUA) for a subset of the 0.7 MHz, 1 MHz, and 2 MHz data acquired by the Matsukawa laboratory using conventional analysis (black circles), Bayesian analysis with the original (unfiltered) signals (blue squares), Bayesian analysis after filtering with Butterworth filter 1 (red squares), and Bayesian analysis after filtering with Butterworth filter 2 (maroon squares).

from the Matsukawa laboratory, as shown in Figure 7.22. Similar results were seen for the Bayesian-estimated transmission coefficient-related terms  $A$ .

Based on these results, it does not appear that frequency filtering the signals input into the Bayesian algorithm to those frequencies used in the conventional analysis significantly reduces the sample thickness dependence observed in the shortened Lexan<sup>TM</sup> data from either laboratory.

## 7.4.2 Iteration of the Bayesian method

Another proposed idea, which was applied to the shortened Lexan<sup>TM</sup> data taken by our laboratory, was to iterate the Bayesian algorithm. The Bayesian model for one-mode plastic data contained three parameters to be estimated:  $A$ ,  $\beta$ , and  $c$ . The iteration process consisted of first running the Bayesian algorithm with  $A = 1$ . By setting  $A$  to one, all the

TABLE 7.11: Comparison of the Bayesian-estimated nBUA when  $A$  is allowed to vary and when  $A$  is set to 1.

<b>Sample thickness (mm)</b>	<b>11 mm</b>	<b>14 mm</b>	<b>18 mm</b>	<b>22 mm</b>	<b>26 mm</b>	<b>30 mm</b>
<b>Original Bayesian (<math>A \neq 1</math>)</b>	4.45	4.41	4.41	4.39	4.38	4.36
<b>Iterated Bayesian (<math>A = 1</math>)</b>	4.73	4.61	4.53	4.48	4.46	4.41

loss should be put into the  $\beta$  term, thus providing an upper limit for the slope of attenuation. This first step also provided the estimate for the speed,  $c$ . The second step of the iteration was to rerun the Bayesian algorithm with the speed parameter set to the value estimated in step one, the upper limit of  $\beta$  to be that value given by step one, and allowing  $A$  to vary between 0 and 1. For both step one and step two, the Bayesian algorithm is only estimating two parameters since the other parameter is fixed at a constant value. This iteration of the Bayesian method was applied to 6 of the 11 sample thicknesses from the shortened Lexan<sup>TM</sup> sample.

The results of  $\beta$  from step one of the iterated Bayesian method are displayed in Table 7.11. As expected, when compared to the original Bayesian ( $A \neq 1$ ) estimates for nBUA, the results of  $\beta$  after step one are consistently larger since all of the loss must be accounted for by this term. Step one of the iterated Bayesian method also produced  $\beta$  values that were more sample thickness dependent than the original Bayesian method. This is likely caused by the sample-thickness dependence of the  $A$  term being folded into the  $\beta$  term since  $A$  was forced to be 1. The velocity estimated by step one of the Bayesian iteration was unchanged

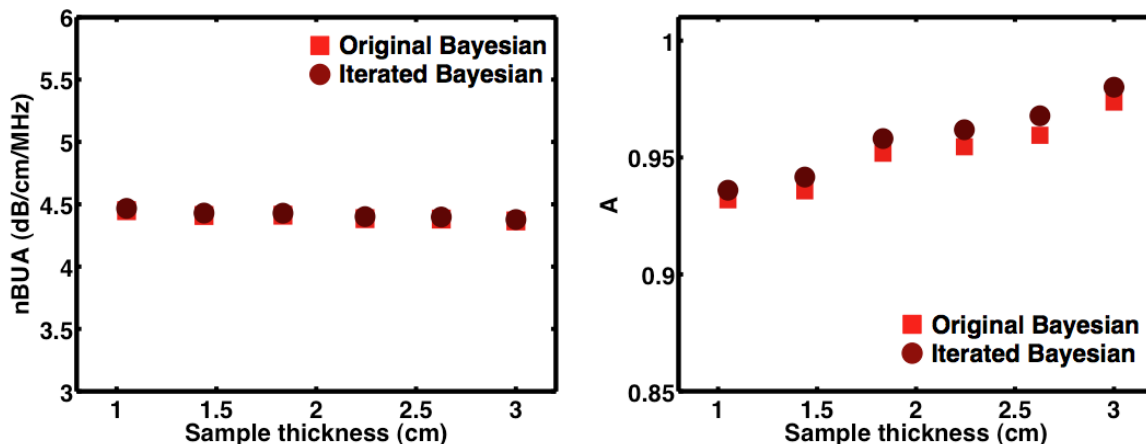


FIGURE 7.23: Comparison of the original Bayesian (red squares) and the iterated Bayesian (maroon circles) results for nBUA (left panel) and  $A$  (right panel) as a function of sample thickness from measurements on the shortened Lexan<sup>TM</sup> sample.

from the original Bayesian method.

For step two of the Bayesian iteration, the upper limit for  $\beta$  for all sample thicknesses was set to 4.75 dB/cm/MHz, which was the largest value estimated by step one, and the lower limit was set to 4.3 dB/cm/MHz. The velocity,  $c$ , was fixed at the value determined by step one. The results of step two of the iterative Bayesian method for nBUA and  $A$  are shown in Figure 7.23. There was no significant difference in the values estimated by the original Bayesian method and the iterative Bayesian method for either nBUA or  $A$ , and no reduction in the observed sample thickness dependence of these parameters.

## 7.5 Position of sample within the ultrasonic field

In most through-transmission studies, the transmitting and receiving transducers are placed approximately twice the focal length apart, with the sample being studied placed halfway between the two transducers such that the focus of the transmitting transducer is

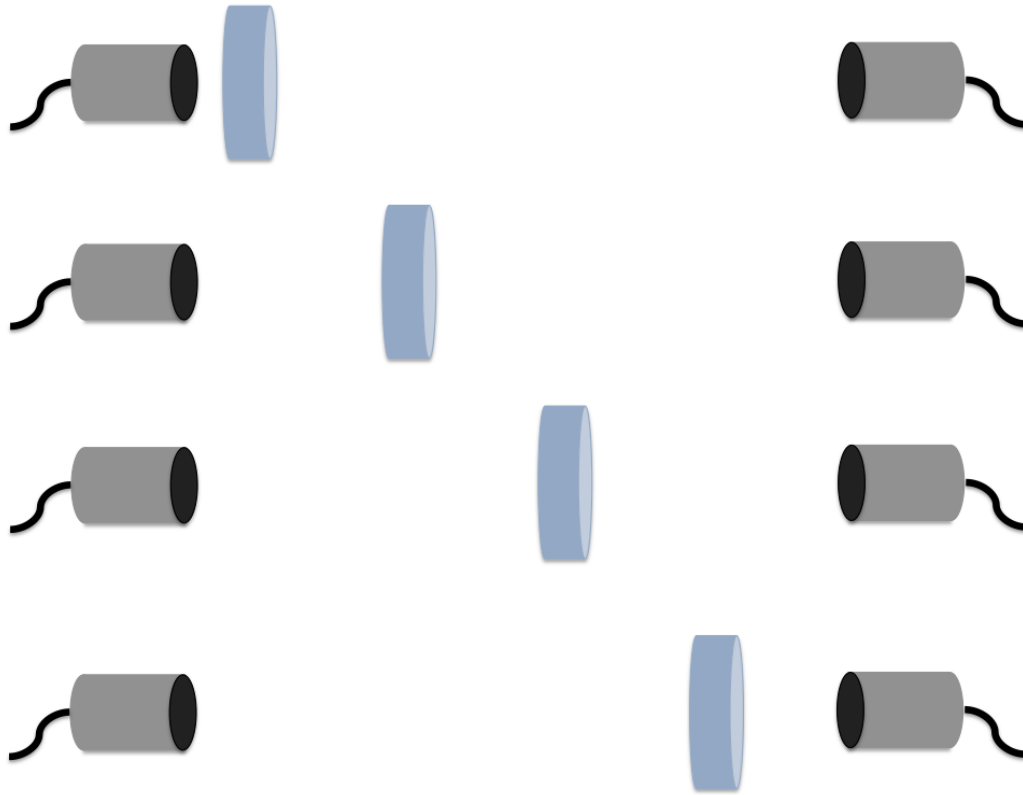


FIGURE 7.24: The experimental configuration for testing if the position of the sample within the ultrasonic field effects the received signal. The same experiment was performed with 1 MHz and 2.25 MHz center frequency transducers using Lexan<sup>TM</sup> samples with thicknesses of 20 mm and 40 mm.

located just inside the front surface of the sample. This transducer and sample arrangement was thought to produce the best acquired signal and reduce potential diffraction-related effects. Simulations done in our Laboratory by alum Kirk Wallace suggested that the position of the sample does not affect the signal acquired by the receiving transducer. To examine experimentally whether the location of the sample between the transmitting and receiving transducer does matter, two Lexan<sup>TM</sup> samples with thicknesses of approximately 20 mm and 40 mm were measured using both 1 MHz and 2.25 MHz focused transducers. For each set of transducers, the transmitting and receiving transducers were separated by approximately twice their reported focal length, which was 8 inches for the 1 MHz transducers and was 5 inches for the 2.25 MHz transducers. Data were acquired at six different distances from the transmitting transducer as illustrated in Figure 7.24 for both thicknesses of Lexan<sup>TM</sup>. For the 1 MHz transducers, the samples were placed at 0.5, 1, 2, 3, 4, and 5 inches from the transmitting transducer. For the 2.25 MHz transducers, data were acquired for when the samples were positioned 0.5, 1, 1.5, 2, 2.5, and 3 inches from the transmitting transducers.

The results for the 1 MHz transducers are shown in Figures 7.25 and 7.26. Figure 7.25 shows the radiofrequency signals that have propagated through the 20 mm thick Lexan<sup>TM</sup> sample positioned at 0.5 inches, 2 inches, and 4 inches from the transmitting transducer. The rf signals appeared not to change amplitude, shape, or arrival time. This was confirmed by measuring the peak-to-peak amplitudes of the acquired signals at different sample positions. Figure 7.26 shows the peak-to-peak amplitude of the signals traveling through both the 20 mm and 40 mm Lexan<sup>TM</sup> samples using the 1 MHz transducers. The amplitude stays exactly constant as a function of sample position in relation to the transmitting transducer

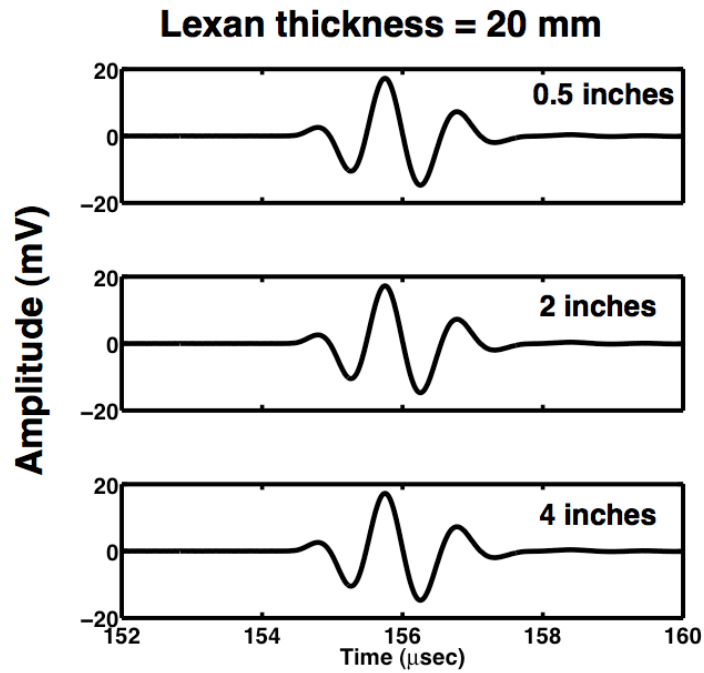


FIGURE 7.25: Radiofrequency signals that have propagated through a 20 mm thick Lexan<sup>TM</sup> sample positioned at 0.5 inches (top panel), 2 inches (middle panel), and 4 inches (bottom panel) from the transmitting transducer. This data was from the 1 MHz set of transducers.

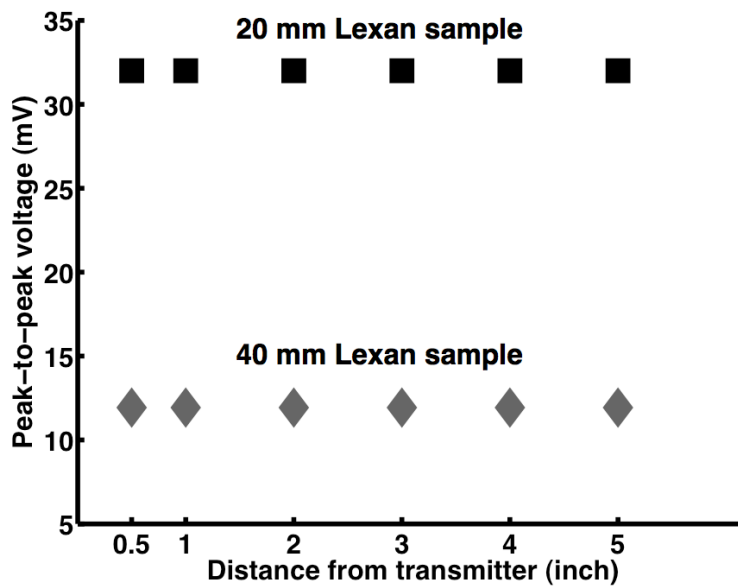


FIGURE 7.26: Peak-to-peak voltages of the rf signals that have propagated through 20 mm and 40 mm thick Lexan<sup>TM</sup> samples positioned at six distances from the 1 MHz transmitting transducer.

Similar results were observed for the 2.25 MHz transducers. These results suggested that the locations of the samples were not factors in the observed sample thickness variation.

## 7.6 Systematically varying the surface losses

In order to investigate the effects of varying the transmission (or insertion) losses without affecting the attenuation coefficient, multiple samples of Lexan<sup>TM</sup> were measured in the arrangement shown in Figure 7.27 using a focused matched pair of transducers with a nominal center frequency of 1 MHz. The number of samples placed between the aligned transducers ranged from one sample (2 interfaces) up to 4 samples (8 total interfaces). The complete set of sample combinations along with their respective total thicknesses and number of interfaces is listed in Table 7.12. The thickness of each individual Lexan<sup>TM</sup> sample was measured using digital calipers. For all of these sample combinations, the attenuation coefficients and slopes of attenuation (nBUA) should be the same since these parameters are intrinsic properties of Lexan<sup>TM</sup>. However, the insertion losses should vary based on the number of samples since the number of water-sample interfaces varies.

The phase velocities of all 15 Lexan<sup>TM</sup> sample combinations were determined using the broadband phase spectroscopy methods discussed in Section 3.3. The phase velocities as a function of frequency for all 15 sample combinations are shown in Figure 7.28. The average phase velocity at 1 MHz of all the sample combinations ( $N = 15$ ) was  $2193 \pm 1.0$  m/s, which are consistent with earlier measurements made by our Laboratory (Anderson *et al.*, 2010; Bauer *et al.*, 2007). To further validate the measurements, a prediction of the dispersion was

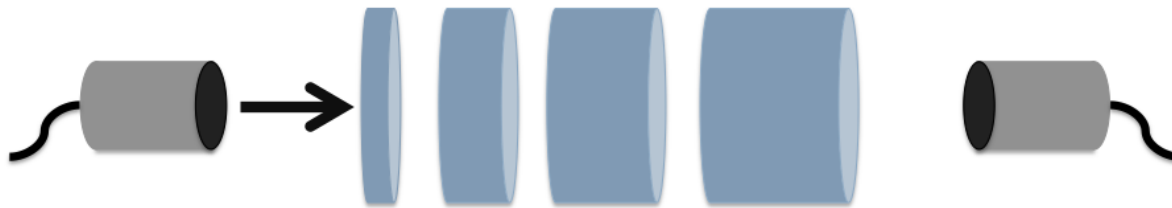


FIGURE 7.27: The experimental configuration for varying the surface losses or the Bayesian  $A$  term. The number of Lexan<sup>TM</sup> samples ranged from one sample (2 surfaces) between the transducers up to four samples (8 surfaces). This experiment was expected to alter the insertion losses or  $A$  term, but not to alter the attenuation coefficient or nBUA.

determined using the nearly local Kramers-Kronig relations with one subtraction (Waters *et al.*, 2003). The method for the Kramers-Kronig prediction is described in Section 3.3.1. The experimentally measured phase velocity at 1 MHz, the nominal center frequency, was used to set the absolute level of the predicted phase velocity. The Kramers-Kronig prediction agreed well with the average broadband phase velocity as shown in Figure 7.29.

The signal loss as a function of frequency for the 15 Lexan<sup>TM</sup> sample combinations is shown in Figure 7.30. For a fixed number of samples (or number of interfaces), the signal loss, at a given frequency, is larger for thicker samples, as expected. This is because signal loss is explicitly dependent on the sample thickness. The magnitude of the signal loss is also dependent on the number of interfaces that are present as the signal is propagated from the transmitting transducer to the receiving transducer. The signal losses were reduced to attenuation coefficients using the conventional analysis methods described in Section 3.3.2. The predicted insertion losses, determined using the transmission coefficients defined in Equation 3.17, are listed in Table 7.13 for the corresponding number of interfaces (2, 4, 6,



TABLE 7.12: The combination of Lexan<sup>TM</sup> samples used along with their respective effective length and number of surfaces.

<b>Sample(s)</b>	<b>Effective length (mm)</b>	<b># of surfaces</b>
<b>L1</b>	<b>10.04</b>	<b>2</b>
<b>L2</b>	<b>19.99</b>	<b>2</b>
<b>L3</b>	<b>29.99</b>	<b>2</b>
<b>L4</b>	<b>40.02</b>	<b>2</b>
<b>L1 + L2</b>	<b>30.03</b>	<b>4</b>
<b>L1 + L3</b>	<b>40.03</b>	<b>4</b>
<b>L1 + L4</b>	<b>50.06</b>	<b>4</b>
<b>L2 + L3</b>	<b>49.98</b>	<b>4</b>
<b>L2 + L4</b>	<b>60.01</b>	<b>4</b>
<b>L3 + L4</b>	<b>70.01</b>	<b>4</b>
<b>L1 + L2 + L3</b>	<b>60.02</b>	<b>6</b>
<b>L1 + L2 + L4</b>	<b>70.05</b>	<b>6</b>
<b>L1 + L3 + L4</b>	<b>80.05</b>	<b>6</b>
<b>L2 + L3 + L4</b>	<b>90.00</b>	<b>6</b>
<b>L1 + L2 + L3 + L4</b>	<b>100.04</b>	<b>8</b>

or 8). The mass density of these Lexan<sup>TM</sup> samples were measured, using a mass scale and volume measurements, to be approximately 1193 kg/m<sup>3</sup>. The attenuation coefficients as a function of frequency are displayed in Figure 7.31 for the individual sample combinations (N=15) as well as the average attenuation coefficient. All 15 combination of Lexan<sup>TM</sup> samples produced similar attenuation coefficients even though the number of interfaces varied from 2 surfaces up to 8 surfaces. This implies that the predicted insertion losses in Table 7.13 were

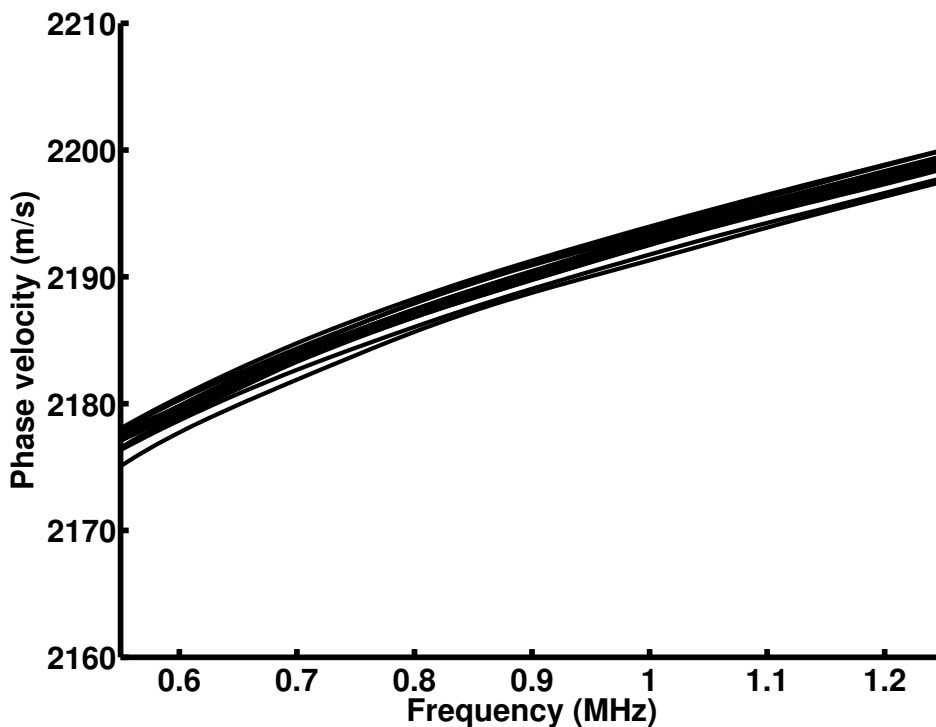


FIGURE 7.28: The phase velocities as a function of frequency, determined by conventional phase spectroscopy, for the 15 Lexan<sup>TM</sup> sample combinations listed in Table 7.12.

reasonably accurate.

A comparison of the Bayesian-derived and conventionally-derived phase velocity at 1 MHz as a function of sample length are shown in Figure 7.32 for all 15 sample combinations. The color of each data point represents the number of sample interfaces that the ultrasonic wave propagated through for that particular data set. The phase velocities estimated by the Bayesian algorithm agreed very well with the phase velocities determined using phase spectroscopy. This implies that varying the number of interfaces does not affect phase velocities measurements by either method of analysis.

The slope of the attenuation coefficient (nBUA) determined using conventional analysis methods showed a slight dependence on sample length and no systematic dependence on the

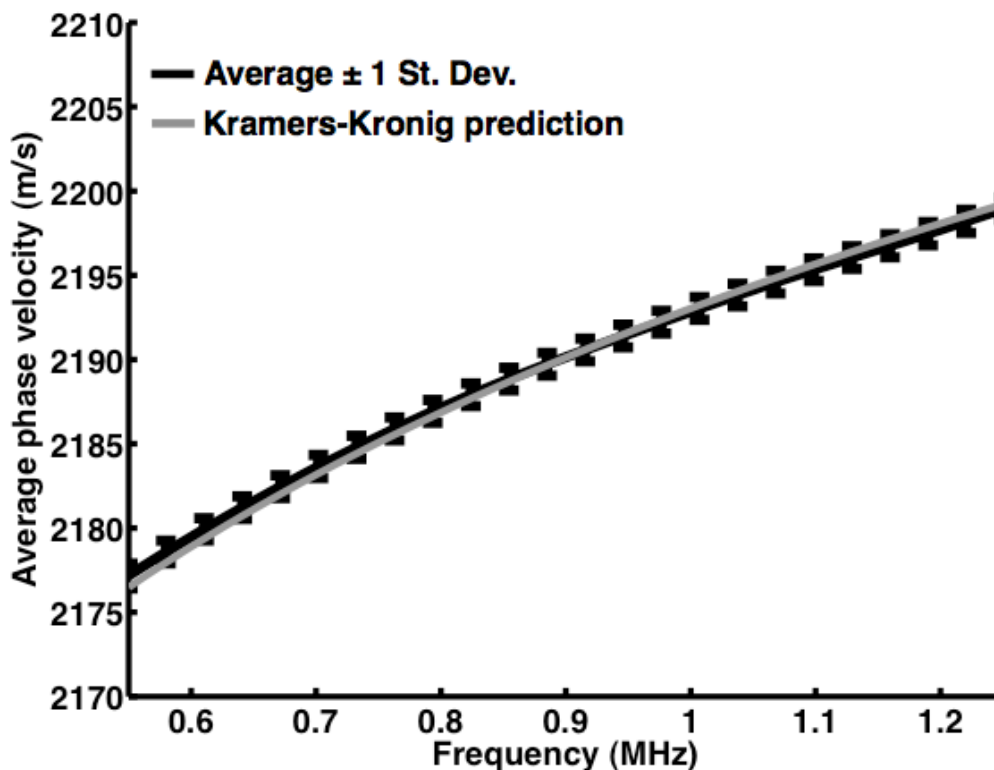


FIGURE 7.29: The average phase velocity of the 15 Lexan<sup>TM</sup> sample combinations and the Kramers-Kronig prediction for the dispersion. Error bars are plus or minus one standard deviation.

number of interfaces, as seen in Figure 7.33. This result is consistent with the fact that nBUA should only be dependent on the losses within the sample and not the losses occurring at the interfaces. In contrast, the Bayesian-estimated nBUA displayed a significant dependence on sample thickness, causing it to differ substantially from the conventional result, especially for total sample thicknesses greater than 50 mm. For the thickest total sample length ( $d \sim 100$  mm), the Bayesian-determined nBUA was 0.65 dB/cm/MHz smaller than the nBUA determined using conventional analysis methods.

Figure 7.34 shows the results, as a function of sample thickness, for  $A$  determined using Bayesian probability theory compared to the predicted transmission coefficient-related term,

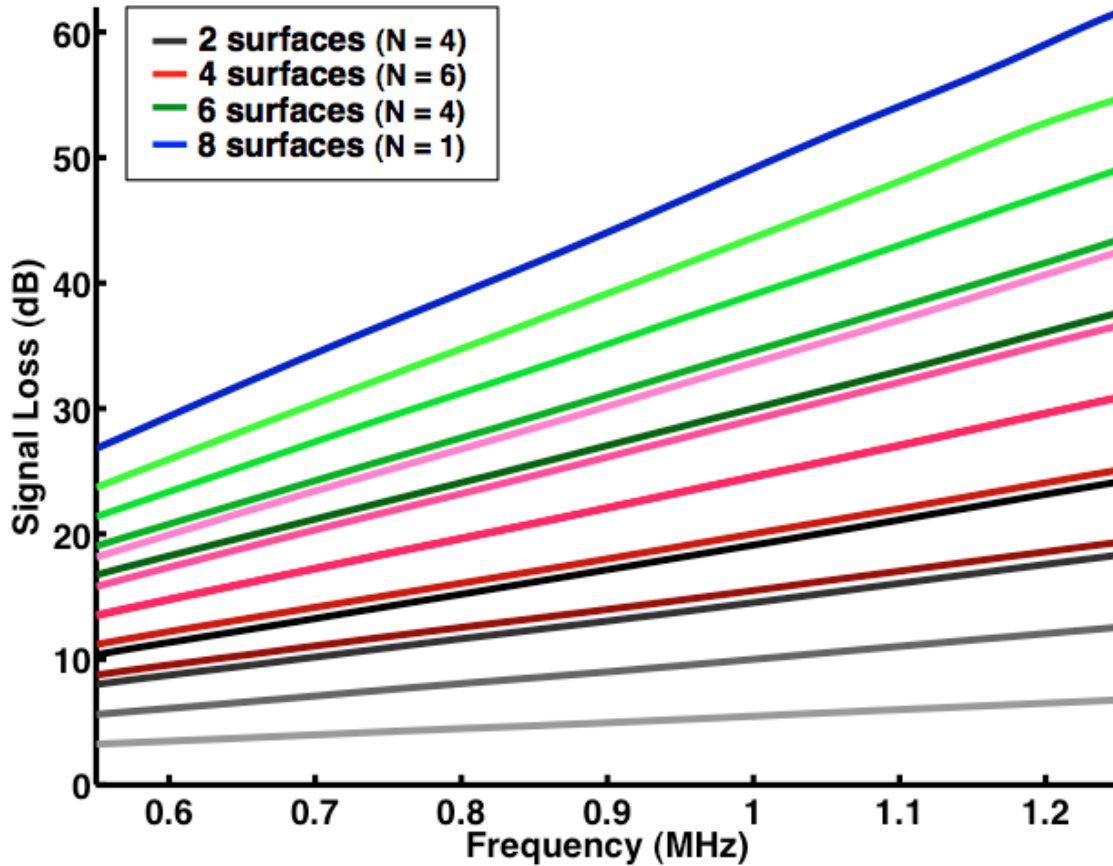


FIGURE 7.30: Signal losses of the 15 Lexan™ sample combinations as listed in Table 7.12. The different shades of black, red, green, and blue represent different combinations (or total thickness) of samples with 2, 4, 6, and 8 interfaces, respectively.

TABLE 7.13: The predicted insertion losses and the predicted transmission coefficient-related  $A$  terms for the number of total sample interfaces.  $A_2$ ,  $A_4$ ,  $A_6$ , and  $A_8$  represent the  $A$  term for 2, 4, 6, and 8 total interfaces, respectively.

<b># of surfaces</b>	<b>Predicted Insertion Loss (dB)</b>	<b>Predicted <math>A</math></b>
<b>2</b>	<b>0.68</b>	<b><math>A_2 = 0.92</math></b>
<b>4</b>	<b>1.37</b>	<b><math>A_4 = (A_2)^2 = 0.85</math></b>
<b>6</b>	<b>2.05</b>	<b><math>A_6 = (A_2)^3 = 0.79</math></b>
<b>8</b>	<b>2.73</b>	<b><math>A_8 = (A_2)^4 = 0.73</math></b>

as given in Table 7.13. Since the impedance difference between the water and the Lexan<sup>TM</sup> samples, which is determined using the phase velocity at the center frequency and the mass density of the media, does not change with sample thickness, the predicted  $A$  terms are also independent of the total sample thickness. In contrast, the Bayesian-estimated  $A$  terms displayed a noticeable dependence on sample thickness, although the trend changed with the number of the interfaces present. For two interfaces (one sample), the Bayesian-estimated transmission coefficient-related term increased linearly with sample thickness and had a value higher than that predicted using conventional methods. This implies that for thicker samples, less loss was attributed to the  $A$  term. This result was unexpected since the corresponding nBUA values also decreased with increasing sample thickness (for one sample present). Therefore, as the sample thickness increased, the net total loss (both insertion loss and sample loss) decreased. A similar trend was seen for four surfaces (two samples), until the sample thickness exceeded 60 mm. For a total sample thickness less than 60 mm, the

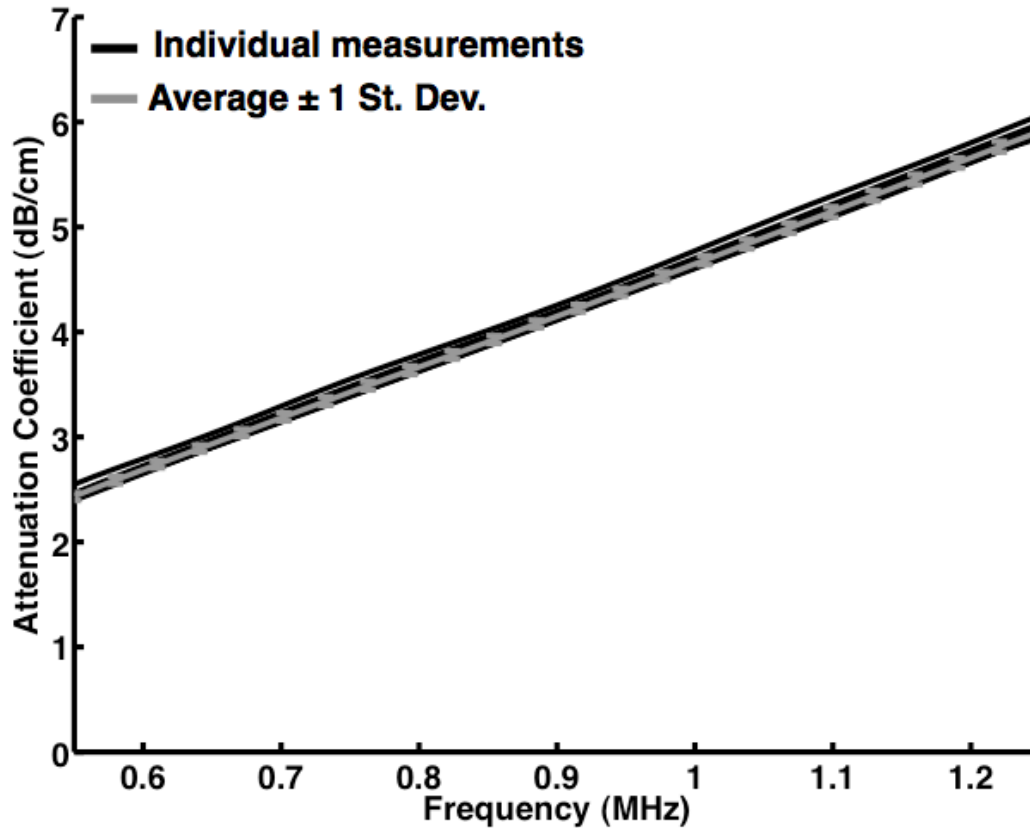


FIGURE 7.31: The attenuation coefficients of the 15 Lexan<sup>TM</sup> sample combinations (black lines) along with the average attenuation coefficient (gray line). Error bars represent plus or minus one standard deviation.

Bayesian-estimated  $A$  term increased with sample thickness and was larger than the predicted  $A$  term. When the total sample thickness exceeded 60 mm, the Bayesian transmission coefficient-related  $A$  term started to decrease and grew closer in value to the predicted value. For 6 surfaces (three samples), the Bayesian  $A$  term systematically decreased with increasing sample thickness, starting off larger than the predicted value but then becoming smaller than the predicted value. This trend continued with the data from 8 surfaces (four samples), with the  $A$  term obtained with Bayesian analysis being significantly smaller than that predicted.

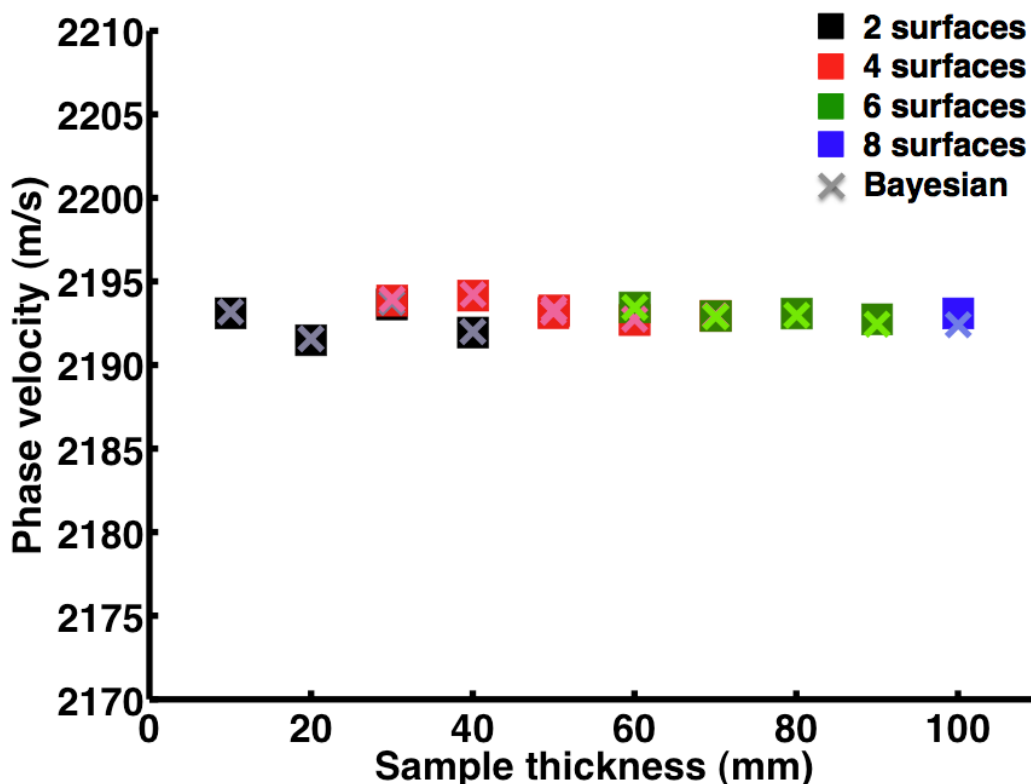


FIGURE 7.32: The phase velocities at 1 MHz as a function of total sample thickness using both conventional phase spectroscopy (squares) and Bayesian analysis (crosses) for the 15 combinations of Lexan<sup>TM</sup> samples listed in Table 7.12. The colors of the squares and crosses represent the number of water-sample interfaces that are present for that data set.

The conventional method of determining the transmission coefficient-related term  $A$ , by finding the zero-frequency intercept of the signal loss curve, was also applied to this data set and the results are shown as a function of the number of interfaces in Figure 7.35. The  $A$  terms based on the signal loss intercept displayed even more dependence on sample length than the calculated and Bayesian-estimated  $A$  terms. Even more problematic was the fact that the majority of the transmission coefficient-related terms determined using the signal loss intercept had values greater than one, which implied that energy was gained instead of lost at the surfaces. One possible explanation is diffraction, which will be discussed later in

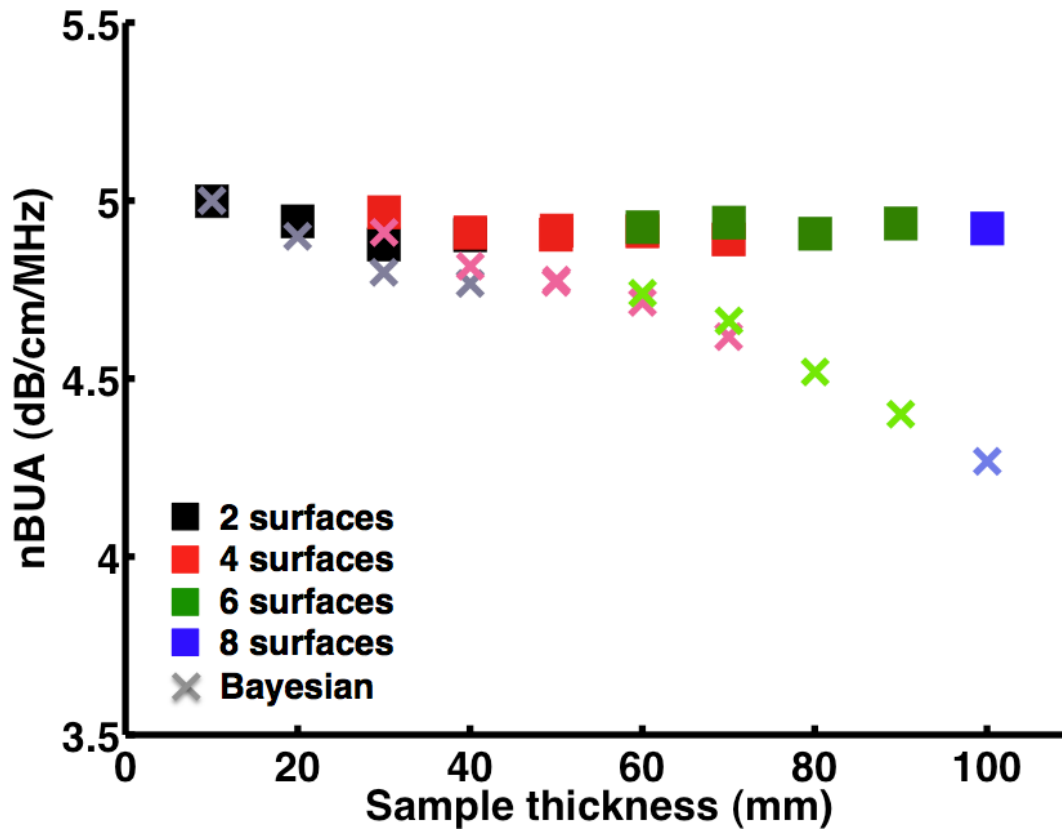


FIGURE 7.33: The slopes of attenuation (nBUA) as a function of total sample thickness using both conventional analysis (squares) and Bayesian analysis (crosses) for the 15 combinations of Lexan<sup>TM</sup> samples listed in Table 7.12. The colors of the squares and crosses represent the number of water-sample interfaces that are present for that data set.

Section 7.8.

## 7.7 Constant thickness while varying surface losses

In order to explore further the potential effects caused by varying the surface losses (by increasing the number of interfaces), the five combinations of Lexan<sup>TM</sup> samples that had a total sample length of approximately 100 mm were measured, as illustrated in Figure 7.36. One configuration had two samples (4 interfaces), three configurations had three samples



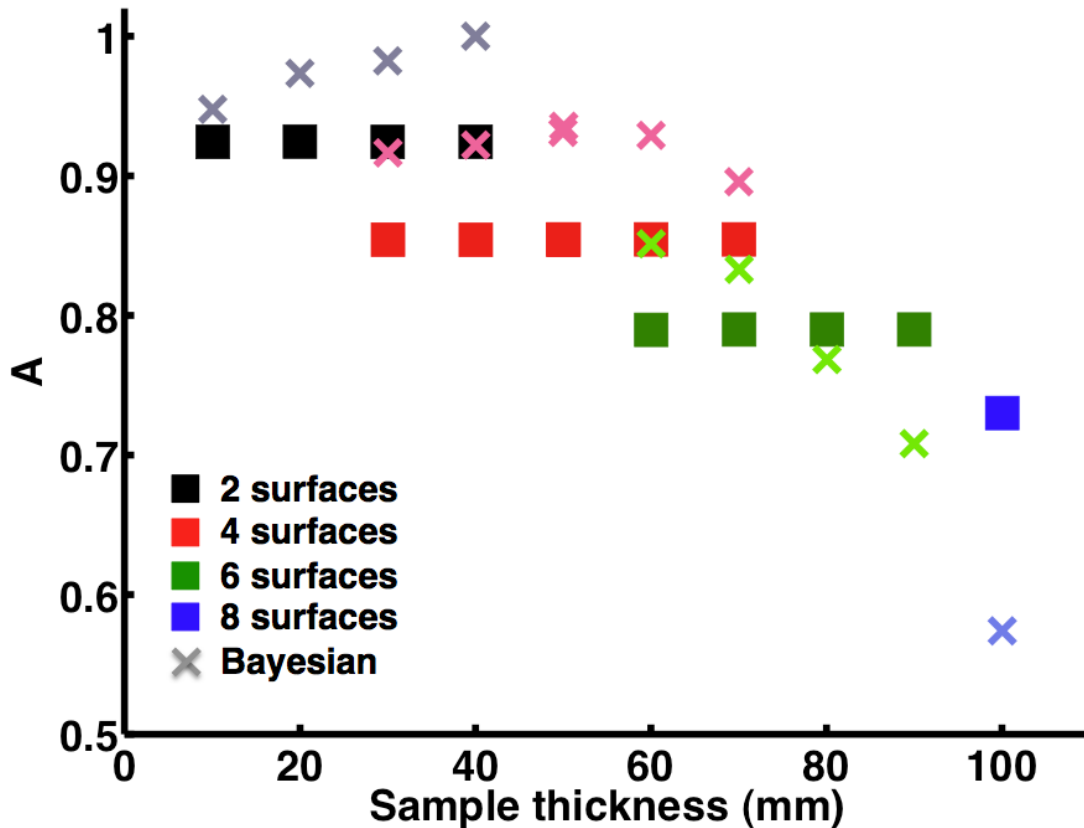


FIGURE 7.34: The transmission coefficient-related  $A$  terms as a function of total sample thickness using Bayesian analysis (crosses) and calculated (squares) for the 15 combinations of Lexan<sup>TM</sup> samples listed in Table 7.12. The colors of the squares and crosses represent the number of water-sample interfaces that are present for that data set.

(6 interfaces), and another configuration had four samples (8 interfaces) positioned between the transmitting and receiving transducers. In this experiment, a matched pair of 0.5 inch diameter, 4 inch focus transducers with a nominal center frequency of 1 MHz were used in a through-transmission arrangement. As seen in Figure 7.37, the radiofrequency (rf) signals acquired from the five sample configurations have similar shapes (and thus similar frequency components), but have different amplitudes and arrive at different times. The peak-to-peak amplitudes for the five Lexan<sup>TM</sup> sample combinations are displayed in Figure 7.38, and shows that as the number of water-sample interfaces increased, the signal amplitude

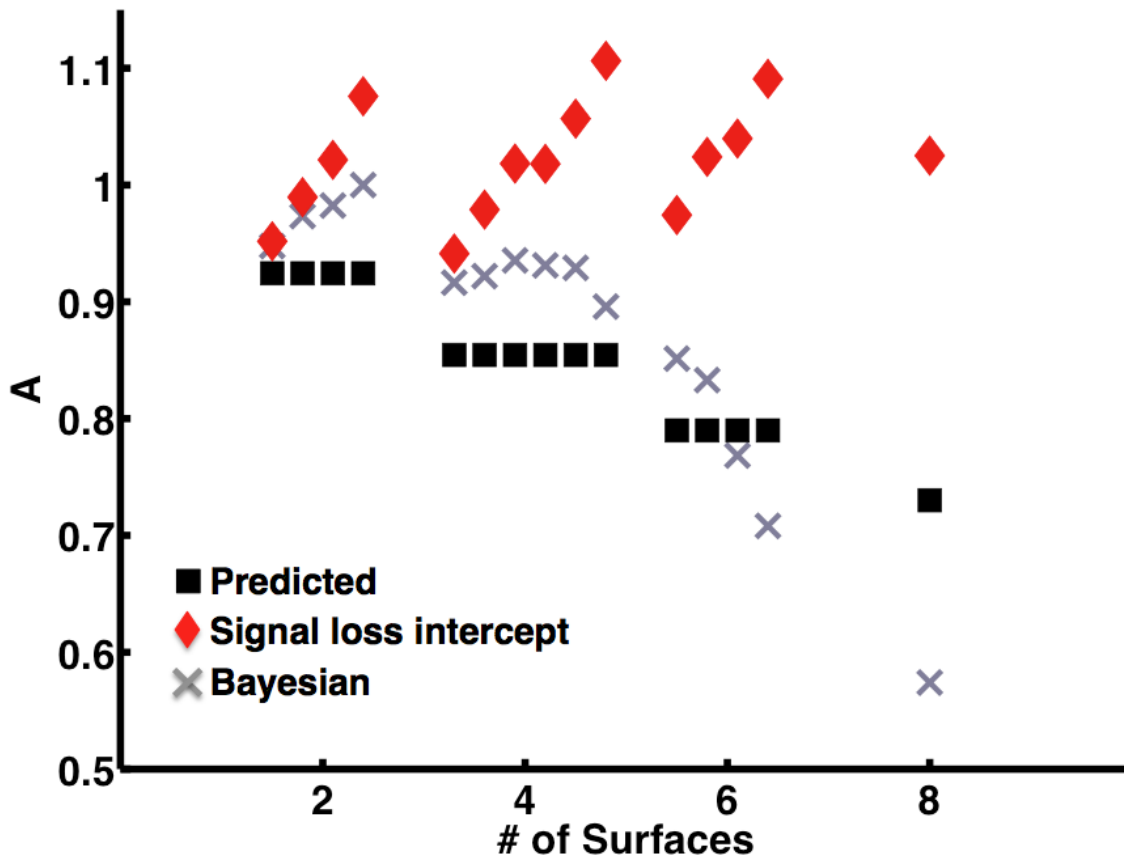


FIGURE 7.35: The transmission coefficient-related  $A$  terms as a function of total number of interfaces using impedance differences (black squares), Bayesian analysis (gray crosses), and the zero-frequency intercepts of the signal loss curve (red diamonds) for the 15 combinations of Lexan<sup>TM</sup> samples listed in Table 7.12.

decreased systematically.

The data acquired for the five sample combinations were analyzed using both conventional and Bayesian methods. A comparison of the phase velocity at 1 MHz determined using both analysis methods is shown in Figure 7.39. For both conventional and Bayesian analysis, there was a slight increase in the phase velocity as the number of interfaces increased, although the change was only  $\sim 1$  m/s for each additional sample. The Bayesian and conventional phase velocities differed in value by approximately 1 m/s for all five sample combinations.

Signal loss versus frequency plots for the five sample combinations determined using conventional analysis are shown in Figure 7.40. As anticipated, the signal losses, at a given frequency, increased with an increasing number of interfaces. The offset at 1 MHz between four and six interfaces and six and eight interfaces was, on average, 0.86 dB. Based on predicted insertion losses determined using the calculated transmission coefficients, this offset was expected to be approximately 0.68 dB. Although the signal loss offsets were not identical to the predicted values, the attenuation coefficients of the five sample combinations were very similar, as shown in Figure 7.41. The attenuation coefficient at 1 MHz did slightly increase with an increase in the number of interfaces, but the change was only 0.02 dB/cm.

The slope of the attenuation (nBUA) for both conventional and Bayesian analysis are shown in Figure 7.42 for the five combinations of Lexan<sup>TM</sup> samples. For both types of analysis, the resulting nBUAs were approximately independent of the number of interfaces present, which should be expected. However, the Bayesian-estimated nBUAs were, on average, 0.65 dB/cm/MHz smaller than the nBUAs determined using conventional methods. A similar trend was observed for the transmission coefficient-related  $A$  terms shown in Figure 7.43. As

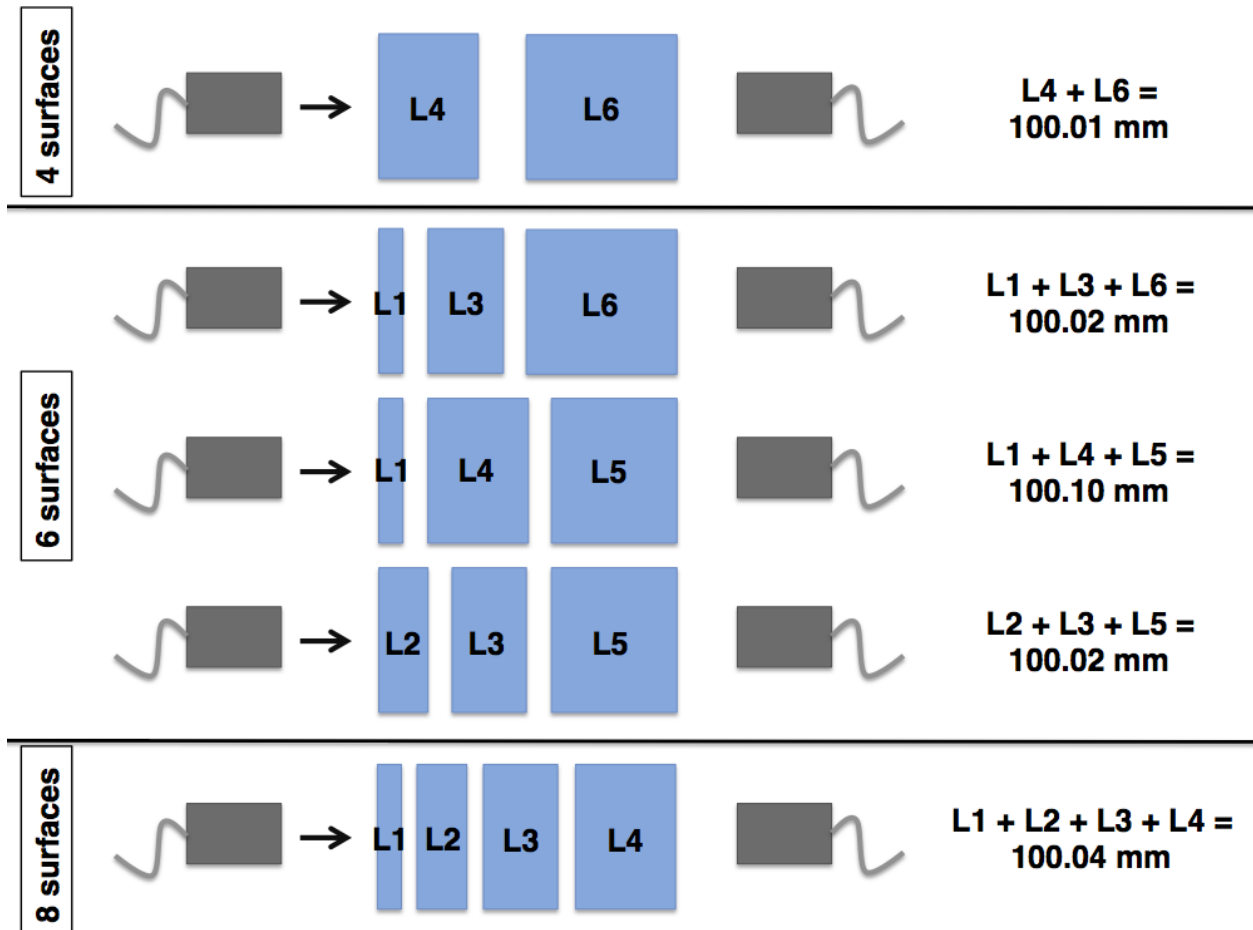


FIGURE 7.36: The experimental and sample configurations used for varying the number of interfaces while keeping the overall sample thickness approximately constant. In this experiment, two samples (4 interfaces), three samples (6 surfaces), or four samples (8 surfaces) were placed between two matched, focused 0.5 inch diameter transducers with a nominal center frequency of 1 MHz. All five sample combinations yielded a total sample length of approximately 100 mm.

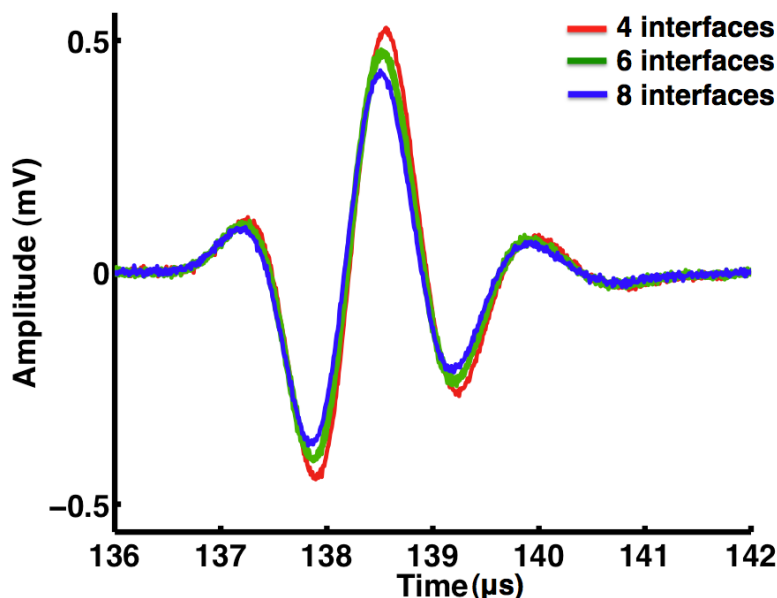


FIGURE 7.37: The radiofrequency (rf) traces acquired from going through two samples (red), three samples (green), or four samples (blue) of Lexan<sup>TM</sup>. As the number of samples (and thus interfaces) increased, the rf traces shifted to the left in time and decreased in peak-to-peak amplitude.

predicted, the transmission coefficient-related  $A$  term depended on the number of interfaces present. However, the Bayesian estimated  $A$  was, on average, 0.16 smaller than the predicted value. Based on the results for both nBUA and the  $A$  terms, the Bayesian algorithm is allocating more loss to insertion (that is, surface) losses and less loss to bulk (sample) losses than the conventional analysis. When both types of losses (surface and bulk) are taken into account using the expression  $A * \exp[-\beta f d]$ , the conventional analysis has more overall loss than that estimated by the Bayesian algorithm, as illustrated in Figure 7.44. In this figure, the predicted time-domain sample traces for conventional and Bayesian analysis were generated using the values of  $A$ ,  $\beta$ , and  $c$  determined by the respective analysis method and inserted into the propagation model discussed in Section 3.4. Based on these results, conventional analysis appeared to overestimate the total loss producing large residuals, whereas

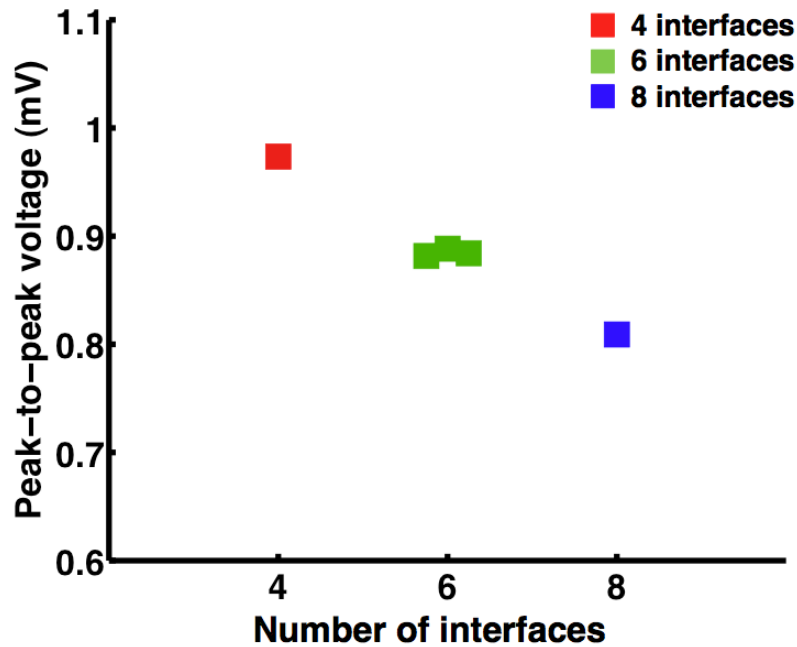


FIGURE 7.38: The peak-to-peak amplitude of the radiofrequency signals that propagated through the five Lexan<sup>TM</sup> sample combinations that all had an approximate total sample length of 100 mm, as shown in Figure 7.36. As the number of water-sample interfaces increased, the signal amplitude decreased systematically.

the Bayesian method seemed to fit the experimentally acquired data quite accurately.

## 7.8 Effects of Diffraction

The formula for the attenuation coefficient given in Equation 3.23 makes two assumptions about the ultrasonic field. The first is that the phase sensitive sum over the face of the receiving transducer, which results in some phase cancellation, does not change between measurements. The second is that the axial diffractive pattern remains unchanged between measurements. If these assumptions are not valid, then the observed signal loss may have contributions arising from these additional factors, thus producing an error in the attenuation

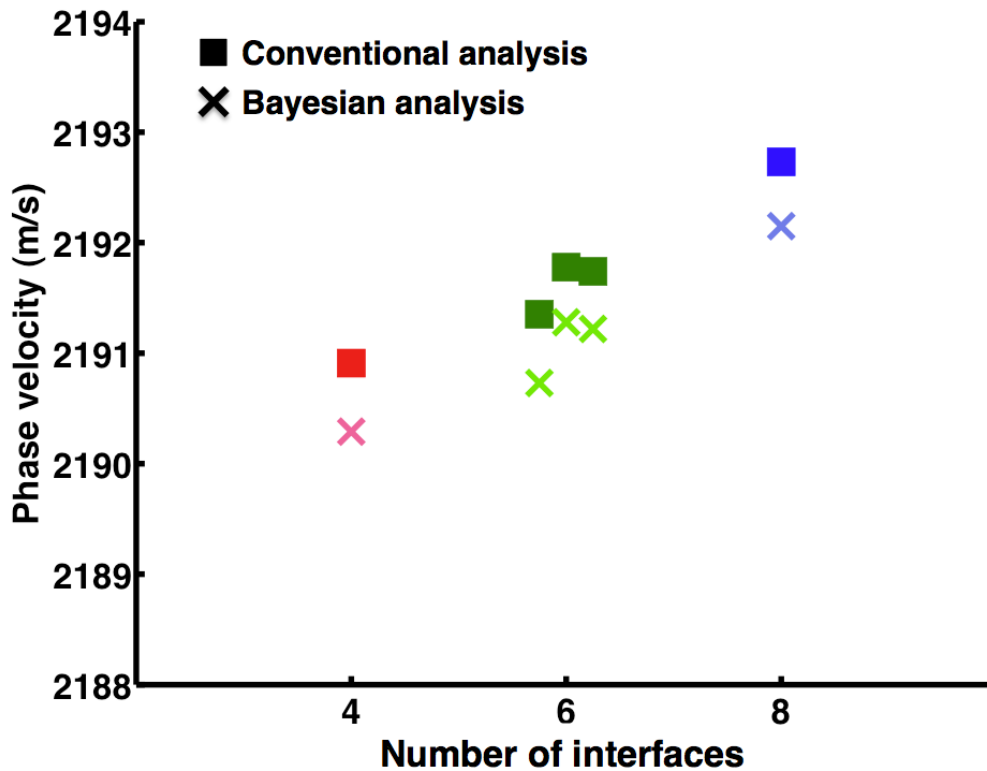


FIGURE 7.39: Phase velocity at 1 MHz as a function of the number of interfaces of the five Lexan<sup>TM</sup> sample combinations that all had an approximate total sample length of 100 mm, determined using conventional phase spectroscopy (squares) and Bayesian analysis (crosses). The colors of the squares and crosses represent the number of interfaces present.

coefficient (Lloyd, 2010). As will be discussed, diffractive effects depend on the thickness of the sample being insonified. Therefore, diffraction was a possible cause for the sample thickness dependence observed in the equine bone study discussed in Chapter 6 and in the plastic studies discussed earlier in this chapter. An experimental diffraction correction has been published by Xu and Kaufman (1993). An independent derivation was carried out by Christopher Lloyd, an alumnus of the Laboratory for Ultrasonics ((Lloyd, 2010)). The formalism developed by Lloyd (2010) will be used in this section.

The near field distance ( $N$ ) for a given continuous wave (single frequency) of a planar

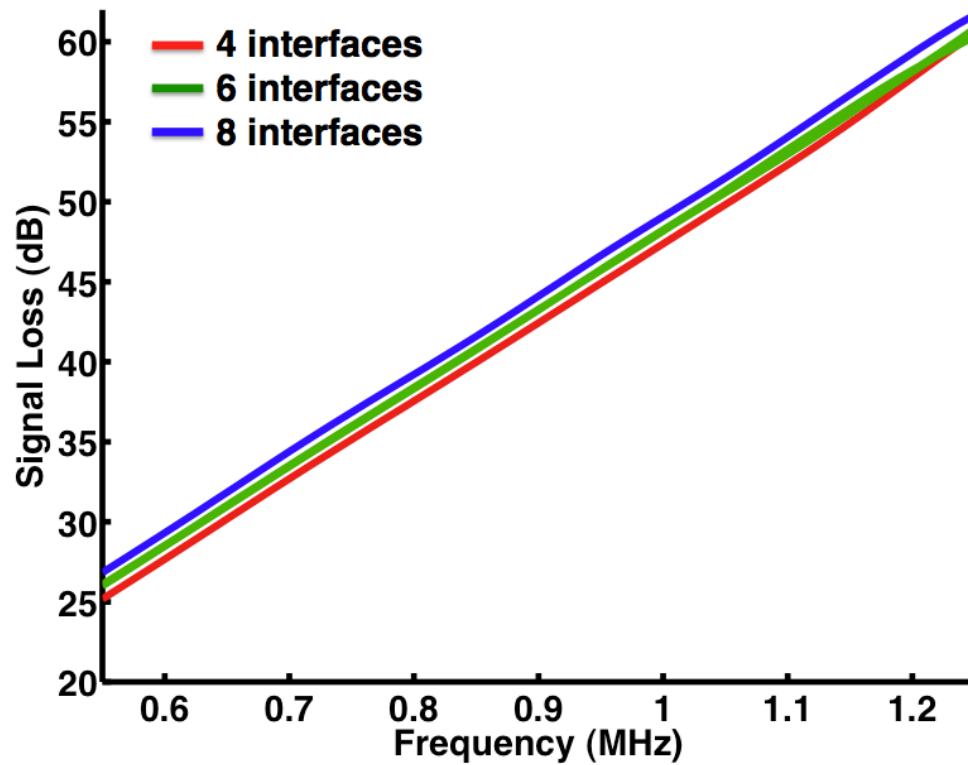


FIGURE 7.40: Signal losses of the five Lexan<sup>TM</sup> sample combinations that all had an approximate total sample length of 100 mm, determined using conventional log-spectral subtraction. At a given frequency, the signal loss increased with an increasing number of interfaces.



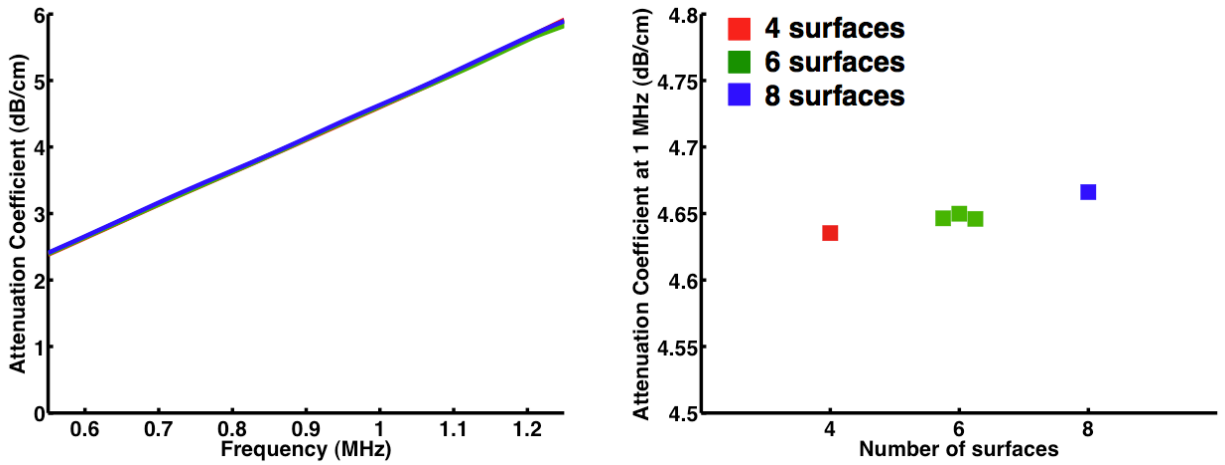


FIGURE 7.41: Left: Attenuation coefficients versus frequency of the five Lexan<sup>TM</sup> sample combinations that all had an approximate total sample length of 100 mm. Right: The attenuation coefficients at 1 MHz as a function of the number of interfaces.

transducer is given by

$$N = \frac{a^2}{\lambda} * \left[ 1 - \left( \frac{\lambda}{2a} \right)^2 \right] \quad (7.11)$$

where  $a$  is the radius of the transmitting transducer and  $\lambda$  is the wavelength of the emitted ultrasonic signal. The near field distance is the last and strongest of the maxima in the ultrasonic field along the axial direction. For all of the transducers (0.5 inch to 1.125 inch diameters) and frequencies (0.5 to 2.25 MHz) used in this thesis, the term  $\lambda/2a \ll 1$  and can be ignored. Therefore, the near field distance can be approximated by

$$N \approx \frac{a^2}{\lambda} = \frac{a^2 f}{c} \quad (7.12)$$

where  $c$  is the speed of sound of the material and  $f$  is the frequency of the signal. For a given experimental measurement, the frequency and transducer radius are fixed, and therefore, by Equation 7.12 the near field distance is inversely proportional to the sound speed.

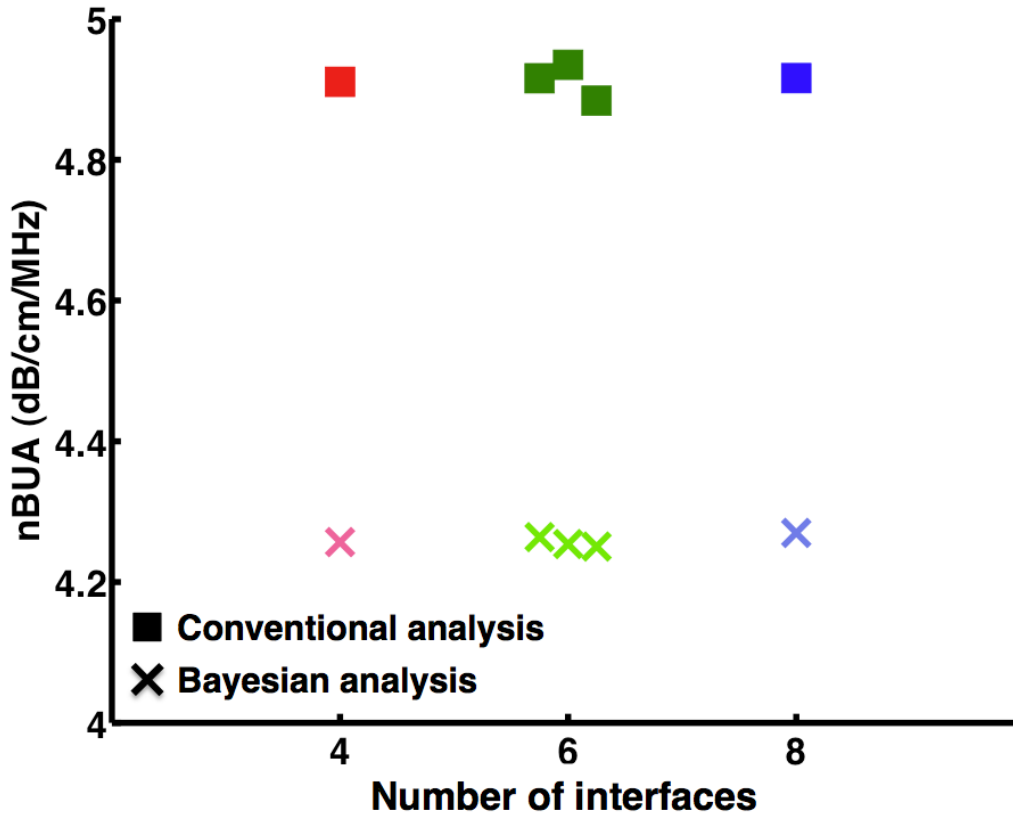


FIGURE 7.42: Slopes of attenuation (nBUA or  $\beta$ ) as a function of the number of interfaces of the five Lexan<sup>TM</sup> sample combinations that all had an approximate total sample length of 100 mm, determined using conventional analysis (squares) and Bayesian analysis (crosses). The colors of the squares and crosses represent the number of interfaces present.

Equation 7.12 can be rewritten as

$$N \cdot c = \text{constant} = a^2 f \quad (7.13)$$

The terms on the right do not change for a given experimental setup because the frequency and aperture of the transmitting transducer remain fixed between measurements. The terms on the left are related to each other in an inverse manner. An interpretation of Equation 7.8 is that for a given fixed location in the diffractive field, the propagation distance to that specific location in the diffractive field varies inversely with the speed of sound of the propagation medium (Lloyd, 2010).

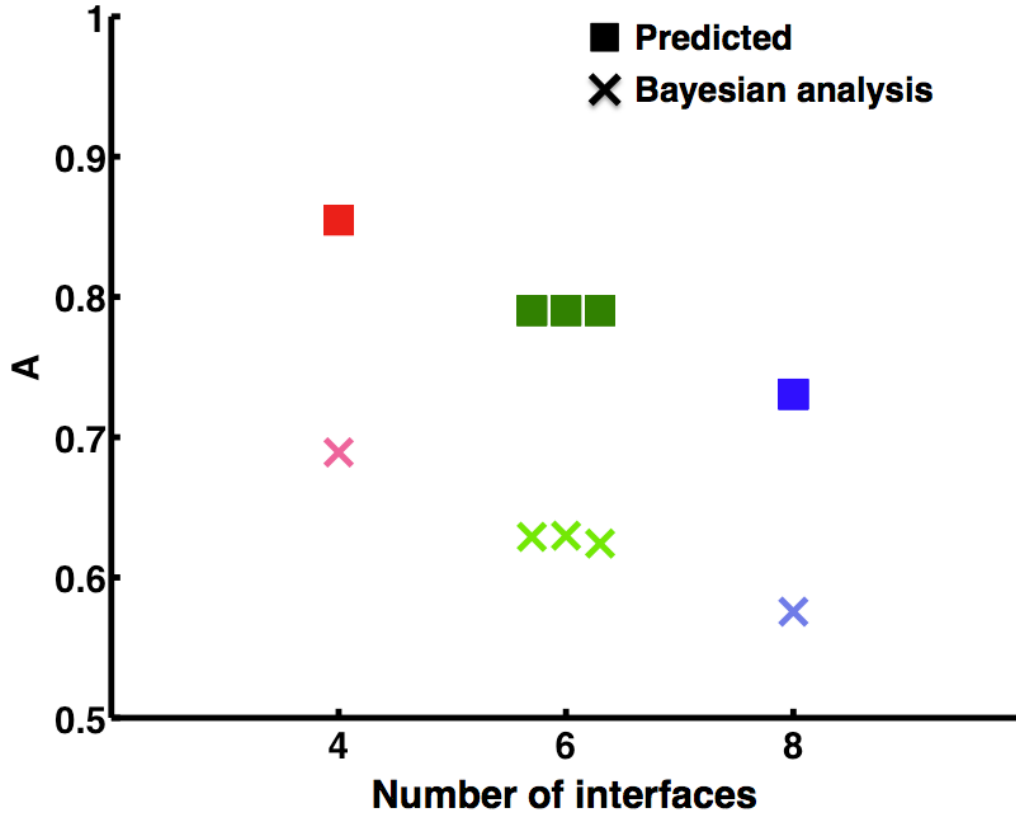


FIGURE 7.43: Transmission coefficient-related  $A$  terms as a function of the number of interfaces of the five Lexan<sup>TM</sup> sample combinations that all had an approximate total sample length of 100 mm, determined using Bayesian analysis (crosses) or calculated (squares). The colors of the squares and crosses represent the number of interfaces present.

The terms on the left side of Equation 7.8 can be rewritten as the product of the propagation distance between the transmitting and receiving transducers,  $L_{ref}$ , and the speed of sound in the host medium,  $c_{ref}$ , for a reference measurement as illustrated in Figure 7.45. This product,  $L_{ref}c_{ref}$ , is fixed. For the measurement of a sample with a speed  $c_{samp}$  and thickness  $d$ , the position of the receiving transducer,  $L_{samp}$  can be found by

$$L_{ref}c_{ref} = constant = (L_{samp} - d)c_{ref} + dc_{samp} \quad (7.14)$$

Equation 7.14 can be rearranged to solve for the position of the receiving transducer when

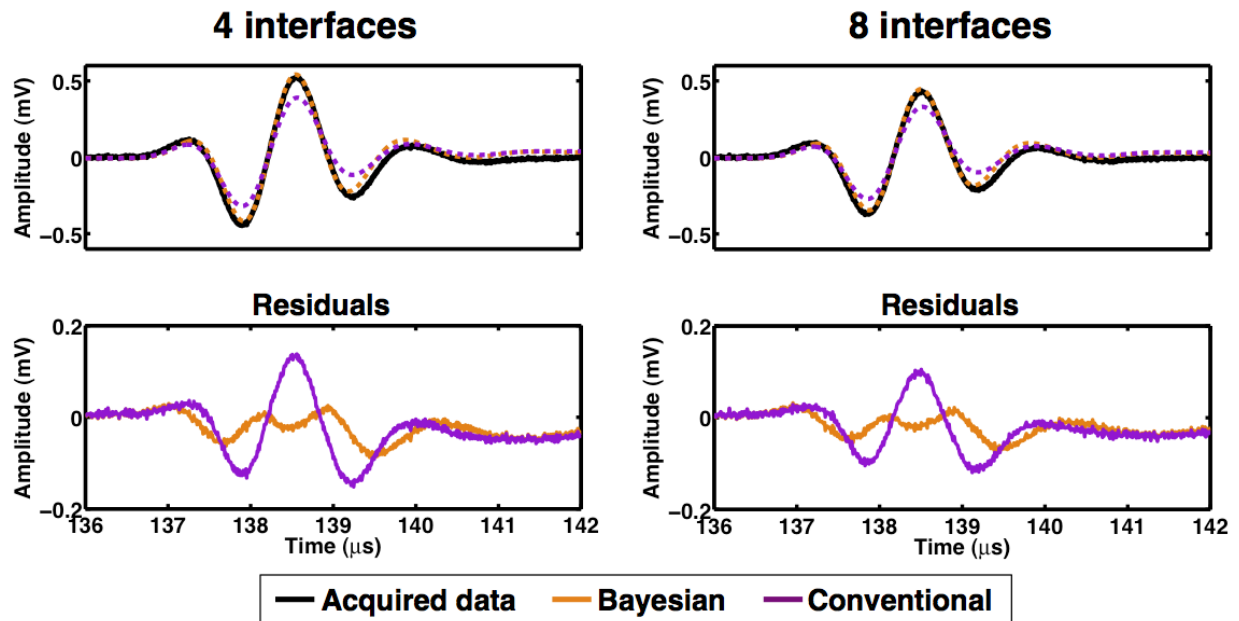


FIGURE 7.44: Predicted sample signals for conventional (purple) and Bayesian (orange) methods using their respective values of  $A$ ,  $\beta$ , and  $c$  in the propagation model discussed in Section 3.4 for the sample combination with 4 interfaces (left) and 8 interfaces (right). The black signal corresponds to the experimentally acquired trace. The bottom panel of each graph shows the residual (or difference) of the experimental signal and the predicted signals.

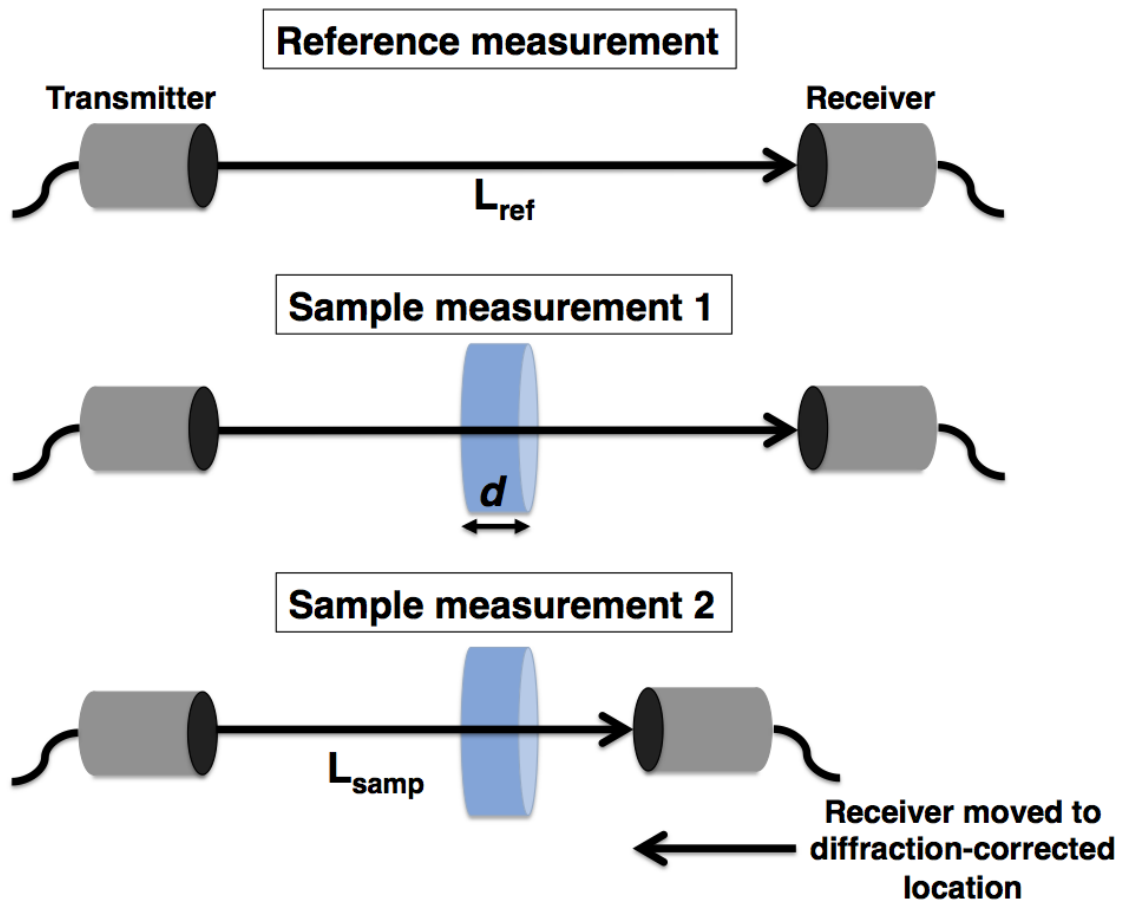


FIGURE 7.45: The experimental configuration for measuring the attenuation properties of the Lexan<sup>TM</sup> samples implementing the diffraction correction.

the sample is inserted

$$L_{samp} = L_{ref} + d \left( 1 - \frac{c_{samp}}{c_{ref}} \right) \quad (7.15)$$

Equation 7.15 has three regimes depending on the ratio of the sample speed of sound to the reference speed of sound. If the sample and the host medium have the same speeds of sound, then the path lengths between the transmitting and receiving transducers ( $L_{ref}$  and  $L_{samp}$ ) are the same, regardless of the sample thickness. If the speed of sound in the sample is less than that in the reference medium, the term in the parentheses is positive and  $L_{samp}$  is greater than  $L_{ref}$ . If the speed of sound in the sample is greater than that in the reference medium (as is true for all the studies in this thesis), the ratio of speeds is greater than one and the term in parentheses is negative. Therefore, the total path length for the sample measurement,  $L_{samp}$ , must be shorter than the path length for the reference measurement,  $L_{ref}$ , by a factor proportional to the sample thickness. Experimentally, this means that the receiving transducer must be moved closer to the transmitting transducer, by a distance of  $\Delta L = L_{samp} - L_{ref}$ , when taking the sample measurement in order to be at the same location in the diffractive field as in the reference measurement.

The effects of diffraction were studied using six samples of Lexan<sup>TM</sup> with thicknesses listed in Table 7.14. Measurements were taken using the same set of 1 MHz center frequency, focused transducers used in earlier studies in this chapter. The experimental diffraction corrections, given by Equation 7.15, were calculated using the measured phase velocities at the center frequency for each thickness of Lexan<sup>TM</sup>. Table 7.14 displays the diffraction correction for each of the six Lexan<sup>TM</sup> phantoms, with a negative sign indicating that the receiving transducer must be moved closer to the transmitting transducer when acquiring

TABLE 7.14: The mean thicknesses of the six Lexan<sup>TM</sup> samples used in the study on diffraction effects. The diffraction corrections were calculated using Equation 7.15. The negative correction indicates that the receiving transducer must be moved closer to the transmitting transducer for the sample measurements.

<b>Sample</b>	<b>Sample thickness (mm)</b>	<b>1 MHz Diffraction correction (<math>\Delta L</math>)</b>
L1	10.04	-4.76 mm
L2	19.99	-9.47 mm
L3	29.99	-14.21 mm
L4	40.02	-18.96 mm
L5	30.03	-23.71 mm
L6	40.03	-28.42 mm

the sample measurement. For each of the six Lexan<sup>TM</sup> samples, the three measurements illustrated in Figure 7.45 were acquired. Two sample measurements were acquired for each Lexan<sup>TM</sup> phantom: one measurement when the transmitting and receiving transducers were separated by the same propagation distance as the reference measurement,  $L_{ref}$ , and another measurement after the receiving transducer was moved by the diffraction-corrected distance listed in Table 7.14.

The peak-to-peak amplitudes of the sample signals acquired at the reference measurement transducer separation differed slightly from the amplitudes of the sample signals acquired at the diffraction-corrected transducer separation, as shown in Figure 7.46. The amplitudes of both the diffraction-corrected and the not diffraction-corrected sample signals displayed the same trend with sample thickness, decreasing logarithmically with increasing sample thickness, as expected. However, it was unexpected that the difference in peak-to-peak amplitude

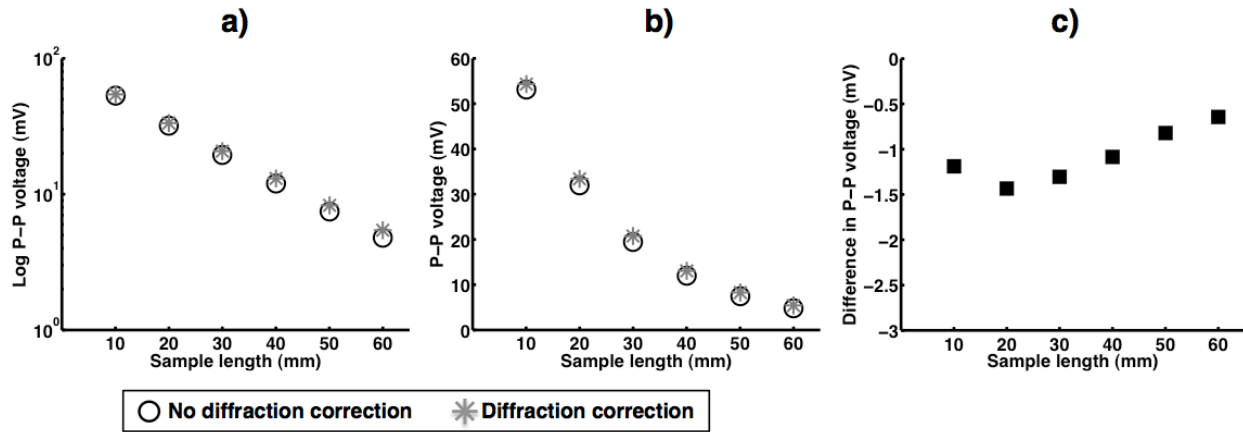


FIGURE 7.46: Peak-to-peak amplitude of the sample traces for the six Lexan<sup>TM</sup> phantoms for a typical (not diffraction corrected) measurement and one that has been corrected for diffraction. (a) The peak-to-peak amplitudes shown on a log scale. (b) The same peak-to-peak amplitudes displayed on a linear scale. (c) The difference in P-P amplitude between the not diffraction corrected sample signal and the diffraction corrected sample signal.

between the diffraction-corrected and the not diffraction-corrected sample signals seemed to decrease with increasing sample thickness. Since the diffraction correction is proportional to the sample thickness, it was expected that the amplitudes of diffraction-corrected and the not diffraction-corrected sample signals would diverge as the sample thickness increased.

Both sets of data (diffraction corrected and not diffraction corrected) on the six Lexan<sup>TM</sup> phantoms were analyzed with conventional and Bayesian methods. The phase velocities, as determined by conventional phase spectroscopy, are shown in Figure 7.47. The phase velocity at 1 MHz was consistent over the six samples measured and were consistent with the phase velocity measurements taken in Sections 7.6 - 7.7 on combinations of the same Lexan<sup>TM</sup> samples.

The attenuation coefficients for the six Lexan<sup>TM</sup> phantoms determined using conventional analysis methods are displayed in Figure 7.48 for both the diffraction-corrected and not diffraction-correction measurements. The attenuation coefficients from the not diffrac-



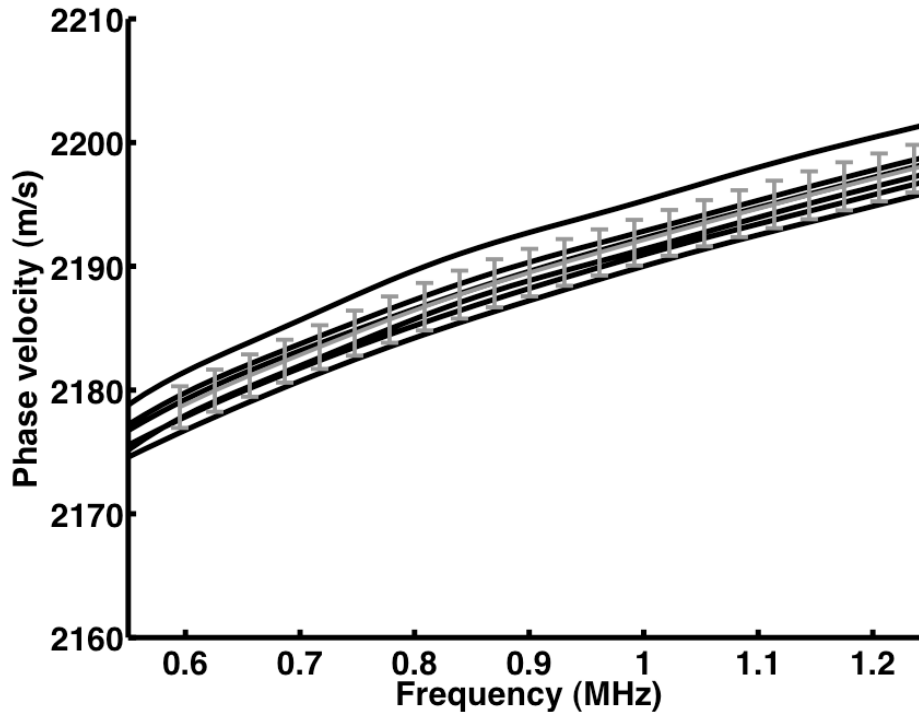


FIGURE 7.47: The phase velocities as a function of frequency, determined using conventional phase spectroscopy, for the six thicknesses of Lexan<sup>TM</sup> listed in Table 7.14. The average phase velocity ( $\pm$  one standard deviation) is also displayed.

tion corrected measurements on the six Lexan<sup>TM</sup> samples agreed remarkably well. This seemed to imply that diffraction effects were not significant. If the effects of diffraction were large enough and were not adequately compensated for, it was expected that the attenuation coefficients would show more disparities. This figure shows that the diffraction-corrected attenuation coefficient was smaller than the attenuation coefficient that was not diffraction corrected. This was consistent with the amplitude data shown in Figure 7.46, since the diffraction-corrected sample signals always had a larger peak-to-peak amplitude than the not diffraction corrected signals. An unexpected result was that the differences between the diffraction-corrected attenuation coefficients at 1 MHz and the not diffraction corrected attenuation coefficients were approximately constant with sample thickness, as listed in Ta-

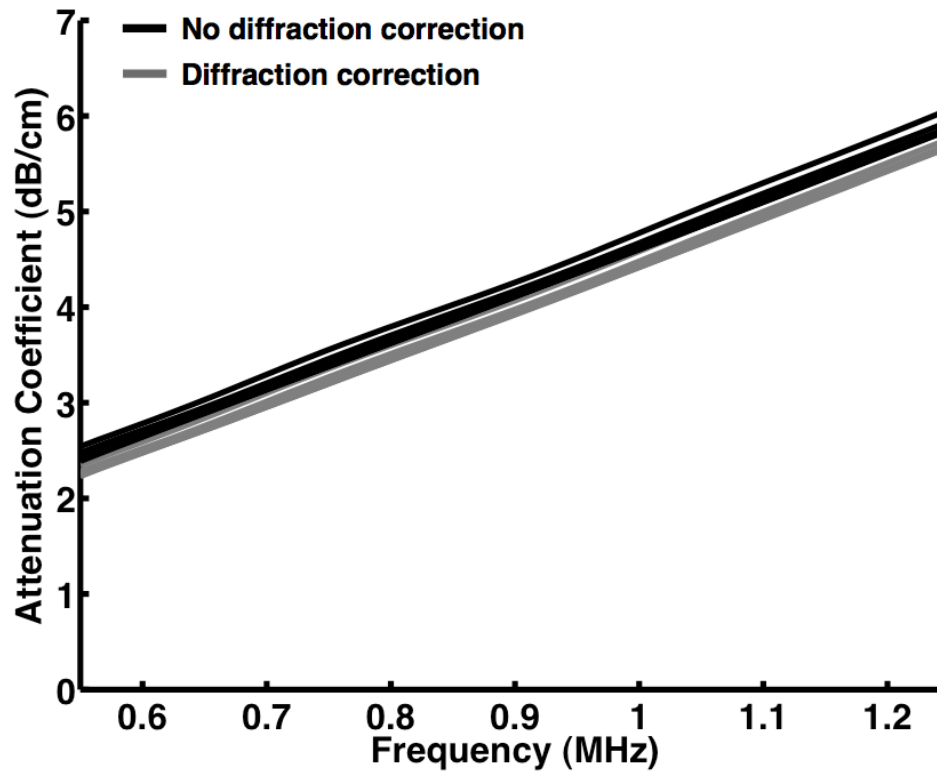


FIGURE 7.48: The attenuation coefficients plotted as a function of frequency, determined using conventional analysis methods, for the six thicknesses of Lexan<sup>TM</sup> listed in Table 7.14. The black lines represent the measurements that were not diffraction corrected and the gray lines represent the measurements that were diffraction corrected.

TABLE 7.15: The attenuation coefficient at 1 MHz for the six Lexan<sup>TM</sup> phantoms for a typical (not diffraction corrected) measurement and one that has been corrected for diffraction. The difference between the attenuation coefficient at 1 MHz for the not diffraction corrected measurement and the attenuation coefficient at 1 MHz for the diffraction corrected measurement is displayed in the last column.

	<b>Attenuation Coefficient at 1 MHz (dB/cm)</b>		
<b>Sample</b>	<b>Not Diffraction Corrected</b>	<b>Diffraction Corrected</b>	<b>Difference (dB/cm)</b>
L1	4.81	4.62	0.19
L2	4.71	4.52	0.19
L3	4.65	4.46	0.19
L4	4.64	4.45	0.19
L5	4.64	4.46	0.18
L6	4.64	4.45	0.19

ble 7.15. Since the diffraction correction is proportional to sample thickness, it was again expected that the difference between the attenuation coefficients would increase with increasing sample thickness.

The slopes of attenuation (nBUA) determined using conventional analysis for both diffraction-corrected and not diffraction corrected measurements are listed in Table 7.16 for the six thicknesses of Lexan<sup>TM</sup>. The differences between the diffraction-corrected nBUAs and the nBUAs that were not diffraction corrected were negligible. If only the amplitudes (and not the shapes) of the signals are different between diffraction-corrected and not diffraction corrected measurements, then the slopes of the attenuation coefficient would remain unchanged. Based on the results shown in Tables 7.15 and 7.16 it appeared that diffraction was not having

TABLE 7.16: The slope of the attenuation coefficient (nBUA) for the six Lexan<sup>TM</sup> phantoms for a typical (not diffraction corrected) measurement and one that has been corrected for diffraction. The difference between the nBUA for the not diffraction corrected measurement and the nBUA for the diffraction corrected measurement is displayed in the last column.

	<b>Slope of Attenuation (dB/cm/MHz)</b>		
<b>Sample</b>	<b>Not Diffraction Corrected</b>	<b>Diffraction Corrected</b>	<b>Difference (dB/cm)</b>
L1	4.99	5.00	-0.00
L2	4.93	4.93	-0.01
L3	4.86	4.86	-0.01
L4	4.88	4.88	-0.00
L5	4.90	4.89	0.01
L6	4.91	4.88	0.03

a significant effect, or at least was not displaying the expected sample thickness dependence.

Figure 7.49 shows the comparison between the phase velocity at 1 MHz determined using conventional phase spectroscopy and the phase velocity estimated by the Bayesian algorithm for the six thicknesses of Lexan<sup>TM</sup>. As has consistently been the case, the Bayesian and conventional phase velocity results were almost identical and were approximately independent of sample thickness.

The results of nBUA as a function of sample thickness are shown in Figure 7.50. As discussed above, conventional analysis applied to both diffraction-corrected and not diffraction-corrected measurements yielded similar slopes of attenuation. The conventional nBUA displayed some sample thickness dependence for the shorter sample lengths (i.e. 10 mm sample). However, this may be due to other experimental effects such as sample alignment and not an

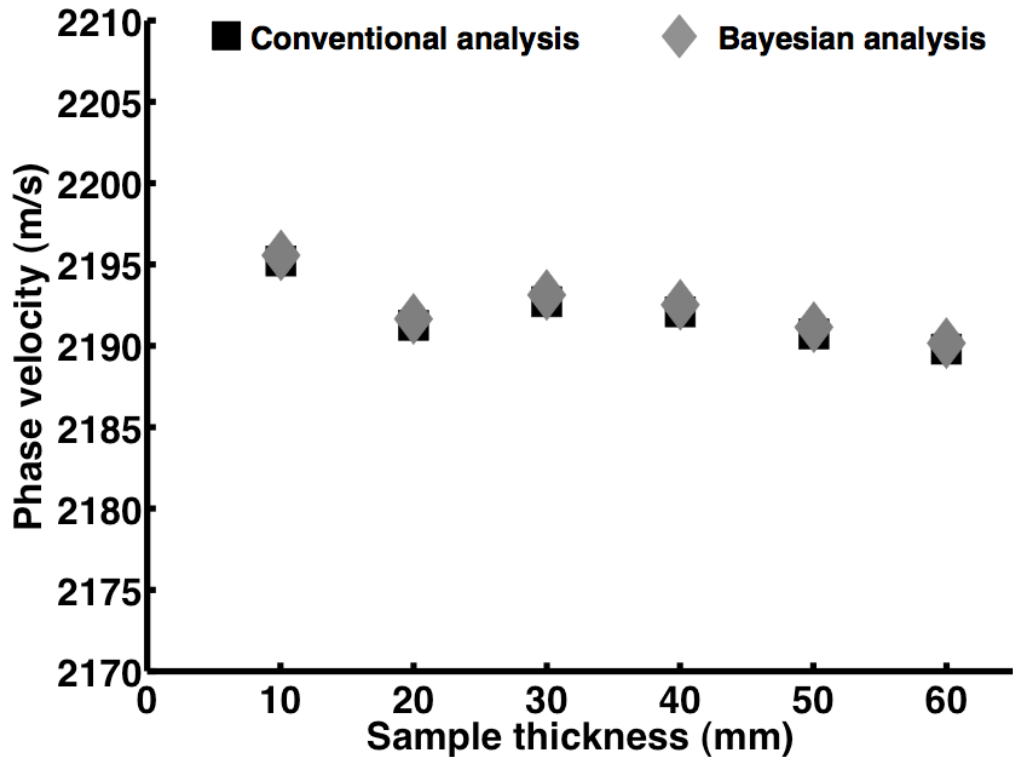


FIGURE 7.49: Comparison of the phase velocity at 1 MHz as a function of sample thickness determined using conventional analysis methods (black squares) and Bayesian analysis methods (gray diamonds).

effect of diffraction. In contrast, Bayesian analysis of the diffraction-corrected measurements and the not diffraction-corrected measurements yielded estimates of nBUA that systematically decreased with increasing sample thickness. The diffraction-corrected measurements analyzed by the Bayesian algorithm estimated values of  $\beta$  as low as 4.48 dB/cm/MHz for the thickest Lexan<sup>TM</sup> sample ( $d = 60$  mm).

The results for the transmission coefficient-related term  $A$  as a function of sample thickness are shown in Figure 7.51. The predicted  $A$  term, determined using the impedance difference between water and Lexan<sup>TM</sup> with the experimentally-determined velocity and mass density, was approximately independent of sample thickness as expected. Bayesian analysis

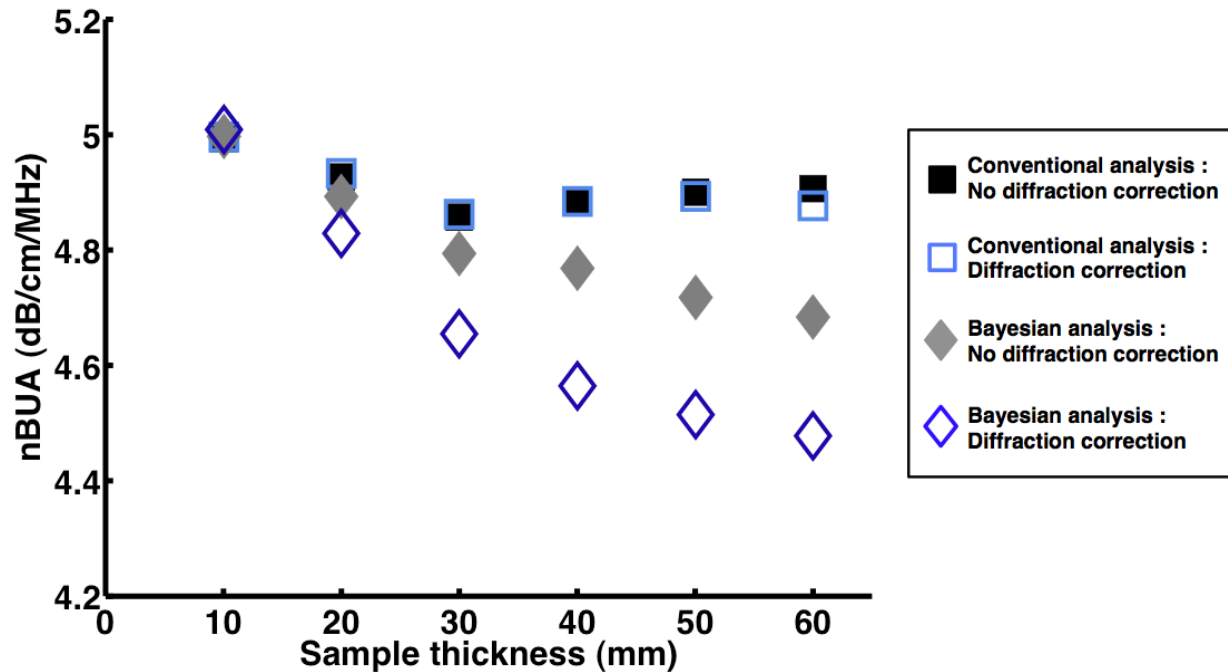


FIGURE 7.50: Comparison of the slope of the attenuation coefficient (nBUA) as a function of sample thickness determined using conventional and Bayesian analysis methods on both measurements not corrected for diffraction and for measurements corrected for diffraction.

of the not diffraction-corrected measurements yielded values of  $A$  that were always greater than the predicted value of 0.92, and that increased with sample thickness until reaching the maximum value of  $A = 1$  by sample thickness  $d = 40$  mm and remaining at that value for thicker samples of Lexan<sup>TM</sup>. Similar results were observed for Bayesian analysis of the diffraction-corrected measurements. However, in that case, the estimate of  $A$  reached the maximum value of 1 by sample thickness  $d = 20$  mm, and remained at that value for all thicker samples. These results, in conjunction with the results of  $\beta$  in Figure 7.50, implied that as sample thickness increased the Bayesian algorithm estimated less total (surface plus bulk) loss, and put the majority of the loss in the  $\beta$  term (since  $A = 1$  for most thicknesses). The Bayesian estimates of the diffraction-corrected measurements are lower (less lossy) than

the estimates of the not diffraction-corrected measurements because of the amplitude differences in the sample signals discussed above.

The transmission coefficient-related  $A$  terms obtained from the zero-frequency intercept of the signal loss versus frequency plot were also determined and are plotted in Figure 7.51. Both the diffraction-corrected and not diffraction-corrected  $A$  terms using the signal loss intercept showed significant sample thickness dependence, even more than either Bayesian estimate. Both diffraction-corrected and not diffraction-corrected  $A$  terms had values much greater than one, implying that energy was gained. Similar results for the  $A$  terms determined by signal loss intercept were observed in Sections 7.4 and 7.6.

Since the values of  $\beta$  and  $A$  determined using Bayesian analysis were significantly different from those determined using conventional analysis, especially for thicker samples, model waveforms were generated using both sets of parameters to investigate how well the models fit the experimental data. This was done for both the diffraction-corrected and the not diffraction-corrected measurements on the 60 mm thick Lexan<sup>TM</sup> phantom. The 60 mm Lexan<sup>TM</sup> sample was chosen because the discrepancies between the Bayesian and conventional results were the largest among the sample thicknesses measured. The values of  $A$ ,  $\beta$ , and  $c$ , shown in Figures 7.49 - 7.51, were put into the wave propagation model along with the reference (water-path-only) signal and forward propagated to generate a model sample signal. Two model waveforms were generated using the same conventional results for  $\beta$  and  $c$  but different values for  $A$ . One model waveform used the predicted value of  $A = 0.92$ , while the other model waveform used the  $A$  value determined by the zero-frequency intercept of the signal loss versus frequency plot.

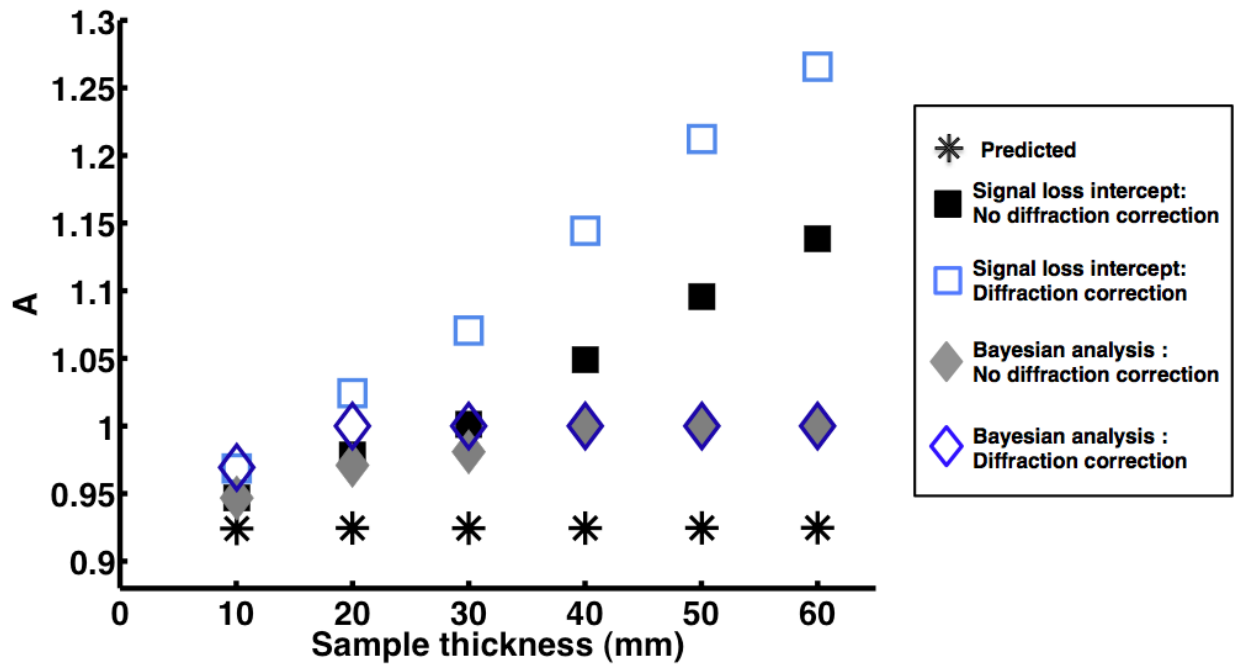


FIGURE 7.51: Comparison of the transmission coefficient-related term ( $A$ ) as a function of sample thickness for the six thicknesses of Lexan<sup>TM</sup>. The predicted  $A$  was determined using the impedance difference between water and Lexan<sup>TM</sup> with the experimentally-determined velocity and mass density. Bayesian analysis methods were applied to measurements not corrected for diffraction and to measurements corrected for diffraction. The conventional results were determined by the zero-frequency intercept of the signal loss versus frequency curve.



Figure 7.52 shows the comparison of the three model fits (two conventional and one Bayesian) to the experimental data that did not correct for diffraction from the 60 mm Lexan<sup>TM</sup> sample. These results imply that using the conventional parameter results with the predicted  $A$  term generates a model waveform that has more loss than the experimental signal. The conventional model waveform using the  $A$  term determined from the signal loss versus frequency intercept fit the experimental signal very well, although an  $A$  value greater than one does not make physical sense. It seems that having a  $A$  greater than one is counteracting the loss from  $\beta$ , thus producing a better fit. The model waveform generated using the Bayesian estimated parameters fit the experimental data very well, even though all the loss was placed into the  $\beta$  term (since  $A = 1$ ) and the estimate of  $\beta$  was smaller than the  $\beta$  determined by conventional analysis methods.

Similar results were observed for the diffraction-corrected measurements on the 60 mm Lexan<sup>TM</sup> phantom and are displayed in Figure 7.53. In this case, the predicted transmission coefficient-related term  $A$  along with the conventional results for  $\beta$  and  $c$  generated a model waveform that did an even worse job of fitting the experimental data than the not diffraction-corrected case discussed in the previous paragraph. Similar to the results shown in Figure 7.52, the Bayesian-generated model fit the experimental waveform the best.

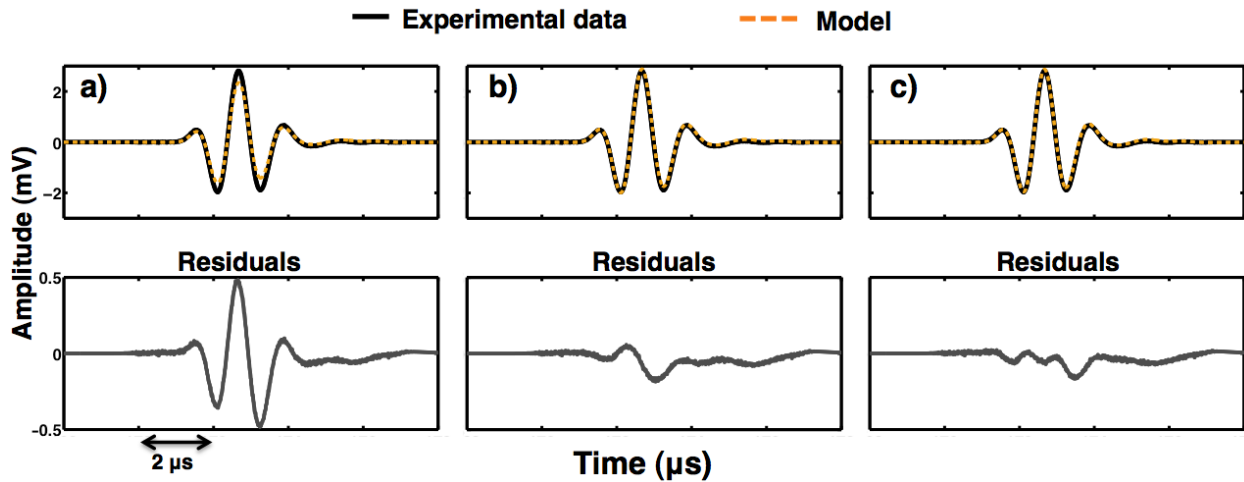


FIGURE 7.52: Comparison of model waveforms to the experimental data from the 60 mm thick Lexan<sup>TM</sup> phantom with no diffraction correction. (a) Model waveform generated using the propagation model with the values determined by conventional analysis for  $A$ ,  $\beta$ , and  $c$ . In this panel,  $A$  is the predicted value of  $A = 0.92$ . (b) Model waveform generated with the values determined by conventional analysis. In this panel,  $A$  is the value determined by the zero-frequency intercept of the signal loss versus frequency plot. (c) Model waveform generated using the values of  $A$ ,  $\beta$ , and  $c$  estimated by the Bayesian algorithm.

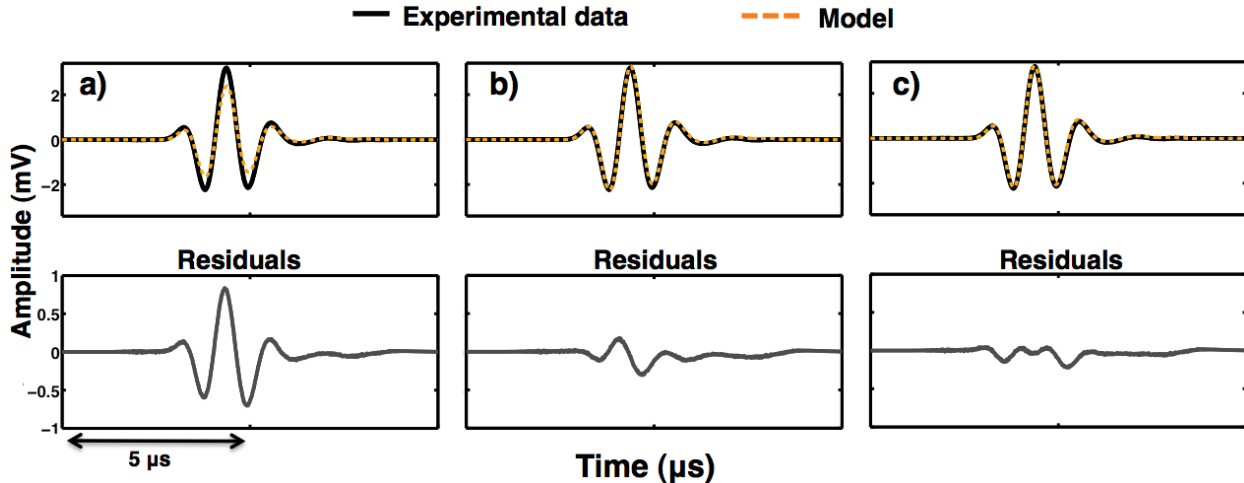


FIGURE 7.53: Comparison of model waveforms to the experimental data from the 60 mm thick Lexan<sup>TM</sup> phantom that was diffraction corrected. (a) Model waveform generated using the propagation model with the values determined by conventional analysis for  $A$ ,  $\beta$ , and  $c$ . In this panel,  $A$  is the predicted value of  $A = 0.92$ . (b) Model waveform generated with the values determined by conventional analysis. In this panel,  $A$  is the value determined by the zero-frequency intercept of the signal loss versus frequency plot. (c) Model waveform generated using the values of  $A$ ,  $\beta$ , and  $c$  estimated by the Bayesian algorithm.

## 7.9 Effects of receiver location relative to the transmitting transducer

Since the diffraction study discussed in the previous section did not reduce the observed distance-dependence of the parameters  $A$  and  $\beta$ , a more thorough study was carried out to investigate if the location of the receiving transducer, in relation to the transmitting transducer, affected the ultrasonic parameters determined by either conventional or Bayesian analysis. This study used the same pair of transducers and experimental set-up implemented in the diffraction experiment. Both reference and sample measurements were acquired with the receiver at specific axial locations. The receiving transducer was moved axially from +40 mm to -40 mm in 10 mm steps, with 0 mm being the normal separation between the transmitting and receiving transducer (typically twice the focal length of the transducer). The 1 MHz transducers used in this study were typically separated by 8 inches (203 mm). The axial translation of the receiving transducer from -40 mm (closer to transmitting transducer) to +40 mm (further from transmitting transducer) corresponded to more than 1.5 inches in either direction from the original transducer separation (0 mm). In order to prevent any backlash effects, the receiving transducer which was attached to a computerized motion controller was moved beyond the +40 mm location first and then only moved in one direction during the data collection. The measurements presented in this section were made on a 40 mm thick Lexan<sup>TM</sup> phantom.

The data collected in this study was analyzed two different ways. The data was first analyzed using the reference and sample data acquired at the same axial location (or same

distance from transmitting transducer). Comparing reference measurements to sample measurements acquired at the same receiver position is the typical way to collect and analyze ultrasonic data. This analysis technique should provide insight into if the axial location of the receiver, in relation to the transmitting transducer, matters. It was already shown earlier in this chapter that the position of the sample between the transmitting and receiving transducer does not effect the results.

The second way the data was analyzed was to compare the reference data taken at the normal transducer separation ( $\Delta L = 0$  mm) to the sample data acquired when the receiving transducer was moved to nine axial locations ( $\Delta L = -40$  mm,  $-30$  mm,  $-20$  mm,  $-10$  mm,  $0$  mm,  $+10$  mm,  $+20$  mm,  $+30$  mm,  $+40$  mm). This was an expansion of the diffraction study discussed above. In the diffraction study, the diffraction correction for the 40 mm thick Lexan<sup>TM</sup> phantom was approximately  $-19$  mm (receiver moved closer to transmitter). In this study, one of the acquired axial positions was  $\Delta L = -20$  mm, which was approximately the diffraction-corrected distance, in addition to eight other sample receiver locations.

### **Analysis of reference and sample data from same axial locations**

Reference and sample measurements on the 40 mm thick Lexan<sup>TM</sup> sample were acquired at nine axial locations and were analyzed using both conventional and Bayesian analysis. Figure 7.54 shows the peak-to-peak amplitudes of the reference and sample signals as a function of receiver location. Both the reference and sample signals displayed a systematic (approximately linear) decrease in P-P amplitude as the receiver was moved away from the transmitting transducer. This systematic dependence was unexpected since the effects of

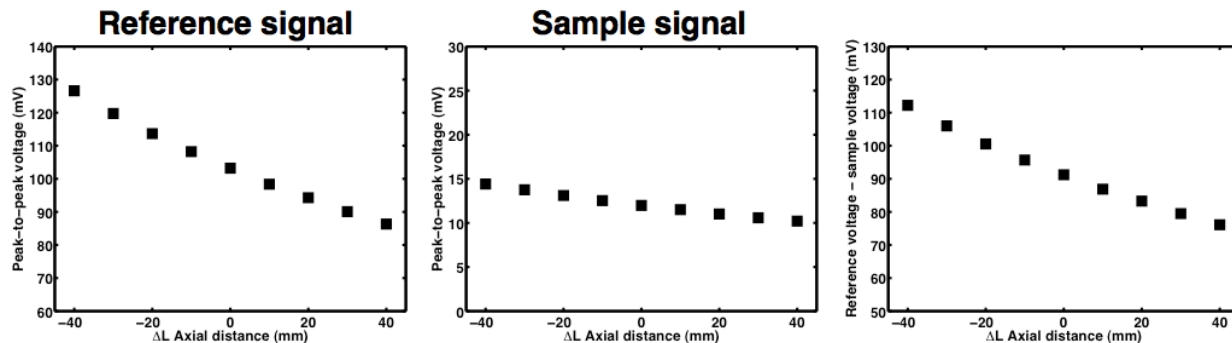


FIGURE 7.54: The peak-to-peak amplitude of the reference (water-path-only) signal and the sample signal as a function of distance from the transmitting transducer for measurements made on the 40 mm thick Lexan<sup>TM</sup> phantom.  $\Delta L = 0$  mm corresponds to the receiving transducer located at twice the focal length (8 inches) from the transmitting transducer. The third panel shows the difference in peak-to-peak voltage of the reference and sample signals as a function of axial location.

diffraction and phase cancellation both within the field and at the face of the receiving transducer are not necessarily linear with axial location. The peak-to-peak amplitude of the reference signal changed more rapidly than the P-P amplitude of the sample signal. The amplitude of the reference signal decreased by approximately 0.5 mV per millimeter of axial translation, while the amplitude of the sample signal decreased by only 0.05 mV per millimeter of axial translation. Although the amplitudes of the reference and sample signals do suggest that the position of the receiver may matter, these results cannot be used to infer the effects of receiver position on the attenuation properties, such as  $\beta$ , since amplitude measurements assume a narrowband signal, not a broadband signal like the one that was used in this study.

Signal loss measurements were determined by log-spectral subtraction for the nine axial locations. The predicted insertion (surface) losses were calculated to be approximately 0.68 dB. This was the total loss at both front and back surfaces. Thus, it was expected (by

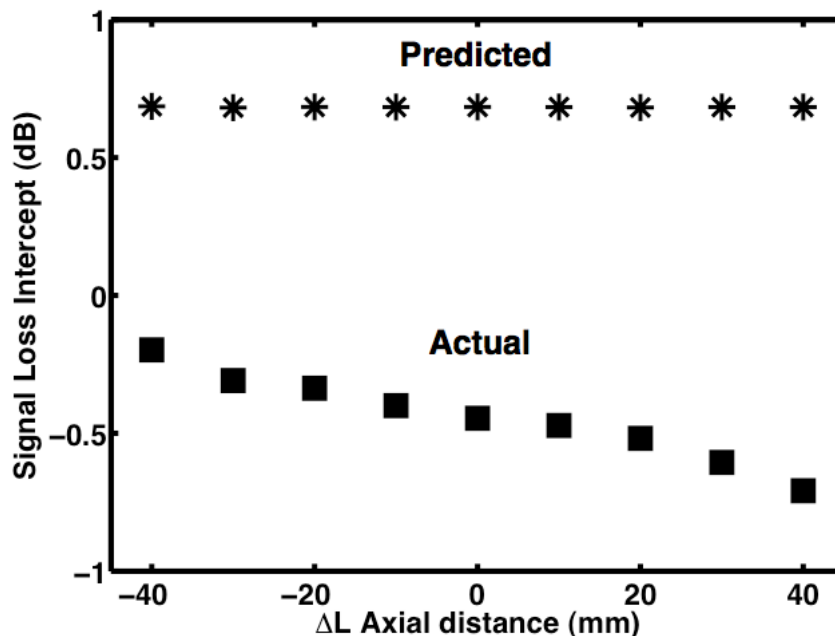


FIGURE 7.55: The predicted and actual zero-frequency intercepts of the signal loss as a function of the axial location of the receiving transducer. Reference and sample measurements were analyzed for the same axial location.

theory) that the zero-frequency intercept of the signal loss versus frequency plots should be approximately 0.68 dB. However, the actual zero-frequency intercepts of the signal loss curves were all negative values and decreased with increasing transducer separation, as shown in Figure 7.55. As will be seen later in Figure 7.58, these negative signal loss intercepts correspond to transmission coefficient-related terms that are greater than one, implying that energy was gained, not lost at the surfaces. Although this result did not follow the predictions, it was consistent with the results of the other Lexan<sup>TM</sup> studies in this chapter.

The attenuation coefficient, determined using conventional analysis methods, of the 40 mm Lexan<sup>TM</sup> phantom at the nine axial locations are shown in Figure 7.56. They appeared to be consistent with each other even though the receiving transducer was moved over a range of 3 inches. However, when the data was examined on a finer scale, it was discovered that the

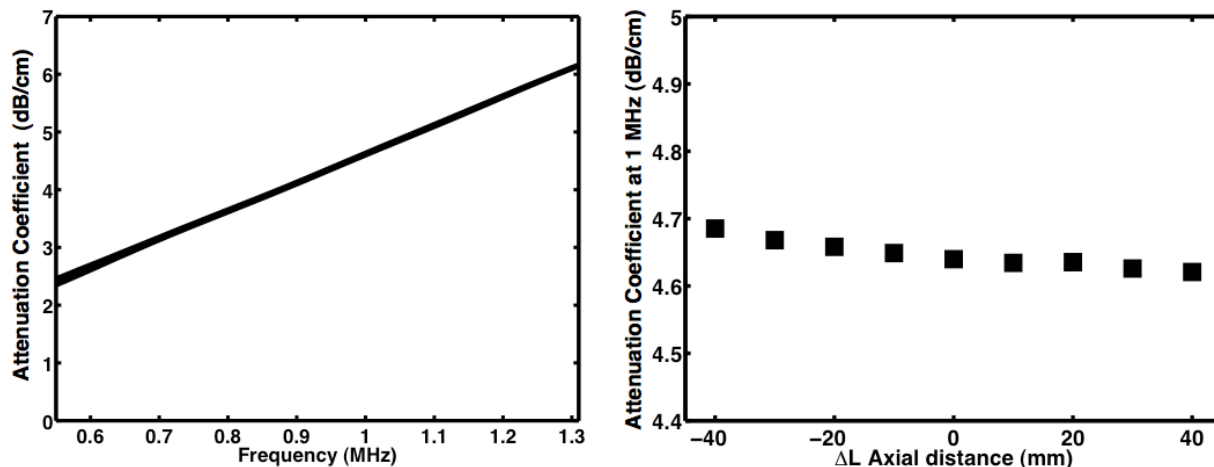


FIGURE 7.56: Left panel: Attenuation coefficient as a function of frequency for the 40 mm Lexan<sup>TM</sup> phantom for data acquired at 9 axial locations. Right panel: The attenuation coefficient at 1 MHz as a function of the axial location of the receiving transducer. Reference and sample measurements were analyzed for the same axial location.

attenuation coefficient at 1 MHz decreased slightly as the receiving transducer was moved farther away from the transmitting transducer. However, the change in the attenuation coefficient when moving the receiving transducer from -40 mm to +40 mm was only 0.06 dB/cm. This result was consistent with, but not fully explained by, the decrease of the signal loss intercept with axial location.

The slopes of the attenuation coefficient (nBUA) as functions of the axial location of the receiving transducer for the 40 mm Lexan<sup>TM</sup> phantom are shown in Figure 7.57 and Table 7.17 for both conventional and Bayesian analysis. Consistent with other studies in this thesis, the  $\beta$  estimated by the Bayesian algorithm was smaller than the  $\beta$  determined using conventional analysis for all axial locations. The slope of attenuation determined using conventional methods increased slightly as the receiving transducer was moved farther away from the transmitting transducer, whereas the nBUA estimated by the Bayesian algorithm

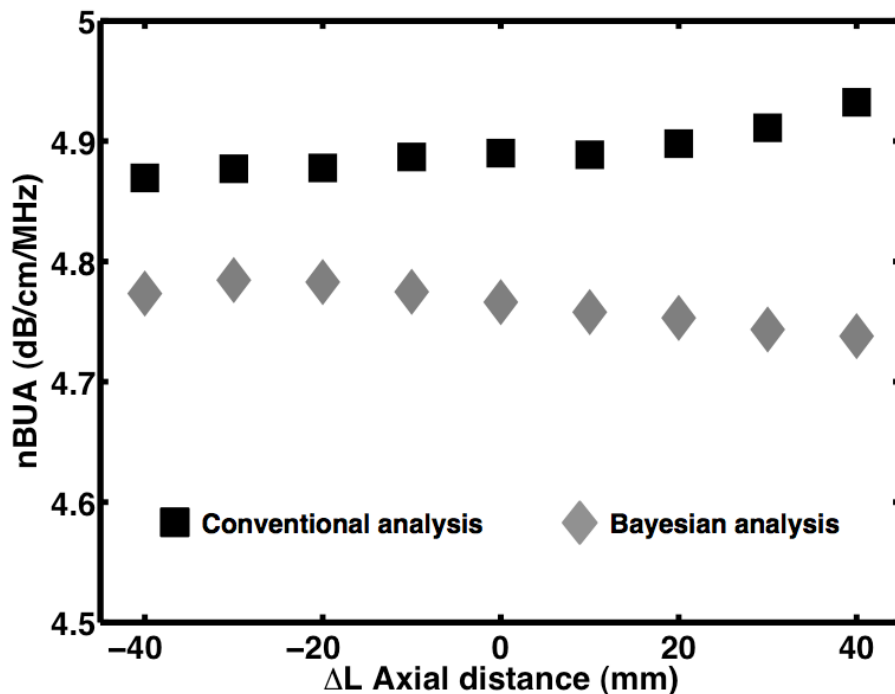


FIGURE 7.57: The slope of the attenuation coefficient (nBUA) determined using conventional and Bayesian analysis methods as a function of the axial location of the receiving transducer. Reference and sample measurements were analyzed at the same axial location.

decreased with increased transducer separation.

The results for the transmission coefficient-related terms ( $A$ ) are shown in Figure 7.58 as a function of the axial location of the receiving transducer. The predicted value was calculated to be approximately 0.92 and constant over all transducer positions. Similar to the results in the other Lexan<sup>TM</sup> studies presented in this chapter, the results of the Bayesian algorithm estimated the  $A$  term to be a value of one for all transducer positions except for  $\Delta L = -40$  mm. This implied that all the loss was attributed to bulk loss ( $\beta$ ) and none attributed to surface losses. Using the zero-frequency intercept of the signal loss plot to determine the  $A$  term yielded values that were greater than one for all locations and increased with increasing separation between the transducers.



TABLE 7.17: The slopes of the attenuation coefficient (nBUA) for the 40 mm thick Lexan<sup>TM</sup> phantom for nine axial locations of the receiving transducer determined using conventional and Bayesian analysis methods. Reference and sample measurements were analyzed at the same axial location.

Axial location ( $\Delta L$ ) (mm)	Conventional $\beta$ (dB/cm/MHz)	Bayesian $\beta$ (dB/cm/MHz)
-40 mm	4.87	4.77
-30 mm	4.88	4.79
-20 mm	4.88	4.78
-10 mm	4.89	4.78
0 mm	4.89	4.77
+10 mm	4.89	4.76
+20 mm	4.90	4.75
+30 mm	4.91	4.74
+40 mm	4.93	4.74

The results of this study implied that the location of the receiving transducer relative to the transmitting transducer had small, mostly negligible effects on the ultrasonic parameters determined using either conventional or Bayesian analysis. It may be possible that the small effects seen in this study were caused by diffraction, which were not taken into account.

### Analysis of reference and sample data from different axial locations

For this study, the sample signals acquired when the receiving transducer was moved to nine axial locations in the ultrasonic field were compared to the reference signal acquired at the typical transducer separation (twice the focal length or  $\Delta L = 0$  mm). For receiver position  $\Delta L = 0$  mm, the sample and reference signal were analyzed for the same transducer separation, which is the typical analysis method. For receiver position  $\Delta L = -20$  mm, the

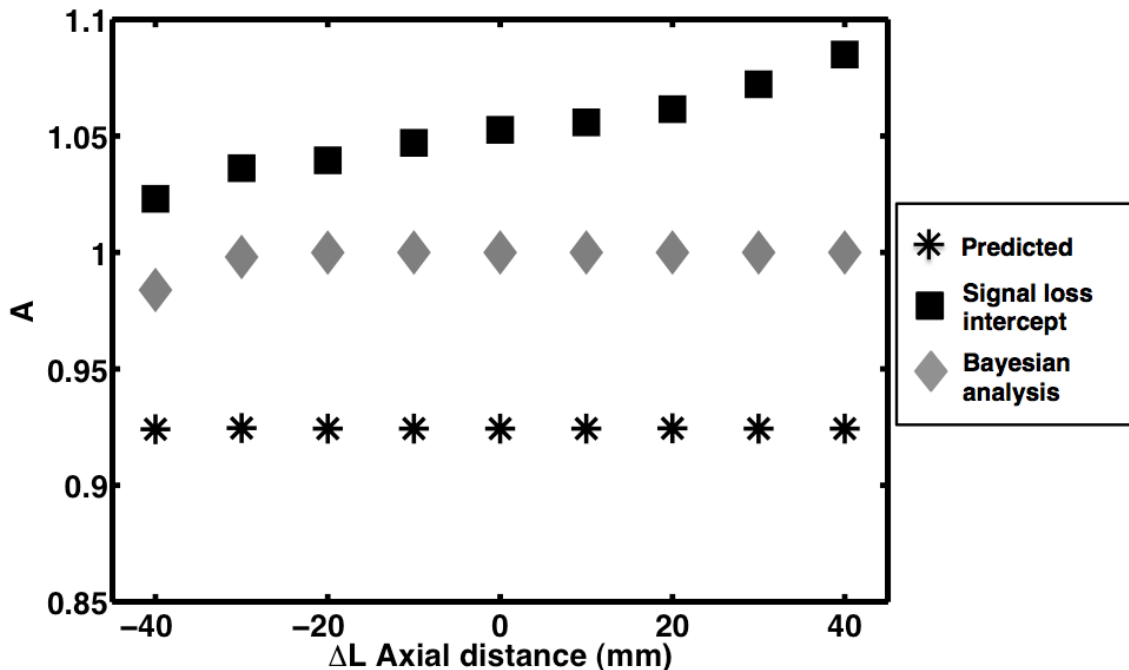


FIGURE 7.58: The transmission coefficient-related  $A$  term determined using conventional and Bayesian analysis methods as a function of the axial location of the receiving transducer. The predicted value of  $A$  is also displayed. Reference and sample measurements were analyzed at the same axial location.

sample signal acquired at  $\Delta L = -20$  mm was compared to the reference signal at  $\Delta L = 0$  mm, which is the diffraction-corrected analysis for the 40 mm thick Lexan<sup>TM</sup> phantom. It was hoped that this study would shed light on the diffraction-correction used in Section 7.8 and perhaps identify a diffraction correction that produced results that agreed with predicted values.

Figure 7.59 shows the zero-frequency intercept of the signal loss versus frequency plot as a function of the axial location of the receiving transducer. As before, the predicted signal loss intercept was calculated to be approximately 0.68 dB and independent of receiver location. The actual signal loss intercept was dependent significantly on receiver position, increasing linearly with increasing transducer separation. Based on these results, it appeared

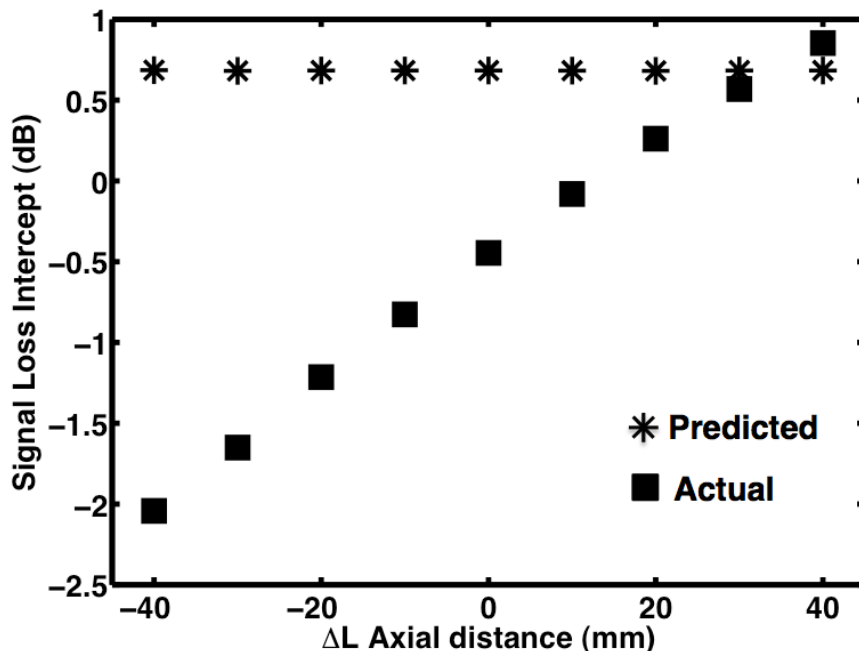


FIGURE 7.59: The predicted and actual zero-frequency intercepts of the signal loss as a function of the axial location of the receiving transducer. Sample measurements at the nine axial locations of the receiving transducer were compared to the reference measurement at the typical transducer separation ( $\Delta L = 0$  mm).

that moving the receiving transducer to  $\Delta L = +30$  mm yielded a signal loss intercept that was close to the predicted value.

The attenuation coefficients for the 40 mm thick Lexan<sup>TM</sup> phantom when sample data was acquired at nine axial locations is shown in Figure 7.60. All the attenuation coefficients plotted as a function of frequency appeared to have the same slope but had a vertical offset from each other. This effect can be seen more clearly in the right panel of Figure 7.60, which displays the attenuation coefficient at 1 MHz as a function of the axial position of the receiving transducer. As was expected, the attenuation coefficient at 1 MHz for  $\Delta L = 0$  mm agreed with the non-diffraction-corrected attenuation coefficient presented in Section 7.8, while the attenuation coefficient at 1 MHz for  $\Delta L = -20$  mm agreed with the diffraction-

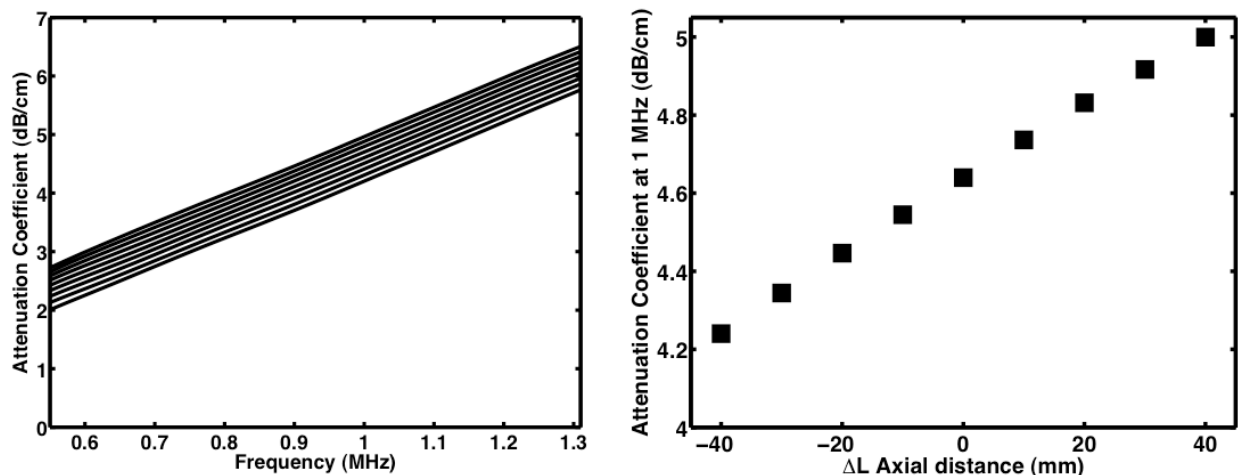


FIGURE 7.60: Left panel: Attenuation coefficient as a function of frequency for the 40 mm Lexan<sup>TM</sup> phantom for data acquired at 9 axial locations. Right panel: The attenuation coefficient at 1 MHz as a function of the axial location of the receiving transducer. Sample measurements at the nine axial locations of the receiving transducer were compared to the reference measurement at the typical transducer separation ( $\Delta L = 0$  mm).

corrected attenuation coefficient for the 40 mm thick Lexan<sup>TM</sup> sample. The attenuation coefficient at 1 MHz consistently increased by approximately 0.1 dB/cm for every 10 mm the receiving transducer was moved away from the transmitting transducer.

The slopes of the attenuation coefficient (nBUA) as a function of the axial location of the receiving transducer for the 40 mm Lexan<sup>TM</sup> phantom are shown in Figure 7.61 and Table 7.18 for both conventional and Bayesian analysis. The slopes of attenuation determined using conventional methods were consistent with the nBUA values determined in the previous section with the sample and reference data analyzed at the same axial location. This suggested that conventionally-determined  $\beta$  may be relatively less susceptible to diffraction-related effects even though the attenuation coefficient is influenced. This was in contrast to the nBUA estimated by the Bayesian algorithm which increased linearly from 4.34 dB/cm/MHz to 4.77 dB/cm/MHz when the receiving transducer was moved from  $\Delta L$

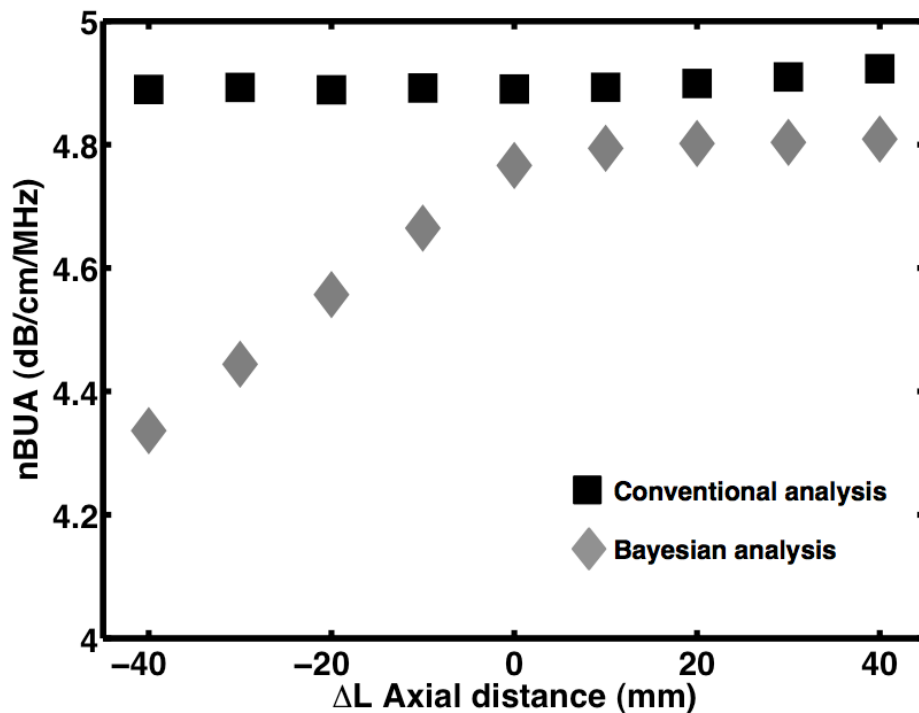


FIGURE 7.61: The slope of the attenuation coefficient (nBUA) determined using conventional and Bayesian analysis methods as a function of the axial location of the receiving transducer. Sample measurements at the nine axial locations of the receiving transducer were compared to the reference measurement at the typical transducer separation ( $\Delta L = 0$  mm).

= -40 mm to  $\Delta L = 0$  mm, and then remained at a relatively constant value for all other axial locations.

An opposite trend was observed for the Bayesian-estimated  $A$  term shown in Figure 7.62 as a function of axial location of the receiving transducer. For axial locations  $\Delta L = -40$  mm through  $\Delta L = 0$  mm, the Bayesian algorithm estimated the value of  $A$  to be equal to one, and for axial locations greater than  $\Delta L = 0$  mm, the estimated  $A$  term decreased linearly. The transmission coefficient-related term determined using the signal loss intercept decreased linearly across all axial locations. The values of  $A$  determined by the Bayesian algorithm and the signal loss intercept agreed with those found in Section 7.8 for the 40 mm

TABLE 7.18: The slopes of the attenuation coefficient (nBUA) for the 40 mm thick Lexan<sup>TM</sup> phantom for nine axial locations of the receiving transducer determined using conventional and Bayesian analysis methods. Sample measurements at the nine axial locations of the receiving transducer were compared to the reference measurement at the typical transducer separation ( $\Delta L = 0$  mm).

Axial location ( $\Delta L$ ) (mm)	Conventional $\beta$ (dB/cm/MHz)	Bayesian $\beta$ (dB/cm/MHz)
-40 mm	4.89	4.34
-30 mm	4.89	4.44
-20 mm	4.89	4.56
-10 mm	4.89	4.67
0 mm	4.89	4.77
+10 mm	4.89	4.79
+20 mm	4.90	4.80
+30 mm	4.91	4.80
+40 mm	4.92	4.81

thick Lexan<sup>TM</sup> sample. Based on these results, it appeared that the  $A$  term determined by both the Bayesian algorithm and the signal loss intercept agreed the best with the predicted value for  $\Delta L = +30$  mm, and agreed quite poorly for  $\Delta L = -20$  mm, which was the value predicted by the diffraction correction in Equation 7.15.

## 7.10 Discussion

The sample-thickness dependence of the ultrasonic parameters observed in studies presented in this thesis on both equine cancellous bone, which permits two longitudinal wave modes, and on Lexan<sup>TM</sup> phantoms, which permits only one longitudinal wave mode, is perplexing and still currently unexplained. This unexpected phenomenon is not limited to our

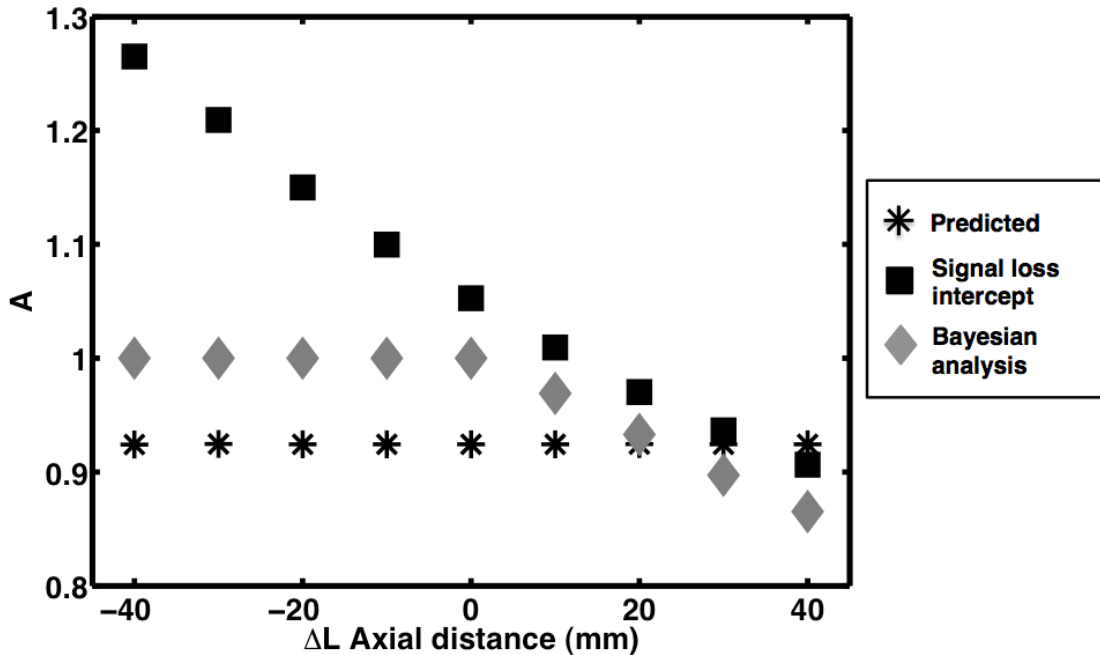


FIGURE 7.62: The transmission coefficient-related term  $A$  determined using conventional and Bayesian analysis methods as a function of the axial location of the receiving transducer. The predicted values of  $A$  are also displayed. Sample measurements at the nine axial locations of the receiving transducer were compared to the reference measurement at the typical transducer separation ( $\Delta L = 0$  mm).

data and the Bayesian technique. Keith Wear, a former post doc in the Laboratory for Ultrasonics and current researcher at the FDA, recently reported similar sample thickness dependences with data acquired from bovine cancellous bone and analyzed with a modified least-squares Prony's method, which decomposes the received signal into its fast and slow wave components in a fashion that is analogous to that of the Bayesian method (Wear *et al.*, 2014).

The variation with sample thickness may be the result of several different effects working in combination, thus making it difficult to determine the exact causes. One potential series of experiments that may provide additional insights into the observed sample-thickness dependence would be to remeasure the samples studied in this chapter using a two-dimensional

array of point-like receivers (hydrophones). The data collected could then be processed using phase-insensitive analysis methods to determine if phase cancellation at the face of the phase sensitive receiving transducer is contributing to the sample-thickness effects seen in this thesis. Such a data set would permit the use of well-known focusing techniques (including simple time-of-flight focusing and correlation focusing) that might yield additional insights.

## 7.11 Summary and conclusions

A series of systematic studies were performed on Lexan<sup>TM</sup> phantoms to explore the possible explanations for the sample-thickness dependence of the ultrasonic parameters observed in the measurements of equine bone presented in the previous chapter.

Initial measurements were acquired on three Lexan<sup>TM</sup> phantoms with approximate thicknesses of 10, 20, and 40 mm. These data were used to perform consistency checks of the Bayesian algorithm and the propagation model, and to investigate the influence of noise levels. The frequency-independent loss term  $A$  in the propagation model used in the Bayesian model was explicitly defined in terms of the amplitude transmission coefficients along with inclusion of the explicit complex acoustic impedances that account for loss. However, this change to the propagation model did not produce any significant changes in the Bayesian estimate of  $A$  or any of the other parameters. Another study determined that nonlinear propagation effects were not present in these experiments.

Measurements were also carried out on a systematically shortened Lexan<sup>TM</sup> phantom



with dimensions similar to those of the equine specimen. The results of Bayesian and conventional analysis on this data set were consistent with those results from the initial Lexan<sup>TM</sup> measurements. The phase velocity results estimated by the Bayesian algorithm were in excellent agreement with the phase velocities determined by conventional analysis. Additionally, neither analysis method produced phase velocities that were sample-thickness dependent. However, the Bayesian-estimated nBUA was consistently smaller than the conventionally-determined nBUA and also displayed a modest, systematic dependence with sample thickness. A similar trend was seen for the transmission coefficient-related  $A$  term. While the predicted  $A$  term was independent of sample thickness, the Bayesian-estimated  $A$  increased systematically with thickness and was always larger than the predicted value. However, the conventionally-determined  $A$ , found by the zero-frequency intercept of the signal loss, had even larger values which for larger sample thickness even surpassed the value of one. Band-pass Butterworth filters were applied to this data set to limit the range of frequency present in the signals used as input into the Bayesian algorithm to those frequencies used in conventional analysis. The application of frequency filters produced a slight, but insignificant reduction in the sample thickness dependence of the Bayesian-estimated nBUA and  $A$  term.

The location of the sample between the transmitting and receiving transducers was determined to have no effect. The effects of the position of the receiving transducer, relative to the transmitting transducer, was also studied. Analysis of the reference and sample measurements acquired at the same axial location yielded nBUA and  $A$  values that were modestly dependent on the axial location of the receiving transducer. This implies that the receiver location may cause an effect (presumably due to alterations in the ultrasonic

field as it propagates) but the magnitude of that effect may be negligible depending on the lossiness of the sample being studied. The effects of diffraction were also described and studied using six thicknesses of Lexan<sup>TM</sup>, ranging from approximately 10 mm up to 60 mm. The predicted diffraction correction did not reduce the sample-thickness dependence and actually increased the dependence observed in the Bayesian-estimated nBUA and  $A$  term. There was no change observed in the nBUA determined by conventional methods for the diffraction-corrected data.

Additional studies were carried out to vary systematically the surface losses. This was done to further explore the issue of surface losses versus volume (that is, bulk) losses. The results found for nBUA were consistent with those results from the other Lexan<sup>TM</sup> studies. While the nBUA determined using conventional analysis was approximately constant with sample thickness, the Bayesian-estimated nBUA decreased systematically with increasing sample thickness. This trend was observed for each number of surfaces. A more complicated dependence with sample thickness and number of surfaces was observed for the Bayesian-estimated  $A$  term.

In all of the studies carried out in this chapter, the model waveform generated using the parameters estimated by the Bayesian algorithm fit the experimental sample waveform better than the waveform generated using the parameters determined by either conventional analysis or predictions.

The studies and results presented in this chapter provide insight into the potential contributors of the observed sample thickness dependence. Although none of the studied tests corrected this unexpected behavior, some of the possible causes were eliminated.

## Bibliography

- Anderson, C. C., Bauer, A. Q., Holland, M. R., Pakula, M., Laugier, P., Bretthorst, G. L., and Miller, J. G. (2010), “Inverse problems in cancellous bone: estimation of the ultrasonic properties of fast and slow waves using Bayesian probability theory”, *J Acoust Soc Am* **128**(5), 2940–48.
- Bauer, A. Q., Marutyan, K. R., Holland, M. R., and Miller, J. G. (2007), “Is the Kramers-Kronig relationship between ultrasonic attenuation and dispersion maintained in the presence of apparent losses due to phase cancellation?”, *J Acoust Soc Am* **122**(1), 222–28.
- Kay, S. M. and Marple, J., S. L. (1981), “Spectrum analysis - A modern perspective”, *Proceedings of the IEEE* **69**(11), 1380–1419.
- Lloyd, C. (2010), “Enhancing nonlinear ultrasonic methods for laboratory and clinical applications”, Ph.D. thesis, Washington University in St. Louis.
- Wallace, K. D. (2001), “Characterization of the nonlinear propagation of diffracting, finite amplitude ultrasonic fields”, Ph.D. thesis, Washington University in St. Louis.
- Waters, K. R., Hughes, M. S., Mobley, J., and Miller, J. G. (2003), “Differential forms of the Kramers-Kronig dispersion relations”, *IEEE Trans Ultrason Ferroelectr Freq Control* **50**, 68–76.
- Wear, K., Nagatani, Y., Mizuno, K., and Matsukawa, M. (2014), “Temporal evolution of fast and slow waves during propagation through bovine cancellous Bbone in vitro”, Abstract: IEEE International Ultrasonics Symposium .
- Xu, W. and Kaufman, J. (1993), “Diffraction correction methods for insertion ultrasound attenuation estimation”, *IEEE Trans Biom Eng* **40**, 563–570.

# CHAPTER 8

---

## SUMMARY AND CONCLUDING REMARKS

This dissertation detailed simulated and experimental studies that investigated the physics underlying the interaction between cancellous bone and ultrasound. A central theme was the comparison between the results determined by conventional analysis methods and the results estimated by a Bayesian probability theory analysis method. An additional, unexpected need emerged to investigate the sample-thickness dependence of the ultrasonic parameters obtained by either method of analysis.

Chapter 2 provided background information related to bone physiology, as well as the use of quantitative ultrasound to diagnose and monitor osteoporosis. The potential presence of two longitudinal wave modes (fast and slow waves) propagating in bone was also discussed along with the complications that may arise from overlapping waves.

Chapter 3 described the methods of analysis that were used in later chapters of this thesis. An overview of how ultrasonic parameters of interest are determined by conventional analysis methods were presented. A brief introduction to Bayesian probability theory was given along with an explanation of how Bayesian methods in conjunction with a two-mode

---

wave propagation model can be used to provide estimates of the ultrasonic parameters for fast and slow waves.

Studies carried out on human calcaneal bone specimens were the focus of Chapter 4. Conventional and Bayesian analysis methods were applied to data acquired on eight human heel bone samples with insonification in the medial-lateral (perpendicular) direction. Although the received sample signals all appeared to be comprised of a single wave mode, the Bayesian algorithm was able to successfully separate the received trace into its fast and slow wave components. The results showed that the phase velocity for the single (unseparated) wave mode lay between the fast and slow wave velocities, and that the nBUA for the single mode was much greater than the nBUA associated with either the fast or slow waves. This implied that performing conventional analysis on a wave that is comprised of two overlapping waves modes may overestimate the true signal loss. Results also showed that the Bayesian-estimated parameters for the fast and slow waves correlated moderately well with microstructural parameters determined by microCT measurements.

Chapter 5 investigated the effects of overlapping fast and slow waves on measurements of the attenuation as a function of sample thickness along with the method of analysis employed in determining the attenuation properties. Two methods of analysis were applied to simulated data for a range of sample thicknesses. Applying time-domain analysis to broadband data yielded apparent attenuations that were sample length dependent. In contrast, performing frequency-domain analysis on separated (by the Bayesian algorithm) fast and slow waves resulted in attenuation coefficients that were independent of sample length.

In Chapter 6, conventional analysis and Bayesian parameter estimation were applied to

---

ultrasonic data acquired on a cancellous bone specimen extracted from an equine radius. The sample was systematically shortened in 0.5 mm increments from approximately 12 mm down to 0.5 mm, with measurements taken at each sample length. Conventional analysis methods were performed on the sample lengths that were sufficiently long as to permit separation of the fast and slow waves in the time-domain. Bayesian analysis was performed on data from all sample lengths. Over the same sample lengths, the average Bayesian and conventional results for phase velocity and nBUA agreed quite well. However, it was found (unexpectedly) that the parameters obtained by both conventional and Bayesian analysis displayed small, systematic variations with sample length.

The unexpected sample thickness dependence of the ultrasonic parameters observed in Chapter 6 was investigated more thoroughly using one-mode Lexan phantoms in Chapter 7. A series of systematic studies were performed to eliminate or confirm the cause or causes of the observed sample thickness dependence. Although no clear cause was found, the results among the various studies performed on Lexan were very consistent and provided some insights into the potential contributors of the observed sample thickness dependence. In spite of these unexplained observations, the studies in this thesis represent a potentially useful advance in the understanding of the physics of the interaction between cancellous bone tissue and ultrasound.